NOVEL METHOD FOR SYNTHESIS OF NANOCOMPOSITES

SAIKAT MANDAL

DECEMBER 2004

NOVEL METHOD FOR SYNTHESIS OF NANOCOMPOSITES

THESIS SUBMITTED TO

UNIVERSITY OF PUNE

FOR THE DEGREE OF

DOCTOR OF PHILOSOPHY

IN

CHEMISTRY

BY

SAIKAT MANDAL

PHYSICAL & MATERIALS CHEMISTRY DIVISION
NATIONAL CHEMICAL LABORATORY
PUNE 411 008
INDIA

DECEMBER 2004

Dedicated

to my

Parents..

C E R T I F I C A T E

This is to certify that the work discussed in the thesis entitled **“NOVEL METHOD FOR SYNTHESIS OF NANOCOMPOSITES”** by **SAIKAT MANDAL** for the Degree of ***Doctor of Philosophy*** in Chemistry was carried out under my supervision at the Physical & Materials Chemistry Division in National Chemical Laboratory, Pune. Such material as has been obtained from other sources has been duly acknowledged in this thesis. To the best of my knowledge, the present work or any part thereof, has not been submitted to any other university for the award of any other degree or diploma.

Date: Dr. Murali Sastry

Place: Pune (Research Guide)

DECLARATION BY RESEARCH SCHOLAR

I hereby declare that the thesis entitled "**NOVEL METHOD FOR SYNTHESIS OF NANOCOMPOSITES**", submitted for the Degree of ***Doctor of Philosophy*** in Chemistry to the University of Pune, has been carried out by me at the Physical & Materials Chemistry Division, National Chemical Laboratory, Pune 411 008, India, under the supervision of Dr. Murali Sastry. The work is original and has not been submitted in part or full by me for any other degree or diploma to this or any other University.

Date: Saikat Mandal

Place: Pune

ACKNOWLEDGEMENTS

A journey is easier when you travel together. Interdependence is certainly more valuable than independence. This thesis is the result of the work whereby I have been accompanied and supported by many people. It is a pleasant opportunity for me to express my gratitude for all of them. First and foremost, with a deep sense of gratitude, I wish to express my sincere thanks to my supervisor, Dr. Murali Sastry for his immense help in planning and executing the works in time. His enthusiasm and integral view on research and his mission of providing only high-quality work and nothing less, has made a deep impression on me. His trust and scientific excitement inspired me in the most crucial moments of making right decisions and I find myself privileged to have worked under his kind guidance.

It gives me great pleasure to thank Dr. R. V. Chaudhari, Homogeneous Catalysis Division, National Chemical Laboratory, for his valuable suggestions and making all the facilities available to me for the catalytic reactions.

I'm grateful to Dr P. Ratnaswamy and Dr. S. Sivaram, former and present Directors of NCL, Pune for giving me the opportunity to work in this institute and providing the basic infrastructure for my research work.

I am highly indebted to Dr. P. Ganguly, Dr. S. K. Date and Dr. S. Pal, former and present Heads, Physical Chemistry Division for allowing me to use all the available facilities in the division and for their constant encouragement.

I wish to thank Ms. Renu Pasricha and Dr. S. R. Sainkar, who were always ready to do my TEM and SEM samples respectively, which was a boost to my enthusiasms. My sincere thanks to Dr. N. R. Pavaskar, Dr. A. B. Mandale and Mr. A. B. Gaikwad from the Center for Materials Characterization, NCL for all the characterizations required during my research work.

My heartfelt thanks to my former colleagues Anand, Madhukumar, Ashavani and Vidya for their help, support, interest and valuable hints.

I would never forget the company I had, of my fellow research scholars from my lab. In particular, I am thankful to Sumant, Kannan and Sujatha for their help.

I would like to take this opportunity to thank all my lab mates who have helped me in all possible ways. Thank-you Debabrata, Amit, Anita, Shankar, Hrushikesh, Senthil, Minakshi, Ambarish, Tanushree, Akhilesh, Vipul, Sourabh, Atul, Ritwik, Deepti and Prathap for giving me the feeling of being home at work. A special thank to Rajendra, Catalysis Division, for doing catalytic measurements.

Working under a single roof, it was a pleasant company of Dr. B. L.V. Prasad and Ms. S. Adyanthaya who have always helped me in one-way or the other.

I wish to thank my other colleagues at NCL, Nirmalya, Trupti, Vandana, Girish, Jadav, Deka, Pranjal and Mahesh for their cooperation.

The cooperation I received from other faculty members and support staff of Physical Chemistry Division is gratefully acknowledged. I will be failing in my duty if I do not mention the library staff and administrative staff of NCL for their timely help.

I would like to express my appreciation to my friends, Kartick, Subarnada, Kausikda, Saptarshida, Somnathda, Sujatadi, Arindamda, Mahuadi, Bikashda, Debasisda, Anirban, Debasis Samanta, Prabalda, Babuda, Debdut, Kartick Mondal, Soumitra, Prabhas, Pradip, Anamitra, Pallavi, Sukhen and Senapati for the wonderful time I had with them.

The thesis could not have been completed without the endless love and blessings from my family. I wish to thank my parents, who taught me the value of hard work and rendered me enormous support during the whole tenure of my research work. I also wish to thank my brothers, sisters, grandmothers, uncles and aunts for their unwavering faith in my capabilities, which has always encouraged me to go ahead, especially during difficult times.

Finally, my thanks are due to University Grants Commission, Government of India, for awarding the research fellowship.

The chain of my gratitude would be definitely incomplete if I forget to thank the first cause of this chain, using Aristotle's words, 'The Prime Mover'. My deepest gratitude for inspiring and guiding this humble being.

December, 2004 *Saikat Mandal*

Table of Contents

CHAPTER 4: Synthesis of phase-pure metal core-shell nanoparticles using Keggin ions as UV-switchable reducing agents

CHAPTER 5: Synthesis and assembly of metal and semiconductor nanoparticles using Keggin ions as a new class of inorganic scaffolds

CHAPTER 6: Conclusions

Chapter 1

Introduction

Nanomaterials have actually been produced and used by human being for hundreds of years- the beautiful ruby red color of some glass is due to gold nanoparticles trapped in the glass matrix. The decorative glaze known as luster, found on some medieval pottery, contains metallic spherical nanoparticles dispersed in a complex way in the glaze, which gives rise to its special optical properties. The techniques used to produce these materials were considered trade secrets at that time, and are not completely understood even today. If we rearrange the atoms in coal we can make diamond. If we rearrange the atoms in sand and add a few other trace elements we can make computer chips. Although widespread interest in nanomaterials is recent, the concept was raised over 40 years ago. In a classic talk given by Richard Feynman on December 29th 1959 at the annual meeting of the American Physical Society at the Caltech entitled 'There's Plenty of Room at the Bottom' said, "*The principles of physics, as far as I can see, do not speak against the possibility of maneuvering things atom by atom. It is not an attempt to violate any laws; it is something, in principle, that can be done; but in practice, it has not been done because we are too big*." Nanomaterials and nanoscale engineering will play a critical role in the future of information technology and biotechnology. Indeed, they are already an integral part of today's data storage media, semiconductor manufacturing, biomedical research and emerging memory, computing, optical, and sensing devices. Nanoparticles, quantum dots, nanowires, nanotubes, and nanoscale films along with new nanofabrication technologies such as chemical self-assembly and novel soft lithography techniques that will allow for continued advancements in a diverse range of products, from non-volatile memory and hard disk drives to drug delivery systems and chemical sensors.

1.1 Why nanomaterials?

Good things come in small packages. The unique properties of nanomaterials and structures on the nanometer scale have sparked the attention of materials developers. Over the past decade, nanomaterials; materials with structural features (particle size or grain size, for example) of at least one dimension in the range 1-100 nm, have been the subject of enormous interest. Technology in the twenty first century requires the miniaturization of devices into nanometer sizes while their ultimate performance is dramatically enhanced. This raises many issues regarding new materials for achieving specific functionality and selectivity and therefore recently there is tremendous excitement in the study of nanoscale materials with respect to their fundamental properties, organization to form superstructures and applications. Nanomaterials can be metals, ceramics, polymeric materials, or composite materials. The unit of nanometer derives its prefix nano from a Greek word meaning dwarf or extremely small. One nanometer spans 3-5 atoms lined up in a row. By comparison, the diameter of a human hair is about 5 orders of magnitude larger than a nanoscale particle. Nanomaterials are not simply another step in miniaturization, but a different arena entirely; the nanoworld lies midway between the scale of atomic and quantum phenomena, and the scale of bulk materials. At the nanomaterial level, the laws of atomic physics, rather than behaving as in traditional bulk materials, do affect some material properties. The unusual physicochemical and optoelectronic properties of nanoparticles arise primarily due to confinefent of electrons within particles of dimension smaller than the bulk electron delocalization length; this process is termed as quantum confinement [1-3]. Nano-materials, a new branch of materials research, are attracting a great deal of attention because of their potential applications in areas such as optoelectronics [4,], catalysis [5], single-electron transistors and light emitters [6], nonlinear optical devices [7] and photoelectrochemical applications [8]. A greater understanding of the manipulation of matter at the nanoscale has led to a number of advances in materials science, ranging from the development of novel optical and electonic properties and the formation of high strength materials which, mimic nature to stimuli-responsive materials applicable to a range of applications. The variety of nanomaterials is great, and their range of properties and possible applications appear to be enormous, from extraordinarily tiny electronic devices, including miniature batteries, to biomedical uses, and as packaging films, superabsorbants, components of armor, and parts of automobiles. What makes these nanomaterials so different and so

intriguing? Their extremely small feature size is of the same scale as the critical size for physical phenomena. Surfaces and interfaces are also important in explaining nanomaterial behavior. In bulk materials, only a relatively small percentage of atoms will be at or near a surface or interface (like a crystal grain boundary). In nanomaterials, the small feature size ensures that many atoms, perhaps half or more in some cases, will be near interfaces. Surface properties such as energy levels, electronic structure, and reactivity can be quite different from interior states, and give rise to quite different material properties.

1.2 Various methods for generation of nanocrystalline particulate thin films

One important aspect of nanotechnology in the context of commercial application is the organization and packaging of nanoparticles in thin film form. One of the emerging challenges in nanotechnology is the in-plane spatial control over the nanoparticle structures formed. Several methods of nanofabrication have been developed in the past few years, among these techniques are chemical vapor deposition, atomic layer deposition, colloidal assembly and molecular beam epitaxy. The assemblies of organized nanoparticles films have become increasingly important. The methods used for the assembly of ultrathin films with various degrees of molecular order and stability include spin coating and solution casting, thermal deposition, layer-by-layer assembly, chemical self-assembly and the Langmuir-Blodgett techniques. Many of these approaches require a fairly well controlled environment and sophisticated equipment and there of involve high capital and operating costs. Furthermore, limitations exist in the range of materials that may be incorporated using these methods particularly in the combination of broad range of organic and inorganic materials. The organization of nanoparticles in thin film form is an important element on the way of commercially harnessing the exciting application potential of nanoscale matter. Commercial exploitation of many properties of nanoparticles, especially in the optoelectronics industry, would require the assembly of nanoparticles in the form of thin films either as monolayers or multilayer superlattices. In recent years, there has been considerable interest in collective physical properties, which can be attained from assembling nanoparticles into thin films using both novel nanoparticle compositions and assembling strategies [9,10]. The thin films of organized nanoparticles displayed promising characteristics for the fabrication of light-emitting diodes, nonlinear optical devices and electrically conductive films. Organization of functional

nanoparticulate entities into spatially well-defined arrays provides a means to extend the desirable properties of these systems to the macroscopic level, allowing the eventual realization of complex devices.

Self-assembly methods provide a powerful tool to help achieve this goal of organizing nanoparticulate systems into well-defined structures. It is well known that immersion of films of coinage metals such as gold, silver and copper in organic solutions of alkanethiols results in the spontaneous assembly of densely packed monolayers of the alkanethiols on the substrate surface [11]. These monolayers have been termed 'self-assembled monolayers' or SAMs [11]. As a means for the fabrication of thin films with useful morphologies, the self-assembly of nanoparticles has been often employed because of its simple and cost-effective process. One of the most remarkable molecules–substrate interactions is the spontaneous self-organization of atoms and molecules on surfaces into well-ordered arrays; the supramolecular assemblies that form often possess both short- and long-range order. In particular, the spontaneous organization (self-assembly) of surfactant molecules adsorbed on transition metal surfaces has been of growing importance over the past two decades. The field of self-assembly has grown rapidly since the discovery of these structures and their ability to modify the physical and chemical properties of a surface, [12-14]. Self-assembled monolayers (SAMs) are typically formed from the exposure of a surface to molecules with chemical groups that possess strong affinities for the substrate or a material patterned on it. How well these assemblies order is a function of the nature of the chemical interaction between substrate and adsorbate, as well as the type and strengths of intermolecular interactions between the adsorbates that are necessary to hold the assembly together. Molecules ''binding to'' surfaces are either described in terms of physisorption, in which the enthalpies of interactions are rather low (considered to be $\Delta H < 10$ kcal/ mol, typically from van der Waals forces), or in terms of chemisorption with $\Delta H > 10$ kcal/mol. Strengthening interactions between molecules and substrates and between molecules themselves include phenomena such as hydrogen bonding, donor–acceptor and/or ion pairing, and the formation of covalent bonds, rendering the assemblies more stable than their physisorbed counterparts. Other studies have focused upon directly ''grafting'' molecules to surfaces, such as the attachment of aryl-functionalized molecules to silicon [15], alkyl-functionalized molecules to germanium via Grignard reactions [16], and molecules to metal surfaces through diazonium salts [17,18], all of which indicate the formation of surface–carbon

bonds. Chemisorbing systems have included the assembly of trialkyl-, trichloro-, or trialkoxysilanes on silicon dioxide surfaces [19-21], carboxylic acids adsorbing onto aluminum oxide and silver surfaces [22-24], and n-alkanethiols chemisorbing to gold surfaces [25,26], to name merely a few. As noted above, particularly well-studied SAMs are those formed on transition metal surfaces (e.g., Au, Ag) and surfactants with electron-rich headgroups (e.g., S, O, N) and n-alkyl tails. The affinities between the surfaces and headgroups are strong enough to form either polar covalent or ionic bonds, and favorable lateral interactions between adjacent molecules are sufficient to draw and hold the assembly together. A variety of terminal functional groups may be envisaged to modify the surface properties of the underlying substrate but what is pertinent to this study is the presence of ionizable terminal functional groups in the SAMs for electrostatic assembly of charged inorganic nanoparticles. After first being introduced by Decher [27], the self-assembly of nanoparticles using electrostatic interaction between colloidal nanoparticles and adsorbed polyelectrolytes, called ‘‘layerby-layer self-assembly technique’’, has been used successfully in the fabrication of multilayer thin film assemblies of metals [28-30], ceramics [31-33] and semiconductors [34]. A number of different methods exist for the electrostatic assembly of inorganic nanoparticles on charged surfaces such as those presented by SAMs [35], Langmuir-Blodgett films [36], biomocromolecules such as DNA [37], proteins [38] etc. A number of groups have used electrostatic attractive forces between charged SAMs and oppositely charged nanoparticles [39-43] to assemble thin films of the nanoparticles. Sastry and co-workers have demonstrated that SAMs of 4-aminothiophenol (4-ATP) chemisorbed on thin films of gold may be used to electrostatically bind with silver nanoparticles charged negatively with carboxylic acid functionality by simple immersion of the SAMs in the aqueous nanoparticle solution [40]. In a different approach based on SAMs, Auer et al. have shown that bis-benzamidines could be used as positively charged bifunctional electrostatic linker molecules in the assembly of negatively charged gold nanoparticles on negatively charged mercaptoundecanoic acid (MUA) SAMs on gold surfaces [39].

Layer-by-layer assembly is an approach based on the alternating adsorption of materials containing complementary charged or functional groups to form integrated ultrathin films [44]. This method, which is most often manifested in the alternation of oppositely charged species, could be used to create highly tuned, functional thin films with nanometer level control of film

composition and structure. Recently there has been a virtual explosion in the number of functional polymers, nanoparticles and organic and inorganic systems put into these films. Furthermore it has been demonstrated that multilayer thin films can exist in a variety of novel and unique geometries and forms using templating and patterning techniques, which make these systems even more applicable to the creation of unique nanoassemblies. One of the most exciting aspects of layer-by-layer assembly is the fact that active elements can be introduced into these films without significant alteration of their electrical and chemical properties. The result is that various components in these films can actually be tuned on a molecular level to enhance electron and ion transport and energy transfer within the layers. It has been demonstrated by many groups for example that photoluminescent and eletroluminescent thin films can be achieved through the incorporation of poly(p-phenyl vinylene) (PPV) precursors or other luminescent polymer systems into multilayer thin films. Most recent studies have expanded on the use of these films as the basis devices. The first report on the electrostatically driven layer-by-layer self-assembly of inorganic colloidal particles on planar surfaces may be traced to the seminal work of Iler [45]. Iler showed that oppositely charged silica and alumina particles could be electrostatically self-assembled in multilayer structures by alternatively immersing the substrate in the two colloidal solutions. Decher and co-workers has demonstrated the layer-by-layer electrostatic self-assembly of cationic and anionic polyelectrolytes as well as multilayer structures consisting of combinations of charged colloidal particles including biomacromolecules such as DNA [46]. Many groups worldwide have now used electrostatically driven layer-by-layer assembly to realize structures containing proteins/polyeletrolytes [47], polyelectrolye/inorganic nanoparticle sandwich structures with nano-magnetite [48], TiO_2/CdS [49], SiO_2, TiO_2 and CeO_2 [50], Au [51-53] alternating layers of positively charged gold and negatively charged silver particles [54] as well as quantum dots of CdSe [55]. Recently Sastry and co-workers have shown that amino acid capped gold nanoparticles can be electrostatically assembled in a layer-by-layer fashion by suitably changing the pH [56]. In general, a number of multilayers systems have been developed in the past few years that utilize the multifunctional nature of alternating layer-by-layer assembly. These include the use of enzymes in combination with redox polymers or molecules such as hydrogen peroxide sensors based on horseradish peroxidase [57]. Multilayer films are excellent platforms for sensors and reactive responsive membranes because they allow the integration of

several functionalities to achieve optical, electronical and conductive detection signals in response to different biological or molecular entities. A unique advantage of the layer-by-layer approach is the ability to incorporate a number of different materials into the layers as long as alternating charge is maintained. A major advantage of layer-by-layer assembly is the ability to combine organic and inorganic functionalities in a seamless fashion due to the intimate contact in the highly interpenetrated molecular layers.

The Langmuir-Blodgett (LB) technique is a potential way to construct film materials with well-defined structure and thickness, controlled at a molecular level by successive deposition of amphiphilic molecular monolayers on an aqueous subphase [58-61]. The Langmuir –Blodgett transfer of amphiphile monolayers from the air-water interface onto solid supports is a powerful tool for creating periodic lattices of many varieties usually composed of bilayers [62]. The LB films consisting of monomolecular layers of amphilic molecules formed at the gas-liquid interface and subsequently transferred onto solid substrates have been used as templating organic structures for the synthesis of several nanostructures by exploiting their highly ordered lamellar structure which acts as a nanoreactor to provide nanocrystals formation in a confined reaction geometry [63]. The air-water interface has long been recognized as an excellent medium for the assembly of inorganic ions [62, 64], biomacromolecules such as proteins [65] and DNA [37,66] and inorganic nanoparticles [67]. Insofar as nanoparticles are concerned, a number of different variants of this technique may be considered depending on the chemical nature of the surface of the nanoparticles. Fendler and co-workers published the first report on using electrostatic interactions for the assembly of size-quantized CdS nanoparticles by Langmuir-Blodgett method [68]. Nanoparticles of metals such as silver and gold [29, 36, 69], semiconductor quantum dots such as CdS [68, 70] and CdTe [71], oxides such as SiO_2, TiO_2 [72], Fe_3O_4 [73] and γ-Fe_2O_3 [74] and latex spheres [75] have been assembled from solution at the air-water interface using electrostatic interactions. If the nanoparticles are hydrophobic, they may be simply floated on the surface of water, compressed into a close-packed monolayer and transferred onto suitable solid supports by the versatile Langmuir-Blodgett method [76-79]. Sastry and co-workers have developed a simple protocol for the hydrophobization of nanoparticles and thereafter they showed that the monolayers films of hydrophobized nanoparticles can be organized at the air-water interface, which can be successfully transferred to solid substrate to obtain closed packed structures [67,77, 80]. This is a very general method

and can be used to grow multilayer films consisting of different layers of nanoparticles in any desired sequence by using different troughs containing the desired nanoparticle solution successively [69(c),81]. The advantage of this approach is the ability to form multilayer nanoparticle films by sequential immersion of solid support into the Langmuir monolayer-nanoparticle complexes by the versatile LB technique.

Sastry and co-workers have developed a technique wherein thermally evaporated films of cationic/anionic lipid molecules may be used to entrap metal ions electrostatically by simple immersion in electrolyte solution [82] leading to the formation of ordered lamellar films almost identical to those obtained by the classical LB method and using this technique they also immobilized DNA, proteins into lipid matrix [83]. This technique is very powerful to make nanocomposites in thin film form.

1.3 Generation of patterned thin films

The fabrication of nanoparticle ensembles with both short and long-range order across a hierarchy of spatial scales remains a major challenge for nanoscience. Patterned nanoparticles on different substrates have been the focus of many investigations due to their unique potential for many applications including nanoelectronics, nanophotonics, magnetoelectronics and biochemical sensing [84-86]. Patterning is of importance in many areas of modern science and technology with applications ranging from the production of integrated circuits, information storage devices and display units to the fabrication of microelectrochemical systems (MEMS), miniaturized sensors, microfluidic devices, biochips, photonic bandgap crystals, micro-optical components and diffractive optical elements. Generally conventional lithographic approaches are nearing fundamental limits and it seems clear that directed self-assembly, an integration of lithography and self-assembly is destined to play an important role across a wide range of nanotechnology applications. This will require a sophisticated understanding of the chemical and physical interactions between lithographically defined patterns and nanoparticles. Fabrications approaches for nanopatterning of surfaces include electron-beam lithography [87], optical and interference lithography [88], imprint lithography [89,90], soft lithography [91], and colloidal [92] and self-assembly lithography [93]. This patterning has been engineered in a variety of ways, either by the selective removal of particular adsorbates, by the selective placement of adsorbates, by the selective reaction of adsorbates, by their destruction with

energetic beams, or by their deliberate removal with scanning probe microscopes moving in a determined pattern and the application of force or delivery of low energy beams. Depending on the application the requirements for a successful lithographic process can vary substantially. The critical feature size of the test patterns is probably the most obvious issue one must consider when selecting a proper lithographic technique. The fabrication of integrated circuits, information storage devices or display units often involves many lithographic steps and demands the use of sophisticated technologies to meet the stringent requirements in terms of throughput, overlay accuracy and resolution. The growing demands for higher densities of integration, less power consumption, better performance and reduction in cost has been and is still the main driving force behind the continuous trend in downsizing the critical dimensions of semiconductor devices. The number of transistors on a chip doubles every 18 months and with the continuation of this trend density beyond 1 billion transistors/cm^2 could be achieved in the foreseeable future. Every method for patterning has limitations and these limitations have prompted the development of many alternative and complementary methods for patterning that differ in the way in which the features of interest are generated. There are various techniques for generating patterns structures.

Patterning of the self-assembled monolayers (SAMs) is an excellent strategy for preparing templates that possess variable surface chemical properties. Modification of SAMs can be conducted either by conventional [94] or state-of-art destructive lithographic processes [95] including atomic-beam [96] and proximal-probe methods [97]. Recently, nondestructive processes have also been reported. For instance, chemical reactions can be induced in the terminal groups of organosilane by a catalytically active transitionmetal- coated atomic force microscope (AFM) tip [98,99]. Not only has there been intense interest in manipulation of the SAMs themselves in order to create complex thin films, SAMs are also used as ultra-thin organic resists in lithography. As a protective, organic layer has been shown to reduce the etching of metal surfaces drastically when exposed to oxidizing solutions, thus features can be patterned into the substrate that support the SAM since the etch rates differ between bare metal and the SAM-covered metal [100-107]. Therefore, SAMs have been used as sacrificial structures to create patterns into metal with a resolution that is often either difficult, time-consuming, or expensive to achieve with state-of-the-art, conventional lithographic tools. It is important to pattern films in order to understand the fundamental interactions and organization

of mixed monolayers on surfaces, but an additional reason for patterning SAMs is to create functional nanostructures completely or in part from the ‘‘bottom up’’. Using particular chemical functional groups or using mixed component SAMs, features of interest such as nanoparticles, cells, proteins, or other biomolecules can be patterned for the creation of higher-ordered structures and architectures if they possess particular affinities for parts of the SAM. The development of patterned SAMs is critical as they can serve as sacrificial structures, as well as both final structures and supports, as the patterning of particular molecules imparts a predisposed reactivity to a surface. Patterned SAMs are also important in applications for nanotechnology. One criterion for the development of nanoelectronic devices is being able to position and to pattern molecular components selectively on surfaces, thus imparting regularity to the overall structure. Self-assembly is a significant experimental approach and a method to isolate and to probe molecules that are candidates for novel nanocircuit components [108,109] on the molecular-scale organization of multicomponent self-assembling films.

Writing by energetic beams on the surface of a substrate is an excellent technique for generating patterns on the substrate. This writing scheme involves the mechanical displacement or modification of a material on the surface of a substrate in a spatially controlled way. The process generally requires a direct contact between the surface of a substrate and a rigid stylus that is moved across the surface to engrave a pattern in relief. The selection of an appropriate stylus depends on the application of the resultant pattern. The writing of high-resolution pattern is often accomplished by scanning tunneling microscopy and atomic force microscopy, which employ ultra sharp tips [110]. Scrapping, plaguing or indentation with a scanning probe has been demonstrated for a rich variety of materials that includes polymers [111], metal oxides [112], self-assembled monolayers [113].

The field of using energetic beams to pattern SAMs has advanced considerably. Energetic beams such as ions, electrons, and photons are routinely used to destroy polymer resists, and etch into other structures. In the process of writing with a beam of photons or other energetic particles the dissipation of beam energy can proceed in a number of different ways and may include various types of physical and chemical process depending on the type of radiation, its dose and the materials that are involved. Focused laser beams have been adapted for a number of different fabrication schemes. The laser assisted ablative micropatterning of a solid surface relies on the removal of a material by species such as radicals that are formed in

the photochemically excited gas [114]. This technique can be applied to a variety of inorganic materials in a localized, well controlled manner whereas the removal of polymers generally requires the use of specially designed laser ablation resists that perform exothermic decomposition of gaseous products with high adsorption coefficients [115]. Focused beams of energetic particles comprising electrons, ions, and electrically neutral metastable atoms provide other means for generating patterns in a proper resist materials [116-118]. These techniques have extremely high-resolution capabilities because of their short wavelength (<0.1 nm) combined with a large depth of focus. However, the effectiveness of polymer resists is limited by their thickness. Other energetic beam technique like electron beam lithography is a feature that can be readily added to most conventional scanning electron microscopy systems. Although high throughput continues to be a major challenge of this technique, electron beam lithography has become a standard tool for writing arbitrary patterns for many technological and scientific applications. A variety of materials have been demonstrated for use with electron-beam lithography, including polymers [119], inorganic materials [120], and SAMs [121]. For using SAMs as etch resists, one can destroy the SAM in a patterned fashion via energetic beams. Some of the earliest work on using SAMs as electron beam resists was by using SAMs of alkanethiolates on GaAs [122], and SAMs of octadecyltrichlorosilane (OTS) on SiO_2 [123].

Techniques using focused ion beams are conceptually related to electron beam lithography. In principle the higher mass of ions may result in patterning capabilities that are less prone to distortions due to back scattering from the substrates. Other advantages include the possibility of highly localized implantation doping, ion-induced deposition and the capability of removing material from a surface using ion milling or ion-beam assisted etching.

Writing with magnetic field is central to information storage technology [124]. In this application the writing element is an inductive device on a recording head, which is used to magnetize small areas of a magnetic medium (e.g. iron oxide particles, or a polycrystalline alloy composed of Co, Cr and Pt) supported on a tape or hard disc. This way bits are generated in the form of magnetization patterns that can encode certain types of signals.

Laser induced chemical vapor deposition has been widely explored as a method for patterning solid substrates, since it is a fast and reliable way to deposit a variety of materials on both planar and nonplanar surfaces [125]. The writing can be carried out in two major variants-

phototolytic decomposition where photon adsorption is accompanied by cleavage of chemical bonds, or pyrolytic decomposition, where heating thermally dissects the precursor compound.

Microcontact printing (μCP), a soft lithographic technique useful in patterning self-assembled monolayers (SAMs), was introduced by Whitesides's group [126,127]. The procedure is remarkably simple and it is a sensible combination of the top-down and bottom-up strategy of material fabrication. This is an efficient method for pattern transfer using poly dimethylsiloxane PDMS as an elastomeric stamp, and self-assembled monolayers of thiol derivatives as ink materials, respectively. This technique uses a structured, elastomeric stamp to deliver molecular "ink" to a substrate upon conformal contact. μCP has been generally used to direct deposition of self-assembled monolayers (SAMs) of thiols and silanes onto coinage metals and silicon substrates, respectively [127,128]. Microcontact printing (μCP) as a method of patterning SAMs has grown in popularity due to the ease of fabricating the printing tools, relatively high spatial resolution of features produced (line widths of <100 nm), and large printing capacity (up to tens of square centimeters of sub-micron-sized features can be printed in parallel). The μCP technique is attractive because it is inherently rapid and can be performed in parallel, for many features can be printed simultaneously with one stamp application. In addition, it is generally cost-effective and can be applied to many substrates and desired patterns. Microcontact printing is a technique relevant to creating patterned areas with a different adsorbate. However, the material and dimensions of the elastomeric stamp limit the resolution of the resulting patterns. Furthermore, the reproducibility of the process is dependent on the stamp's resistance to degradation, the replication accuracy of the contact pressure that is applied to the substrate, and registration with other surface features. μCP has several advantages over conventional photolithography, including being inexpensive, simple, adaptable to large areas and nonplanar surfaces, and fast. This technique is now commonly used for the surface patterning of biomaterials where the cell substrate interaction, regulated by chemically and topographically modified surfaces, is one of the dominant factors of cell culturing and functioning.

Inkjet printing has recently emerged as an attractive technique for depositing minute quantities of material on surfaces with good spatial control [129]. In this technique small volumes of liquid ink from a reservoir are ejected through a nozzle and dispensed onto the substrate. Two modes of operation exist in which the liquid is either pumped through the nozzle

to form a continuous jet of liquid or in which small droplets are generated by applying an acoustic or thermal pulse. IJP has a range of advantageous attributes and some of them are particularly relevant when reel to reel manufacturing of patterns on flexible substrates is desired: i) it is contact free technique, ii) it is capable of providing high throughput, in particular when a large number of nozzles are used in parallel, iii) it allows the simultaneous printing of different materials delivered from multiple nozzles and iv) it provides good alignment capabilities and a precise control over the volume of deposited materials. Interesting application for IJP that has been actively explored is related to the fabrication of biochips.

Dip-pen nanolithography (DPN) has been demonstrated as a high-resolution technique for writing liquid-based ink on substrates [130]. Dip-pen nanolithography (DPN) is a variety of scanning probe lithography ("direct-writing") developed by Mirkin and coworkers, where molecules are transferred by means of an AFM tip to a substrate [131]. In this technique the ink is loaded onto an AFM tip and delivered to the surface of a substrate via a thin water meniscus that forms between the tip and the substrate thereby serving as a medium for ink transport with nanometer dimensions. As the scanning probe tip can be positioned or programmed to move in certain patterns, it is possible to use DPN to pattern SAMs with different molecular components; these patterns can then be used for the further design of nanoscale structures, by either selective molecular reaction or deposition in the patterned areas. The concept of DPN is that the positive printing of molecules is directly analogous to writing [131]. By holding the thiol-laden AFM tip in contact with a gold substrate for varying amounts of time either by allowing the tip to dwell in a certain location at a fixed distance from the substrate or simply by rastering the tip at a particular speed, it is possible to pattern different size features (i.e., dots, lines) by allowing molecules to diffuse down to the substrate. DPN has been successfully applied to pattern a broad range of materials including alkanethiol monolayers on gold [132], colloidal particles or sols [133], inorganic metal salts [134], polymers [135], bio molecules such as proteins, DNA on a variety of substrates [136].

By printing molecules with different terminal functional groups in patterned manner it is possible to perform chemistry in pre-determined locations. Patterned films can be used as templates for the selective deposition of other nanoscale materials. Recently Sastry and co-workers have demonstrated that *Candida bombicola* yeast cells may be immobilized onto patterned thermally evaporated fatty amine thin films (octadecylamine, ODA) and the use of

the enzyme cytochrome P450 present in the yeast cells to catalyze in situ the ω-hydroxylation of arachidonic acid (AA) to 20-hydroxyeicosatetraenoic acid (20-HETE) [137]. Therefore, patterned films used as templates for the deposition and selective adsorption of different materials in order to create higher order architectures for uses in thin film.

1.4 Templates as building blocks

Although the realization of nanoscale electronics is a subject of great priority for industrial technology, modern techniques based on lithography have grown increasingly complicated with attempts to achieve further miniaturization. Successful routes toward nanoscale electronics include the use of macromolecules and small molecules as building blocks for electronic devices. Nanoparticles, such as metal and semiconductor colloids with diameters of one to a few nanometers, are particularly attractive candidates [138-142]. Thus, the ability to organize, interconnect and address nanoparticles on surfaces is an important hurdle to overcome in order to fully realizes nanoscale electronics. Intensive studies have been devoted to assembling nanoparticles into ordered two- or three-dimensional superstructures due to their significant electronic [143] and optical properties [144] and their promising applications in information storage devices [145]. The properties of the assembled nanoparticles are mostly different from those of the individual nanoparticles or their macroscopic equivalents. The ability to synthesize ordered assembly configuration of the nanoparticles could provide a new horizon to study the collective properties and develop future nanoscaled optical, electronic, and information storage devices. Many natural materials that have specific binding properties in molecular recognition and self-assembly can be used as a template to organize and interconnect assemblies of nanoparticles on surfaces [146-149]. In recent years, interest in nanoparticle self-assembly has centered on the generation of open and complex structures in two dimensions and of nanowires in one dimension. Such structures are of importance in view of their potential applications in micro- and nano- electronic devices [150,151]. Self-assembly alone produces close-packed arrays; therefore, some degree of control over the assembly process is required to form open and complex structures. Many synthetic methods for the preparation of inorganic nanoparticles have been reported, including controlled precipitation [152], seeded growth [153], and confined synthesis in structured templates [154,155]. Template-directed synthesis represents a straightforward route to nanoparticles. In

this approach nanoparticles are generated in situ with the morphology complementary to that of the template. A number of templates have been used, including hard solid templates such as zeolites [156], glasses [157], layered solids [158], molecular sieves [159,160], alumina membranes [161], and self-organized media such as micelles (of surfactants and block copolymers) [162-169] and vesicles [170-172]. Biomolecular structures have typical size dimensions from the lower nanometer size range up to several micrometers together with well-defined surface functionalities. Because of their molecular recognition capabilities, many among them are able to self-assemble into complex, well-defined, and extended superstructures. Recently, biological systems have been explored as building blocks in the bottom-up assembly and generation of new inorganic materials and devices with advanced structures and functionalities [173-175]. For example, well-defined nanoparticles have been synthesized by the mineralization of proteins [176] and viruses [177-180]. The specific recognition properties of oligonucleotides [181,182] and antibodies [183] have been used to generate three-dimensional well-ordered aggregates of metal nanoparticles. Motivated by future applications in nanoelectronics, researchers have employed DNA strands to create conductive silver [184-186], palladium [187], platinum [188,189] or copper [190] nanowires. Here, alignment of nanoparticles into long chains to form nanowires has been achieved by using biomolecular templates such as phospholipid tubules [191], DNA molecules [192-198], protein fibers [199], and tobacco mosaic viruses [200]. Carbon nanotubes have also been used as templates to assemble bundles of gold particles [201-203]. In the case of hard solid templates, the fabricated nanoparticles are embedded inside the matrix and thus it is hard to remove the templates after the synthesis. It is also difficult for the further processing of the nanoparticles. In contrast, templates such as micelles and vesicles can produce and stabilize dispersed nanoparticles, which simplifies postprocessing. Ordered (such as hexagonal) arrays of nanoparticles have been obtained via a polymeric micellar route, and the templates can be removed completely by oxygen plasma [204,205]. However, the instability of these templates limits their potential applications. Once the templates decompose under harsh conditions (such as elevated temperatures or change of solvent), the nanoparticles will lose their stabilization layer and may undergo aggregation. Recently, fabrication of inorganic nanoparticles in solid polymer matrixes has attracted more and more attention [206-210] because the combination of inorganic nanoparticle and polymer provides a simple route to stable and processable materials

integrating the promising properties of both components. However, these composites normally cannot be redissolved while preserving the colloidal state of nanoparticles. Among polymeric templates, the single polymer molecule represents an important type because isolated nanocomposites based on a single molecule can be obtained, which have very desirable processing characteristics. Building 3-D structures is a particular challenge in biomimetic materials chemistry. Conceptually, the simplest way of producing such structures is to build inside or on a preorganized extended template (scaffold) using building blocks that represent a significant volume fraction of the composite structure. For example, there is considerable interest in the production of inorganic framework materials containing well-defined pore networks. In general, strategies for synthesizing these materials rely on using templates, the size and nature of which dictate the pore architecture. Microporous materials are prepared using molecular templates [211] while at the meso length scale supramolecular aggregates are required [212]. The organic or inorganic template material can be removed by heat treatment [213], microwave irradiation [214], washing with organic solvents [215], calcinations [216] or simple dissolution of the core particles [217], which finally results in the formation of an inorganic material possessing a morphology directly related to the organic or inorganic template.

1.5 Beauty of core-shell nanoparticles

In above section it has been discussed that the organization of metal nanoparticles into diverse structures is essential for their application in optical, electronic, and magnetic devices [218]. Metal nanoparticles have been assembled into monolayer or multilayer thin films on planar surfaces [219], 2D or 3D superlattices [220], nanowires [221], macroporous structures [222], and colloidal aggregates [223]. Recently, metal nanoparticles have also found use as building blocks to construct core-shell particles [224] and hollow spheres [225]. Such core-shell nanoparticle assemblies are interesting, because assemblies such as these should possess both desirable features of the core nanoparticle as well as the deposited metals, and their properties might be conveniently tailored by altering the composition or size of the deposited materials. Advanced materials derived from core-shell composite particles are of extensive scientific and technological interest, due to their unique and tailored properties for various applications in materials science [225]. The nanoscale coating of colloid particles with

materials of different composition is currently an active area of research. Such coatings not only stabilize colloidal dispersions but also allow modification and tailoring of the particle properties (e.g., optical, magnetic, catalytic) depending on the coating composition [226]. In principle, one can achieve a precise control over the optical properties of these core-shell colloids by fine-tuning the chemical composition, structure, and dimensions of the cores or shells.

Nanosized bimetallic colloidal particles exhibit unique optical, electronic, magnetic, and catalytic properties [227] distinct not only from the bulk metals but also from the corresponding monometallic particles as well. Two main groups of bimetallic colloids exist, alloys and layered (core-shell) colloids. Bimetallic colloids can be prepared [228] by simultaneous co-reduction of two kinds of metal ions with or without the protective agent (usually a polymer or a surfactant) or by successive reduction of one metal over the nuclei of another. Two approaches widely used for the surface modification of particles are the direct precipitation of (inorganic) shell materials from solution and the layer-by-layer deposition of charged species. Among the inorganic coatings, metal oxides have been of significant interest. Silica has been used extensively to coat different colloid particles, including noble metal colloids. Liz-Marzan and coworkers have shown that a vitreophilic metal nanoparticle surface facilitates the formation of uniform silica coatings [229]. Gold nanoparticles were made vitreophilic by using the coupling agent (3-aminopropyl)trimethoxysilane, and silica coatings were obtained by subsequent exposure of the particles to a sodium silicate solution followed by the Stober process [230]. In a recent study, Hardikar and Matijevic have also used the Stober process for silica coating on silver nanoparticles [231]. Recently, Mulvaney et.al. [232] reported the encapsulation of metal clusters and semiconductor by silica shells. The silica shell allows for stabilization against photochemical degradation and high fluorescence quantum yields. Titania is another metal oxide that is of interest for coating applications as; it is widely known to be a useful catalyst [233]. Other metal oxide, such as Fe_2O_3@MgO and Fe_2O_3@CaO have greatly enhanced efficiencies over pure MgO and CaO catalysts for SO_2 adsorption, H_2S removal, and chlorocarbon destruction [234].

Semiconductor nanocrystals (quantum dots, QDs) possess a number of advantageous features, such as light emitters and fluorescent labels [235], as compared to ionic and molecular chromophores. The ability to discriminate many different colors simultaneously under long-

term excitation holds great promise for fluorescent labeling technologies, especially in biology [236]. In this respect, organic dye molecules suffer from several limiting factors. First, their narrow absorption bands make it difficult to excite several colors with a single excitation source. In addition, due to the large spectral overlaps between the emissions of dye fluorophores, multicolor imaging requires complex mathematical analysis of the data [237]. Second, the emission intensity of organic dyes depends on their environment, and photobleaching imposes a stringent upper limit on the number of photons detectable per molecule. Third, the fast fluorescence emission of the dyes (<5 ns) coincides with a high degree to short-lived autofluorescence background from many naturally occurring species, reducing therefore the signal-to-noise ratio. In contrast, semiconductor nanocrystals emit light with a decay time on the order of a few tens of nanoseconds (~ 30-100 ns) at room temperature [238]. The fluorescence decay is slower than the auto fluorescence background decay, but fast enough to maintain a high photon turnover rate. The core-shell geometry has allowed for the enhancement of luminescence of semiconductor nanoparticles [239]. The growth of a wide band gap (e.g., ZnS) semiconducting shell around a narrow band gap (e.g., CdSe) core has resulted in core/shell materials with higher luminescence quantum yields than single component semiconductor nanocrystal materials [240]. Core/shell systems reported include CdS/$Cd(OH)_2$ [241] CdSe/ZnS [242], ZnS/CdS [243], CdS/HgS [244], HgS/CdS [245], CdS/PbS [246], CdSe/ZnSe [247], and CdSe/CdS [248], with accounts of improved luminescence quantum yields, decreased fluorescence lifetimes, and benefits related to the tailoring of relative band gap positions between the two materials. Further passivation of the nanocrystal surface by a thin shell of a higher band gap material does not significantly modify the absorption and emission features but increases the nanoparticle quantum yield up to 50-70% [249]. The passivation shell also imparts an efficient photochemical stability, so that the photobleaching is reduced, and the number of photons a single nanocrystal can emit dramatically increases.

Metal-coated colloidal core-shell composite particles have their potential use as catalysts, because their catalytic properties [250] are superior to those of single metallic nanoparticles. They are also of importance because of the change in their surface plasma band energy [251] relative to that of the separate metals with potential use in sensors, substrates for surface-enhanced Raman scattering, and colloidal entities with unique optical properties [252].

Among various systems, transition metals containing core-shell nanoparticles are particularly interesting because these systems can have multiple functions that do not exist in single-component compounds and unique properties that exist only in nm-sized materials. For instance, core-shell nanoparticles have been tested as catalysts in various chemical reactions, and both core and shell are actively involved in the catalytic processes [253]. Preparation and characterization of colloids (hydrosols) of bimetallic nanoparticles constituting various combinations of noble metals was the subject of numerous papers, e.g., Au- Pd [254], Au-Pt [255], Ag-Pd [256], Ag-Pt [257], and Ag-Au [258]. Nanoparticles composed of free-electron-like metals such as Ag and Au are known to provide strong resonance optical responses to irradiation by light [259], which result in amplification of light-induced processes undergone by molecules localized on their surfaces, such as Raman scattering, giving rise to surface-enhanced Raman scattering (SERS) [260]. Optical properties of bimetallic nanoparticles comprised of Ag and Au are thus the subject of considerable interest. Comparison of the calculated and measured surface plasmon (SP) extinction spectra was frequently employed as one of the criteria of distinguishing between an alloyed and/or layered (core-shell) structure of the bimetallic Ag-Au nanoparticles. Recently, a strategy for extracting optical constants of the core and/ or the shell material of bimetallic Ag-Au nanoparticles from their measured SP extinction spectra was reported [261] and can be employed as SERS-active surfaces. Because of high catalytic activity of Pd and Pt, bimetallic colloids of gold and silver in combination with Pd and Pt have been studied in great detail. Generally core-shell nanoparticles are prepared by the successive reduction of one metal ion over the core of another [262,263]. The latter process often leads to the formation of fresh nuclei of the second metal in solution, in addition to a shell around the first metal core [263], and is clearly undesirable from the application point of view. Recently Sastry and co-workers have developed a strategy to overcome this drawback by immobilization of a reducing agent on the surface of the core metal which, when exposed to the second metal ions, would reduce them, thereby leading to the formation of a thin metallic shell [264].

1.6 Work described in the thesis

The work described in this thesis address the synthesis and characterization of metal/semiconductor-lipid nanocomposites materials in thin film form, phase pure metal core-

shell nanoparticles and assembly of metal and semiconductor nanoparticles using Keggin ions as novel inorganic templates.

Chapter 2 describes the experimental characterization techniques used for studying synthesized nanoparticles in this thesis. These techniques include thermal evaporation of fatty lipids using vacuum deposition unit, Quartz Crystal Microgravimetry (QCM), UV-visible Spectroscopy, Fourier Transform Infrared Spectroscopy (FTIR), Transmission Electron Microscopy (TEM), Scanning Electron Microscopy (SEM), Energy Dispersive Analysis of X-ray (EDAX), X-ray photoemission spectroscopy (XPS), Contact angle measurements and Isothermal titration calorimetry (ITC) that have been extensively used for characterization of the nanocomposites materials in thin films and in solutions. The physical principles underlying the different techniques and their application to understand various aspects of formation of the nanocomposites have been outlined.

Chapter 3 discusses the synthesis of metal and semiconductor nanoparticles in a patterned manner in thermally evaporated lipid films. Earlier in this laboratory, it was shown that thermally evaporated fatty acid/amine films could be spontaneously organized via selective ionic interactions of cations/anions by immersion of the film in a suitable electrolyte solution. This leads to an organized lamellar film structure similar to *c*-axis oriented Y-type Langmuir Blodgett (LB) films. This chapter successfully extends the protocol towards synthesis of metal/semiconductor nanoparticles in-situ in thin films. We show that positively or negatively charged ions can be incorporated into ionizable, thermally evaporated fatty lipid films by immersion of the films in the electrolyte solution. Reduction of metal ions in the lipid matrix yields nanoparticles immobilized on any suitable substrates. The process of metal ion incorporation and reduction may be repeated a number of times to increase the nanoparticle density in the lipid matrix. By this process it is very simple to form metal/semiconductor nanoparticle assemblies in a patterned manner on suitable substrates using suitable masks (e.g., a TEM grid). In this protocol, the metal/semiconductor nanoparticles are faithful to the underlying patterned lipid template and there is very little spillover of the nanoparticles into the gaps of the patterned film indicating a high degree of fidelity to the lipid matrix template. It is conceivable that this process could be extended to more intricate structures using more sophisticated masks. In this chapter the role of host lipid matrix on the structures of synthesized nanomaterials in the lipid thin films has also been discussed.

Chapter 4 deals with the synthesis of metal nanoparticles and phase pure metal core-shell nanoparticles using photoreduced Keggin ions as reducing agent. Core-shell nanoparticles may be conveniently synthesized by the successive reduction of one metal ion over the core of another. However the process often leads to the formation of fresh nuclei of the second metal in solution, in addition to a shell around the first metal core and is clearly undesirable from the application point of view. A possible strategy to overcome this drawback could be based on immobilization of a reducing agent on the surface of the core metal which, when exposed to the second metal ions, would reduce them, thereby leading to the formation of a thin metallic shell. Keggin ions can be reduced electrochemically, photochemically or by other suitable reducing agents and we used photochemically reduced Keggin ions by UV-irradiation to synthesize the gold nanoparticles. Keggin ions stabilize the gold nanoparticles by capping the surface of those metal nanoparticles. Therefore in principle, it is possible to reduce the surface-bound Keggin ions by further UV irradiation and use them as highly localized reducing agents in the synthesis of metal core-shell nanoparticles and by this protocol we have synthesized phase pure Au@Ag, Au@Pd and Au@Pt nanoparticles. The photochemical charging of Keggin ions bound to the core-gold nanoparticles surface is the crucial step for reduction of second metal ions only on the surface of the core metal nanoparticles. The reducing capability of the Keggin ions can be switched on using UV-irradiation and thus we can use them as UV-switchable reducing agent. We have also synthesized palladium nanoparticles capped with Keggin ions by reducing palladium salt using UV-irradiated Keggin ions as reducing agents. The most important palladium-catalyzed reaction in organic chemistry, apart from catalytic hydrogenation, is the Heck reaction. The reaction allows the preparation of substituted alkenes by alkylation or arylation of alkenes with vinyl or aryl halides. Besides Pd nanoparticles in the field of catalyst, polyoxometalates have several advantages as catalysts, which make them economically and environmentally attractive. Being stronger acids, HPAs will have significantly higher catalytic activity than mineral acids. In particular in organic media, the molar catalytic activity of HPA is often 100-1000 times higher than that of H_2SO_4. We have developed the phase transfer protocol for transferring the Keggin-capped Pd nanoparticles into organic phase and used them as multifunctional catalysts for Heck, ring opening of epoxy compounds and esterification reactions.

Chapter 5 describes the assembly of metal/semiconductor nanoparticles using Keggin ions as an inorganic template. There is considerable current interest in the production of inorganic framework materials containing well-defined pore networks such as microporous and mesoporous materials. In addition to organic templates, inorganic templates can also be used in the formation of inorganic materials. The organic or inorganic template material can be removed by heat treatment, microwave irradiation, washing with organic solvents, calcination or simple dissolution of the core particles, which finally results in the formation of an inorganic material possessing a morphology directly related to the organic or inorganic template. In this chapter it has been shown that metal-Keggin ion colloidal particles are excellent templates for the synthesis of organized assemblies of metal nanoparticles, wherein the Keggin ion host plays the role of a UV-switchable reducing agent. Keggin ions are good template for synthesis and assembly of semiconductor nanoparticles also i.e. Keggin ions may be used as a new class of inorganic scaffolds in the synthesis of metal and semiconductor nanoparticle assemblies. Treatment with alkali results in dissolution of the Keggin template leaving behind the metal/semiconductor nanoparticle network reasonably intact.

Chapter 6 summarizes the work presented in the thesis and discusses possible further research in this area. The experimental techniques developed by us have been compared with other contemporary protocols, and the explicit advantages brought out.

1.7 References

[1]. Fendler, J.H. *Membrane Mimetic Chemistry Approach to Advanced Materials*; Springer-Verlag : Berlin, **1992**.

[2]. Henglein, A. *Top. Curr. Chem.* **1988,** *143*, 113.

[3] El-Sayed, M.A. *Acc.Chem.Res.* **2001,** *34*, 257.

[4]. Alivisatos, A.P. *Science* **1996,** *271*, 933.

[5]. (a) Ahmadi, T.; Wang, Z.L.; Green, T.C.; Henglein, A.; El-Sayed, M.A. *Science* **1996,** *272*, 1924. (b) Mandal, S.; Roy, D.; Chaudhari, R. V.; Sastry, M. *Chem. Mater.* **2004**, *16*, 3714. (c) Mandal, S.; Selvakannan, PR.; Roy, D.; Chaudhari, R. V.; Sastry, M. *Chem. Comm.* **2002**, 3002.

[6]. Weller, H. *Angew.Chem.Int.Ed.Engl.* **1998,** *37*, 1658.

[7]. Wang. Y. *Acc.Chem.Res.* **1991,** *24*, 133.

[8]. Mansur, H.S.; Grieser, F.; Marychurch, M.S.; Biggs, S.; Urquhart, R.S.; Furlong, D.N.; *J.Chem.Soc., Faraday Trans*. **1995, *91***, 665.

[9] Ozin, G.A. *Acc. Chem. Res*. **1997**, *30*, 17.

[10] Revice, J.P.; Delafond, J.; Misaelides, P.; Noli, F. *Surf. Coat. Technol*. **1998**, *100*, 243.

[11] Ulman, A. *An Introduction to Ultrathin Organic Films : From Langmuir-Blodgett to Self-Assembly*, Academic Press, San Diego, **1991**

[12] Nuzzo, R.G.; Allara, D.L. *J. Am. Chem. Soc*. **1983**,*105*, 4481.

[13] Nuzzo, R.G.; Zegarski, B.R.; Dubois, L.H. *J. Am. Chem. Soc*. **1987**, *109*, 733.

[14] Sagiv, J. *J. Am. Chem. Soc*. **1980**, *102*, 92.

[15] Allongue, P.; de Villeneuve, C.H.; Pinson, J.; Ozanam, F.; Chazalviel, J.N.; Wallart, X. *Electrochim. Acta*. **1998**, *43*, 2791.

[16] He, J.L.; Lu, Z.H.; Mitchell, S.A.; Wayner, D.D.M. *J. Am. Chem. Soc*. **1998**,*120*, 2660.

[17] Bernard, M.-C.; Chausse, A.; Cabet-Deliry, E.; Chehimi, M.M.; Pinson, J.; Podvorica, F.; Vautrin-Ul. C. *Chem. Mater*. **2003**, *15*, 3450.

[18] Kosynkin, D.V.; Tour, J.M. *Org. Lett*. **2001**, *3*, 993.

[19] Ulman, A. *Chem. Rev*. **1996**, *96*, 1533.

[20] Allara, D.L.; Parikh, A.N.; Rondelez, F. *Langmuir* **1995**, *11*, 2357.

[21] Parikh, A.N.; Schivley, M.A.; Koo, E.; Seshadri, K.; Aurentz, D.; Mueller, K.; Allara, D.L. *J. Am.Chem. Soc*. **1997**, *119*, 3135.

[22] Allara, D.L.; Nuzzo, R.G. *Langmuir* **1985**, *1*, 45.

[23] Laibinis, P.E.; Hickman, J.J.; Wrighton, M.S.; Whitesides, G.M. *Science* **1989**, *245*, 845.

[24] Laibinis, P.E.; Whitesides, G.M. *J. Am. Chem. Soc*. **1992**,*114*, 1990.

[25] Bain, C.D.; Troughton, E.B.; Tao, Y.T.; Evall, J.; Whitesides, G.M.; Nuzzo, R.G. *J. Am. Chem. Soc*. **1989**, *111*, 321.

[26] Laibinis, P.E.; Fox, M.A.; Folkers, J.P.; Whitesides, G.M. *Langmuir* **1991**, *7*, 3167.

[27] Decher, G.; Hong, J.; Schmitt, J. *Thin Solid Films* **1992**, *210*, 831.

[28] Motojima, S.; Iwamori, N.; Haltori, T.; Kurosawa, K. *J. Mater. Sci*. **1986**, *21*, 1363.

[29] (a) Sastry, M.; Patil, V.; Mayya, K. S. *Langmuir* **1997**, 13, 4490. (b) Sastry, M.; Patil, V.; Sainkar, S. R. *J. Phys. Chem. B* **1998**, 102, 1404. (c) Patil, V.; Sastry, M. *Langmuir* **2000**, 16, 2207. (d) Patil, V.; Sastry, M. *Langmuir* **1997**, 13, 5511.

[30] Kong, H.S.; Glass, J.T.; Davis, R.F. *Appl. Phys. Lett*. **1986**, *49*, 1074.

[31] Nishino, S.; Powell, J.A.; Will, H.A. *Appl. Phys. Lett.* **1983**, *42*, 460.

[32] Goleeki, I.; Reidinger, F.; Mari, J. *Appl. Phys. Lett*. **1992**, *60*, 1703.

[33] Wahab, Q.; Sardela Jr., M.R.; Hultman, L.; Henry, A.; Willander, M.; Janzen, E.; Sundgren, J.E. *Appl. Phys. Lett*. **1994**, *65*, 725.

[34] (a) Herminghaus, S. *Science* **1998**, *282*, 916. (b) Patil, V.; Sastry, M. *J. Chem. Soc., Faraday Trans*.**1997**, 93, 4347.

[35] (a) Bandyopadhyay, K,; Sastry, M.; Patil, V.; Vijayamohanan, K. *Langmuir*, **1997**, *13*, 866. (b) Sastry, M.; Patil, V.; Mayya, K. S. *J. Phys.Chem.B.* **1997**, *101*, 1167.

[36] (a) Sastry, M.; Mayya, K. S.; Patil, V.; Paranjape, D. V.; Hegde, S. G. *J. Phys. Chem. B* **1997**, *101*, 4954. (b) Mayya, K. S.; Sastry, M. *J. Phys. Chem. B* **1997**, *101*, 9790. (c) Mayya, K. S.; Sastry, M. *Langmuir* **1998**, *14*, 74.

[37] (a) Sastry, M.; Ramakrishnan, V.; Pattarkine, M.; Gole, A.; Ganesh, K. N. *Langmuir* **2000**, 16, 9142. (b) Sastry, M.; Ramakrishnan, V.; Pattarkine, M.; Ganesh, K. N. *J. Phys. Chem. B* **2001**, 105, 4409.

[38] (a) Gole, A.; Dash, C.; Rao, M.; Sastry, M. *Chem. Commun*. **2000**, 297. (b) Gole, A.; Dash, C.; Mandale, A. B.; Rao, M.; Sastry, M. *Anal. Chem*. **2000**, 72, 4301.

[39] Auer, F.; Scotti, M.; Ulman, A.; Jordan, R.; Sellergren, B.; Garno, J.; Liu, G.-Y. *Langmuir* **2000**, *16*, 7554.

[40]. Gole, A.; Sainkar, S.R.; Sastry, M. *Chem.Mater*. **2000**, *12*, 1234.

[41] Chan, E.W.L.; Yu, L. *Langmuir* **2002**, *18*, 311.

[42] He, H.X.; Zhang, H.; Li, Q.C.; Zhu, T.; Li, S.F.Y.; Liu, Z.F. *Langmuir* **2000**, *16*, 3846.

[43] (a) Bandyopadhyay, K.; Patil, V.; Sastry, M.; Vijayamohanan, K. *Langmuir*, **1998**, *14*, 3808. (b) Colvin, V. L.; Goldstein, A. N.; Alivisatos, A. P. *J. Am. Chem. Soc*. **1992**, *114*, 5221.

[44] (a) Decher, G. *Science* **1997**, *277*, 1232, (b) Liu, Y.; Wang, A.; Claus, R.; *J. Phys. Chem. B* **1997**, *101*, 1385. (c) Kumar, A.; Mandale, A.B.; Sastry, M. *Langmuir*, **2000**, *16*, 6921.

[45] Iler, R.K. *J.Colloid Interface Sci.* **1966**, *21*, 569.

[46] (a) Decher, G.; Hong, J. –D.; Schmitt, J. *Thin Solid Films* **1992**, *210*, 504. (b) Lvov, Y.; Essler, F.; Decher, G.; *J. Phys. Chem*. **1993**, *97*, 13773.

[47] Caruso, F.; Niikura, K.; Furlong, D.N.; Okahata, Y. *Langmuir* **1997**, *13*, 3427.

[48] Mamedov, A.; Ostrander, J.; Aliev, F.; Kotov, N.A. *Langmuir* **2000**, *16*, 3941.

[49] Hao, E.; Yang, B.; Ren, H.; Qian, X.; Xie, R.; Shen, J.; Li, D. *Mater.Sci.Engg.C.* **1999**, *10*, 119.

[50] Lvov, Y.; Ariga, K.; Onda, M.; Ichinose, I.; Kunitake, T. *Langmuir* **1997,** *13*, 6195.

[51] Maya, L.; Muralidharan, G.; Thundat, T.G.; Kenik, E.A. *Langmuir* **2000**, *16*, 9151.

[52] Feldheim, D.L.; Grabar, K.C.; Natan, M.J.; Mallouk, T.E.; *J.Am.Chem.Soc.* **1996**, *118*, 7640.

[53] He, J.-A.; Valluzzi, R.; Yang, K.; Dolukhanyan, T.; Sung, C.; Kumar, J.; Tripathy, S.K.; Samuelson, L.; Balogh, L.; Tomalia, D.A. *Chem.Mater.* **1999**, *11*, 3268.

[54] Kumar, A.; Mandale, A.B.; Sastry, M. *Langmuir* **2000**, *16*, 6921.

[55] Cassagneau, T.; Mallouk, T.E.; Fendler, J.H. *J.Am.Chem.Soc.* **1998**, *120*, 7848.

[56] Kumar, A.; Mukherjee, P.; Guha, A.; Adyantaya, S.D.; Mandale, A.B.; Kumar, R.; Sastry, M. *Langmuir* **2000**, *16*, 9775.

[57] Balabushevich, N. G.; Tiourina, O. P.; Volodkin, D. V.; Larionova, N. I.; Sukhorukov, G. B. *Biomacromolecules*, **2003**, *4*, 1191.

[58] Kuhn, H. *Pure Appl. Chem.* **1979**, *51*, 341.

[59] Kuhn, H. *Pure Appl. Chem.* **1981**, *53*, 2105.

[60] Tredgold, R.T. *Rep. Prog. Phys.* **1987**, *50*,1609.

[61] Blinov, L.M. *Russian Chem. Rev.* **1983**, *52*,713.

[62] (a) Ganguly, P.; Paranjape, D.V.; Sastry, M. *Langmuir* **1993**, *9*, 577. (b) Ganguly, P.; Paranjape, D.V.; Patil, K. R.; Sastry, M. Rondelez, F. *Langmuir* **1997**, *13*, 1114.

[63] Swami, A.; Kumar, A.; Selvakannan, PR.; Mandal, S.; Pasricha, R.; Sastry, M. *Chem. Mater.* **2003,** *15*, 17.

[64] (a) Clemente-Leon, M.; Coronado, E.; Delhaes, P.; Gomez-Garcia, C.J.; Mignotaud, C. *Adv.Mater.* **2001**, *13*, 574. (b) Ganguly, P.; Paranjape, D.V.; Sastry, M. *J.Am.Chem.Soc.* **1993**, *115*, 793.

[65] Riccio, A.; Lanzi, M.; Antolini, F.; De Nitti, C.; Tavani, C.; Nicolini, C. *Langmuir* **1996**, *12*, 1545.

[66] Ebara, Y.; Mizutani, K.; Okahata, Y. *Langmuir* **2000**, *16*, 2416.

[67] (a) Sastry, M.; Patil, V.; Mayya, K. S.; Paranjape, D. V.; Singh, P.; Sainkar, S. R. *Thin Solid Films* **1998**, *324*, 239. (b) Sastry, M.; Gole, A.; Patil, V. *Thin Solid Films* **2001**, *384*, 125.

[68] Tian, Y.; Wu, C.; Fendler, J.H. *J.Phys.Chem.* **1995**, *98*, 4913.

[69] (a) Mayya, K. S.; Patil, V.; Sastry, M. *Langmuir* **1997**, 13, 2575-2577. (b) Mayya, K. S.; Patil, V.; Sastry, M. *J. Chem. Soc., Faraday Trans*.**1997**, 93, 3377. (c) Sastry, M.; Mayya, K.S. *J.Nano.Res.*, **2000**, *2*, 183.

[70] Mayya, K.S.; Patil, V.; Kumar, P.M.; Sastry, M. *Thin Solid Films*, **1998**, *312*, 300.

[71] Zhavnerko, G.K.; Agabekov, V.E.; Gallyamov, M.O.; Yaminsky, I.V.; Rogach, A.L. *Coll.Surf.A.*, **2002**, *202*, 233.

[72] Muramatsu,K.; Takahashi, M.; Tajima, K.; Kobayashi, K. *J.Colloid Interface Sci.*, **2001**, *242*, 127.

[73] Lee, D.K.; Kang, Y.S.; Lee, C.S.; Stroeve, P. *J.Phys.Chem.B.*, **2002**, *106*, 7267.

[74] Kang, Y.S.; Lee, D.K.; Lee, C.S.; Stroeve, P. *J.Phys.Chem.B.* **2002**, *106*, 9341.

[75] Du, H.; Bai, Y.B.; Hui, Z.; Li, L.S.; Chen, Y.M. Tang, X.Y.; Li, T.J. *Langmuir*, **1997**, *13*, 2538.

[76] Fendler, J.H.; Meldrum, F. *Adv.Mater.* **1995**, *5*, 607 and references therein.

[77] Damle, C.; Gole, A.; Sastry, M. *J.Mater.Chem.* **2000**, *10*, 1389.

[78] Kurth, D.G.; Lehmann, P.; Lesser, C. *Chem.Commun.* **2000**, 949.

[79] Chen, X.Y.; Li, J.R.; Jiang, L. *Nanotechnology* **2000**, *11*, 189.

[80] Swami, A.; Kumar, A.; Selvakannan, PR.; Mandal, S.; Sastry, M. *J. Colloid Int. Sci*. **2003**, *260* ,367.

[81] Sastry, M.; Rao, M.; Ganesh, K. N. *Acc. Chem. Res*. **2002**, *35*, 847.

[82] (a) Ganguly, P.; Sastry, M.; Pal, S.; Shashikala, M.N. *Langmuir*, **1995,** *11***,** 1078. (b) Sastry, M. *Nanoparticles: Building block for Nanotechnology* **2004**, Ed. Rotello, V. Kluwer Academic/Plenum Publishers USA.

[83] (a) Sastry, M.; Ramakrishnan, V.; Pattarkine, M.; Ganesh, K. N. *J. Phys. Chem. B* **2001**, *105*, 4409. (b) Sastry, M. *Trends Biotechnol.* **2002**, *20*, 185 and references therein.

[84] (a) Wijnhoven, J. E. G. J.; Vos, W. L. *Science* **1998**, *281*, 802. (b) Gates, B.; Xia, Y. *Appl. Phys. Lett*. **2001**, *78*, 3178. (c) Ross, C. A.; Haratani, S.; Castano, F. J.; Hao, Y.; Hwang, M.; Shima, M.; Cheng, J. Y.; Vogeli, B.; Farthoud, M.; Walsh, M.; Smith, H. I. *J. Appl. Phys*. **2002**, *91*, 6848.

[85] Moller, R.; Csaki, A.; Kohler, J. M.; Fritzsche, W. *Langmuir*, **2001**, *17*, 5426.

[86] Castano, F. J.; Hao, Y.; Hwang, M.; Ross, C. A.; Vogeli, B.; Smith, H. I.; Haratani, S. *Appl. Phys. Lett*. **2001**, *79*, 1504.

[87] Blaaderen, A. V.; Ruel, R.; Wiltzius, P. *Nature*, **1997**, *385*, 321.

[88] Lee, S. C.; Malloy, K.J.; Brueck, S. R.J. *J. Appl. Phys*. **2001**, *90*, 4163.

[89 Zhang, J.; Alsayed, A.; Lin, K. H.; Sanyal, S.; Zhang, F.; Pao, W. J.; Balagurusami, V. S.; Heiney, P. A.; Yoah, A. G. *Appl. Phys. Lett*. **2002**, *81*, 3176.

[90] Aizenberg, J.; Braun, P. V.; Wilzius, P. *Phys.Rev.Lett*. **2000**, *84*, 2997.

[91] Yang, S. M.; Ozin, G. A. *Chem.Commun*, **2000**, 2507.

[92] Denis, F. A.; Hanarp, P.; Sutherland, D. S. Dufrene, Y. F. *Nano Lett*. **2002**, *2*, 1419.

[93] Zheng, H.; Lee, I.; Rubner, M. F.; Hammond, P. T. *Adv. Mater*. **2002**, *14*, 569.

[94] Collins, R. J.; Bae, I. T.; Scherson, D. A.; Sukenik, C. N. *Langmuir* **1996**, *12*, 5509.

[95] Lercel, M. J.; Craighead, H. G.; Parikh, A. N.; Seshadri, K.; Allara, D. L. *Appl. Phys. Lett*. **1996**, *68*, 1504.

[96] Thywissen, J. H.; Johnson, K. S.; Younkin, R.; Dekker, N. H.; Berggren, K. K.; Chu, A. P.; Prentiss, M.; Lee, S. A. *J. Vac. Sci. Technol., B* **1997**, *15*, 2093.

[97] Liu, G.-Y.; Xu, S.; Qian, Y. *Acc. Chem. Res*. **2000**, *33*, 457.

[98] Blackledge, C.; Engebretson, D. A.; McDonald, J. D. *Langmuir* **2000**, *16*, 8317.

[99] Maoz, R.; Cohen, S. R.; Sagiv, J. *Adv. Mater*. **1999**, *11*, 55.

[100] Kumar, A.; Whitesides, G.M. *Appl. Phys. Lett*. **1993**, *63*, 2002.

[101] Wilbur, J.L.; Kumar, A.; Kim, E.; Whitesides, G.M. *Adv. Mater*. **1994**, *6*, 600.

[102] Kim, E.; Kumar, A.; Whitesides, G.M. *J. Electrochem. Soc*. **1995**,*142*, 628.

[103] Gorman, C.B.; Biebuyck, H.A.; Whitesides, G.M. *Chem. Mater*. **1995**, *7*, 252.

[104] Xia, Y.N.; Zhao, X.M.; Whitesides, G.M. *Microelectron. Eng*. **1996**, *32*, 255.

[105] Delamarche, E.; Hoole, A.C.F.; Michel, B.; Wilkes, S.; Despont, M.; Welland, M.E.; Biebuyck, H. *J. Phys. Chem. B* **1997**, *101*, 9263.

[106] Geissler, M.; Schmid, H.; Bietsch, A.; Michel, B.; Delamarche, E. *Langmuir* **2002**, *18*, 2374.

[107] Love, J.C.; Wolfe, D.B.; Chabinyc, M.L.; Paul, K.E.; Whitesides, G. M. *J. Am. Chem. Soc*. **2002**, *124*, 1576.

[108] Bumm, L.A.; Arnold, J.J.; Cygan, M.T.; Dunbar, T.D.; Burgin, T.P.; Jones II, L.; Allara, D.L.; Tour, J.M.; Weiss, P.S. *Science* **1996**, *27*,1705.

[109] Donhauser, Z.J.; Mantooth, B.A.; Kelly, K.F.; Bumm, L.A.; Monnell, J.D.; Stapleton, J.J.; Price Jr., D.W.; Rawlett, A.M.; Allara, D.L.; Tour, J.M.; Weiss, P.S. *Science* **2001**, *292*, 2303.

[110] Liu, G. Y.; Xu, S.; Qian, Y. *Acc.Chem.Res*. **2000**. *33*, 457.

[111] Iwata, F.; Kobayashi, K.; Sasaki, A.; Kawata, Y.; Egami, C.; Sugihara, O.; Tuchimori, M.; Watanable,O. *Nanotechnology*, **2002**, *13*, 138.

[112] Santinacci, L.; Djenizian, T.; Schmuki, P. *Appl. Phys.Lett*. **2001**, *79*, 1882.

[113] (a) Liu, J. F.; Cruchon-Dupeyrat, S.; Garno, J. C.; Frommer, J.; Liu, G. Y. *Nano Lett*. **2002**, *2*, 937. (b) Kaholek, M.; Lee, W. K.; LaMattina, B.; Caster, K. C.; Zauscher, S. *Nano Lett*. **2004**, 4, 373.

[114] Dyer, P. E.; Maswadi, S. M.; Walton, C.D.; Erosz, M.; Fletcher, P. D. I.; Paunov, V. N. *Appl. Phys. A*. **2003**, *77*, 391.

[115] (a) Dyer, P. E. *Appl. Phys. A*. **2003**, *77*, 167. (b) Lippert, T.; Hauer, M.; Phipps, C. R.; Wokaun, A. *Appl. Phys. A*. **2003**, *77*, 259.

[116] Cerrina, F.; Marrian, C. *MRS Bull*. **1996**, *21*, 56.

[117] Frost, F.; Rauschenbach, B. *Appl. Phys. A*. **2003**, *77*, 1.

[118] (a) Pool, R. *Science* **1992**, *255*, 1513. (b) Berggren, K. K.; Bard, A.; Wilbur, J. L.; Gillaspy, J.D.; Helg, A.G.; McClelland, J.J.; Rolston, S. L.; Phillips, W. D.; Prentiss, M.; Whitesides, G. M. *Science* **1995**, *269*, 1255.

[119] (a) Muller, D. A.; Tzou, Y.; Raj, R.; Silcox, J. *Nature* **1993**, *366*, 725. (b) Batson, P. E. *Nature* **1993**, *366*, 727.

[120] Fujita, J.; Watanabe, H.; Ochiai, Y.; Manako, S.; Tsai, J.S.; Matsui, S. *Appl. Phys. Lett*.**1995**, *66*, 3065.

[121] Gillen, G.; Wight, S.; Bennett, J.; Tarlov, M. J. *Appl. Phys. Lett*.**1994**, *65*, 534.

[122] Tiberio, R.C.; Craighead, H.G.; Lercel, M.; Lau, T.; Sheen, C.W.; Allara, D.L. *Appl. Phys. Lett*. **1993**, *62*, 476.

[123] Carr, D.W.; Lercel, M.J.; Whelan, C.S.; Craighead, H.G.; Seshadri, K.; Allara, D.L. *J. Vac. Sci.Technol. A* **1997**, *15*, 1446.

[124] Weller, D.; Doerner, M. F. *Annu. Rev. Mater. Sci*. **2000**, *30*, 611.

[125] Miehr, A.; Fischer, R. A.; Lehmann, O.; Stuke, M. *Adv.Mater. Opt. Electron* **1996**, *6*, 27.

[126] Xia, Y.; Kim, E.; Mrksich, M.; Whitesides, G. M. *Chem. Mater*. **1996**, *8*, 601.

[127] Xia Y, Whitesides G. M. *Angew Chem Int Ed* **1998**, 37, 550.

[128] St. John, P. M.; Craighead, H. G. *Appl. Phys. Lett.* **1996**, *68*, 1022.

[129] (a) Calvert, P. Chem. Mater. 2001, 13, 3299. (b) de Gans, B. J.; Duineveld, P. C.; Schubert, U.S. *Adv. Mater*. **2004**, *16*, 203.

[130] Ginger, D. S.; Zhang, H.; Mirkin, C. A. *Angew. Chem. Int. Ed*. **2004**, *43*, 30.

[131] Piner, R.D.; Zhu, J.; Xu, F.; Hong, S.H.; Mirkin, C.A. *Science* **1999**, *283*, 661.

[132] (a) Hong, S.; Zhu, J.; Mirkin, C. A. Science 1999, 286, 523. (b) Zhang, H.; Chung, S. W.; Mirkin, C. A. *Nano Lett*. **2003**, *3*, 43.

[133] (a) Ali, M. B.; Ondarcuhu, T.; Brust, M.; Joachim, C. *Langmuir*, **2002**, *18*, 872. (b) Garno, J. C.; Yang, Y.Y.; Amro, N. A.; Cruchon-Dupeyrat, S.; Chen, S. W.; Liu, G. Y. *Nano Lett*. **2003**, *3*, 389.

[134] (a) Li, Y.; Maynor, B. W.; Liu, J. *J. Am. Chem. Soc*. **2001**, *123*, 2105. (b) Maynor, B. W.; Liu, J. *Langmuir*, **2001**, *17*, 2575.

[135] (a) Maynor, B.W.; Filocamo, S. F.; Grinstaff, M. W.; Liu, J. J. *J. Am. Chem. Soc*. **2002**, *124*, 522. (b) Lim, J. H.; Mirkin, C.A. *Adv. Mater*. **2002**, *14*, 1474.

[136] Demers, L. M.; Park, S. –J.; Taton, T. A.; Li, Z.; Mirkin, C. A. *Angew. Chem. Int. Ed*. **2001**, *40*, 3071.

[137] Phadtare, S.; Parekh, P.; Shah, S.; Tambe, A.; Joshi, R.; Sainkar, S. R.; Prabhune, A.; Sastry, M. *Biotechnol. Prog.* **2003,** *19*, 1659.

[138] Shiigi, H.; Yamamoto, Y.; Yakabe, H.; Tokonami, S.; Nagaoka, T. *Chem. Commun.* **2003**, 1038.

[139] Torimoto, T.; Yamashita, M.; Kuwabata, S.; Sakata, T.; Mori, H.; Yoneyama, H. *J. Phys. Chem. B* **1999**, *103*, 7799.

[140] Kim, S.-H.; Markovich, G.; Rezvani, S.; Choi, S. H.; Wang, K. L.; Heath, J. R. *Appl. Phys. Lett*. **1999**, *74*, 317.

[141] Berven, C. A.; Clarke, L.; Mooster, J. L.; Wybourne, M. N.; Hutchison, J. E. *Ad*v. *Mater*. **2001**, *13*, 109.

[142] Thelander, C.; Magnusson, M. H.; Deppert, K.; Samuelson, L.; Poulsen, P. R.; Nygard, J.; Borggreen *J. Appl. Phys. Lett.* **2001**, *79*, 2106.

[143] Kamar, A.; Whitesides, G. M. *Science* **1994**, *263*, 601.

[144] Mullen, K.; Ben-Jacob, E.; Jaklevic, R.C.; Schuss, Z. *Phys.Rev. B* **1988**, *37*, 98. [145] Jin, B. Y.; Ketteren, J. B. *Adv. Phys*. **1988**, *38*, 189.

[146] Yamashita, I. *Thin Solid Films* **2001**, *393*, 12.

[147] Macmillan, R. A.; Paavola, C. D.; Howard, J.; Chan, S. L.; Zaluzec,N. J.; Trent, J. D. *Nature Mater*. **2002**, *1*, 247.

[148] Lee, S. W.; Mao, C.; Flynn, C. E.; Belcher, A. M. *Science* **2002**,*296*, 892.

[149] Scheibel, T.; Parthasarathy, R.; Sawicki, G.; Lin, X.-M.; Jaeger, H.; Lindquist, S. L. *Proc. Natl. Acad. Sci. U.S.A.* **2003**, *100*, 4527.

[150] Heath, J. R.; Kuekes, P. J.; Snyder, G.; Williams, R. S. *Science* **1998**, *280*, 1717.

[151] D'Amico, S.; Maruccio, G.; Visconti, P.; D'Amone, E.; Cingolani, R.; Rinaldia, R.; Masierob, S.; Spadab, G.P.; Gottarellib, G. *Microelectronics Journal* **2003**, *34*, 961.

[152] Spanhel, L.; Haase, M.; Weller, H.; Henglein, A. *J. Am. Chem.Soc.* **1987**, *109*, 5649.

[153] Yu, H.; Gibbons, P. C.; Kelton, K. F.; Buhro, W. E. *J. Am. Chem.Soc.* **2001**, *123*, 9198.

[154] Huczko, A. *Appl. Phys. A: Mater. Sci. Proc.* **2000**, *70*, 365.

[155] Trindade, T.; O'Brien, P.; Pickett, N. L. *Chem. Mater.* **2001**, *13*,3843.

[156] Wang, Y.; Herron, N. *J. Phys. Chem.* **1987**, *91*, 257.

[157] Shinojima, H.; Yumoto, J.; Uesugi, N.; Omi, S.; Asahara, Y.*Appl. Phys. Lett.* **1989**, *55*, 1519.

[158] Cassagneau, T.; Hix, G. B.; Jones, D. J.; Maireles-Torres, P.; Rhomari, M.; Roziere, J. *J. Mater. Chem.* **1994**, *4*, 189.

[159] Brenchley, M. E.; Weller, M. T. *Angew. Chem.* **1993**, *105*, 1726.

[160] Blasse, G.; Dirksen, G. J.; Brenchley, M. E.; Weller, M. T.*Chem. Phys. Lett.* **1995**, *234*, 177.

[161] Xia, Y.; Yang, P.; Sun, Y.; Wu, Y.; Mayers, B.; Gates, B.; Yin,Y.; Kim, F.; Yan, H. *Adv. Mater.* **2003**, *15*, 353.

[162] Meyer, M.; Wallberg, C.; Kurihara, K.; Fendler, J. H. *Chem.Commun.* **1984**, 90.

[163] Lianos, P.; Thomas, J. K. *Chem. Phys. Lett.* **1986**, *125*, 299.

[164] Pileni, M. P.; Motte, L.; Petit, C. *Chem. Mater.* **1992**, *4*, 338.

[165] Petit, C.; Lixon, P.; Pileni, M. P. *J. Phys. Chem.* **1990**, *94*, 1598.

[166] Petit, C.; Jain, T. K.; Billoudet, F.; Pileni, M. P. *Langmuir* **1994**,*10*, 4446.

[167] Antonietti, M.; Wenz, E.; Bronstein, L.; Seregina, M. *Adv.Mater.* **1995**, *7*, 1000.

[168] Spatz, J. P.; Moessmer, S.; Hartmann, C.; Mo¨ller, M.; Herzog, T.; Krieger, M.; Boyen, H. G.; Ziemann, P.; Kabius, B. *Langmuir* **2000**, *16*, 407.

[169] Forster, S.; Antonietti, M. *Adv. Mater.* **1998**, *10*, 195.

[170] Tricot, Y. M.; Fendler, J. H. *J. Phys. Chem.* **1986**, *90*, 3369.

[171] Watzke, H. J.; Fendler, J. H. *J. Phys. Chem.* **1987**, *91*, 854.

[172] Korgel, B. A.; Monbouquette, H. G. *J. Phys. Chem.* **1996**, *100*,346.

[173] Dujardin, E.; Mann, S. *Adv. Mater.* **2002**, *14*, 775.

[174] Niemeyer, C. M. *Angew. Chem., Int. Ed.* **2001**, *40*, 4129.

[175] Storhoff, J.; Mirkin, C. *Chem. Rev.* **1999**, *99*, 1849.

[176] Wong, K.; Mann, S. *Adv. Mater.* **1996**, *8*, 929.

[177] Shenton, W.; Douglas, T.; Young, M.; Stubbs, G.; Mann, S. *Adv.Mater.* **1999**, *11*, 253.

[178] Dujardin, E.; Peet, C.; Stubbs, G.; Cluver, J.; Mann, S. *NanoLett.* **2003**, *3*, 413.

[179] Knez, M.; Bittner, A. M.; Boes, F.; Wege, C.; Jeske, H.; Maiss,E.; Kern, K. *Nano Lett.* **2003**, *8*, 1079.

[180] Douglas, T.; Young, M. *Nature* **1998**, *393*, 152.

[181] Mirkin, C.; Letsinger, R.; Mucic, R.; Storhoff, J. *Nature* **1996**, *382*, 607.

[182] Cao, Y.; Jin, R.; Mirkin, C. *J. Am. Chem. Soc.* **2001**, *123*, 7961.

[183] Connolly, S.; Fitzmaurice, D. *Adv. Mater.* **1999**, *11*, 1202.

[184] Braun, E.; Eichen, Y.; Sivan, U.; Ben-Yoseph, G. *Nature* **1998**, *391*, 775.

[185] Keren, K.; Krueger, M.; Gilad, R.; Ben-Yoseph, G.; Sivan, U.;Braun, E. *Science* **2002**, *297*, 72.

[186] Keren, K.; Berman, R.; Braun, E. *Nano Lett.* **2004**, *4*, 323.

[187] Richter, J.; Mertig, M.; Pompe, W. *Appl. Phys. Lett.* **2001**, *78*,536.

[188] Ford, W.; Harnack, O.; Yasuda, A.; Wessels, J. *Adv. Mater.*2001, *13*, 1793.

[189] Mertig, M.; Ciacchi, L. C.; Seidel, R.; Pompe, W.; De Vita, A.*Nano Lett.* **2002**, *2*, 841.

[190] Monson, C.; Woolley, A. *Nano Lett.* **2003**, *3*, 359.

[191] Schnur, J. M.; Proce, R.; Schoen, P.; Yager, P.; Clavert, J. M.;Georger, J.; Singh, A. *Thin Solid Films* **1987**, *152*, 181.

[192] Mirkin, C. A.; Letsinger, R. L.; Mucic, R. C.; Storhoff, J. J. *Nature***1996**, *382*, 607.

[193] Alivisatos, A. P.; Johnsson, K. P.; Peng, X.; Wilson, T. E.; Loweth,C. J.; Bruchez, M. P., Jr.; Schultz, P. G. *Nature* **1996**, *382*, 609.

[194] Braun, E.; Eichen, Y.; Sivan, U.; Ben-Yoseph, G. *Nature* **1998**,*391*, 775.

[195] Ford, W. E.; Harnack, O.; Yasuda, A.; Wessels, J. M. *Adv. Mater*.**2001**, *13*, 1793.

[196] Monson, C. F.; Woolley, A. T. *Nano Lett*. **2003**, *3*, 359.

[197] Nakao, H.; Shiigi, H.; Yamamoto, Y.; Tokonami, S.; Nagaoka,T.; Sugiyama, S.; Ohtani, T. *Nano Lett*. **2003**, *3*, 1391.

[198] Karanas, A. G.; Wang, Z. X.; Bates, A. D.; Brust, M. *Angew.Chem., Int. Ed*. **2003**, *42*, 191.

[199] Scheibel, T.; Parthasarathy, R.; Sawicki, G.; Lin, X.-M.; Jaeger,H.; Lindquist, S. L. *Biophys*. **2003**, *100*, 4527.

[200] Dujardin, E.; Peet, C.; Stubbs, G.; Culver, J. N.; Mann, S. *NanoLett*. **2003**, *3*, 413.

[201] Fullam, S.; Cottell, D.; Rensmo, H.; Fitzmaurice, D. *Adv. Mater*.**2000**, *12*, 1430.

[202] Jiang, K.; Eitan, A.; Schadler, L. S.; Ajayan, P. M.; Siegel, R. W.*Nano Lett*. **2003**, *3*, 275.

[203] Ellis, A. V.; Vijayamohanan, K.; Goswami, R.; Chakrapani, N.;Ramanathan, L. S.; Ajayan, P. M.; Ramanath, G. *Nano Lett*. **2003**, *3*, 279.

[204] Spatz, J. P.; Moessmer, S.; Hartmann, C.; Moller, M.; Herzog, T.; Krieger, M.; Boyen, H. G.; Ziemann, P.; Kabius, B. *Langmuir* **2000**, *16*, 407.

[205] Boyen, H.-G.; Kastle, G.; Zurn, K.; Herzog, T.; Weigl, F.;Ziemann, P.; Mayer, O.; Jerome, C.; Mo¨ller, M.; Spatz, J. P.; Garnier, M. G.; Oelhafen, P. *Adv. Funct. Mater*. **2003**, *13*, 359.

[206] Mo¨ller, M.; Kuenstle, H.; Kunz, M. *Synth. Met.* **1991**, *41*, 1159.

[207] Moffitt, M.; McMahon, L.; Pessel, V.; Eisenberg, A. *Chem. Mater*. **1995**, *7*, 1185.

[208] Moffitt, M.; Eisenberg, A. *Chem. Mater*. **1995**, *7*, 1178.

[209] Moffitt, M.; Vali, H.; Eisenberg, A. *Chem. Mater*. **1998**, *10*, 1021.

[210] Ciebien, J. F.; Clay, R. T.; Sohn, B. H.; Cohen, R. E. *New J.*

[211] (a) Bein, T. *Chem. Mater*. **1996**, *8*, 1636. (b) Davis, M. E. *Chem.Eur. J*. **1997**, *3*, 1745.

[212] (a) Goltner, C. G.; Antonietti, M. *Adv. Mater*. **1997**, *9*, 431. (b) Antonietti, M.; Goltner, C. *Angew. Chem*. **1997**, *109*, 944. (c) Zhao, D. Y.; Yang, P. D.; Huo, Q. S.; Chmelka, B. F.; Stucky, G.D. *Curr. Opin. Solid State Mater. Sci*. **1998**, *3*, 111.

[213] (a) Caruso, F.; Lichtenfeld, H.; Giersig, M.; Mo¨hwald, H. *J. Am.Chem. Soc*. **1998**, *120*, 8523. (b) Caruso, F.; Caruso, R. A.;Mo¨hwald, H. *Science* **1998**, *282*, 1111. (c) Caruso, F.; Caruso, R.A.; Mo¨hwald, H. *Chem. Mater*. **1999**, *11*, 3309. (d) Rogach, A.;Susha, A.; Caruso,

F.; Sukhorukov, G.; Kornowski, A.; Kershaw,S.; Mohwald, H.; Eychmuller, A.; Weller, H. *Adv. Mater*. **2000**,*12*, 333.

[214] Hall, S. R.; Shenton, W.; Engelhardt, H.; Mann, S. *Chem. Phys.Chem*. **2001**, *3*, 184.

[215] Lowenstam, H. A.; Weiner, S., On *Biomineralization*; Oxford University Press: Oxford, **1989**.

[216] (a) Young, J. R.; Davis, S. A.; Bown, P. R.; Mann, S. *J. Struct.Biol.* **1999**, *126*, 195. (b) Mann, S. *J. Chem. Soc., Dalton Trans*.**1997**, 3953.

[217] Rowson, J. D.; Leadbeater, B. S. C.; Green, J. C. *Br. Phycol. J*.**1986**, *21*, 359.

[218] Shipway, A. N.; Kaltz, E.; Willner, I. *ChemPhysChem*. **2000**, *1*,18.

[219] (a) Musick, M. D.; Keating, C. D.; Natan, M. J. *Chem. Mater*. **1997**,*9*, 1499. (b) Gittins, D. I.; Bethell, D.; Nichols, R. J.; Schiiffrin, D. J. *Adv. Mater*. **1999**, *11*, 737.

[220] (a) Whetten, R. L.; Shafigullin, M. N.; Khoury, J. T.; Schaaf, T. G.; Vezmar, I.; Alvarez, M. M.; Wilkinson, A. *Acc. Chem. Res.* **1999**, *32*, 397. (b) Collier, C. P.; Vossmeyer, T.; Heath, J. R. *Annu. Rev. Phys. Chem*. **1998**, *49*, 371. (c) Taleb, A.; Petit, C.; Pileni, M. P. *J. Phys. Chem. B* **1998**, *102*, 2214. (7) Wang, Z. L. *Adv. Mater*. **1998**, *10*, 13. (d) Kiely, C. J.; Fink, J.; Brust, M.; Bethell, D.; Schiffrin, D. J. *Nature* **1998**, *396*, 444.

[221] (a) Marinakos, S. M.; Brousseau, L. C.; Jones, A.; Feldheim, D. L. *Chem. Mater*. **1998**, *10*, 1214. (b) Zhou, Y.; Yu, S. H.; Cui, X. P.; Wang, C. Y.; Chen, Z. Y. *Chem. Mater*. **1999**, *11*, 545. (c) Korgel, B. A.; Fitzemaurice, D. *Adv. Mater*. **1998**, *10*, 661. (d) Simon, U.; Schon, G.; Schmid, G. *Angew. Chem., Int. Ed. Engl*. **1993**, *32*, 250. (e) Kumar, A.; Pattarkine, M.; Bhadhade, M.; Mandale, A. B.; Ganesh, K. N.; Datar, S. S.; Dharmadhikari, C. V.; Sastry. M. *Adv. Mater*. **2001**, *13*, 341. (f) Hermanson, K. D.; Lumsdon, S. O.; Williams, J. P.; Kaler, E. W.; Velev, O. D. *Science* **2001**, *294*, 1082. (g) Sun, Y.; Gates, B.; Mayers, B.; Xia, X. *Nano Lett.* **2002**, *2*, 165.

[222] Velev, O. D.; Tessier, P. M.; Lenhoff, A. M.; Kaler, E. W. *Nature* **1999**, *401*, 548. [223] (a) Mirkin, C. A.; Letsinger, R. L.; Music, R. C.; Storhoff, J. J. *Nature* **1996**, *382*, 607. (b) Shenton, W.; Davis, S. A.; Mann, S. *Adv. Mater*. **1999**, *11*, 449. (c) Boal, A. K.; Llhan, F.; Derouchy, J. E.; Thurn-Albrecht, T.; Russell, T. P.; Rotello, V. M. *Nature* **2000**, *404*, 746. (d) Maye, M. M.; Chun, S. C.; Han, L.; Rabinovich, D.; Zhong, C. J. *J. Am. Chem. Soc*. **2002**, *124*, 4958.

[224] (a) Graf, C.; van Blaaderen, A. *Langmuir* **2002,** *18*, 524. (b) Oldenburg, S. J.; Averitt, R. D.; Westcott, S. L.; Halas, N. J. *Chem. Phys. Lett*. **1998**, *288*, 243. (c) Westcott, S. L.; Oldenburg, S. J.; Randall Lee, T.; Halas, N. J. *Langmuir* **1998**, *14*, 5396.
(d) Ji, T.; Lirtsman, V. G.; Avny, Y.; Davidov, D. *Adv. Mater*. **2001**, *13,* 1254. (e) Dokoutchaev, A.; James, J. T.; Koene, S. C.; Pathak, S.; Prakash, G. K. S.; Thompson, M. E. *Chem. Mater*. **1999**, *11*, 2389. (f) Chen, C. W.; Chen, M. Q.; Serizawa, T.; Akashi, M. *Chem. Commun*. **1998**, 831. (g) Chen, C. W.; Serizawa, T.; Akashi, M. *Chem.*
Mater. **1999**, *11*, 1381. (h) Chen, C. W.; Chen, M. Q.; Serizawa, T.; Akashi, M. *Adv. Mater.* **1998**, *10*, 122. (i) Cassagneau, T.; Caruso, F. *Adv. Mater.* **2002**, *14*, 732. (b)
Cassagneau, T.; Caruso, F. *J. Am. Chem. Soc.* **2002**, *124*, 8172.(j) Kobayashi, Y.; Salgueirino-Maceira, V.; Liz-Marzan, L. M *Chem. Mater*. **2001**, *13*, 1630. (k) Zhong, Z.; Mastai, Y.; Koltypin, Y.; Zhao, Y.; Gedanken, A. *Chem. Mater.* **1999**, *11*, 2350. (l) Ramesh, S.; Cohen, Y.; Prosorov, R.; Shafi, K. V. P. M.; Aurbach, D.; Gedanken, A. *J. Phys. Chem. B* **1998**, *102*, 10234

[225] Wong, M. S.; Cha, J. N.; Choi, K.; Deming, T. J.; Stucky, G. D. *Nano Lett.* **2002**, *2*, 583.

[225] (a) Caruso, F.; Spasova, M.; Salgueirno-Maceria, V. *Ad*V. *Mater*. **2001**, *13*, 1090.
(b) Giersig, M.; Ung, T.; Mulvancy, P. *Ad*V. *Mater*. **1997**, *9*, 570. (c) Giersig, M.; Liz-Marzan, L. M.; Ung, T.; Su, D. S. Mulvancy, P. *Ber. Bunsen-Ges. Phys. Chem.* **1997**, *191*, 11617. (d) Caruso, F.; Lichtenfeld, H.; Mo¨hwald, H. *J. Am. Chem. Soc.* **1998**, *120*, 8523. (e) Caruso, F.; Caruso, R.; Mo¨hwald, H. *Science* **1998**, *282*, 1111. (f) Walsh, D.; Mann, S. *Nature* **1995**, *377*, 320. (g) Correa-Duarte, L. M.; Giersig, M.; Liz-Marzan, L. M. *Chem. Phys. Lett.* **1998**, *286*, 497.

[226] (a) Caruso, F. *Adv. Mater.* **2001**, *13*, 11. (b) Oldfield, G.; Ung, T.; Mulvaney, P. *Adv. Mater.* **2000**, *12*, 1519. (c) Hall, S. R.; Davis, S. A.; Mann, S. *Langmuir* **2000**, *16*, 1454. (d) Matijevic, E. *Langmuir* **1994**, *10*, 8.

[227] (a) Turkevich, J.; Kim, G. *Science* **1970**, *169*, 873. (b) Schmid, G.; West, H.; Malm, J. O.; Bovin, J. O.; Grenthe, C. *Chem. Eur. J.* **1996**, *2*, 1099. (c) Toshima, N.; Harada, M.; Yamazaki, Y.; Asakura, K. *J. Phys.Chem.* **1992**, *96*, 9927. (d) Toshima, N.; Hirakawa, K. *Polym. J.* **1999**, *31*, 1127. (e) Han, W. S.; Kim, Y.; Kim, K. *J. Colloid Interface Sci.* **1998**, *208*, 272. (f) Lee, I.; Han, S. W.; Kim, K. *Chem. Commun*. **2001**, 1782. (g) Cottancin, E.; Lerme, J.; Gaudry, M.; Pellarin, M.; Vialle, J. L.; Broyer, M.; Prevel, B.; Treilleux, M.; Melinon, P. *Phys.*

Rev. B **2000**, *62*, 5179. (h) Treguer, M.; de Cointet, C.; Remita, H.; Khatouri, J.; Mostafavi, M.; Amblard, J.; Belloni, J. *J. Phys. Chem. B* **1998**, *102*, 4310. (i) Lu, P.; Dong, J.; Toshima, N. *Langmuir* **1999**, *15*, 7980.

[228] Schmid, G. *Clusters and Colloids*; VCH: Weinheim, **1994**.

[229] Liz-Marzan, L. M.; Giersig, M.; Mulvaney, P. *Langmuir* **1996**, *12*, 4329.

[230] Stober, W.; Fink, A.; Bohn, E. *J. Colloid Interface Sci.* **1968**, *26*, 62.

[231] Hardikar, V. V.; Matijevic, E. *J. Colloid Interface Sci.* **2000**, *221*, 133.

[232] Mulvaney, P.; Liz-Marzan, L. M.; Giersig, M.; Ung, T. *J. Mater.Chem.* **2000**, *10*, 1259.

[233] (a) Kamat P. V. *Nanoparticles and Nanostructured Films*; J. H. Fendler, Ed.; Wiley-VCH: Weinheim, **1998**; Chapter 9, and references therein. (b) Stafford, U.; Gray, K. A.; Kamat, P. V. *J. Phys. Chem.* **1994**, *98*, 6343. (c) Ciambelli, P.; Bagnasco, G.; Lisi, L. *Appl. Catal. B* **1992**, *1*, 61.

[234] (a) Decker, S.; Klabunde, K. J. *J. Am. Chem. Soc.* **1996**, *118*, 12465. (b) Jiang, Y.; Decker, S.; Mohs, C.; Klabunde, K. J. *J. Catal.* **1998**, *180*, 24-35. (c) Carnes, C. L.; Klabunde, K. J. *Chem. Mater.* **2002**, *14*, 1806- 1811. (19) Luo, J.; Maye, M. M.; Lou, Y.; Han, L.; Hepel, M.; Zhong, C. J.

[235] (a) Bruchez, M.; Moronne, M.; Gin, P.; Weiss, S.; Alivisatos, A. P. *Science* **1998**, *281*, 2013. (b) Chan, W. C. W.; Nie, S. *Science* **1998**, *281*, 2016.

[236] (a) Bruchez, M. J.; Moronne, M.; Gin, P.; Weiss, S.; Alivisatos, A. P. *Science* **1998**, *281*, 2013. (b) Chan, W. C. W.; Nie, S. *Science* **1998**, *281*, 2016.

[237] Tsurui, H.; Nishimura, H.; Hattori, S.; Hirose, S.; Okamura, K.; Shirai, T. J. *Histochem. Cytochem.* **2000**, *48*, 653.

[238] Nirmal, N.; Norris, D. J.; Kuno, M.; Bawendi, M. G.; Efros, Al. L.; Rosen, M. *Phys. Re*V. *Lett.* **1995**, *75*, 3728.

[239] (a) Dabbousi, B. O.; Rodriguez-Viejo, J.; Mikulec, F. V.; Heine, J. R.; Mattoussi, H.; Ober, R.; Jensen, K. F.; Bawendi, M. G. *J. Phys. Chem. B* **1997**, *101*, 9463-9475. (b) Danek, M.; Jensen, K. F.; Murray, C. B.; Bawendi, M. G. *Chem. Mater.* **1996**, *8*, 173-180. (c) Peng, X. G.; Schlamp, M. C.; Kadavanich, A. V.; Alivisatos, A. P. *J. Am. Chem. Soc.* **1997**, *119*, 7019-7029. (d) Hines, M. A.; Guyot-Sionnest, P. *J. Phys. Chem.* **1996**, *100*, 468.

[240] (a) Peng, X.; Schlamp, M. C.; Kadavanich, A. V.; Alivisatos, A. P. *J. Am. Chem. Soc*. **1997**, *119*, 7019. (b) Malik, M. A.; O'Brien, P.; Revaprasadu, N. *Chem. Mater*. **2002**, *14*, 2004. (c) Reiss, P.; Bleuse, J.; Pron, A. *Nano Lett.* **2002**, *2*, 781.

[241] Spanhel, L.; Haase, M.; Weller, H.; Henglein, A. *J. Am. Chem.Soc.* **1987**, *109*, 5649.

[242] (a) Kortan, A. R.; Hull, R.; Opila, R. L.; Bawendi, M. G.; Steigerwald, M. L.; Carrol, P. J.; Brus, L. E. *J. Am. Chem. Soc*. **1990**, *112*, 1327. (b) Hines, M. A.; Guyot-Sionnest, P. *J. Phys. Chem.* **1996**, *100*, 468.

[243] Weller, H.; Koch, U.; Gutierrez, M.; Henglein, A. *Ber. Bunsen-Ges. Phys. Chem.* **1987**, *91*, 88.

[244] Hasselbarth, A.; Eychmuller, A.; Eichburger, R.; Giesi, M.;Mews, A.; Weller, H. *J. Phys. Chem.* **1993**, *97*, 5333.

[245] Hasselbarth, A.; Eychmuller, A.; Weller, H. *J. Lumin.* **1992**, *53*, 112.

[246] Zhou, H. S.; Honma, I.; Sasahara, H.; Komiyama, H.; Kraus, J. W. *Chem. Mater*. **1994**, *6*, 1534.

[247] (a) Kortan, A. R.; Hull, R.; Opila, R. L.; Bawendi, M. G.; Steigerwald, M. L.; Carrol, P. J.; Brus, L. E. *J. Am. Chem. Soc*. **1990**, *112*, 1327.(b) Danek, M.; Jensen, K. F.; Murray, C. B.; Bawendi, M. G. *Chem.Mater.* **1996**, *8*, 173.

[248] (a) Peng, X.; Schlamp, M. C.; Kadavanich, A. V.; Alivisatos, A. P. *J. Am. Chem. Soc*. **1997**, *119*, 7019.(b) Tian, Y.; Newton, T.; Kotov, N. A.; Guldi, D. M.; Fendler, J. H. *J. Phys. Chem*. **1996**, *100*, 8927. (c) Banin, U.; Bruchez, M.; Alivisatos, A. P.; Ha, T.; Weiss, S.; Chemla, D. S.*J. Chem. Phys*. **1999**, *110*, 1195.

[249] (a) Dabbousi, B. O.; Rodriguez-Viejo, J.; Mikulec, F. V.; Heine, J. R.; Mattoussi, H.; Ober, R.; Jensen K. F.; Bawendi M. G. *J. Phys. Chem. B* **1997**, *101*, 9463. (b) Hines, M. A.; Guyot-Sionnest, Ph. *J. Phys. Chem.* **1996**, *100*, 468. (c) Peng, X.; Schlamp, M. C.; Kadavanich, A. V.; Alivisatos, A. P. *J. Am. Chem. Soc.* **1997**, *119*, 7019.

[250] (a) Toshima, N.; Yonezawa, T.; Kushihashi, K. *J. Chem. Soc., Faraday Trans.* **1993**, *89*, 2537. (b) Toshima, N.; Harada, M.; Yamazaki, Y.; Asakura, K. *J. Phys. Chem.* **1992**, *96*, 9927. (c) Wang, Y.; Toshima, N. *J. Phys. Chem. B* **1997**, *101*, 5301.

[251] (a) Han, S. W.; Kim, Y.; Kim, K. *J. Colloid Interface Sci.* **1998**, *208*, 272. (b) Link, S.; Wang, Z. L.; El-Sayed, M. A. *J. Phys. Chem. B* **1999**, *103*, 3529.

[252] (a) Gittins, D. I.; Susha A. S.; Wannemacher, R. *Ad*V. *Mater*. **2002**, *14*, 508. (b) Oldenburg, S. J.; Jackson, J. B.; Westcott, S. L.; Halas, N. J. *Appl. Phys. Lett*. **1999**, *75*, 2897. (c) Pham, T.; Jackson, J. B.; Halas, N. J.; Lee, T. R. *Langmuir* **2002**, *18*, 4915.

[253] (a) Klabunde, K. J.; Mulukutla, R. S. In *Nanoscale Materials in Chemistry*; Klabunde, K. J., Ed.; John Wiley and Sons: 2001, pp 223-261. (b) Somorjai, G. A.; Borodko, Y. G. *Catal. Lett.* **2001**, *76*, 1-5. (7) Weller, D.; Doerner, M. F. *Annu. Re*V. *Mater. Sci.* **2000**, *30*, 611- (c) Zhong, C. J.; Maye, M. M. *Ad*V. *Mater.* **2001**, *13*, 1507-1511. (d) Schmid, G. In *Metal Clusters in Chemistry*; Braunstein, P., Oro, L. A., Raithby, P. R., Eds.; Wiley-VCH: Weinheim, 1999; Vol. 3, pp 1325-1341.

[254] (a) Turkevich, J.; Kim, G. *Science* **1970**, *169*, 873. (b) Schmid, G.; West, H.; Malm, J. O.; Bovin, J. O.; Grenthe, C. *Chem. Eur. J.* **1996**, *2*, 1099. (c) Toshima, N.; Harada, M.; Yamazaki, Y.; Asakura, K. *J. Phys.Chem.* **1992**, *96*, 9927. (d) Toshima, N.; Hirakawa, K. *Polym. J.* **1999**, *31*, 1127. (e) Harada, M.; Asakura, K.; Toshima, N. *J. Phys. Chem.* **1993**, *97*, 5103. (d) Yonezawa, T.; Toshima, N. *J. Chem. Soc., Faraday Trans.* **1995**, *91*, 4111. (f) Seregina, M. V.; Bronstein, L. M.; Platonova, O. A.; Chernyshov, D. M.; Valetsky, P. M.; Hartmann, J.; Wenz, E.; Antonietti, M. *Chem. Matter.* **1997**, *9*, 923. (g) Lee, A. F.; Baddeley, C. J.; Hardacre, C.; Ormerod, R. M.; Lambert, R. M. *J. Phys. Chem.* **1995**, *99*, 6096. (h) Mizukoshi, Y.; Okitsu, K.; Maeda, Y.; Zamamoto, T. A.; Oshima, R.; Nagata, Y. *J. Phys. Chem. B* **1997**, *101*, 7033. (i) Schmid, G.; Lehnert, A.; Malm, J. O.; Bovin, J. O. *Angew. Chem., Int. Ed. Engl.* **1991**, *30*, 874.

[255] (a) Liz-Marzan, L. M.; Philipse, A. P. *J. Phys. Chem.* **1995**, *99*, 15120. (b) Yonezawa, T.; Toshima, N. *J. Mol. Catal.* **1993**, *83*, 167. (c) Schmid, G.; West, H.; Mehles, H.; Lehnert, A. *Inorg. Chem.* **1997**, *36*, 891.

[256] (a) Michaelis, M.; Henglein, A.; Mulvaney, P. *J. Phys. Chem.* **1994**, *98*, 6212. (b) Esumi, K.; Wakabayashi, M.; Torigoe, K. *Colloids Surf., A***1996**, *109*, 55. (c) Silvert, P.-Y.; Vijayakrishnan, V.; Vibert, P.; Herrera- Urbina, R.; Elhsissen, K. T. *Nanostruct. Mater.* **1996**, *7*, 611. (d) Torigoe, K.; Esumi, K. *Langmuir* **1993**, *9*, 1664.

[257] Torigoe, K.; Nakajima, Y.; Esumi, K. *J. Phys. Chem.* **1993**, *97*, 8304.

[258] (a) Aihara, N.; Torigoe, K.; Esumi, K. *Langmuir* **1998**, *14*, 4945. b) Itakura, T.; Torigoe, K.; Esumi, K. *Langmuir* **1995**, *11*, 4129. (c) Teo, B. K.; Keating, K.; Kao, Y. H. *J. Am. Chem. Soc.* **1987**, *109*, 3494. (d) Shi, H. Z.; Zhang, L. D.; Cai, W. P. *J. Appl. Phys.* **2000**, *87*, 1572. (e)

Hostetler, M. J.; Zhong, C. J.; Yen, B. K. H.; Anderegg, J.; Gross, S. M.; Evans, N. D.; Porter, M.; Murray, R. W. *J. Am. Chem. Soc.* **1998**, *120*, 9396. (f) Han, W. S.; Kim, Y.; Kim, K. *J. Colloid Interface Sci.* **1998**, *208*, 272. (g) Papavassiliou, G. C. *J. Phys. F*: *Metal Phys.* **1976**, *6*, L103. (h) Lee, I.; Han, S. W.; Kim, K. *Chem. Commun*. **2001**, 1782. (i) Cottancin, E.; Lerme, J.; Gaudry, M.; Pellarin, M.; Vialle, J. L.; Broyer, M.; Prevel, B.; Treilleux, M.; Melinon, P. *Phys. Rev. B* **2000**, *62*, 5179. (j) Chen, Y. H.; Yeh, C. S. *Chem. Commun*. **2001**, 371. (k) Sato, G.; Kuroda, S.; Takami, A.; Yonezawa, Y.; Hada, H. *Appl. Organomet. Chem.* **1991**, *5*, 261. (10) Link, S.; Wang, Z. L.; El-Sayed, M. A. *J. Phys. Chem. B* **1999**, *103*, 3529. (11) Freeman, R. G.; Hommer, M. B.; Grabar, K. C.; Jackson, M. A.; Natan, M. J. *J. Phys. Chem.* **1996**, *100*, 718. (12) Morriss, R. H.; Collins, L. F. *J. Chem. Phys.* **1964**, *41*, 3357. (13) Mulvaney, P.; Giersig, M.; Henglein, A. *J. Phys. Chem.* **1993**, *97*, 1. (14) Treguer, M.; de Cointet, C.; Remita, H.; Khatouri, J.; Mostafavi, M.; Amblard, J.; Belloni, J. *J. Phys. Chem. B* **1998**, *102*, 4310. (15) (a) Lu, P.; Dong, J.; Toshima, N. *Langmuir* **1999**, *15*, 7980. (b) Takenaka, T.; Eda, K. *J. Colloid Interface Sci.* **1985**, *105*, 342. (16) Chen, Y. H.; Nickel, U. *J. Chem. Soc., Faraday Trans.* **1993**, *89*, 2479. (17) (a) Sinzig, J.; Quinten, M. *Appl. Phys.A***1994**, *58*, 157. (b) Sinzig, J.; Radtke, U.; Quinten, M.; Kreibig, U. *Z. Phys. D* **1993**, *26*, 242. (c) Rivas, L.; Sanchez-Cortes, S.; Garcý´a-Ramos, J. V.; Morcillo, G. *Langmuir* **2000**, *16*, 9722. (d) Shibata, T.; Bunker, B. A.; Zhang, Z.; Meisel, D.; Vardeman, C. F., II; Gezelter, J. D. *J. Am. Chem. Soc.* **2002**, *124*, 11989. (e) Mallik, K.; Mandal, M.; Pradhan, N.; Pal, T. *Nano Lett.* **2001**, *1*, 319.

[259] Bohren, C. F.; Huffman, D. R. *Absorption and Scattering of Light by Small Particles*; Wiley: New York, **1983**.

[260] Moskovits, M. *Rev. Mod. Phys.* **1985**, *57*, 783.

[261] Moskovits, M.; Srnova´-Sloufova´ , I.; Vlc¡kova´ , B. *J. Chem. Phys.* **2002**, *116*, 10435.

[262] Ah, C. S.; Hong, S. D.; Jang, D.-J. *J. Phys. Chem. B* **2001**, *105*, 7871.

[263] Srnova-Sloufova, I.; Lednicky, F.; Gemperle, A.; Gemperlova, J. *Langmuir* **2000**, *16*, 9928.

[264] (a) Mandal, S.; PR. Selvakannan.; Pasricha, R.; Sastry, M. *J. Am. Chem. Soc*.**2003**, *125*, 8440. (b) PR. Selvakannan.; Swami, A.; Srisathiyanarayanan, D.; Shirude, P.S.; Pasricha, R.; Mandale, A.B.; Sastry, M. *Langmuir*, **2004**, *20*, 7825.

Chapter 2

Characterization Techniques

The search for new applications of nanostructured system is now a major area of research in materials science and technology. To exploit the full potential that nano-systems offer, it is important to characterize them properly. Characterization of nanoparticles is indispensable to understand the behavior and properties of nanoparticles, aiming at implementing nanotechnology, controlling their behavior and designing new nanomaterial systems with super performance. The different characterization techniques used during the course of the present work are discussed in this chapter.

Materials containing nanometer sized crystallites or phases frequently show interesting and useful new properties in comparison to bulk properties of similar materials. Technologies for fabrication processes of nanophase materials are currently developed in various fields of biological, chemical and physical sciences. The evolution of nanomaterials towards new applications requires knowledge on effects of processing routes and on aspects of long-term stability. Analyzing and understanding of structural and chemical changes on these extremely small scales are therefore crucial for further success. The current most challenging tasks are property characterization and characterizations are carried out using a variety of microscopy and spectroscopy techniques. This chapter is devoted in explaining the basic principles and techniques used for characterization. The main emphasis of this thesis is the formation of nanocompopsites and these nanocomposites have been characterized by a host of techniques such as quartz crystal microgravimetry **(**QCM), Uv-vis. spectroscopy, Fourier transform infrared (FTIR), X-ray Diffraction (XRD), X-Ray photoelectron spectroscopy (XPS), scanning electron microscopy (SEM), transmission electron microscopy (TEM), and isothermal titration calorimetry (ITC) measurements.

2.1 Quartz Crystal Microgravimetry (QCM) Study

The advantage of conceptual simplicity, relative ease of modification, chemical inertness of the substrates, low cost and ready availability of piezoelectric transducers makes quartz crystal microgravimetry (QCM) a powerful tool to study various adsorption processes and has been used to study adsorption of gases [1] self-assembled monolayers (SAMs) [2] Langmuir-Blodgett films [3], nanoparticles [4], and biomolecules [5]. For the work discussed in this thesis, QCM has been extensively used to follow the kinetics of ion incorporation into lipid matrix.

2.1.1 Basic Principles:

Piezoelectricity as first reported in 1880 by Curie brothers (Jacques and Pieree Curie) describes the generation of electrical charges on the surface of a solid caused by pulling, preassure or torsion. The piezoelectric effect is the production of electric displacement by applying mechanical stress. In contrast the occurrence of a mechanical deformation arising

from an external electric field is called the converse piezoelectric effect, i.e. the converse piezoelectric effect results in a strain in the crystal when an electric field is applied.

The mechanical stress applied to the surface of various crystals including quartz, Rochelle salt ($NaKC_4H_4O_6$, $4H_2O$) and tourmaline afforded a corresponding electrical potential across the crystal whose magnitude is proportional to the applied stress. This property only exists in materials that are acentric, i.e. those that crystallize in noncentrosymmetric space groups. A single crystal of an acentric material will possess a polar axis due to dipoles associated with the orientation of atoms in the crystalline lattice. The charges generated in a quartz crystal under stress are due to the shift of dipoles resulting from the displacement of atoms in acentric crystalline materials. If a stress is applied across an appropiate direction, the resulting atomic displacement will result in a corresponding change in the net dipole moment. This action will produce a net charge in electrical charge on the faces of the crystal, the degree and the direction of this charge depending upon the relative orientation of the dipoles and the crystal faces.

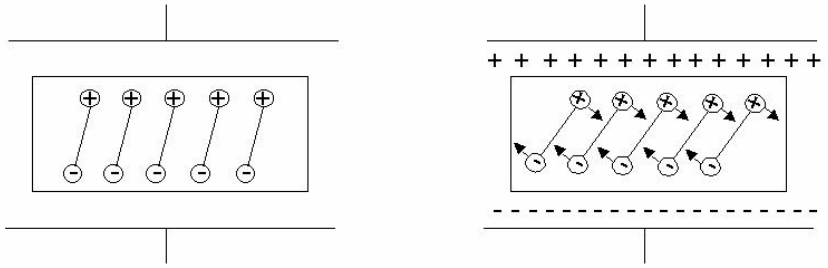

Figure 2.1: Schematic shows the converse piezoelectric effect for shear motion.

The electric field induces reorientation of the dipoles of the acentric material resulting in a lattice strain and shear deformation of the material. Application of an electric field across the crystal produces a shear strain proportional to the applied potential. In quartz this deformation is elastic. The opposite polarity produces an identical strain, but in the opposite direction. It follows that an alternating potential across the crystal causes a vibrational motion in the quartz crystal with amplitude parallel to the surface of the crystal. The result of the vibrational motion of the quartz crystal is the establishment of a transverse acoustic wave that propagates across the thickness of the crystal (t_q), reflecting back into the crystal at the surfaces. A standing wave condition can therefore be established when the acoustic wavelength

is equal to $2t_q$. The frequency of the acoustic wave in this resonant condition is given by the equation 1.

$$\mathbf{f_0 = v_{tr}/2t_q \quad \text{……..(1)}}$$

where, v_{tr} is the transverse velocity of sound in AT-cut quartz crystal.

When a uniform layer of a foreign material is added to the surface of the quartz crystal, the acoustic wave will travel across the interface between the quartz and the layer, will propagate through the foreign layer. If the assumption is made that the acoustic properties of the foreign layer are identical to those of quartz, this system can be treated as a composite resonator, in which the change in thickness due to foreign layer is treated as tantamount to a change in the quartz crystal thickness.

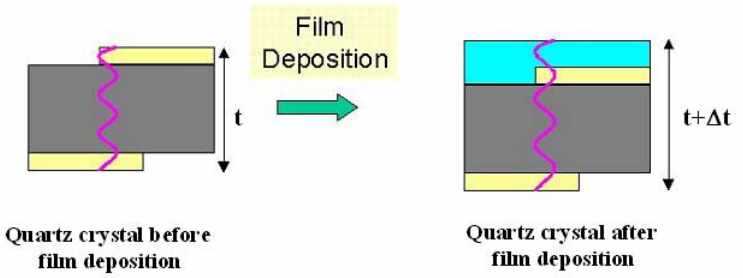

Figure 2.2: Schematic shows the change in thickness after deposition of foreign material on quartz crystal.

A fractional change in thickness (Δt) then results in a fractional change in frequency. The acoustic wavelength is longer in the composite resonator due to the greater thickness, resulting in a low resonant frequency compared to the quartz crystal.

$$\mathbf{\Delta f/f_0 = - \Delta t/t_q}$$

$$\textbf{Since } \mathbf{f_0 = v_{tr}/2t_q} \textbf{ (from equation 1)}$$

$$\mathbf{\therefore \Delta f/f_0 = - (2f_0.\, \Delta t)/v_{tr} \quad \text{……..(2)}}$$

where Δf is the measured frequency shift, f_0 = the frequency of the quartz crystal prior to a mass change, v_{tr} = transverse velocity.

Δt is new expressed as an areal density Δm/A obtained by the relationship, $\Delta t = \Delta m/\rho_q.A$ where Δm = the mass change, A = the piezoelectrically active area, ρ_q = the density of quartz (2.65 gm/cm^3), μ_q = shear modulus (2.95×10^{11} $gmcm^{-1}s^{-2}$).Therefore the implicit assumption in this treatment is the density and the transverse velocity associated with this material is identical to

that quartz. This is equivalent to stating that the acoustic impedance $\rho_q.v_{tr} = (\rho_q.\ \mu_q)^{1/2}$ is assumed to be identical in two materials.

Substituting $v_{tr} = (\mu_q/\rho_q)^{1/2}$ and $\Delta t = \Delta m/\rho_q.A$ in equation 2 we will get

$$\mathbf{\Delta f/f_0 = - (2f_0.\ \Delta m/\rho_q.A)/\ (\mu_q/\rho_q)^{1/2}}$$

Simplifying this equation we get $\mathbf{\Delta f = -(2f_0^2.\ \Delta m)/(A.\ \mu_q^{1/2}\rho_q^{1/2}).}$ **……(3)** and this the well-known Sauerbrey equation.

Depending on the cut-angle a large number of different resonator types such as thickness shear mode, plate resonators can be obtained from mother crystal with eigenfrequency ranging from $5x10^2$ –$3x10^8$ Hz. Generally AT-cut quartz crystals are used for QCM purposes, being cut with an angle of 35.25^0 to Z-axis. AT-cut quartz crystal exhibits a high frequency stability of $\Delta f/f = 10^{-8}$, which makes them well suited for many electronic devices. Since AT-cut quartz crystals have a temperature coefficient that is almost zero between $0\text{-}50^0$C, this particular cut is the most suitable one for QCM sensors.

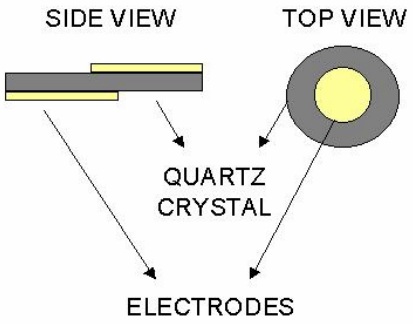

Figure 2.3: Schematic shows a typical QCM crystal.

2.1.2 Quartz Crystal Microgravimetry (QCM) measurements:

In the work described in this thesis we have used a gold coated AT-cut 6 MHz quartz crystal. The frequency counter used was an Edwards FTM5 instrument operating at a frequency stability and resolution of $\pm$ 1 Hz. At this resolution and the type of quartz crystal used, the mass resolution would be 12 ng/cm^2. We have used QCM technique in the following way. Different thickness films of lipids such as stearic acid, octadecylamine, hexadecylaniline were deposited on gold-coated 6 MHz quartz crystal for quartz crystal microbalance (QCM) measurements by thermal evaporation in an Edwards E306A vacuum coating unit at a pressure of better that 1×10^{-7} Torr. The film thickness and deposition rate were monitored *in-situ* using

an Edwards FTM5 frequency counter. After deposition of the lipid films these crystals were immersed into different electrolyte solutions for different experiments and the change in frequency of the quartz crystal was measured *ex-situ* after thorough washing (in deionized water) and drying (in flowing nitrogen) of the crystal for various times of immersion of the crystal in the electrolyte solution. The frequency changes were converted to mass loading using the standard Sauerbrey formula [6].

We would like to point out possible errors in the interpretation of the QCM data using the simple Saurbrey formula. Most QCM investigations assume that the film layer shows rigid behaviour and no slip at the resonator-fluid boundary, while using Saurbrey equation [2a,b]. These asssumptions are valid when dealing with studies on inorganic thin films, wherein the film deposited is rigid enough to be considered "quartz like". However while dealing with lipid films that are being intercalated with ions such as Ag^{+}, Cd^{2+}, $AuCl_4^{-}$, one would need to consider factors such as viscoelastic effects, high mass loadings, surface roughness, surface stress, interfacial slippage and non uniform mass distribution in any piezoelectric measurement [2a,b]. The thin films in our case (about 500 Å), low mass loadings (about 6-12 μg) as compared to total weight of the crystal, and assuming uniform mass distribution over the film surface supports the validity of the use of Saurbrey equation in our case.

2.2 UV-Visible Spectroscopy Study

2.2.1 Basic Principles:

The UV-visible range is a tiny part of the total electromagnetic spectrum, and is generally taken to be from wavelengths of 190 nm at the high energy UV end to about 750 nm at the red end of the spectrum. The range is not an arbitrary assignation; rather the energies of this particular radiation are sufficiently high to promote various electron transitions within a molecule. Other regions of the spectrum correspond to different types of transitions and hence different spectroscopies. For example, IR radiation is not energetic enough to cause electron transitions. All radiation is quantised; that is to say it can only exist as discrete amounts of energy (quanta, photons in the case of light). This gives rise to the concept that the energy possessed by, say, an electron is also quantised, and thus we talk about the energy levels of the electron. The electron is able to change its energy level by gaining or losing energy, but only in amounts exactly corresponding to the difference between the two levels. So the promotion of

the electron from the ground state (lowest possible energy) at energy E1 to energy E2 can only occur if the molecule absorbs a photon which has an energy = (E2 - E1). This electron at a higher energy is said to be excited & to be in an excited state. Excited states only last for very short periods of time (1 to 10 nanoseconds), because the higher energy state is energetically unstable, and the extra energy is lost through relaxation processes such as emission of light or heat.

The absorption of UV or visible radiation corresponds to the excitation of outer electrons. There are three types of electronic transition, which can be considered;

1. Transitions involving π, σ, and *n* electrons
2. Transitions involving charge-transfer electrons
3. Transitions involving *d* and *f* electrons (not covered in this Unit)

Possible *electronic* transitions of π, σ, and *n* electrons are

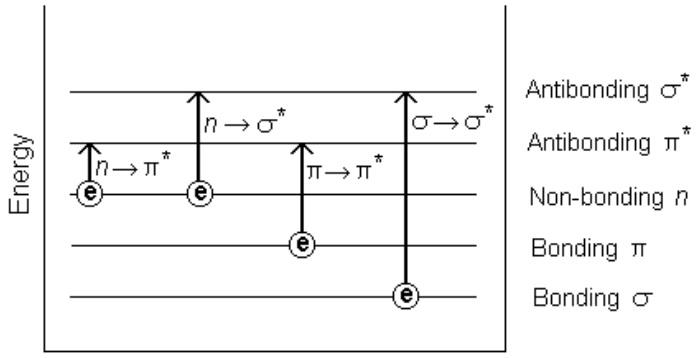

Figure 2.4: Schematic shows the possible electronic transitions.

$\sigma \rightarrow \sigma^*$ Transitions

An electron in a bonding σ orbital is excited to the corresponding antibonding orbital. The energy required is large. For example, methane (which has only C-H bonds, and can only undergo $\sigma \rightarrow \sigma^*$ transitions) shows an absorbance maximum at 125 nm. Absorption maxima due to $\sigma \rightarrow \sigma^*$ transitions are not seen in typical UV-Vis. spectra (200 - 700 nm).

$n \rightarrow \sigma^*$ Transitions

Saturated compounds containing atoms with lone pairs (non-bonding electrons) are capable of $n \rightarrow \sigma^*$ transitions. These transitions usually need less energy than $\sigma \rightarrow \sigma^*$ transitions. They

can be initiated by light whose wavelength is in the range 150 - 250 nm. The number of organic functional groups with $n \rightarrow \sigma^*$ peaks in the UV region is small.

$n \rightarrow \pi^*$ and $\pi \rightarrow \pi^*$ Transitions

Most absorption spectroscopy of organic compounds is based on transitions of *n* or π electrons to the π^* excited state. This is because the absorption peaks for these transitions fall in an experimentally convenient region of the spectrum (200 - 700 nm). These transitions need an unsaturated group in the molecule to provide the π electrons. Molar absorbtivities from $n \rightarrow \pi^*$ transitions are relatively low, and range from 10 to100 L mol^{-1} cm^{-1}. $\pi \rightarrow \pi^*$ transitions normally give molar absorbtivities between 1000 and 10,000 L mol^{-1} cm^{-1}. The solvent in which the absorbing species is dissolved also has an effect on the spectrum of the species. Peaks resulting from $n \rightarrow \pi^*$ transitions are shifted to shorter wavelengths (*blue shift*) with increasing solvent polarity. This arises from increased solvation of the lone pair, which lowers the energy of the *n* orbital. Often (but *not* always), the reverse (i.e. *red shift*) is seen for $\pi \rightarrow \pi^*$ transitions. This is caused by attractive polarisation forces between the solvent and the absorber, which lower the energy levels of both the excited and unexcited states. This effect is greater for the excited state, and so the energy difference between the excited and unexcited states is slightly reduced - resulting in a small red shift. This effect also influences $n \rightarrow \pi^*$ transitions but is overshadowed by the blue shift resulting from solvation of lone pairs. Many inorganic species show charge-transfer absorption and are called *charge-transfer complexes*. For a complex to demonstrate charge-transfer behaviour, one of its components must have electron donating properties and another component must be able to accept electrons. Absorption of radiation then involves the transfer of an electron from the donor to an orbital associated with the acceptor. Molar absorbtivities from charge-transfer absorption are large (greater that 10,000 L mol^{-1} cm^{-1}). Many molecules absorb ultraviolet or visible light. The absorbance of a solution increases as attenuation of the beam increases. Absorbance is directly proportional to the path length, *b*, and the concentration, *c*, of the absorbing species. *Beer's Law* states that $\mathbf{A = \varepsilon bc}$, where **A** is the measured absorbance, $\boldsymbol{\varepsilon}$ is a wavelength-dependent absorptivity coefficient, **b** is the cell-path length, and **c** is the analyte concentration. When working in concentration units of molarity, the Beer-Lambert law is where is the wavelength-dependent molar absorptivity coefficient with units of $\mathbf{M^{-1}cm^{-1}}$. Experimental measurements

are usually made in terms of transmittance (T), which is defined as: $\mathbf{T = I / I_o}$ where I is the light intensity after it passes through the sample and Io is the initial light intensity. The relation between A and T is: $\mathbf{A = -\log T = - \log (I / I_o)}$.

Modern absorption instruments can usually display the data as transmittance, %-transmittance, or absorbance. Measuring the amount of light that a sample absorbs and applying Beer's law can determine an unknown concentration of an analyte. If the absorptivity coefficient is not known, the unknown concentration can be determined using a working curve of absorbance versus concentration derived from standards. The Beer-Lambert Law has some limitations such as;

(a) There is a concentration limit above which it is not reliable. This upper limit varies from analyte to analyte, but a rough rule of thumb would be to say ca. 0.01 M. The reason for the limit is that at high concentrations, or if an electrolyte is present, then electrostatic interactions between neighboring molecules distort their electronic energy levels. Remember, it is electron transitions between these levels that give the absorption characteristics of the molecule, and so we can expect that the distortions give rise to enhanced or decreased absorption at the analysis wavelength. Either way will result in a non-linear relationship between absorbance & concentration. Especial care should be taken while analyzing large organic ions where non-linearity may be found down to very low concentrations (for methylene blue, the calibration graph does not become linear until the concentration is less than 0.000001 M.

(b) Chemical Deviations: if the system under analysis changes chemically, then the analysis will fail. One of the commonest examples of this type of behavior is seen as pH is altered. For example, dichromate actually exists in equilibrium with two other chromium species, each having their own particular value of the molar absorptivity. As the pH is altered, the amounts of these three forms present vary, and the absorption at a particular wavelength will also vary. The ratio of the three forms will even vary with dilution. For this and other pH sensitive systems, it is necessary to buffer the system to retain a constant amount of the three forms.

(c) Instrumental Deviations: the Beer-Lambert Law was derived strictly on the basis of monochromatic radiation (single wavelength), but this is not practical to obtain (the smaller the range of wavelengths selected by the monochromator, the harder & more expensive it is). To get around this problem we need to make our measurement at a region of the spectrum where the molar absorptivity is very similar for all the wavelengths passed on by the monochromator.

This will be the case at absorption maximum. Other instrumental factors, which may affect linearity, are stray light and dirty/unmatched cells.

The instrument needs to generate UV-visible radiation, select the wavelength of interest, and measure the amount absorbed after it has been passed through the sample. The schematic diagram below shows the major constituents in a simple instrument.

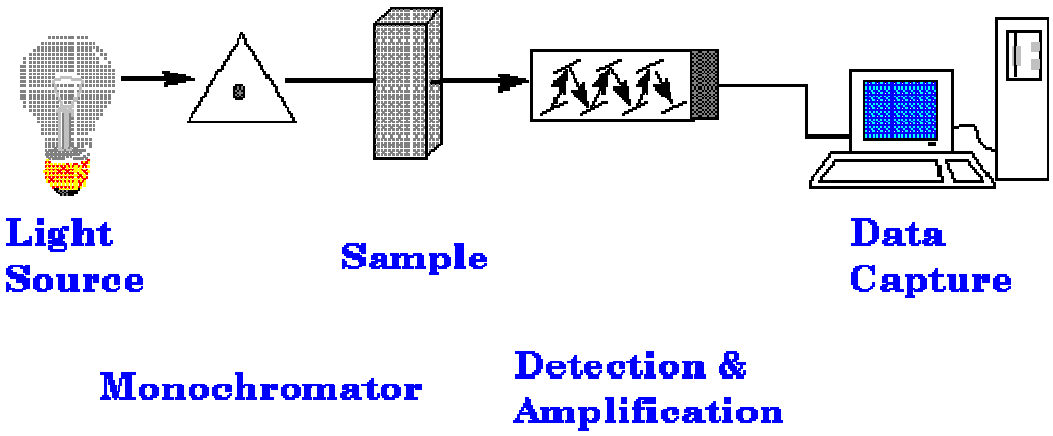

Figure 2.5: Schematic shows the diagram of an UV-visible spectrophotometer.

The source of the radiation needs to be continuous over the range of wavelengths of interest. The earliest sources were simple tungsten filament bulbs (light-bulbs!) but they have since been superceded with time by tungsten-halogen lamp. Such light sources cover the wavelength range beyond 320 nm, but to reach further down into the UV regime, an additional source is essential. Deuterium arc lamp is used for this purpose, which gives a continuous spectrum below 400 nm.

A monochromator ("single colour") is used to select the wavelength at which an absorption measurement is to be made. In actual fact, it is not practically possible to obtain one wavelength; rather a narrow range of wavelengths (known as the bandpass) is selected. There are two main choices of monochromator: a prism, or a diffraction grating. The former was the original component, but now most modern instruments employ gratings. The primary advantage of gratings over prisms is their smaller bandpass, but they do have the disadvantage of giving more than one order of diffraction (see Bragg diffraction). This means that if the monochromator is set at 600 nm for example, then it will also pass 300 nm (second order)

radiation. This problem is easily overcome by the use of filters to remove the unwanted radiation.

The principle requirement of any detector is that its electrical output (voltage) is directly proportional to the intensity of the radiation hitting it. In addition, the detector should to be sensitive enough to produce a measurable electrical signal from a reasonably small number of photons. A number of designs have been used over the years but the most common type is the photomultiplier tube, due to its sensitivity & response to a wide wavelength range. These devices consist of a cathode (electrically negative), coated with a photoemissive material, which emits an electron on being hit by a photon of light. Electrons emitted by the cathode are repelled by the -ve charge & accelerated towards an anode (+ve), to which they collide energetically releasing more electrons. Further, anodes at an increasingly +ve voltage increase the number of electrons at the end of the detector, which develops an electrical signal that can be amplified by normal electronics. Atypical detector of this type may have 10 anodes with about 100 V potential differences between successive anodes. A relatively new type of detector, which has been commercially available since 1970s is the photodiode array. Such semiconductor detectors were originally relatively expensive, but real prices have dropped & many modern instruments use such a device. These detectors are composed of thousands of photodiodes arranged side by side in a thin strip of about 2 cm x 25 microns. Each diode is initially charged up and the connecting electronics device monitors the level of charge. If such diodes are exposed to light, they lose their charge proportionally, depending on the radiation intensity. The use of these detectors requires a slightly different instrumental layout. The radiation from the source is passed straight through the sample (not monochromated) to a fixed diffraction grating where it is dispersed in the normal way. The dispersed radiation hits the photodiode array which has been arranged in such a way that one end corresponds to the maximum wavelength to be measured, and the other to the minimum wavelength (see diagram). Obviously, the middle region of the array monitors intermediate wavelengths. The great advantage of this type of detector is that there is no sequential scanning of the wavelengths (which may take several minutes), rather the entire spectrum is measured simultaneously.

Single beam spectrophotometers are relatively cheap, simple, portable & ideally suited to quantitative analysis. It is not possible to scan through the entire spectrum with such an

instrument because both the source intensity & the detector response vary with the wavelength. The instrument would record a "spectrum" even without a sample present! To record an accurate value of the absorbance it is necessary to zero the instrument on a reference/blank before every measurement. Thus, this is essentially a single wavelength measurement of absorbance. This is not a problem for quantitative analysis, which is carried out at a single wavelength anyway. Double beam spectrophotometers instruments have been designed to eliminate the problem of the single beam device & are necessarily more complex & expensive. They are usually not portable but are able to scan the entire spectrum as well as make measurements at a single wavelength. The light from the source is alternatively split into one of two beams by a rotating mirror sometimes called a "chopper"; one beam is passed through the sample & the other through the reference cell. The detector alternately sees the beam from the sample & the reference & its net output, which ideally would be a oscillating square-wave, gives the ratio of I to Io directly i.e. the reference correction is made automatically.

Gold and silver particles with diameters on the nanometer scale show very bright colors. The bright colors of noble metal nanoparticles are due to the resonant excitation of a collective oscillation of the conduction band electrons in the particles termed surface plasmon resonance. Conduction electrons (-) and ionic cores (+) in a metal form a plasma state. When external electric fields (electro-magnetic waves, electron beams etc.) are applied to a metal, electrons move so as to screen perturbed charge distribution, further move beyond the neutral states, and again return to the neutral states and so on. This collective motion of electrons is called a "plasma oscillation." The surface plasmon resonance is a collective excitation mode of the plasma localized near the surface. Electrons confined in a nanoparticle conform the surface plasmon mode.

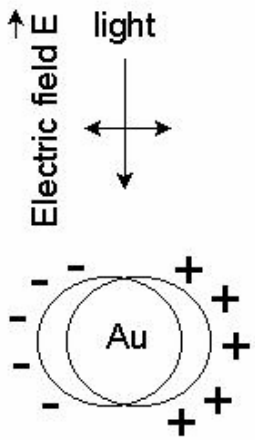

Figure 2.6: Schematic shows the polarization of a spherical metal particle by the electrical field vector of the incoming light.

Since the diameter of a nanoparticle is of the order of the penetration depth of electromagnetic waves in metals, the excitation light is able to penetrate the particle. The field inside the particle shifts the conduction electrons collectively with respect to the fixed positive charge of the lattice ions. The electrons build up a charge on the surface at one side of the particle. The attraction of this negative charge and the positive charge of the remaining lattice ions on the opposite side results in for a restoring force. If the frequency of the excitation light field is in resonance with the eigenfrequency of this collective oscillation, even a small exciting field leads to a strong oscillation. The magnitude of the oscillation depends only on the damping involved, which can be both radiative and nonradiative. The resonance frequency is mainly determined by the strength of the restoring force. This force depends on the separation of the surface charges, i.e. the particle size, and the polarizability of the medium between and around the charges, which depends on the embedding medium and the polarizability of the core electrons of the metal particle. The alternating surface charges effectively form an oscillating dipole, which radiates electromagnetic waves. The resonance frequency of the surface plasmon is different from an ordinary plasma frequency. Since it arises from the electron confinement in the nanoparticle. Since the dielectric function tends to become continuous at the interface (surface), the oscillation mode shifts from the ordinary plasmon resonance and exponentially decays along the depth from the surface. Light absorption by small metal particles is best described by Mie's theory [7]. The absorption spectrum of particles in a given solvent can be calculated from the optical constants of the bulk metal, although the absorption of the particles

is often vastly different from that of the bulk metal itself [7]. The simplest case is when the particles are spherical and their size is small compared to the wavelength of light, and the particles are well separated in solution. Within the particle size of about 3-20 nm, the absorbance spectrum does not depend strongly on the particle size. This is because the particles are below the size at which higher order terms in the Mie formula for the absorption constant become significant.

$$\alpha = \frac{18\,\pi}{\ln 10}\;\frac{10^5}{\lambda}\;\frac{M\,n_0^3}{\rho}\;\frac{\varepsilon_2}{(\varepsilon_1 + 2\,n_0^2) + \varepsilon_2^2}$$

Thus, one has to regard only the dipole term, which depends only on the total metal concentration in the solution and not on particle size. The absorption coefficient in mol^{-1}. L. cm^{-1} is calculated from the relation [7,8] where λ is the wavelength of light in nanometers, M and ρ are the molecular weight and density of the metal, n_o is the refractive index of the solvent and ε_1 and ε_2 are the real and imaginary parts of the dielectric constant of the metal. When the size of the particles becomes smaller than the mean free path of the electrons, the absorption bands are broadened; this is accounted for by using size-corrected values of ε_2 [7,8].

$$\boldsymbol{\varepsilon_2 = \varepsilon_{2(bulk)} + (\omega_p^{\,2} / \omega^3)(v_F/R)}$$

where ω is the light frequency, ω_P the plasmon frequency, v_F the electron velocity at the Fermi level and R the particle radius (R/v_F, mean time of the free movement of the electrons). Resonance with the incident light is reached at the wavelength, where the negative value of ε_1 of the metal is equal to twice the dielectric constant of the medium. Gold particles possess plasmon resonances in the visible range (~514 nm). This surface sensitivity of colloidal nanoparticles has been used to study adsorption/chemisorption of thiols[9], biomolecules [10] etc. A colorimetric detection system using biomolecules and nanoparticles to detect antigen-antibody [11] and DNA mismatch detection [12] has also been studied.

2.2.2. UV-vis spectroscopy measurements:

UV-vis spectroscopy measurements of a 500 Å thick metal nano-lipid film on quartz during the different stages of nanoparticle formation were carried out on a Hewlett-Packard HP 8542A diode array spectrophotometer operated at a resolution of 2 nm. UV-vis spectroscopy

measurements of the Ag/CdS-PTA solution at different stages of treatment were carried out on a on a Jasco UV-vis spectrophotometer (V570 UV-VIS-NIR) operated at a resolution of 2 nm. The optical properties of the core-shell nanoparticle (Au@Ag, Au@Pt, Au@Pd) solutions at different stages of preparation were also monitored on a Jasco UV-vis spectrophotometer (V570 UV-VIS-NIR) operated at a resolution of 2 nm.

2.3 Fourier Transform Infrared (FTIR) Spectroscopy Study

Infrared (IR) spectroscopy is one of the most common spectroscopic techniques used by organic and inorganic chemists. Simply, it is the absorption measurement of different IR frequencies by a sample positioned in the path of an IR beam. The main goal of IR spectroscopic analysis is to determine the chemical functional groups in the sample. Different functional groups absorb characteristic frequencies of IR radiation. Using various sampling accessories, IR spectrometers can accept a wide range of sample types such as gases, liquids, and solids. Thus, IR spectroscopy is an important and popular tool for structural elucidation and compound identification. Infrared radiation spans a section of the electromagnetic spectrum having wavenumbers from roughly 13,000 to 10 cm^{-1}, or wavelengths from 0.78 to 1000 μm. It is bound by the red end of the visible region at high frequencies and the microwave region at low frequencies. IR absorption positions are generally presented as either wavenumbers ($\overline{\nu}$) or wavelengths (λ). Wavenumber defines the number of waves per unit length. Thus, wavenumbers are directly proportional to frequency, as well as the energy of the IR absorption. The wavenumber unit (cm^{-1}, reciprocal centimeter) is more commonly used in modern IR instruments that are linear in the cm^{-1} scale. In the contrast, wavelengths are inversely proportional to frequencies and their associated energy. At present, the recommended unit of wavelength is μm (micrometers), but μ (micron) is used in some older literature. Wavenumbers and wavelengths can be interconverted using the following equation:

$$\overline{\nu}\ (\text{in cm}^{-1}) = [1/\lambda\ (\text{in } \mu\text{m})] \times 10^4$$

IR absorption information is generally presented in the form of a spectrum with wavelength or wavenumber as the x-axis and absorption intensity or percent transmittance as the y-axis. Transmittance, T, is the ratio of radiant power transmitted by the sample (I) to the radiant power incident on the sample (I_0). Absorbance (A) is the logarithm to the base 10 of the reciprocal of the transmittance (T).

$$\mathbf{A = \log_{10}(1/T) = -\log_{10}T = -\log_{10}(I/I_0)}$$

The transmittance spectra provide better contrast between intensities of strong and weak bands because transmittance ranges from 0 to 100% *T* whereas absorbance ranges from infinity to zero. The analyst should be aware that the same sample would give quite different profiles for the IR spectrum, which is linear in wavenumber, and the IR plot, which is linear in wavelength. It will appear as if some IR bands have been contracted or expanded. The IR region is commonly divided into three smaller areas: near IR, mid IR, and far IR.

2.3.1 Basic Principles:

The principles of IR can be explained by classical as well as quantum theories. The classical model considers a simple ball and spring model wherein diatomic molecule with two masses m_1 and m_2 are connected by a spring. According to Hooke's law when spring is displaced,

$$\mathbf{F = -kx}$$

Where F = opposing restoring force; k = force constant; x = displacement from equilibrium position. This is simple harmonic equation wherein the relation gives the frequency of vibration:

$$\nu = \frac{1}{2\pi}\cdot\sqrt{\frac{k}{\mu}}$$

Where μ is the reduced mass. Using simple laws of mechanics, a system of masses joined by springs has a number of fundamental modes of vibration each of which has a particular natural frequency. Consider an oscillator such as the electric vector of electromagnetic radiation coupled to a system of masses such as a polyatomic molecule. By scanning through a range of frequencies some may be 'tuned' to the various fundamental modes of vibration by virtue of a change in dipole moment associated with that vibration. So, a series of absorption take place for a polyatomic molecule as we scan through a range of frequencies, radiation is absorbed each time we 'tune-in' or 'come into resonance' with the natural frequency of a fundamental mode which is capable of dipolar interaction.

At temperatures above absolute zero, all the atoms in molecules are in continuous vibration with respect to each other. When the frequency of a specific vibration is equal to the

frequency of the IR radiation directed on the molecule, the molecule absorbs the radiation. Each atom has three degrees of freedom, corresponding to motions along any of the three Cartesian coordinate axes (x, y, z). A polyatomic molecule of *n* atoms has 3*n* total degrees of freedom. However, 3 degrees of freedom are required to describe translation, the motion of the entire molecule through space. Additionally, 3 degrees of freedom correspond to rotation of the entire molecule. Therefore, the remaining $3n - 6$ degrees of freedom are true, fundamental vibrations for nonlinear molecules. Linear molecules possess $3n - 5$ fundamental vibrational modes because only 2 degrees of freedom are sufficient to describe rotation. Among the $3n - 6$ or $3n - 5$ fundamental vibrations (also known as normal modes of vibration), those that produce a net change in the dipole moment may result in an IR activity and those that give polarizability changes may give rise to Raman activity. Naturally, some vibrations can be both IR- and Raman-active. The total number of observed absorption bands is generally different from the total number of fundamental vibrations. It is reduced because some modes are not IR active and a single frequency can cause more than one mode of motion to occur. Conversely, additional bands are generated by the appearance of overtones (integral multiples of the fundamental absorption frequencies), combinations of fundamental frequencies, differences of fundamental frequencies, coupling interactions of two fundamental absorption frequencies, and coupling interactions between fundamental vibrations and overtones or combination bands (Fermi resonance). The intensities of overtone, combination, and difference bands are less than those of the fundamental bands. The combination and blending of all the factors thus create an unique IR spectrum for each compound. Infrared radiation is absorbed and the associated energy is converted into these type of motions. The absorption involves discrete, quantized energy levels. However, other rotational motions usually accompany the individual vibrational motion. These combinations lead to the absorption bands and not the discrete lines, commonly observed in the mid IR region.

Modern IR instruments more commonly use Fourier-transform techniques with a Michelson interferometer. An infrared spectrophotometer is composed of an IR light source, a sample container, and a prism to separate light by wavelength, a detector, and a recorder (which produces the infrared spectrum).

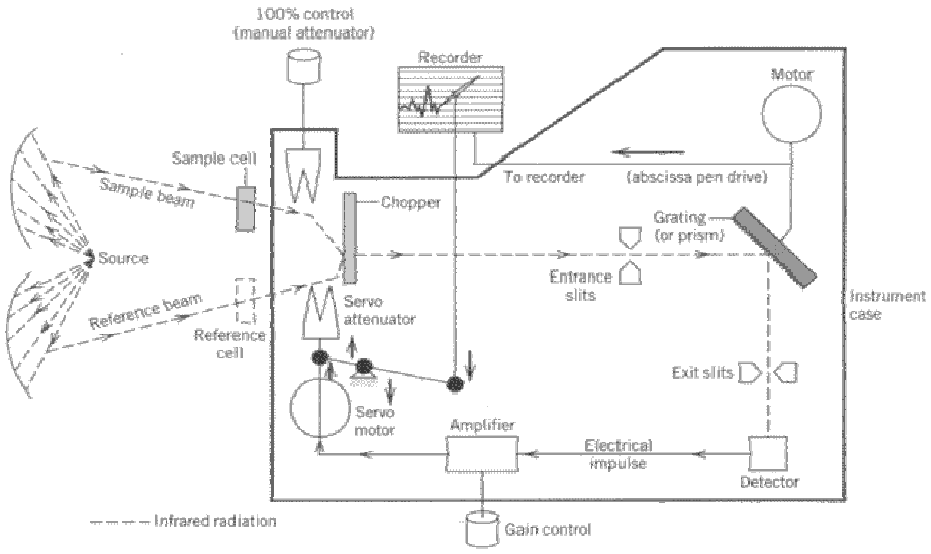

Figure 2.7: Schematic shows the diagram of an infrared spectrophotometer.

FTIR instruments have distinct advantages:

(a) Better speed and sensitivity (Felgett advantage). A complete spectrum can be obtained during a single scan of the moving mirror, while the detector observes all frequencies simultaneously.

(b) An FTIR instrument can achieve the same signal-to-noise (S/N) ratio of a dispersive spectrometer in a fraction of the time (1 sec or less versus 10 to 15 min). The S/N ratio is proportional to the square root of the total number of measurements. Because multiple spectra can be readily collected in 1 min or less, sensitivity can be greatly improved by increasing S/N through coaddition of many repeated scans.

© Energy-wasting slits are not required in the interferometer because dispersion or filtering is not needed. Instead, a circular optical aperture is commonly used in FTIR systems. The beam area of an FT instrument is usually 75 to 100 times larger than the slit width of a dispersive spectrometer. Thus, more radiation energy is made available. This constitutes a major advantage for many samples or sampling techniques that are energy-limited.

(d) Internal laser reference (Connes advantage). The use of a helium neon laser as the internal reference in many FTIR systems provides an automatic calibration in an accuracy of better than 0.01 cm^{-1}. This eliminates the need for external calibrations.

(e) Simpler mechanical design. There is only one moving part, the moving mirror, resulting in less wear and better reliability.
(f) Elimination of stray light and emission contributions. The interferometer in FTIR modulates all the frequencies. The unmodulated stray light and sample emissions (if any) are not detected.
(g) Powerful data station, Modern FTIR spectrometers are usually equipped with a powerful, computerized data system. It can perform a wide variety of data processing tasks such as Fourier transformation, interactive spectral subtraction, baseline correction, smoothing, integration, and library searching.

2.3.2 Fourier Transform Infra-Red (FTIR) Spectroscopy measurements:

For FTIR measurements the films were deposited on silicon substrates for variety of reasons. Si substrate is chemically very stable and generally not very reactive even at high temperatures. It is excellent for optical studies of deposited films in the visible region using reflection techniques. It does not very strong lattice absorption bands in the useful regions of the infrared and thus can be used for transmission studies in this region. To correct for the lattice absorption bands in silicon, a blank silicon substrate is used as a reference. All FTIR data presented in the thesis been presented as obtained except for baseline correction. FTIR measurements of the 500 Å thick metal/semiconductor nano-lipid film on Si (111) wafer during the different stages of nanoparticle formation were carried out on a Shimadzu FTIR-8201 PC instrument operated in the diffuse reflectance mode at a resolution of 4 cm^{-1}. Fourier transform infrared (FTIR) spectroscopy measurements from different nanoparticle solutions at different stages of treatment in the different experiments discussed in this thesis were prepared by solution-casting films onto Si(111) wafers. FTIR measurements were carried out on a Perkin-Elmer-Spectrum One FTIR spectrometer operated at a resolution of 4 cm^{-1}.

2.4 X-ray Diffraction (XRD) Study

In 1895 after discovering X-ray by Rontgen, von Laue demonstrated that X-ray could be diffracted by crystal in 1912. In 1935 Le Galley first constructed X-ray powder diffractometer. Largely metallurgists and mineralogists use powder diffraction primarily to study structural imperfections.

2.4.1 Basic Principles:

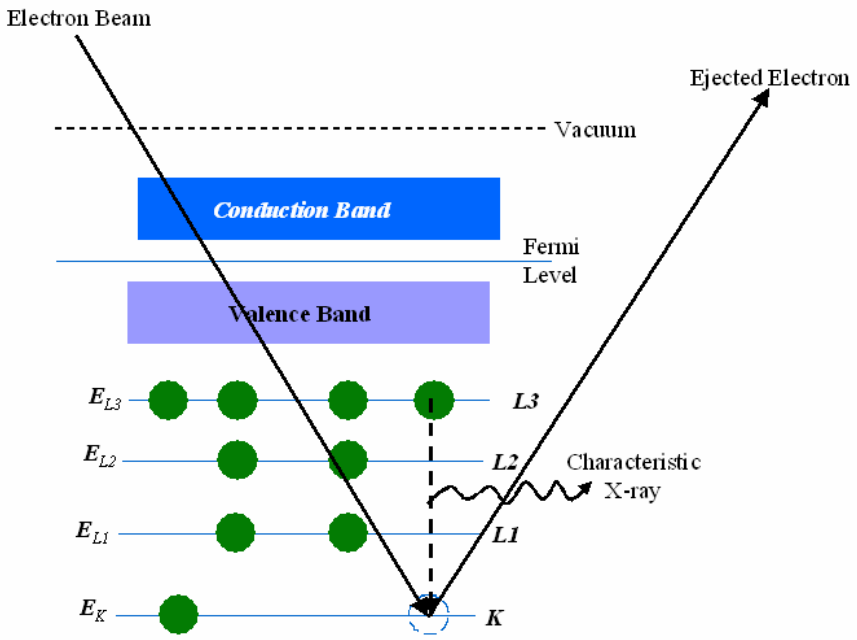

Figure 2.8: Schematic shows the processes that contribute to the generation of X-rays.

X-rays are electromagnetic radiation with wavelength of the order of 10^{-10} m. They are typically generated by bombarding a metal with high-energy electrons. The high-energy electron must penetrate through the outer electron shells and interact with the inner-shell (or core) electrons. If more than a critical amount of energy is transferred to an inner-shell electron, that electron is ejected; i.e. it escapes the attractive field of the nucleus, leaving a hole in the inner shell and generates ionized atom. The ionized atom can return almost to its lowest energy (ground state) by filling in the missing electron with one from the outer shells. It is this transition which is accompanied either by the emission of an X-ray or an Auger electron.

In 1913, Sir W.H. Bragg and his son Sir W.L. Bragg gave the famous Bragg's Law ($n\lambda = 2d \sin\theta$) to explain why the cleavage faces of crystals appear to reflect X-ray beams at certain angles of incidence (θ). The variable *d* is the distance between atomic layers in a crystal, and the variable lambda λ is the wavelength of the incident X-ray beam, n is an integer. This observation is an example of X-ray wave interference commonly known as X-ray diffraction (XRD), and was direct evidence for the periodic atomic structure of crystals postulated for several centuries. Although Bragg's law was used to explain the interference pattern of X-rays

scattered by crystals, diffraction has been developed to study the structure of all states of matter with any beam, e.g., ions, electrons, neutrons, and protons, with a wavelength similar to the distance between the atomic or molecular structures of interest.

A crystal may be defined as a collection of atoms arranged in a pattern that is periodic in 3D. Crystals are necessarily solids, but not all solids are crystalline. In a perfect single crystal all atoms in the crystal are related either through translational symmetry or point symmetry. Polycrystalline materials are made up of a great number of tiny single crystals. In powder diffraction method we can get the information from peak positions, crystal system, space group symmetry, translational symmetry, unit cell dimension, qualitative phase identification, from peak intensities unit cell contents, point symmetry and from peak shapes and widths crystalline size, non-uniform microstrain, extended defects. Deviations from ideal crystallinity, such as finite crystallite size and strain lead to broadening of the diffraction lines. By analyzing this broadening it is possible to extract information about the microstructure of a material. A perfect crystal would extend in all directions to infinity, so we can say that no crystal is perfect due to its finite size. This deviation from perfect crystallinity leads to a broadening of the diffraction peaks. However above a certain size (~ 0.1-1μm) this type of broadening is negligible. Crystallite size is a measure of the size of a coherently diffraction domain. Due to presence of polycrystalline aggregates crystallite size is not generally the same thing as particle size. In 1918 Scherrer first observed that small crystallite size could give rise to line broadening. He derived a well-known equation for relating the crystallite size to the broadening, which is called the "Scherrer formula".

$$\mathbf{D_v = k\lambda/(\beta.\cos\theta)}$$

where, D_v = volume weighted crystallite size, k = Scherrer constant, somewhat arbitrary value that falls in the range 0.87-1, λ = wavelength of the X-ray radiation, β = integral breadth of a reflection (in radians 2θ) located at 2θ.

2.4.2. X-ray Diffraction (XRD) measurements:

Samples for XRD measurements from metal nano-lipid composite thin films and drop-coated films of nanoparticle solutions on glass substrates were performed in the transmission mode on a Philips PW 1830 instrument operating at 40 kV voltages and a current of 30 mA with Cu K_α radiation.

We have used XRD for the determination of the lamellar lipid bilayer structure. After ion incorporation of ions into lipid matrix, XRD analysis gives spectra of (0,0,l) reflections arising due to the layer-by-layer structure similar to the *c*-axis oriented LB films. The spacing between the reflections can be converted to the 'd' values using Bragg's law. This spacing gives us an idea whether the periodicity of the lipid bilayer stacks is maintained or if there is some tilt in the chains of the lipid stacks.

2.5 Scanning Electron Microscopy (SEM) Study

Scanning Electron Microscopy is extremely useful for the direct observations of surfaces because they offer better resolution and depth of field than optical microscope. The Scanning Electron Microscope creates the magnified images by using electrons instead of light waves. The SEM shows very detailed 3-dimensional images at much higher magnifications than is possible with a light microscope. The images created without light waves are rendered black and white. In a very brief way SEM works under vacuum in a column where an electron gun emits a beam of high-energy electrons. This beam travels downward through a series of magnetic lenses designed to focus the electrons to a very fine spot. Near the bottom, a set of scanning coils moves the focused beam back and forth across the specimen, row by row. As the electron beam hits each spot on the sample, secondary electrons are knocked loose from its surface. A detector counts these electrons and sends the signals to an amplifier. The final image is built up from the number of electrons emitted from each spot on the sample. A detailed explanation of how a typical SEM functions:

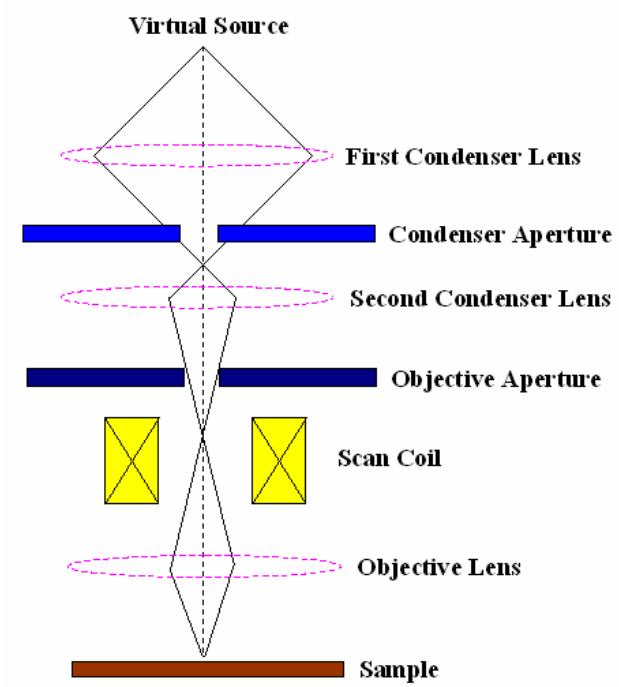

Figure 2.9: Schematic shows the diagram of Scanning Electron Microscope.

1. The "Virtual Source" at the top represents the electron gun producing a stream of monochromatic electrons.
2. The stream is condensed by the first condenser lens (usually controlled by the "coarse probe current knob"). This lens is used to both form the beam and limit the amount of current in the beam. It works in conjunction with the condenser aperture to eliminate the high-angle electrons from the beam.
3. The condenser aperture constricts the beam by eliminating some high-angle electrons.
4. The second condenser lens forms the electrons into a thin, tight, coherent beam and is usually controlled by the "fine probe current knob".
5. A user selectable objective aperture further eliminates high-angle electrons from the beam.
6. A set of coils then "scan" or "sweep" the beam in a grid fashion (like a television), dwelling on points for a period of time determined by the scan speed (usually in the microsecond range).
7. The final lens, the Objective, focuses the scanning beam onto the part of the specimen desired.

8. When the beam strikes the sample (and dwells for a few microseconds) interactions occur inside the sample and are detected with various instruments.
9. Before the beam moves to its next dwell point these instruments count the number of interactions and display a pixel on a CRT whose intensity is determined by this number (the more reactions the brighter the pixel).

2.5.1 Working Principles:

The instrument can be simplified into three major sections: a) electron-optical 'column'; b) vacuum system and c) electronics and display system. A tungsten filament is heated to 2700 K, which produces electrons that are accelerated towards the anode disc. Electrostatic shaping of the electron beam under vacuum gives a beam diameter of about 50 μm. Ultimate performance of the SEM is mainly limited by the diameter of the beam and hence two lenses and condensers demagnify the beam to around 5 nm. The scanning coils deflect this beam and sweep it over the specimen surface. A cathode-ray display tube is scanned synchronously with the electron beam. The brightness of the display tube is modulated by the signal, which arises from the interaction of the beam with the surface element, which is probed. The strength of this signal is translated into image contrast. Secondary electrons, which the beam probe liberates from the specimen surface, are collected and used as the contrast signal. The yield of collected electrons depends on the nature of the specimen surface and on its inclination with respect to the probing beam. Consequently, one obtains pictures with a high perspective appearance.

Specimen-Beam interaction: There are different types of interactions of the electron beam possible with the sample. The energetic electrons in the microscope strike the sample and various reactions can occur as shown below.

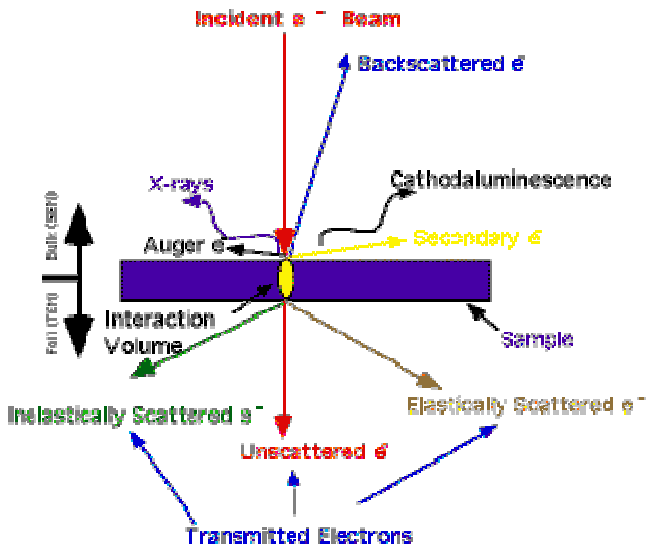

Figure 2.10: Schematic shows the diagram of Specimen-Beam interactions.

Backscattered electrons produced by an incident electron colliding with an atom in the specimen, which is nearly normal to the incident's path. The incident electron is then scattered "backward" 180 degrees. The production of backscattered electrons varies directly with the specimen's atomic number or “specimen interaction volume”. Specific interaction volume is the volume inside the specimen in which interactions occur while being struck with an electron beam. This volume depends on the following factors:

(a) Atomic number of the material; higher atomic number materials absorb or stop more electrons and so have a smaller interaction volume.

(b) Accelerating voltage being used; higher voltages penetrate farther into the sample and generate larger interaction volumes.

(c) Angle of incidence for the electron beam; the greater the angle (further from normal) the smaller the volume.

This differing production rates causes higher atomic number elements to appear brighter than lower atomic number elements. This interaction is utilized to differentiate parts of the specimen that have different average atomic number. These elastically scattered electrons usually called 'backscattered electrons' are used for SEM imaging.

Secondary electron produced by an incident electron passing "near" an atom in the specimen, near enough to impart some of its energy to a lower energy electron (usually in the K-shell). This causes a slight energy loss and path change in the incident electron and the ionization of

the electron in the specimen atom. This ionized electron then leaves the atom with a very small kinetic energy (5eV) and is then termed a "secondary electron". Each incident electron can produce several secondary electrons. Due to their low energy, (5eV only) secondary electrons that are very near to the surface (<10nm) can exit the sample and be examined. Any changes in topography of the sample that are larger than this sampling depth will change the yield of secondary due to collection efficiencies. Collection of these electrons is aided by using a "collector" in conjunction with the secondary electron detector. The collector is a grid or mesh with a +100V potential applied to it which is placed in front of the detector, attracting the negatively charged secondary electrons to it which then pass through the grid-holes and into the detector to be counted. When a Secondary Electrons collide with the solid-state semiconductor detector an electron-hole pairs are created which are then counted. This quantity is translated into a pixel intensity and displayed on the CRT, forming the image

Energy Dispersive analysis of X-rays (EDAX) is a technique, which is based on the characteristic X-ray peaks that are generated when an energetic electron beam interacts with the specimen. X-ray is produced by the de-energization of the specimen atom after a secondary electron is produced. Since a lower shell (usually K-shell) electron was emitted from the atom, during the secondary electron process an inner (lower energy) shell now has a vacancy. A higher energy electron can "fall" into the lower energy shell, filling the vacancy. As the electron "falls" it emits energy, usually X-rays to balance the total energy of the atom so it. X-rays or Light emitted from the atom will have a characteristic energy, which is unique to the element from which it originated. Each element produces characteristic x-rays that may be used to identify the presence of that element in the region being examined. Comparison of the relative intensities of x-ray peaks may be used to determine the relative concentrations of each element in the specimen. Elements with an atomic number less than that of carbon (Z=5) are not generally detectable.

2.5.2 Scanning electron microscopy (SEM) and energy dispersive analysis of X-rays (EDX) measurements:

Scanning electron microscopy (SEM) and energy dispersive analysis of X-rays (EDX) measurements from the patterned metal/semiconductor-lipid films were carried out on a Leica Stereoscan-440 scanning electron microscope equipped with a Phoenix EDX attachment. EDX

spectra were recorded in the spot-profile mode by focusing the electron beam onto specific regions of the metal/semiconductor nano-lipid patterned film. Samples SEM and EDX analysis from the nanoparticle solutions at different stages of treatment in different experiments discussed in this thesis were prepared by solution-casting films onto Si (111) wafers and the measurements were also carried out on a Leica Stereoscan-440 scanning electron microscope equipped with a Phoenix EDX attachment.

2.6 Transmission Electron Microscopy (TEM) Study

The transmission electron microscope (TEM) operates on the same basic principles as the light microscope but uses electrons instead of light. What we can see with a light microscope is limited by the wavelength of light. TEM uses electrons as "light source" and their much lower wavelength makes it possible to get a resolution thousand times better than that with a light microscope. We can see objects to the order of a few angstrom (10^{-10} m). For example, we can study small details in the cell or different materials down to near atomic levels. The possibility for high magnifications has made the TEM a valuable tool in both medical, biological and materials research.

2.6.1 Working Principle:

A TEM works much like a slide projector. A projector shines a beam of light through (transmits) the slide, as the structures and objects on the slide affect the light passes through it. These effects result in only certain parts of the light beam being transmitted through certain parts of the slide. This transmitted beam is then projected onto the viewing screen, forming an enlarged image of the slide. TEM works the same way except that they shine a beam of electrons (like the light) through the specimen (like the slide). Whatever part is transmitted is projected onto a phosphor screen for the user to see. A more technical explanation of a typical TEMs working is as follows:

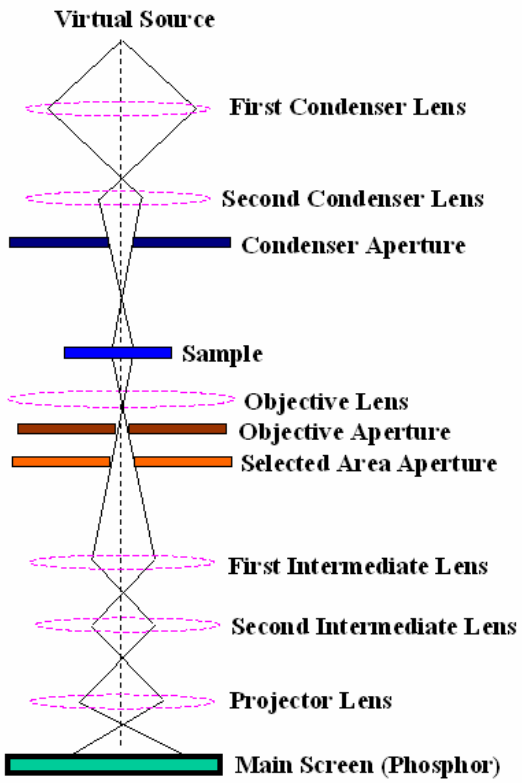

Figure 2.11: Schematic shows the diagram of Transmission Electron Microscope.

1. The "Virtual Source" at the top represents the electron gun, producing a stream of monochromatic electrons.
2. This stream is focused to a small, thin, coherent beam by the use of condenser lenses 1 and 2. The first lens (usually controlled by the "spot size knob") largely determines the "spot size"; the general size range of the final spot that strikes the sample. The second lens (usually controlled by the "intensity or brightness knob" actually changes the size of the spot on the sample; changing it from a wide dispersed spot to a pinpoint beam.
3. The condenser aperture knocks out the high angle electrons beam (those far from the optic axis, the dotted line down the center).
4. The beam strikes the specimen and parts of it are transmitted.
5. This transmitted portion is focused by the objective lens into an image
6. Optional Objective and Selected Area metal aperture can restrict the beam; the Objective aperture enhancing contrast by blocking out high-angle diffracted electrons, the Selected Area aperture enabling the user to examine the periodic diffraction of electrons by ordered arrangements of atoms in the sample.

7. The image is passed down the column through the intermediate and projector lenses, being enlarged all the way.
8. The image strikes the phosphor image screen and light is generated, allowing the user to see the image. The darker areas of the image represent those areas of the sample that fewer electrons were transmitted through (they are thicker or denser) and the lighter areas of the image represent those areas of the sample that more electrons were transmitted through (they are thinner or less dense).

Bright field imaging is an imaging mode in a TEM that uses only unscattered electrons to form the image. Contrast in such an image is entirely due to thickness and density variations in a sample. Unscattered electrons are incident electrons, which are transmitted through the thin specimen without any interaction occurring inside the specimen. The transmission of unscattered electrons is inversely proportional to the specimen thickness. Areas of the specimen that are thicker will have fewer transmitted unscattered electrons and so will appear darker, conversely the thinner areas will have more transmitted and thus will appear lighter.

In dark field imaging a single diffracted beam is used to form the image in a TEM. This causes all regions of the specimen that are not of the same crystal structure and orientation as the region which produced the diffracted beam to be represented as very dark in the final image; allowing phase differentiation visually in the TEM.

In selected area electron diffraction (SAED), an aperture is used to define the area from which a diffraction pattern is formed in a TEM specimen. The resulting patterns contain information about phases present (lattice spacing measurement) and sample orientation

2.6.2. Transmission Electron Microscopy (TEM) measurements:

In order to obtain information on the dimensions of metal/CdS nanoparticles formed in thin film, the metal/CdS nano-lipid films grown on the copper grids were analysed by TEM. These measurements were performed on a Jeol model 1200EX instrument operated at a voltage of 120 kV. Prior to TEM measurements, the excess lipid (stearic acid or octadecylamone) molecules were removed by immersing the lipid-metal/CdS nano composite film in organic solvent (chloroform, hexane) for a period of 15 minutes. Samples for TEM studies from different nanoparticle solutions (aqueous or organic) in different experiment discuused in this thesis were prepared by placing a drop of the nanoparticle solutions on carbon-coated TEM

grids. The films on the TEM grids were allowed to dry for 2 min following which the extra solution was removed using a blotting paper and the TEM measurements were performed on a JEOL model 1200EX instrument operated at an accelerating voltage at 120kV. High Resolution Transmission Electron Microscope (HRTEM) measurements were performed on a JEOL model 2010F UHR instrument operated at an accelerating voltage at 200 keV.

2.7 X-Ray Photoelectron Spectroscopy (XPS) Study

X-ray Photoelectron Spectroscopy known as XPS or ESCA (Electron Spectroscopy for Chemical Analysis) has been developed from the Fifties by Professor K. Siegbahn. The Physics Nobel Prize awarded his work in 1981. The most interesting thing with this technique is its ability to measure binding energy variations of elements resulting from their chemical environment. For the past 20 years, this type of spectrometry emerged as a key tool in surface analysis, mainly because of two major features: (a) Quantitative analysis, (b) Information on the chemical nature and state of the detected elements. By absorbing a photon, an atom gains an energy amount equal to hν. It then releases an electron to regain its original stable energy state. The released electron retains all the energy from the striking photon. It can then escape from the atom, and even further from matter and kinetic energy keeps it moving. With XPS, incident photons usually carry an energy ranging from 1 to 2 KeV. Photoelectron spectroscopy utilizes photo-ionization and energy-dispersive analysis of the emitted photoelectrons to study the composition and electronic state of the surface region of a sample.

2.7.1. Working Principle:

XPS is based on the well-known photoelectric effect first explained by Einstein in 1905. XPS spectral lines are identified by the shell from, which the electron was ejected (1s, 2s, 2p, etc.). The ejected photoelectron has kinetic energy: $KE = h\nu - BE - \Phi_{spec}$ where, hν = energy of photons , BE= Electron Binding Energy , KE= Electron Kinetic Energy, Φ_{spec} = Spectrometer Work Function. The XPS instrument measures the kinetic energy of all collected electrons. The electron signal includes contributions from both photoelectron and Auger electron lines. Photoelectron line energies are dependent on photon energy whereas Auger electron line energies are not dependent on photon energy. If XPS spectra were presented on a kinetic

energy scale, one would need to know the X-ray source energy used to collect the data in order to compare the chemical states in the sample with data collected using another source.

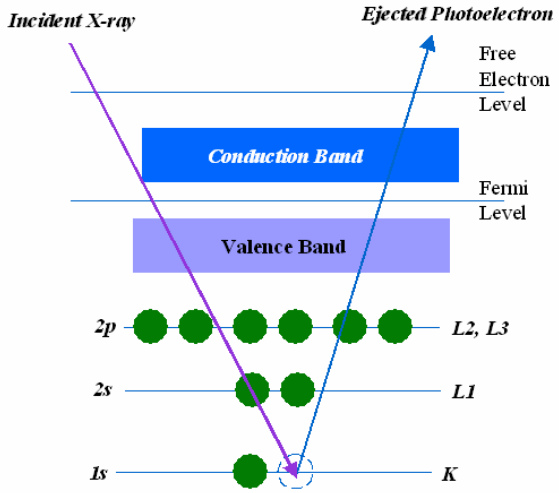

Figure 2.12: Schematic shows the photoelectron processes.

For each and every element, there will be a characteristic binding energy associated with each core atomic orbital i.e. each element will give rise to a characteristic set of peaks in the photoelectron spectrum at kinetic energies determined by the photon energy and the respective binding energies. The presence of peaks at particular energies therefore indicates the presence of a specific element in the sample under study- furthermore; the intensity of the peaks is related to the concentration of the element within the sampled region. Thus, the technique provides a quantitative analysis of the surface composition and is sometimes known by the alternative acronym, ESCA (Electron Spectroscopy for Chemical Analysis).

Closer inspection of the spectrum shows that emission from some levels (most obviously 3p, 3d and 4f) does not give rise to a single photoemission peak, but a closely spaced doublet. Spin-orbit coupling is generally treated using one of two models which correspond to the two limiting ways in which the coupling can occur - these being the *LS* (or Russell-Saunders) coupling approximation and the *j-j* coupling approximation. As an example if we consider the final ionized state of any element within the Russell-Saunders coupling approximation, the $(3d)^9$ configuration gives rise to two states (ignoring any coupling with valence levels) which differ slightly in energy and in their degeneracy.

$^2D_{5/2}$ $g_J = 2x\{5/2\}+1 = 6$

$^2D_{3/2}$ $g_J = 2x\{3/2\}+1 = 4$

These two states arise from the coupling of the $L = 2$ and $S = 1/2$ vectors to give permitted J values of 3/2 and 5/2. The lowest energy final state is the one with maximum J (since the shell is more than half-full), i.e. $J = 5/2$, hence this gives rise to the "lower binding energy" peak. The relative intensities of the two peaks reflects the degeneracies of the final states ($g_J = 2J + 1$), which in turn determines the probability of transition to
such a state during photoionization. The Russell-Saunders coupling approximation is best applied only to light atoms and this splitting can alternatively be described using individual electron *l*-*s* coupling. In this case the resultant angular momenta arise from the single hole in the *d*-shell; a *d*-shell electron (or hole) has $l = 2$ and $s = 1/2$, which again gives permitted *j*-values of 3/2 and 5/2 with the latter being lower in energy. This spin-orbit splitting is of course not evident with *s*-levels ($l = 0$), but is seen with *p, d* & *f* core-levels which all show characteristic spin-orbit doublets. The exact binding energy of an electron depends not only upon the level from which photoemission is occurring, but also upon: (1) The formal oxidation state of the atom and (2) the local chemical and physical environment. Changes in either (1) or (2) give rise to small shifts in the peak positions in the spectrum - so-called chemical shifts. Such shifts are readily observable and interpretable in XP spectra (unlike in Auger spectra) because the technique is of high intrinsic resolution (as core levels are discrete and generally of a well-defined energy) and a one-electron process (thus simplifying the interpretation). Atoms of a higher positive oxidation state exhibit a higher binding energy due to the extra coulombic interaction between the photo-emitted electron and the ion core. This ability to discriminate between different oxidation states and chemical environments is one of the major strengths of the XPS technique.

Modern XPS instruments combine technology from a range of fields including electron optics, X-ray optics, digital/analog electronics, mechanical engineering and software engineering. The complex mixture of these disciplines is challenging to manage at the best of times because of the ever-increasing demands of a maturing technique coupled with the need to satisfy both research and application-orientated customers (from a comparatively small market), which means that state-of-the-art instruments must come at a relatively high price. It

also requires users to be relatively sophisticated in order to exploit the technique to its full potential since they too must appreciate many of the details wrapped up in the systems. With this in mind, exploring the features of a typical system helps to gain some insight into how measurements are performed and what the results mean. The logical components of an XPS instrument are shown in Figure 2.13. X-rays illuminate an area of a sample causing electrons to be ejected with a range of energies and directions. The electron optics, which may be a set of electrostatic and/or magnetic lens units, collect a proportion of these emitted electrons defined by those rays that can be transferred through the apertures and focused onto the analyzer entrance slit. Electrostatic fields within the hemispherical analyzer (HSA) are established to only allow electrons of a given energy (the so called Pass Energy PE) to arrive at the detector slits and onto the detectors themselves.

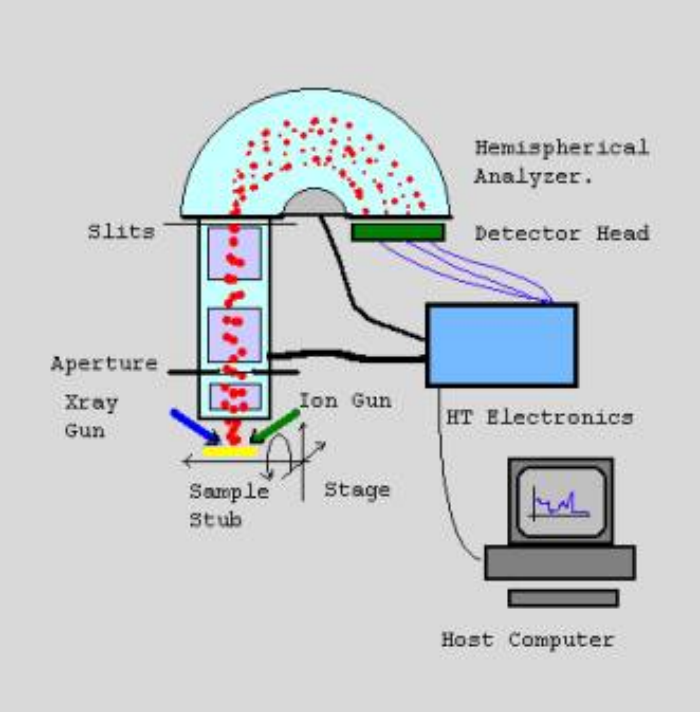

Figure 2.13: Schematic shows the diagram of X-ray photoelectron spectrophotometer.

Electrons of a specific initial kinetic energy are measured by setting voltages for the lens system that both focus onto the entrance slit the electrons of the required initial energy and retards their velocity so that their kinetic energy after passing through the transfer lenses matches the pass energy of the hemispherical analyzer. To record a spectrum over a range of

initial excitation energies it is necessary to scan the voltages applied to these transfer lenses and the prescription for these lens voltages is known as the set of lens functions. These lens functions are typically stored in some configuration file used by the acquisition system. The efficiency with which electrons are sampled by a spectrometer is very dependent on these lens functions and without properly tuned lens functions the performance of an instrument can be severely impaired. Even with a well-tuned system the collection efficiency varies across the many operating modes and it is necessary to characterize an instrument using a corresponding transmission function for each of the lens modes and energy resolutions. A hemispherical analyzer and transfer lenses can be operated in two modes, namely, Fixed Analyzer Transmission (FAT), also known as Constant Analyzer Energy (CAE), or Fix Retard Ratio (FRR) also known as Constant Retard Ratio (CRR). In FAT mode, the pass energy of the analyzer is held at a constant value and it is entirely the job of the transfer lens system to retard the given kinetic energy channel to the range accepted by the analyzer. Most XPS spectra are acquired using FAT. The alternative mode, FRR, scans the lens system but also adjusts the analyzer pass energy to maintain a constant value for the quantity "initial electron energy"/"analyzer PE". This mode is typically used for Auger spectra since the energy interval accepted by the detection system (i.e. resolution) increases with kinetic energy and recovers weak peaks at high kinetic energies while restricting the intense low energy background that could do damage to the detection system.

2.7.2 X-ray Photoemission Spectroscopy (XPS) measurements:

XPS measurements of drop coated films on Si(111) substrates from different nanoparticle solutions were carried out on a VG MicroTech ESCA 3000 instrument at a pressure of better than $1x10^{-9}$ Torr. The general scan and the C1s, W 4f, Pt 4f Au 4f and Pd 3d core level spectra from different samples were recorded with un-monochromatized Mg Kα radiation (photon energy = 1253.6 eV) at pass energy of 50 eV and electron takes off angle (angle between electron emission direction and surface plane) of 60^0. The overall resolution was ~1 eV for the XPS measurements. The core level spectra were background corrected using the Shirley algorithm [13] and the chemically distinct species resolved using a non-linear least squares fitting procedure. The core level binding energies (BE) were aligned with the adventitious carbon binding energy of 285 eV.

2.8 Isothermal Titration Calorimetry (ITC) Study

Every molecular interaction either generates or absorbs small amounts of heat and isothermal titration calorimeter (ITC) can detect these small changes in heat of reaction. In an isothermal titration calorimeter, the heat of reaction is used to follow a titration experiment. This permits determination of the end point (stoichiometry) of a reaction as well as its enthalpy. Each ITC experiment provides a complete thermodynamic profile of the interaction including the binding constant (Ka), the number of binding sites (*n*), enthalpy (ΔH), entropy (ΔS), and free energy (ΔG). Since heat is universally generated or absorbed during any molecular interaction, ITC may be viewed as a universal detector for such interactions. The technique is gaining its importance particularly in the field of biochemistry, because it facilitates determination of substrate binding to enzymes. ITC has been widely used in biochemistry to study protein-ligand [14], protein-protein [15], DNA-RNA [16], DNA-protein [17], and protein-lipid [18] interactions. Recently Sastry and co-workers have used this technique in the field of materials science [19] with the aim of getting a better understanding of the mechanism of ionic interaction as well as the energies involved in this process.

2.8.1 Working Principles:

Recent advances in ITC systems permit the complete characterization of molecular interactions with as little as a few nanomoles of material. An ITC experiment takes only 30–60 min to complete and is highly automated, including instrument operation and data collection and analysis. ITC is used to measure the reaction kinetics using thermal power generated by the conversion of substrate to product. The rate of reaction is directly proportional to thermal power: Power = dQ/d*t* where Q is heat, and t is time. This thermal power change is detectable and measurable. Todd and Gomez have demonstrated that the amount of heat involved in converting n moles of substrate to product is expressed by: $Q = n \times \Delta H_{app} = [P]_{total} \times V_0 \times \Delta H_{app}$, where ΔH_{app} is total molar enthalpy for the reaction (in calories/mole of substrate, determined experimentally by ITC), $[P]_{total}$ is concentration of product generated and V_0 is volume of the ITC cell. It follows that thermal power generated during conversion of substrate to product is: $Power = dQ/dt = (d[P]_{total}/dt) \times V_0 \times \Delta H_{app}$, where $d[P]_{total}/dt$ is equal to rate of product formation (rate of reaction).

2.8.2 Isothermal Titration Calorimeter (ITC) measurements:

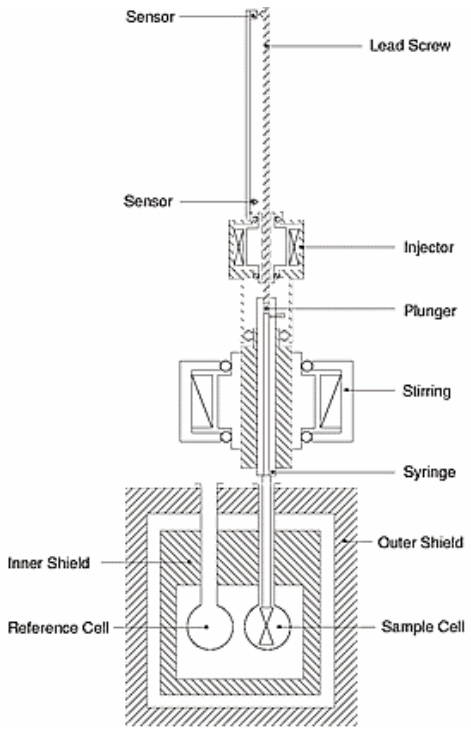

Figure 2.14: Schematic shows the diagram of an isothermal titration calorimeter.

A schematic diagram of the VP-ITC instrument is shown in Fig. 2.14. The instrument utilizes a differential design with two identical cells. All binding processes occur in the sample cell, whose temperature is continuously compared to that of the reference cell, where no reaction takes place. The cells are surrounded by an inner shield, which is maintained at the same temperature as the cells in order to minimize any heat flow to or from the cells. The outer shield is also maintained at the same temperature, to compensate for any changes in room temperature. During operation, a very small constant power is supplied to a heater on the reference cell. The amount of power supplied to the sample cell (feedback power) is continuously adjusted so that its temperature is always identical to that of the reference cell. If, for example, an exothermic reaction occurs in the sample cell, then the feedback power to the sample cell will automatically be reduced to nullify the temperature difference caused by the heat released in the sample cell. The precise amount of heat released by the exothermic process can then be determined since it is exactly equal to the reduction in the amount of feedback heat necessary to reestablish the temperature null between the cells.

To carry out a binding experiment, the macromolecule solution is loaded into the sample cell and the buffer solution is loaded into the reference cell. A long-needle syringe, depicted in Figure 2.14, with a paddle fastened to its end is filled with the appropriate ligand solution. After filling, the syringe is seated into a holder, which is coupled to a linear-motion injector system under software control. The syringe paddle is located inside the sample cell and the entire syringe assembly rotates at a preselected speed to continuously provide proper mixing to the contents of the sample cell. An experiment consists of a number of equal-volume injections of a ligand solution from the syringe into the macromolecule solution contained in the sample cell. Typical results are obtained for an exothermic binding process where each peak is the result of a single injection. It can be seen that with the early injections the peaks are of almost equal size, which indicates that nearly all of the injected ligand is bound by the macromolecule. As the injections progress, the injection peaks decrease in size as the binding sites become saturated and less of the injected ligand is bound. The last several injections, of very small size, show that saturation is virtually complete by the end of the experiment. When the experimental results are analyzed using Origin data analysis software, the area of each injection peak is automatically determined and results are plotted and this plot is referred to as a binding isotherm, where the total heat per injection (kcal per mole of ligand injected) is plotted against the molar ratio of ligand and macromolecule. The precise shape of the binding isotherm contains all of the information necessary to completely characterize the binding reaction. Once the operator activates the curve-fitting routine from the software, the fitting process is carried out automatically to provide the correct stoichiometry (*n*), binding constant (K_a), heat of binding (ΔH), and entropy of binding (ΔS).

2.9 References

[1] (a) Burrell, M. C.; Armstrong, N.R. *Langmuir* **1986**, *2*, 37; (b) Cheek, G.T.; O' Grady, W.E. *J.Electroanal. Chem.*, **1990**, *277*, 341.

[2] (a) Wang, J.; Frostman, L.M.; Ward, M.D. *J.Phys.Chem.* **1992**, *96*, 5224; (b) Buttry, D. A.; Ward, M.D. *Chem. Rev.* **1992**, *92*, 1356.; (c) Geddes, N.J.; Urquhart, R.S.; Furlong, D. N.; Lawrence, C.R.; Tanaka, K.; Okahata, Y. *J. Phys. Chem.*, **1993**, *97*, 13767.

[3] (a) Brust, M.; Etchonique, R.; Calvo, E.J.; Gordillo, G.J. *J.C.S. Chem. Commun.*, **1996**, 1949; (b) Patil, V.; Mayya, K. S.; Pradhan, S. D.; Sastry, M. *J. Am. Chem. Soc*., **1997**, *119*, 9281.

[4] (a) Bright, R.M.; Musick, M.D.; Natan, M.J. *Langmuir* **1998**, *14*, 5695; (b) Sastry, M.; Patil, V.; Sainkar, S. R. *J. Phys. Chem. B*, **1998**, *102*, 1404; (c) Gole, A.; Sainkar, S. R.; Sastry, M. *Chem. Mater*., **2000**, *12*, 1234.

[5] (a) Caruso, F.; Niikura, K.; Furlong, D. N.; Okahata, Y. *Langmuir* **1997**, *13*, 3427.; (b) Caruso, F.; Rodda, E.; Furlong, N.D.; Niikura, K.; Okahata, Y. *Anal. Chem.* **1997**, *69*, 2043; (c) Gole, A.; Dash, C.; Mandale, A. B.; Rao, M.; Sastry, M. *Anal.Chem.* **2000**, *72*, 4301; (d) Gole, A.; Chaudhari, P.; Kaur, J.; Sastry, M. *Langmuir* **2001**, *17*, 5646.

[6] Sauerbrey, G. *Z.Phys*. (Munich) **1959**, *155*, 206.

[7] Mie, G.; *Ann. Phys*., **1908**, *25*, 377.

[8] (a) Mulvaney, P. *Langmuir*, **1996**, *12*, 788; b) Henglein, A. *J. Phys.B*., **1993**, *97*, 5457.

[9] (a) Brust, M.; Walker, M.; Bethell, D.; Schiffrin, D. J.; Whyman, R. J. *Chem. Soc., Chem. Commun*.**1994**, 801; (b) Malinsky, M. D.; Kelly, K. L.; Schatz, G. C.; Van Duyne, R. P. *J. Am. Chem. Soc*.**2001**, *123*, 1471. (c) Mayya, K. S.; Patil, V.; Sastry, M. *Langmuir* **1997**, *13*, 3944. (d) Sastry, M.; Mayya, K. S.; Bandyopadhyay, K. *Colloids Surf. A* **1997**, *127*, 221.

[10] (a) Keating, C.D.; Kovaleski, K.M.; Natan, M.J. *J. Phys. Chem. B.* **1998**, *102*, 9404; (b)) Xu, H.; Bjerneld, E. J.; Kall, M.; Borjesson, L. *Phy Rev Lett*. **1999**, *83*, 4357; (c)) Crumbliss, A.L.; Perine, S.C.; Stonehuerner, J.; Tubergen, K.R.; Zhao, J.; O'Daly, J.P. *Biotech.Bioeng.* **1992**, *40*, 483; (d)) Gole, A.;Dash, C.; Ramakrishnan, V.; Sainkar, S.R.; Mandale, A.B.; Rao, M.; Sastry, M. *Langmuir* **2001**, *17*, 1674.

[11] a) Sastry, M.; Lala, N.; Patil, V.; Chavan, S.P.; Chittiboyina, A.G.; *Langmuir* **1998**, *14*, 4138; (b) Mann, S.; Shenton, W.; Li, M.; Connolly, S.; Fitzmaurice, D. *Adv.Mater*., **2000**, *12*, 147.

[12] (a) Storhoff, J.J.; Elghanian, R.; Mucic, R.C.; Mirkin, C.A.; Letsinger, R.L. *J.Am.Chem.Soc*., **1998**, *120*, 1959; (b) Reynolds, R.A. III.; Mirkin, C.A.; Letsinger, R.L.; *Pure.Appl.Chem*., **2000**, *72*, 229; (c) Mirkin, C. A. *Inorg.Chem.*, **2000**, *39*, 2258.

[13] Shirley, D. A. *Phys. Rev. B* **1972**, *5*, 4709.

[14] Qin, K.; Srivastava, D. K. *Biochemistry* **1998**, *37*, 3499.

[15] Pierce, M. M.; Raman, C. S.; Nall, B. T. *Methods* **1999**, *19*, 213.

[16] Barbieri, C. M.; Li, T. K.; Guo, S.; Wang, G.; Shallop, A. J.; Pan, W.; Yang, G.; Gaffney, B. L.; Jones, R. A.; Pilch, D. S. *J. Am. Chem. Soc.* **2003**, *125*, 6469.

[17] Kunne, A.; Sieber, M.; Meierhans, D.; Allemann, R. K. *Biochemistry* **1998**, *37*, 4217.

[18] Wenk, M. R.; Seelig, J. *Biochemistry* **1998**, *37*, 3909.

[19] (a) Mandal, S.; Rautaray, D.; Sanyal, A.; Sastry, M. *J. Phys. Chem. B* **2004,** *108*, 7126; (b) Joshi, H.; Shirude, P.S.; Bansal, V.; Ganesh, K. N.; Sastry, M. *J. Phys. Chem. B* **2004,** *108*, 11535.

Chapter 3

Synthesis of metal and semiconductor nanoparticles in thermally evaporated lipid thin films

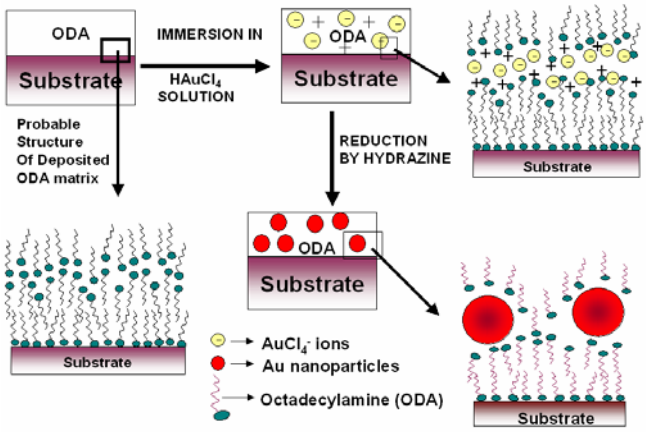

Formation of silver, gold and cadmium sulfide nanoparticles in thermally evaporated lipid film by electrostatic entrapment of ions into lipid matrix has been discussed in this chapter. By this technique patterned structures of metal nanoparticles in thin film form can be synthesized using suitable mask on solid support. Structure of nanomaterials in the lipid thin film depends on the host matrix and reduction process.

The work presented in this chapter has been published in: (1) Mandal, S.; Sastry. M. *Mater.Res.Bull.,* **2002,** *37* , 1613.; (2) Mandal, S.; Sainkar, S.R.; Sastry, M. *Nanotechnology,* **2001**,*12*, 358.; (3) Mandal, S.; Damle, C.; Sainkar, S.R.; Sastry, M. *J.Nanosci. Nanotech*, **2001**, *1*, 281.; (4) Mandal, S. ; Phadtare, S., PR. Selvakannan, Pasricha, R.; Sastry, M. *Nanotechnology,* **2003**,*14*, 878.

3.1 Introduction

Currently a great deal of interest is in the preparation and characterization of organic-inorganic nanocomposites [1-6]. One important aspect of nanotechnology in the context of commercial application is the organization and packaging of nanoparticles in thin film form. One of the emerging challenges in nanotechnology is the in-plane spatial control over the nanoparticle structures formed. A number of protocols have been developed for the self-assembly of nanoparticles as monolayers [7-14] and as superlattice structures [15-24]. In this direction, He et.al. [25] and Aizenburg, Braun and Wiltzius [26] have very recently shown that self-assembled monolayers (SAMs) deposited by microcontact printing (μCP) on gold thin films enable deposition of the monolayers with good spatial control over differing chemical functionality. Using such patterned SAMs, they were able to assemble nanoparticles using electrostatic interaction between the terminal functional groups in the SAM and the charges on the colloidal particles in a spatially programmed manner. Langmuir-Blodgette (LB) films of metal salts of fatty lipids possess a lamellar structure wherein the hydrophilic regions holding the metal ions act as excellent 'nanoscale reactors' for the *in-situ* synthesis of metal and semiconductor nanoparticles by chemical treatment of the ions. Sastry and coworkers have developed a technique wherein thermally evaporated films of cationic/anionic lipid molecules may be used to entrap metal ions electrostatically by simple immersion in electrolyte solution [27] leading to the formation of ordered lamellar films almost identical to those obtained by the classical LB method. Detailed investigations into a new approach for the formation of nanocomposites of metal/semiconductor nanoparticles and fatty lipids by an electrostatically controlled diffusion process has been described in this chapter.

The motivation for the study was from the earlier work on the formation of fatty acid salts by an ion-exchange process [27]. It has been shown that thermally evaporated films of fatty acids can be spontaneously organized via selective ionic interaction of cations by immersion of the film in suitable electrolytes. This leads to an organized lamellar film structure similar to *c*-axis oriented y-type LB films. Recognizing that the principle of ion exchange is quite general, this approach has been extended to the fatty amine films as well, via anion incorporation using $[PtCl_6]^{2-}$, $[TiO(C_2O_4)]^{2-}$ ions. In the following work it has been demonstrated that cations such as Ag^+, Cd^{2+} ions can be incorporated into thermally evaporated anionic matrix fatty acid films and anions such as $AuCl_4^-$ ions into thermally evaporated

cationic matrix by an analogous mechanism followed by reduction of the metal ions *in-situ* thus leading to the formation of metal/semiconductor nanoparticles within the patterned lipid matrix. The process of metal ion incorporation and reduction may be repeated a number of times to increase the nanoparticle density in the lipid matrix. By this process it is possible metal/semiconductor nanoparticle assemblies in a patterned manner on suitable substrates using suitable masks (e.g., a TEM grid). The protocol described shows immense potential for obtaining assemblies of nanoparticles in more intricate patterns as well as to the growth of metal and semiconductor quantum dots in such patterns.

3.2 Synthesis of patterned silver nanoparticle films by incorporation and reduction of silver ions in thermally evaporated fatty acid films

In this section the formation of silver nanoparticle films in a patterned manner on suitable substrates is described. The entire process is illustrated in the schematic shown in Fig.3.1. The first step consists of the deposition of patterned thin films of stearic acid (StA) by vacuum evaporation using a suitable mask on solid substrates (step 1). The patterned fatty acid film is then immersed in aqueous $AgNO_3$ solution and Ag^+ ions incorporated into the lipid matrix by attractive electrostatic interaction with the negatively charged carboxylate ions of the fatty acid molecules (step 2). The silver stearate film is treated with hydrazine vapour to reduce the metal ions *in-situ* thus leading to the formation of silver nanoparticles within the patterned lipid host (step 3). The process of metal ion

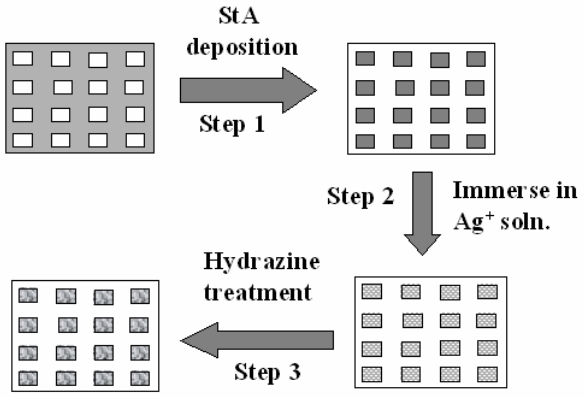

Figure 3.1: Schematic showing the process for obtaining patterned silver nanoparticle assemblies from fatty acid films. It consists of deposition of StA using a TEM grid as a mask on a suitable substrate (step 1). This is followed by immersion in $AgNO_3$ solution and electrostatic entrapment of the Ag^+ ions in the fatty acid matrix (step 2). The final step is the reduction of the Ag^+ ions *in-situ* to yield silver nanoparticles in the patterned lipid matrix (step 3). The reduction process may be followed by further ion incorporation and reduction (steps 2 and 3) in a cyclic manner.

incorporation and reduction may be repeated a number of times to increase the nanoparticle density in the lipid matrix.

3.2.1 Quartz Crystal Microgravimetry (QCM) measurements :

Stearic acid (StA) [$CH_3(CH_2)_{16}COOH$, Aldrich, used as-received] films of 500 Å thickness were deposited on Si (111) wafers, quartz substrates and a gold-coated 6 MHz quartz crystal for quartz crystal microbalance (QCM) measurements as described in chapter 2, section *2.1.2*. After deposition of the StA films, the StA-coated QCM crystal was immersed in 10^{-4} M $AgNO_3$ solution (pH = 5.2) and the change in frequency of the quartz crystal was measured *ex-situ* after thorough washing and drying of the crystal for various times of immersion of the crystal in the electrolyte solution. The frequency of the quartz crystal resonator was measured using an Edwards FTM5 frequency counter that had a frequency resolution and stability of 1 Hz. For the 6 MHz crystal used in this study, this translates into a mass resolution of 12.1 ng/cm^2. The frequency changes were converted to mass loading using the standard Sauerbrey formula [28].

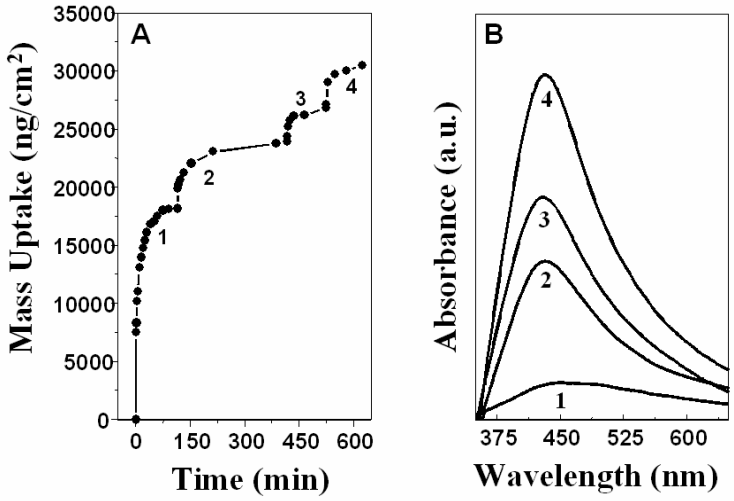

Figure 3.2: (A) QCM mass uptake recorded with time for a 500 Å thick StA film during immersion in a 10^{-4} M $AgNO_3$ solution. Each cycle of immersion (indicated next to the mass uptake curve) is followed by reduction of the Ag^+ ions with hydrazine. B) UV-vis spectra recorded from a 500 Å thick film after 4 successive cycles of Ag^+ incorporation and reduction with hydrazine. The ion incorporation cycle is indicated next to the respective spectra.

Fig. 3.2. (A) shows the QCM mass uptake data recorded for the 500 Å thick StA film during 4 successive cycles of Ag^+ incorporation, the reduction of the silver ions being accomplished by hydrazine treatment as mentioned above. The cycle of ion incorporation is indicated in the figure. At the electrolyte solution pH = 5.2, the StA molecules in the fatty acid film are expected to be completely ionised (since pK_a of StA = 4.5) thus leading to maximum electrostatic interaction between the Ag^+ ions and the carboxylate ions of the lipid film. The QCM mass uptake recorded during the first immersion cycle is seen from Fig.3.2.A to be ca. 18000 ng/cm^2 and is seen to be complete within ca. 100 minutes of immersion. Comparing the silver ion mass uptake with the mass uptake recorded for the as-deposited 500 Å thick StA of 4600 ng/cm^2 results in a Ag^+ : StA molar ratio of ca. 10 : 1. This clearly indicates overcompensation of the negative charge of the fatty acid matrix by the silver ions and is similar to the charge overcompensation that occurs in the layer-by-layer assembly protocol of oppositely charge entities such as polyelectrolytes, biomacromolecules etc [22]. Another important source of uncertainty in estimating the molar ratio of the Ag^+ ions to the StA molecules arises from the method of measurement, viz., QCM. In the QCM measurements, application of the Sauerbrey equation implicitly assumes that the lipid film possesses acoustic properties nearly identical to that of the underlying quartz support [28]. While this is a fair approximation where films of covalently bonded solids are concerned, it is not clear that this approximation is valid for molecular solids such as stearic acid which are held together by weak, van der Waals interactions. Indeed, the acoustic 'stiffness' of the lipid film would be expected to change drastically before and after incorporation of the silver ions making the use of such an approximation even more indeterminate. After the first cycle of ion incorporation, the silver stearate film was treated with hydrazine to form silver nanoparticles in the fatty acid matrix. This results in re-generation of free acid molecules and the possibility of carrying out additional ion incorporation and reduction thus leading to an increase in the nanoparticle density/increase in the size of existing nanoparticles in the lipid matrix. Three additional cycles of ion exchange and reduction were carried out and the QCM mass uptakes recorded for these cycles is shown in Fig.3.2.A. It is observed that the additional mass uptake due to incorporation of Ag^+ ions is much less for these cycles (ca. 4000 ng/cm^2) than for the first cycle (18000 ng/cm^2). This may be due to blockage of diffusion pathways for the Ag^+ ions due to the presence of the silver nanoparticles in the lipid matrix or due to co-ordination of a percentage

of the StA molecules to the surface of the nanoparticles, which would render them unavailable for ion incorporation. A combination of both factors may also contribute to the reduced ion uptake observed.

3.2.2 UV-vis. Spectroscopy measurements:

The formation of silver nanoparticles in the thermally evaporated film was studied by UV-vis spectroscopy measurements. Treatment of the silver stearate films with hydrazine resulted in the film turning to a light brown color indicative of silver nanoparticle formation. The process of silver nanoparticle formation by hydrazine reduction of the Ag^+ ions in a 500 Å thick StA film on quartz during 4 successive cycles of ion entrapment and reduction was followed by UV-vis spectroscopy and the spectra recorded are shown in Fig.3.2.B (the ion incorporation cycle is indicated next to the respective spectrum). A strong resonance at ca. 440 nm is clearly seen in all the films and arises due to excitation of surface plasmon vibrations in the silver nanoparticles [29-30]. Furthermore, the surface plasmon resonance intensity increases with number of cycles of silver ion incorporation indicating an increase in the concentration of the silver nanoparticles in the film. This could be seen as a visible increase in the darkness of the brown coloration in the Ag nano-StA film.

3.2.3 Fourier Transform Infra-Red (FTIR) Spectroscopy measurements:

The process of Ag^+ incorporation in the thermally evaporated StA film is readily studied by FTIR spectroscopy. Fig.3.3 shows the FTIR spectra recorded from the as-deposited 500 Å thick StA film on Si (111) wafer (curve 1); the StA film after the first cycle of Ag^+ ion incorporation (curve 2) and the StA film after 4 cycles of Ag^+ incorporation and hydrazine reduction (curve 3). Three bands labelled a-c at 1695 cm^{-1}, 1520 cm^{-1} and 1470 cm^{-1} respectively have been identified in the figure. The band at 1695 cm^{-1} (feature a, curve 1) is assigned to the carbonyl stretch vibration of the carboxylic acid groups in the StA films (curve 1) and is clearly missing from both the silver stearate (curve 2) and Ag-nano-StA films (curve 3). On formation of silver stearate, the carboxylate stretch frequency appears at 1520 cm^{-1} (feature b, curve 2) and is a clear indication of formation of the metal salt of stearic acid [31].

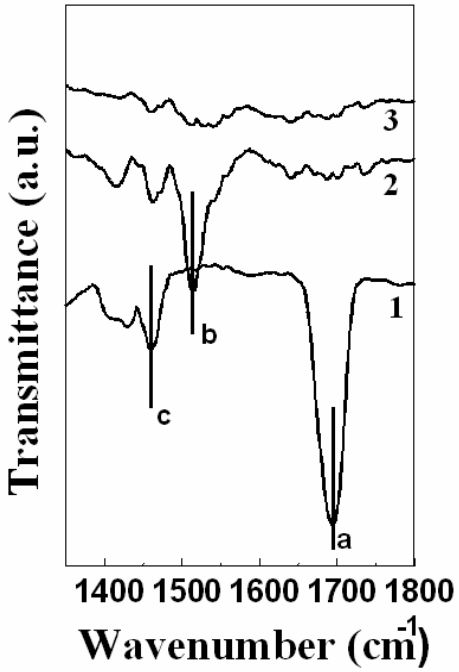

Figure 3.3: FTIR spectra in the spectral range 1350 – 1800 cm^{-1} recorded from an as-deposited 500 Å thick StA film on a Si (111) substrate (curve 1); the StA film after 1 cycle of immersion in $AgNO_3$ solution (curve 2) and the StA film after 4 cycles of ion incorporation and reduction with hydrazine (curve 3). Three prominent FTIR bands labelled a-c are identified in the figure.

After formation of the silver nanoparticles (curve 3), the band at 1520 cm^{-1} splits into two bands and may be attributed to un-reacted silver stearate films and StA molecules bound to the surface of the silver nanoparticles. A third feature at 1470 cm^{-1} is seen in all the spectra and arises from the methylene scissoring vibrations of the StA hydrocarbon chains in the nanocomposite film.

3.2.4 X-ray Diffraction (XRD) measurements:

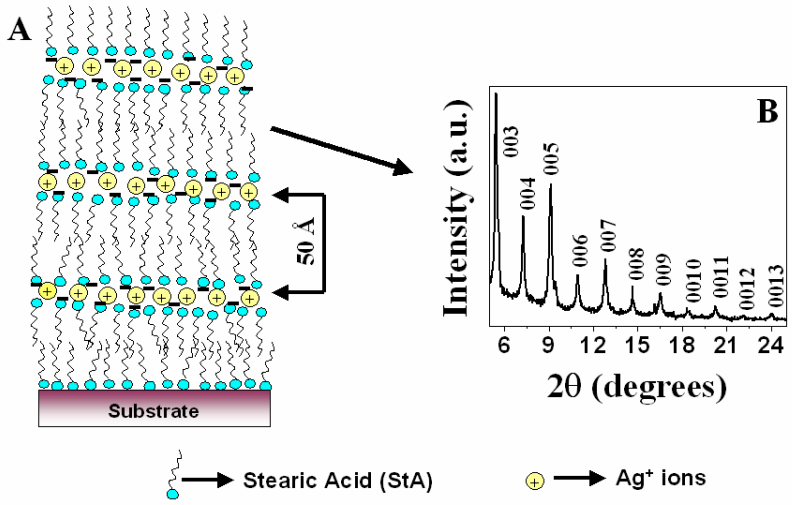

Figure 3.4: (A) Schematic shows the lamellar order of Ag^+-StA film after Ag^+ ions incorporation in the StA matrix. (B) shows the XRD pattern recorded from Ag^+-StA film after Ag^+ ions incorporation in the StA matrix.

Fig.3.4 (A) shows the probable structure of thermally evaporated films of stearic acid after entrapping of Ag^+ metal ions electrostatically by simple immersion in electrolyte solution, which leads to the formation of ordered lamellar films almost identical to those obtained by the classical LB method. At the electrolyte solution pH = 5.2, the StA molecules in the fatty acid film are expected to be completely ionised thus leading to maximum electrostatic interaction between the Ag^+ ions and the carboxylate ions of the lipid film. Fig.3.4 (B) shows the XRD pattern of the Ag^+-StA film after Ag^+ ions incorporation in the StA matrix. The (0 0 l) reflections from the lamellar structure of the Ag^+-StA film can clearly be seen with the distinct odd-even intensity oscillations characteristic of *c*-axis orientation of the film. From the positions of the Bragg reflections, a bilayer thickness value of 50 Å was calculated, in excellent agreement with that expected from the dimensions of stearic acid and Ag^+ ions. The calculated bilayer thickness of stearic acid film from (00l) reflections also agrees with the probable structure of the Ag^+-StA film after incorporation Ag^+ ions in the thermally evaporated StA matrix.

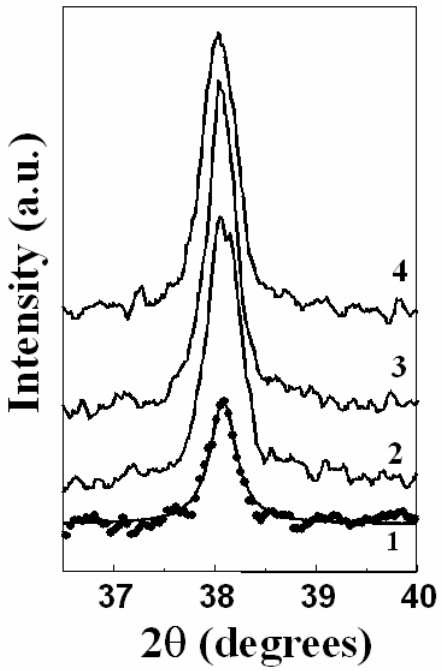

Figure 3.5: The XRD (111) Bragg reflections recorded from a 500 Å thick StA film on Si (111) substrate after each of 4 cycles of Ag^+ ion incorporation and reduction with hydrazine. The cycle of ion incorporation and reduction is indicated next to the respective curve. A Lorentzian fit to the XRD pattern recorded from the StA film after 1 cycle of Ag^+ entrapment and reduction is shown in the figure.

Fig.3.5 shows the XRD patterns recorded from the Ag nano-StA films on Si (111) wafer after 4 successive cycles of Ag^+ incorporation and reduction. An estimate of the silver nanoparticle size grown in the StA matrix by the method outlined above was made from the broadening of the (111) Bragg reflection using the Debye-Scherrer formula [32]. The Lorentzian fit to the XRD pattern from the first cycle film is shown in Fig.3.5. Similar fits (data not shown) were done for the other films as well and the silver nanoparticle sizes estimated from the analysis was 250 Å, 245 Å, 260 Å and 255 Å for cycles 1-4 respectively. This clearly shows that successive cycles of silver ion incorporation and reduction does not result in growth of already nucleated nanoparticles in the lipid matrix. The increase in the plasmon resonance intensity (Fig.3.2.B) mentioned earlier must therefore be attributed to a large extent to nucleation of new silver nanoparticles during each cycle of ion entrapment.

3.2.5 Scanning electron microscopy (SEM) and energy dispersive analysis of X-rays (EDX) measurements:

A 500 Å thick StA film was deposited on a Si (111) wafer using a transmission electron microscope grid as a mask to yield a patterned StA film for scanning electron microscopy (SEM) and energy dispersive analysis of X-rays (EDX) measurements. SEM measurements were carried out on the patterned StA-Ag nano films and EDX spectra were recorded in the spot-profile mode by focusing the electron beam onto specific regions of the Ag nano-StA patterned film. The scanning electron microscopy image recorded after one cycle of Ag^+ ion incorporation and reduction by hydrazine is shown in Fig.3.6.A.

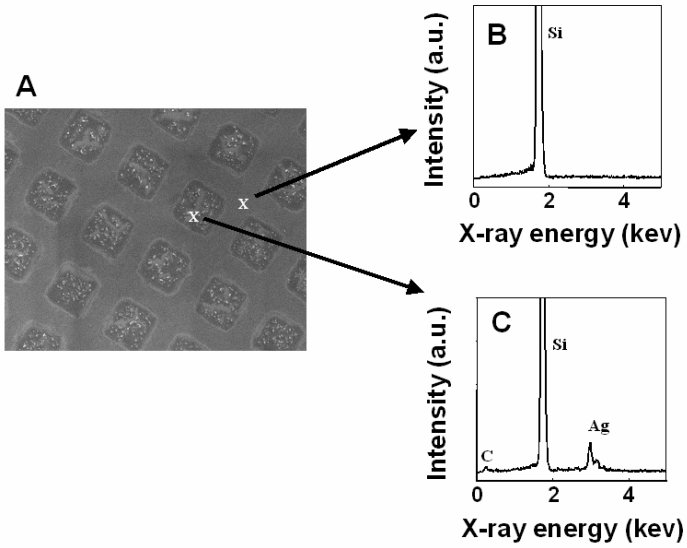

Figure 3.6: (A) SEM picture of a patterned 500 Å thick Ag nano-StA film deposited on a Si (111) substrate. The accompanying EDX profiles (B and C) have been recorded from the regions indicated by crosses in the SEM picture.

The silver nanoparticle assemblies are clearly observed within the squares of the StA matrix. Spot-profile EDX measurements were carried out at points within one of the gaps between the StA segments and on the Ag nano-StA element (indicated by arrows in Fig.3.6.A) and are shown in Figs.3.6.B and 3.6.C respectively. It is seen that while there is strong Ag signature from within the StA elements (Fig.3.6.C), there is no evidence of the silver signals from within the gaps (Fig.3.6.B). This is an important result and clearly shows that the Ag nanoparticles formed by Ag^+ ion incorporation and reduction by hydrazine are faithful to the underlying patterned StA template. It is interesting to note that there is very little spillover of the

nanoparticles into the gaps of the patterned film indicating a high degree of fidelity to the StA template. It is conceivable that this process could be extended to more intricate structures using more sophisticated masks.

The silver nanoparticle films can be synthesized in patterned fatty acid films by an ion complexation and reduction process thus addressing an important gap in available protocols for realizing spatially programmed nanoparticle assemblies.

3. 3 Assembly of CdS nanoparticles in patterned structures by ion entrapment process in thermally evaporated fatty acid films

In this section the formation of cadmium sulfide nanoparticle assemblies in a patterned manner on suitable substrates is described.

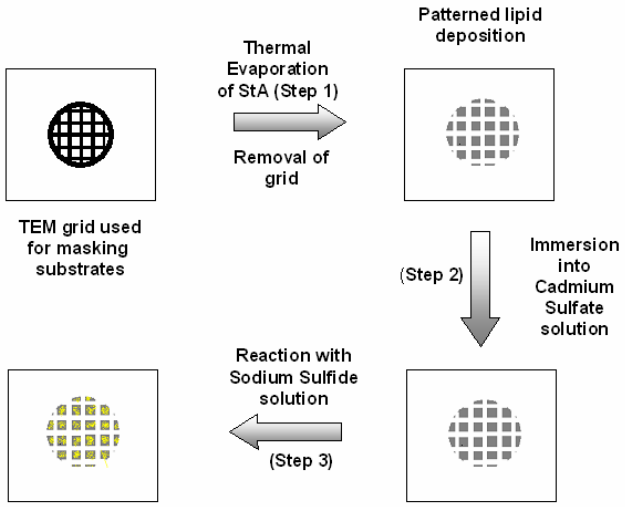

Figure 3.7: Schematic shows the different steps involved in the generation of patterned assemblies of CdS nanoparticles in thermally evaporated stearic acid films.

The entire process is illustrated in the schematic shown in Fig.3.7. The protocol for realizing such structures comprises of the following steps. In the first step, patterned films of a fatty acid are thermally evaporated onto solid supports using suitable masks (e.g., a TEM grid) (step 1). Thereafter, the fatty acid film is immersed in cadmium sulfate solution and Cd^{2+} ions entrapped in the lipid matrix by electrostatic complexation with the carboxylate ions of the fatty acid molecules (step 2). The final step involves the reaction of the entrapped Cd^{2+} ions with Na_2S leading to the *in-situ* generation of cadmium sulfide nanoparticles within the patterned lipid

matrix. This approach shows promise for generating patterned nanoparticle assemblies of different chemical compositions.

3.3.1 Quartz Crystal Microgravimetry (QCM) measurements:

Thin films of stearic acid [StA; $CH_3(CH_2)_{16}COOH$, Aldrich] of 500 Å thickness were thermally deposited onto gold-coated AT–cut quartz crystals for quartz crystal microgravimetry measurements (QCM) as described in earlier chapter, section *2.1.2.* The kinetics of incorporation of Cd^{2+} ions into the stearic acid films was followed by measurement of the change in resonance frequency of the stearic acid covered QCM crystal during immersion into 10^{-4} M aqueous $CdSO_4$ solution (Scheme in Fig.3.7, step 2). The pH of the electrolyte was adjusted to 6 so that maximum ionisation of the carboxylic acid groups in the thermally evaporated StA film would occur, thereby leading to maximum loading of the fatty lipid films with cadmium ions. After thorough washing of the crystal with deionised water and drying in flowing N_2, the frequency measurements and the frequency changes were converted to mass loading as described in chapter 2, section *2.1.2.* Fig.3.8.A shows the QCM mass uptake data recorded from a 500 Å thick StA film during Cd^{2+} incorporation and subsequent reaction with Na_2S as mentioned above. The equilibrium QCM mass uptake recorded during the first immersion cycle in $CdSO_4$ solution (pH = 6)

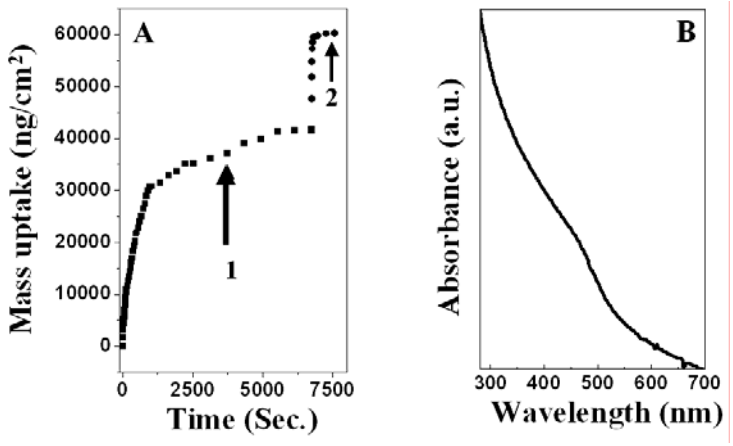

Figure 3.8: (A) QCM mass uptake recorded with time for a 500 Å thick StA film during immersion in a 10^{-4} M $CdSO_4$ solution (cycle 1). Cycle 2 corresponds to reaction of the entrapped Cd^{2+} ions with S^{2-} ions during immersion of the cadmium stearate film in Na_2S solution (see text for details). (B) shows the UV-vis spectrum recorded from a 500 Å thick StA film on quartz after entrapment of Cd^{2+} ions and reaction with Na_2S solution.

is seen from Fig.3.8.A (cycle 1) to be ca. 41,000 ng/cm^2 and is complete within ca. 100 minutes of immersion in the electrolyte. From the mass of StA deposited onto the quartz crystal (ca. 3500 ng/cm^2) it can be easily shown that the Cd^{2+} : StA molar ratio works out ca 18 : 1. This result indicates a high degree of overcompensation of the negative charge in the StA film by the Cd^{2+} ions. It should be noted that such charge overcompensation is known to occur during complexation of macroions like phosphotungstate anions with fatty amine Langmuir monolayers at the air-water interface [33] and is also the mechanism by which layer-by-layer electrostatic assembly occurs on planar surfaces [22]. After this cycle of ion incorporation, the cadmium stearate film was treated with Na_2S to form cadmium sulfide nanoparticles in the fatty acid matrix (Fig.3.8.A, cycle 2). The equilibrium mass uptake during this cycle of formation of CdS yielded a value of ca. 19,000 ng/cm^2. We hesitate to attribute this mass increase entirely due to incorporation of S^{2-} ions since formation of cadmium sulfide would result in regeneration of free carboxylic acid molecules which would in turn facilitate some degree of Na^+ incorporation in the lipid matrix.

3.3.2 UV-vis. Spectroscopy measuremenrs:

The process of CdS nanoparticle formation by Na_2S treatment of the Cd^{2+} ions in a 500 Å thick StA film on quartz was followed by UV-vis spectroscopy and the spectrum recorded is shown in the Fig.3.8.B.The absorption edge was found to occur at ca. 470 nm (determined by taking the derivative of the UV-vis spectrum) which, from the particle size-band edge data of Henglein [29], indicates a particle size of ca. 5.4 nm and therefore, CdS particles in the Q-state regime.

3.3.3 Fourier Transform Infra-Red (FTIR) Spectroscopy measurements:

The process of Cd^{2+} incorporation in the thermally evaporated StA film is readily studied by FTIR spectroscopy.

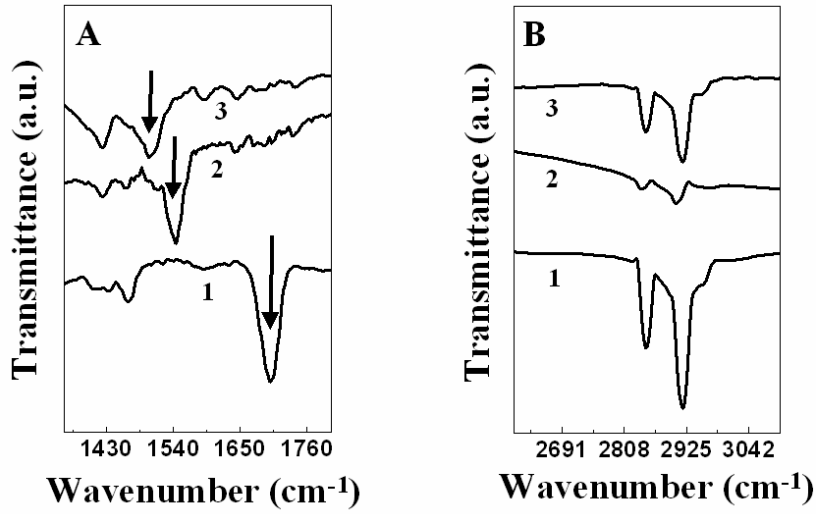

Figure 3.9: (A) FTIR spectra in the range 1350 – 1800 cm^{-1} recorded from an as-deposited 50 nm thick StA film on a Si (111) substrate (curve 1); the StA film after 1 cycle of immersion in $CdSO_4$ solution (curve 2) and the StA film after reaction with Na_2S solution (curve 3). The carbonyl stretch vibration is indicated by an arrow in the three spectra. (B) FTIR spectra in the range 2600 – 3100 cm^{-1} recorded from an as-deposited 50 nm thick StA film on a Si (111) substrate (curve 1); the StA film after 1 cycle of immersion in $CdSO_4$ solution (curve 2) and the StA film after reaction with Na_2S solution (curve 3).

Fig.3.9.A shows the FTIR spectra in the range 1350 – 1800 cm^{-1} recorded from the as-deposited 500 Å thick StA film on Si (111) wafer (curve 1); the StA film after the first cycle of Cd^{2+} ion incorporation (curve 2) and the StA film after formation of CdS nanoparticles in the film (curve 3). The carbonyl stretch vibration occurs at 1700 cm^{-1} in the as-deposited StA film (curve 1, indicated by an arrow) and is characteristic of vibrations from the carboxylic acid group [31]. This band shifts to ca.1540 cm^{-1} on entrapment of Cd^{2+} ions in the acid matrix (curve 2, feature indicated by an arrow) and agrees well with reported values of the C-O stretch vibrations from carboxylate ions in salts of fatty acids. On formation of CdS nanoparticles in the StA matrix, this band further shifts to ca. 1515 cm^{-1} (curve 3, band indicated by an arrow). Fig.3.9.B shows the FTIR spectra recorded in the range 2600 – 3100 cm^{-1} for the StA films under different stages of ion entrapment and nanoparticle formation. The methylene antisymmetric and symmetric vibrations are observed to occur at 2920 and 2850 cm^{-1} for the as-deposited StA film (curve 1); the cadmium stearate film (curve 2) and the CdS nano-StA composite film (curve 3) indicating that the hydrocarbon chains in the lipid matrix and in a close-packed configuration in all the cases [34]. What is interesting is the decrease in intensity of these bands, which is most prominent after formation of the CdS nanoparticles (compare curves 1 and 3). This indicates considerable orientational disorder in the hydrocarbon chains of

the StA molecules and could arise due to binding of the molecules to the surface of the CdS nanoparticles. We have observed such a behavior in our earlier studies of the entrapment of charged colloidal gold particles in thermally evaporated fatty amine films [35].

3.3.4 Transmission Electron Microscopy (TEM) measurements:

The transmission electron micrograph recorded from a 500 Å thick StA film after one cycle of Cd^{2+} ion exchange and subsequent treatment with Na_2S is shown in Fig. 3.10A. The StA matrix was removed from this composite film by soaking the film in chloroform for 30 minutes and carefully removing the TEM grid. A number of well-dispersed particles

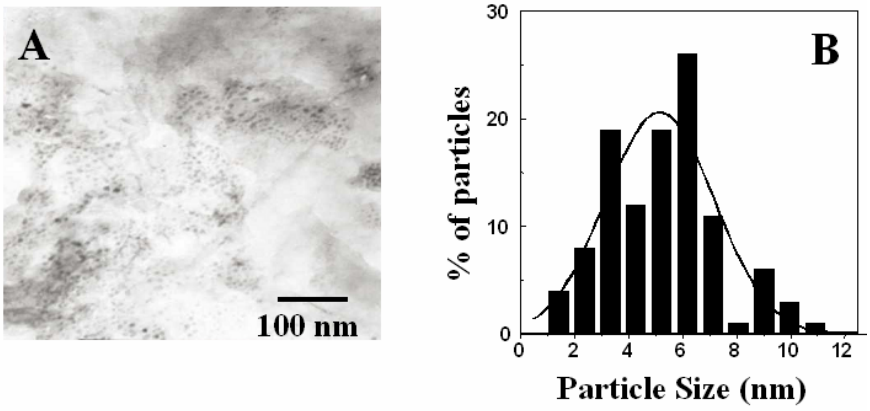

Figure 3. 10: (A) TEM micrograph of a 500 Å thick CdS nano-StA composite film after removal of the StA matrix by soaking in chloroform. (B) Particle size histogram of the CdS nanoparticles imaged in the TEM picture of A. The solid line is a Gaussian fit to the data.

can clearly be seen in the TEM picture with a fairly even size distribution. The particle size histogram for the micrograph shown in Fig.3.10.A is plotted in Fig.3.10.B. A Gaussian fit to the particle size histogram was performed and is shown as a solid line in Fig.3.10.B. This analysis yielded an average particle size of 3.2 ± 0.7 nm which is in good agreement with the size of CdS nanoparticles estimated from the UV-vis spectra.

3.3.5 Scanning electron microscopy (SEM) and energy dispersive analysis of X-rays (EDX) measurements:

A 500 Å thick StA film was deposited on a Si (111) wafer using a transmission electron microscope grid as a mask to yield a patterned StA film for scanning electron microscopy (SEM) and energy dispersive analysis of X-rays (EDX) measurements. SEM measurements were carried out on the patterned StA-CdS nano films and EDX spectra were recorded in the spot-profile mode by focusing the electron beam onto specific regions of the CdS nano-StA patterned film. The scanning electron microscopy image recorded after one cycle of Cd^{2+} incorporation and reaction with Na_2S is shown in Fig.3.11.A. While the individual CdS nanoparticles within the lipid matrix could not be seen due to the fact that they are entrapped within the lipid matrix and not on the surface, it is clear that the grid pattern is faithfully retained after the formation of the CdS nanoparticles. Spot-profile EDX measurements were carried out at points within one of the gaps between the StA segments and on the CdS nano-StA element (indicated by arrows in Fig.3.11.A) and are shown in Figs.3.11. B and C respectively. It is seen while

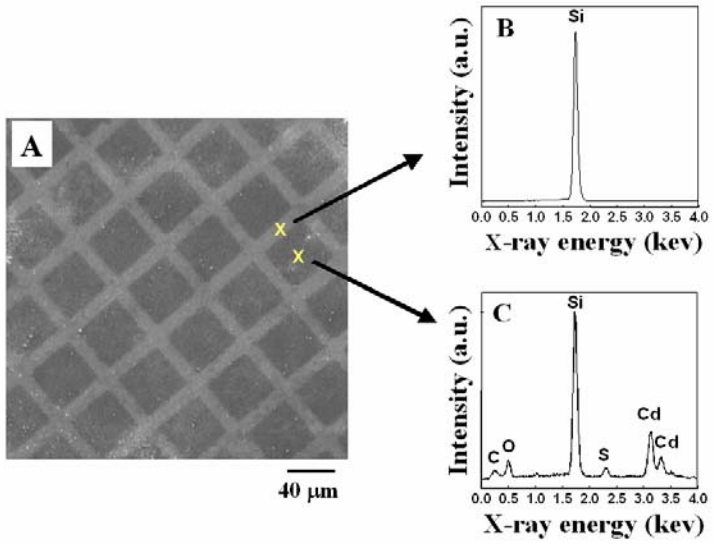

Figure 3.11: (A) SEM picture of a patterned 500 Å thick CdS nano-StA film deposited on a Si (111) substrate. The accompanying EDX profiles (B and C) have been recorded from the regions indicated by crosses in the SEM picture.

there are strong Cd and S signatures from within the StA elements (Fig.3.11.C), there is no evidence of either of the signals from within the gaps (Fig.3.11.B). This is an important result and clearly shows that the CdS nanoparticles formed by Cd ion incorporation and reaction with

Na_2S are faithful to the underlying patterned StA template. It is conceivable that this process could be extended to more intricate structures using sophisticated masks.

Thus CdS nanoparticle films can be synthesized in patterned fatty acid films by an ion exchange technique and subsequent reaction with Na_2S, facilitating the manipulation of nanoparticles to form spatially programmed assemblies.

3.4 Synthesis of gold nanoparticles in patterned manner by electrostatic entrapment of chloroaurate ions in patterned fatty amine films

In this section the formation of gold nanoparticle assemblies in a patterned manner on suitable substrates is described. The protocol for realizing such structures comprises of the following steps. In the first step, patterned films of a fatty amine are thermally evaporated onto solid supports using suitable masks (e.g., a TEM grid). Thereafter, the fatty amine film is immersed in chloroauric acid solution and chloroaurate ($AuCl_4^-$) ions entrapped in the lipid matrix by electrostatic complexation with the ammonium ions of the fatty amine molecules. The final step involves the reduction of the $AuCl_4^-$ ions *in-situ* thus leading to the formation of gold nanoparticles within the patterned lipid matrix.

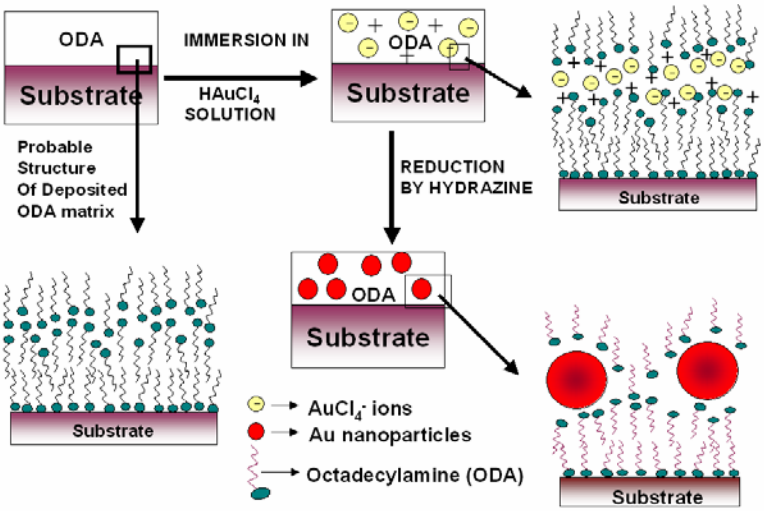

Figure 3.12: Schematic showing the incorporation of $AuCl_4^-$ ions into thermally evaporated ODA matrix by electrostatic interaction and formation of gold nanoparticles after reduction of incorporated $AuCl_4^-$ ions in the lipid matrix. The expected microscopic structure of the metal-lipid composite film is also shown.

The process of metal ion incorporation and reduction may be repeated a number of times to increase the nanoparticle density in the lipid matrix. The entire process is illustrated in the schematic shown in Fig.3.12. When the ODA film is immersed in chloroauric acid solution, chloroaurate ($AuCl_4^-$) ions entrapped in the lipid matrix by electrostatic complexation with the ammonium ions of the fatty amine molecules. After entrapping the chloroaurate ($AuCl_4^-$) ions into the ODA matrix the reduction of the $AuCl_4^-$ ions *in-situ* leads to the formation of gold nanoparticles within the lipid matrix. $AuCl_4^-$ ion entrapment and formation of gold nanoparticles within the patterned lipid matrix has been followed by quartz crystal microgravimetry, UV-vis spectroscopy, Fourier transform infrared spectroscopy, scanning electron microscopy (SEM) and energy dispersive analysis of X-rays (EDX) measurements.

3.4.1 Contact angle measurements:

Contact angle measurements of sessile water drop (1 μl) on 500 Å thick ODA films deposited on Si (111) substrates and metal-lipid composite films were carried out on a Rame Hart 100 Goniometer. For comparison, the contact angles were recorded from films of the $HAuCl_4$ solution drop-dried on Si (111) substrate. The contact angles of a sessile water drop (1 μl volume) on 500 Å thick as-deposited ODA lipid films was ~ 100^0 indicating a hydrophobic surface. After incorporation of $AuCl_4^-$ ions into lipid matrix, the contact angle was found to be ~102^0. These measurements indicate that the $AuCl_4^-$ ions are not adsorbed on the surface of the lipid films but entrapped into the lipid ODA matrix, which agrees with our probable structure of metal-lipid composite film shown in the schematic in Fig.3.12. It is pertinent to mention here that the contact angles measured for the bare Si (111) surface, $HAuCl_4$ film deposited on the Si (111) substrate by evaporation of a drop of the $HAuCl_4$ solution yielded average values of 15^0 and 12^0 respectively, further strengthening the conclusion mentioned above. After reduction of entrapped $AuCl_4^-$ ions in the lipid matrix the contact angle measurement from the nanogold-lipid film had been done and it was ~101^0 which indicates the gold nanoparticles are capped with ODA molecules and the nanoparticles are formed into the lipid matrix as shown in the schematic in Fig.3.12. The above results clearly indicate that the metal ions are immobilized and the metal nanoparticles formed by

reduction *within the lipid matrix* (possibly in the hydrophilic regions) as indicated in the scheme of Figure 3.12 (expected microscopic film structure) and not on the film surface.

3.4.2 Quartz Crystal Microgravimetry (QCM) measurements:

For quartz crystal microbalance (QCM) measurements octadecylamine [$CH_3(CH_2)_{17}NH_2$, Aldrich, used as-received] films of 500 Å thickness were deposited on a gold-coated 6 MHz quartz crystal as described in earlier chapter section *2.1.2*. After deposition of the ODA films, the ODA-coated QCM crystal was immersed in 10^{-4} M $HAuCl_4$ solution (pH = 4.5) and change in the frequency of the quartz crystal was measured *ex-situ* after thorough washing and drying of the crystal for various times of immersion of the crystal in the electrolyte solution. The frequency of the quartz crystal resonator and mass loading were measured as described in earlier section 2.1.2. Fig.3.13.A shows the QCM mass uptake data recorded for the 500 Å thick ODA film during 2 successive cycles of

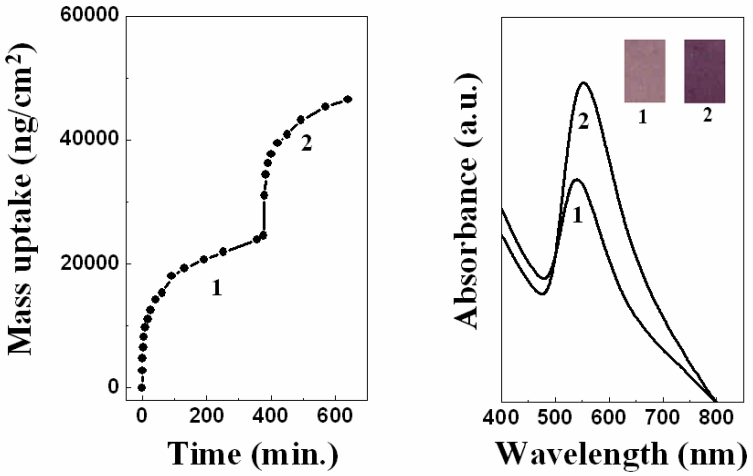

Figure 3.13: (A) QCM mass uptake recorded with time for a 500 Å thick ODA film during immersion in a 10^{-4} M $HAuCl_4$ solution. Each cycle of immersion (indicated next to the mass uptake curve) is followed by reduction of the $AuCl_4^-$ ions with hydrazine (see text for details). (B) UV-vis spectra recorded from a 500 Å thick film after 2 successive cycles of $AuCl_4^-$ ion incorporation and reduction with hydrazine. The ion incorporation cycle is indicated next to the respective spectra. The inset shows colour photographs of a 500 Å thick ODA film on quartz after the 1st (**1**) and 2nd cycle (**2**) of $AuCl_4^-$ ion entrapment and reduction

$AuCl_4^-$ incorporation, the reduction of the Au^{+3} ions being accomplished by hydrazine treatment as mentioned above. The cycle of ion incorporation is indicated in the figure. At the electrolyte solution pH = 4.5, the ODA molecules in the fatty amine film are expected to be completely ionized (pK_b of ODA=10.5) thus leading to maximum electrostatic interaction

between the $AuCl_4^-$ ions and the ammonium ions of the lipid film. The QCM mass uptake recorded during the first immersion cycle is seen from Fig.3.13.A to be ca**.** 23900 ng/cm^2 and is seen to be complete within ca. 360 minutes of immersion. Comparing the chloroaurate ($AuCl_4^-$) ion mass uptake with the mass uptake recorded for the as-deposited 500 Å thick ODA of 4540 ng/cm^2 results in a $AuCl_4^-$: ODA molar ratio of ca. 8 : 1. This clearly indicates overcompensation of the positive charge of the fatty amine matrix by the chloroaurate ($AuCl_4^-$) ions and is similar to the charge overcompensation that occurs in the layer-by-layer assembly protocol of oppositely charge entities such as polyelectrolytes, biomacromolecules etc [22]. After this cycle of ion incorporation, the octadecylammonium-chloroaurate composite film was treated with hydrazine to form gold nanoparticles in the fatty amine matrix. This results in re-generation of free amine molecules and the possibility of carrying out additional ion incorporation and reduction thus leading to an increase in the nanoparticle density/increase in the size of existing nanoparticles in the lipid matrix. The additional cycle of ion exchange and reduction were carried out and the QCM mass uptakes recorded for these cycles is shown in Fig.3.13.A. It is observed that the additional mass uptake due to incorporation of $AuCl_4^-$ ions is less for this cycle (ca.22640 ng/cm^2) than for the first cycle (23900 ng/cm^2). This may be due to blockage of diffusion pathways for the $AuCl_4^-$ ions due to the presence of the gold nanoparticles in the lipid matrix or due to co-ordination of a percentage of the ODA molecules to the surface of the nanoparticles, which would render them unavailable for ion incorporation. A combination of both factors may also contribute to the reduced ion uptake observed.

3.4.3 UV-vis. Spectroscopy measurements:

The process of gold nanoparticle formation by hydrazine treatment of the $AuCl_4^-$ ions in a 500 Å thick ODA film on quartz was followed by UV-vis spectroscopy. Treatment of the octadecylammonium-chloroaurate films with hydrazine resulted in the film turning to a violet color indicative of gold nanoparticle formation. The process of gold nanoparticle formation by hydrazine reduction of the Au^{+3} of $AuCl_4^-$ ions in a 500 Å thick ODA film on quartz during 2 successive cycles of ion entrapment and reduction was followed by UV-vis spectroscopy and the spectra recorded are shown in Fig.3.13.B (the ion incorporation cycle is indicated next to the respective spectrum). A strong resonance at ca. 540 nm for the 1st cycle and ca. 555 nm for the 2nd cycle are clearly seen in the films and arises due to excitation of surface plasmon

vibrations in the gold nanoparticles [36]. Furthermore, the surface plasmon resonance intensity increases with number of cycles of $AuCl_4^-$ ion incorporation indicating an increase in the concentration of the gold nanoparticles in the film. This could be seen as a visible increase in the darkness of the violet coloration in the Au nano-ODA film. The inset of the Fig.3.13.B shows the colour photographs (1 & 2) of the 50 nm thick ODA film on quartz after the 1st cycle and 2nd cycle of $AuCl_4^-$ ion entrapment and reduction process respectively wherein the visible color change is clearly seen.

3.4.4 Fourier Transform Infra-Red (FTIR) Spectroscopy measurements:

The process of $AuCl_4^-$ ion incorporation in the thermally evaporated ODA film is readily studied by FTIR spectroscopy. Fig.3.14 shows the FTIR spectra recorded from the as-deposited 500 Å thick ODA film on Si (111) wafer (curve 1); the ODA film after the

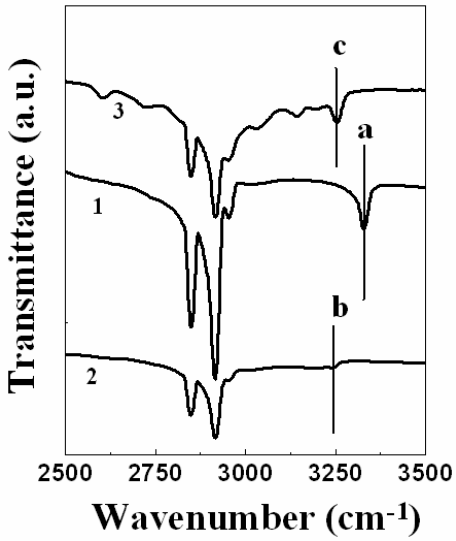

Figure 3.14: FTIR spectra in the spectral range 2500 – 3500 cm^{-1} recorded from an as-deposited 500 Å thick ODA film on a Si (111) substrate (curve 1); the ODA film after 1 cycle of immersion in $HAuCl_4$ solution (curve 2) and the ODA film after ion incorporation and reduction with hydrazine (curve 3). Three prominent FTIR bands labelled a-c are identified in the figure and discussed in the text.

$AuCl_4^-$ ion incorporation (curve 2) and the ODA film after $AuCl_4^-$ incorporation and hydrazine reduction (curve 3). Three bands labelled a-c at 3325cm^{-1}, 3245 cm^{-1} and 3253cm^{-1} respectively have been identified in the figure. The band at 3325 cm^{-1} (feature a, curve 1) is assigned to the N-H stretch vibration of the amine groups in the ODA films (curve 1) and is clearly missing from the octadecylammonium-chloroaurate film (curve 2). On formation of

octadecylammonium-chloroaurate composite film, the N-H stretch frequency appears at 3245 cm^{-1} (feature b, curve 2) and is a clear indication of formation of the chloroaurate salt of octadecylamine [31]. After reduction of Au^{+3} in the octadecylammonium-chloroaurate film by hydrazine treatment, the band appears at 3253cm^{-1} (feature c, curve 3) due to regeneration of free amine groups in the film. The methylene antisymmetric and symmetric vibrations are observed to occur at 2920 and 2850 cm^{-1} respectively for the as-deposited ODA film (curve 1); the octadecylammonium-chloroaurate film (curve 2) and the Au nano-ODA composite film (curve 3) indicating that the hydrocarbon chains in the lipid matrix and in a close-packed configuration in all the cases.

3.4.5 Transmission Electron Microscopy (TEM) measurements:

Fig.3.15.A shows the TEM micrograph recorded from a 500 Å thick Au nano-ODA composite film. In addition to several well-dispersed individual gold nanoparticles

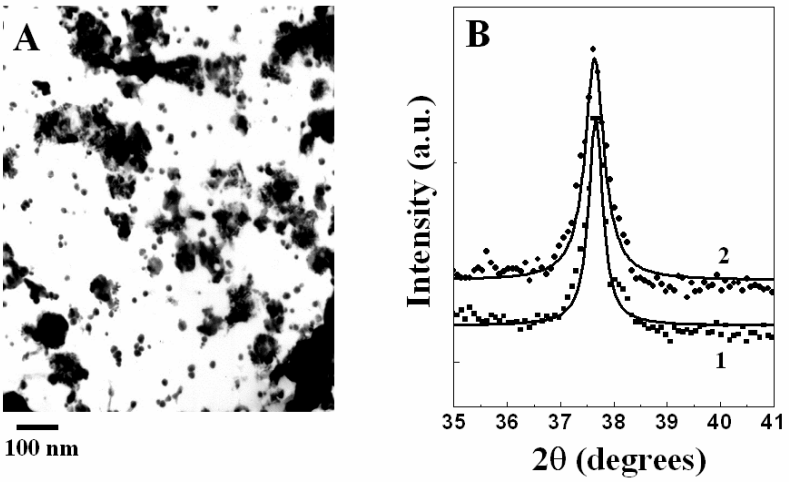

Figure 3.15: (A) TEM micrograph of a 500 Å thick Au nano-ODA composite film recorded after one cycle of $AuCl_4^-$ incorporation and reduction. (B) The XRD (111) Bragg reflection recorded from a 500 Å thick ODA film on a quartz substrate after 2 cycles of $AuCl_4^-$ ion incorporation and reduction with hydrazine. The cycle of ion incorporation and reduction is indicated next to the respective curve. Lorentzian fits to the XRD patterns are shown in the figure as solid lines.

of dimensions in the range 10-30 nm, larger particles of roughly 50-100 nm sizes are also observed in the picture. Closer examination of some of the larger particles shows that they are aggregates of smaller gold particles in close contact. Indeed, examination of the TEM negative by optical microscopy indicated that almost all the larger structures were collections of smaller

nanoparticles of ca. 10-30 nm sizes. We believe the ODA molecules, which form a hydrophobic sheath around the gold nanoparticles as they grow within the lipid matrix, mediate the assembly of the nanoparticles into such superstructures. We recollect that the TEM sample was treated by immersion in hexane for 15 min to remove uncoordinated ODA molecules in the nanocomposite film. The role of the solvent in the assembly of such structures during evaporation cannot be discounted. Whatever be the mechanism behind formation of the larger, aggregated gold nanoparticle structures, it is clear that particles of fairly well defined dimensions are formed within the ODA matrix.

3.4.6 X-ray Diffraction (XRD) measurement:

To estimate of the gold nanoparticle size grown in the ODA matrix by the method outlined above was made from the broadening of the (111) Bragg reflections in the XRD patterns recorded from the films using the Debye-Scherrer formula [32]. Fig.3.15.B shows the XRD patterns recorded from the Au nano-ODA films on quartz substrates after 2 successive cycles of $AuCl_4^-$ incorporation and reduction. The Lorentzian fits to the XRD patterns from the first (curve 1) and second cycle films (curve 2) are shown in Fig.3.15.B and the gold nanoparticle sizes estimated from the analysis were 19.5 nm and 27 nm respectively. These values are in good agreement with the size of gold nanoparticles determined from TEM measurements discussed above. The XRD size estimates indicate that successive cycles of $AuCl_4^-$ ion incorporation and reduction result in growth of already nucleated nanoparticles in the lipid matrix and may also be accompanied by the nucleation of additional particles. The increase in the plasmon resonance intensity (Fig.3.13.B) mentioned earlier must therefore be attributed to a large extent to nucleation of new gold nanoparticles during each cycle of ion entrapment.

3.4.7 Scanning electron microscopy (SEM) and energy dispersive analysis of X-rays (EDX) measurements:

A 500 Å thick ODA film was deposited on a Si (111) wafer using a transmission electron microscope grid as a mask to yield a patterned ODA film for scanning electron microscopy (SEM) and energy dispersive analysis of X-rays (EDX) measurements. SEM

measurements were carried out on the patterned ODA-Au nano films and EDX spectra were recorded in the spot-profile mode by focusing the electron beam onto specific

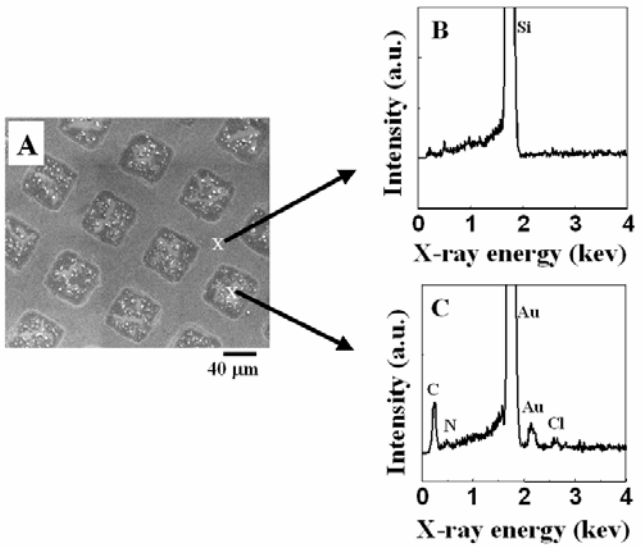

Figure 3.16: (A) SEM picture of a patterned 500 Å thick Au nano-ODA film deposited on a Si (111) substrate. The accompanying EDX profiles (B and C) have been recorded from the regions indicated by crosses in the SEM picture (see text for details).

regions of the Au nano-ODA patterned film. The scanning electron microscopy image recorded after one cycle of $AuCl_4^-$ ion incorporation and reduction by hydrazine is shown in Fig.3.16.A. The gold nanoparticle assemblies are clearly observed within the squares of the ODA matrix. Spot-profile EDX measurements were carried out at points within one of the gaps between the ODA segments and on the Au nano-ODA element (indicated by arrows in Fig.3.16.A) and are shown in Figs.3.16. B and C respectively. It is seen that while there is strong Au signature from within the ODA elements (Fig.3.16.C), there is no evidence of the gold signals from within the gaps (Fig.3.16.B). This is an important result and clearly shows that the Au nanoparticles formed by $AuCl_4^-$ ion incorporation and reduction by hydrazine are faithful to the underlying patterned ODA template. A small Cl signal is also observed within the ODA squares indicating the presence of a small percentage of unreduced entrapped $AuCl_4^-$ ions. It is interesting to note that there is very little spillover of the nanoparticles into the gaps of the patterned film indicating a high degree of fidelity to the ODA template.

Thus the gold nanoparticle films can be synthesized in patterned fatty amine films by a novel ion entrapment and reduction process thus addressing an important gap in available protocols for realizing spatially programmed nanoparticle assemblies. It is conceivable that this process could be extended to more intricate structures using more sophisticated masks.

3.5 Synthesis of fractal gold nanostructures by the spontaneous reduction of chloroaurate ions in thermally evaporated hexadecylaniline films

In this section the formation of gold nanoparticles by the reduction of chloroaurate ions entrapped in thermally evaporated hexadecylaniline films has been described. Simple immersion of the hexadecylaniline films in aqueous chloroauric acid solution leads to the electrostatic entrapment of the gold ions in the film and is followed by their spontaneous reduction in-situ. The gold structures thus formed show a fractal structure of nanoscale dimensions characteristic of diffusion-limited aggregation of gold nanoparticles.

3.5.1 Quartz Crystal Microgravimetry (QCM) measurements:

For quartz crystal for quartz crystal microbalance (QCM) measurements 4-hexadecylaniline (HDA), [Aldrich, used as-received] films of 250 Å thickness were deposited by thermal evaporation on a gold-coated AT-cut 6 MHz as described in chapter 2 section *2.1.2*. After deposition of the HDA films, the HDA-coated QCM crystal was immersed in 10^{-4} M $HAuCl_4$ solution (pH 3.5) and the change in frequency of the quartz crystal was measured ex-situ after thorough washing and drying of the crystal for various times of immersion of the crystal in the $HAuCl_4$ solution. The frequency of the quartz crystal resonator was measured as described in earlier section *2.1.2* of chapter 2. The kinetics of entrapment of the $AuCl_4^-$ ions in the 250 Å thick HDA film during immersion in 10^{-4} M chloroauric acid solution (pH 3.5) was studied by

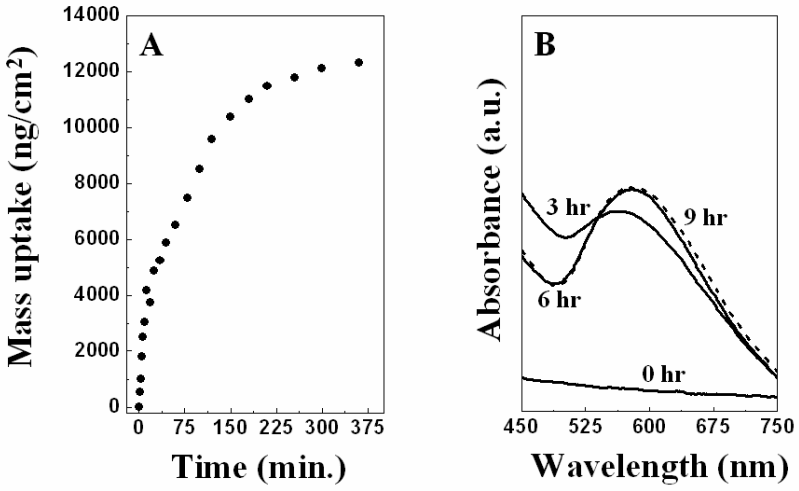

Figure 3.17: (A) QCM mass uptake data recorded *ex situ* from a 250 Å thick HDA film deposited on the QCM quartz crystal during immersion in 10^{-4} M $HAuCl_4$ solution for different periods. (B) UV–visible spectra recorded from a 250 Å thick HDA film after different times of immersion in 10^{-4} M HAuCl4 solution (times of immersion are indicated next to the respective curves).

QCM and the data obtained is shown in Fig.3.17.A. It is observed that there is a fairly large mass uptake due to entrapment of chloroaurate ions in the HDA matrix. At pH 3.5, the HDA molecules are expected to fully protonated leading to electrostatic binding with $AuCl_4^-$ ions. The diffusion of the $AuCl_4^-$ ions into the HDA film is quite rapid and stabilizes within ca. 6 hours of immersion in chloroauric acid solution. The mass loading (ca. 12 $\mu g/cm^2$) is extremely large and considerably in excess of the 1 : 1 HDA : $AuCl_4^-$ molar ratio expected from charge neutrality considerations.

3.5.2 UV-vis. Spectroscopy measurements:

The formation of gold nanoparticles due to the spontaneous reduction of entrapped chloroaurate ions by the film of HDA molecules was followed by UV-vis spectroscopy and clearly illustrated in Fig.3.17.B wherein the UV-vis spectra recorded from a 250 Å thick HDA film after immersing for different time intervals into 10^{-4} M $HAuCl_4$ solution. The growth of an absorption band centered at 590 nm can clearly be seen, this resonance stabilizing after nearly 6 h of immersion. This time interval is in agreement with the QCM results (Fig.3.17.A) where $AuCl_4^-$ ion uptake in the HDA film was complete within 6 hours of immersion. The absorption band at 590 nm is due to excitation of surface plasmon vibrations in the gold nanoparticles formed in the film and is responsible for the intense violet color observed in these films. We

would like to point out that unlike in earlier studies on the formation of gold nanoparticles in lipid thin films where UV irradiation [37] and hydrazine [38] was used to reduce the entrapped metal ions, in this study the host HDA molecules themselves accomplish the reduction of $AuCl_4^-$ ions. The presence of the gold nanoparticle absorption band at 590 nm after 3 h of immersion of the HDA film in $HAuCl_4$ solution indicates that the reduction of the gold ions is fairly rapid and supports our hypothesis of large gold ion mass uptake presented earlier. UV–visible spectra of 250 Å thick HDA deposited film were also recorded for 9 h of immersion in $HAuCl_4$ solution (Fig.3.17.(B), dotted curve). The intensity of the absorbance band was found to be same as the intensity of that for 250 Å thick HDA deposited film for 6 h of immersion. Hence the time period for equilibration of the gold ion concentration in the HDA film estimated from the UV–visible studies is in excellent agreement with the QCM results (Fig. 3.17. (A)) where $AuCl_4^-$ ion uptake in the HDA film was complete within 6 h of immersion.

3.5.3 Transmission Electron Microscopy (TEM) measurements:

Representative TEM pictures obtained from a 250 Å thick HDA film after immersion in 10^{-4} M $HAuCl_4$ solution for 6 h are shown in Fig.3.18. In addition to a number of very small gold nanoparticles of spherical and triangular morphology (about 8–15 nm dimensions) and much more sparsely present large nanoparticles (right-hand corner, Fig.3.18. (B)) evenly distributed over the TEM grid surface, we observed with very high frequency fractal, dendritic gold structures as shown in Figs. 3.18.(A) and (B).

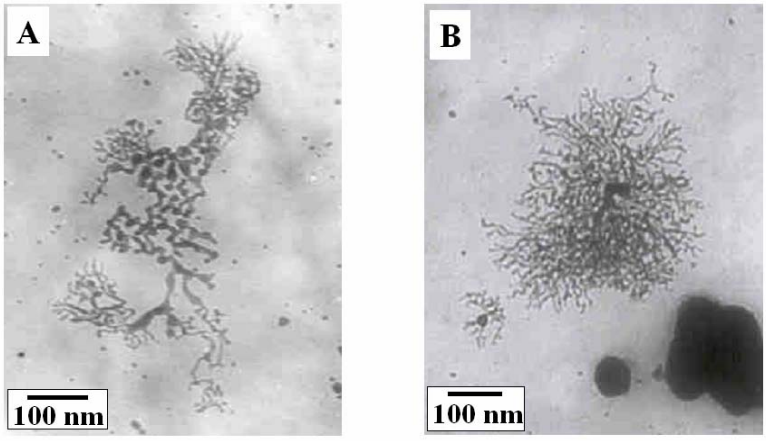

Figure 3.18: (A) and (B): Representative TEM micrographs recorded from a 250 Å thick HDA film after immersion in 10^{-4} M $HAuCl_4$ solution for 6 h.

While the fractal structure is much more open in figure 3.18. (A), the dendritic structure shown in Fig.3.18. (B) is very compact. The fractal dimensions of the central structures shown in Figs. 3.18 (A) and (B) have been estimated to be 1.6 ± 0.02 and 1.8 ± 0.01 respectively. The fractal dimension has been calculated by using the radial mass distribution method. Herein the number of pixels (picture elements) N(R) in a given radius R is measured. Since for a growing fractal $N(R) \sim R^D$, plotting ln N(R) versus ln R results in a curve which has an asymptotic slope equal to D [36]. The error estimated in calculating the fractal dimension is the error in the slope of the asymptotic line. The slope was calculated by the method of least squares. Figs.3.19. (A), (B) and (C) show representative TEM pictures obtained from a 250 Å thick HDA film after immersion in 10^{-4} M $HAuCl_4$ solution for 3, 6 and 9 h respectively. Small gold nanostructures are seen in the Fig. 3.19 (A) whereas a fully-grown fractal structure is seen in Fig. 3.19 (C). From the TEM pictures at different times of immersion, it appears likely that the initially

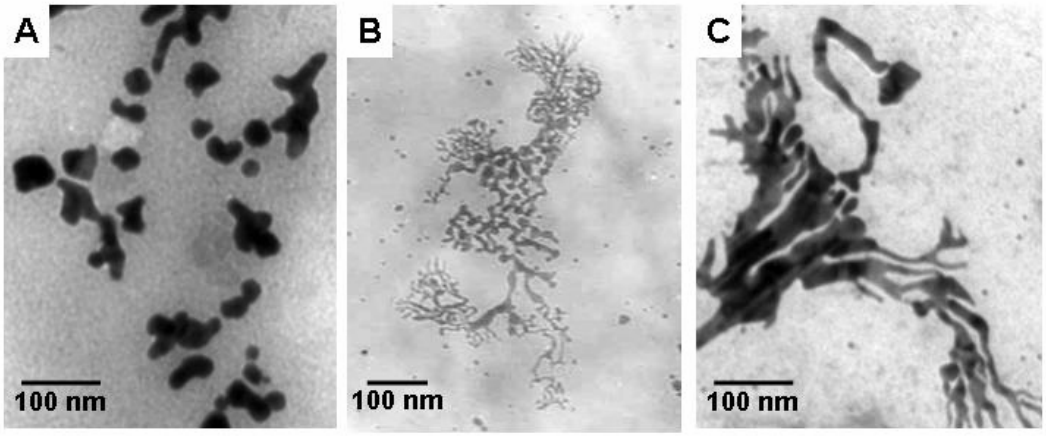

Figure 3.19: (A), (B) and (C) Representative TEM micrographs recorded from a 250 Å thick HDA film after immersion in 10^{-4} M $HAuCl_4$ solution for 3, 6 and 9 h respectively.

small, quasi-spherical gold nanoparticles come close together to form fractal structures by slow diffusion of $AuCl_4^-$ ions in the HDA organic matrix.

3.5.4 X-ray Diffraction (XRD) measurements:

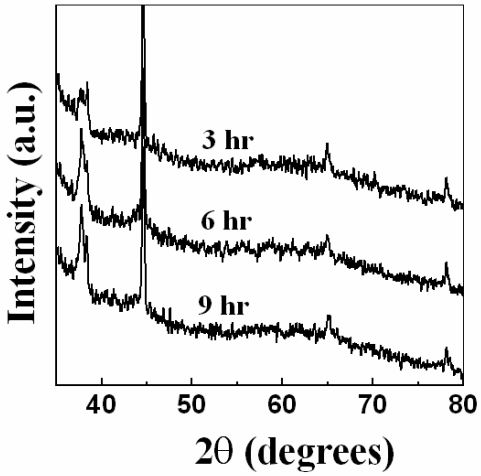

Figure 3.20: XRD pattern recorded from a 250 Å thick HDA film after immersion in 10^{-4} M $HAuCl_4$ solution for different times (times of immersion are indicated next to the respective curves).

Fig.3.20 shows the XRD pattern recorded from a 250 Å thick HDA film deposited on glass after different times of immersion in 10^{-4} M $HAuCl_4$ solution. The diffraction patterns are characteristic of fcc gold with an intense (111) Bragg reflection seen in the patterns. The fact that the (111) peak increases in intensity with time while the other Bragg reflections remain relatively unchanged indicates that the gold nanocrystalline structures are highly oriented along the (111) direction. This indicates oriented growth of the gold nanocrystals in the film along the (111) direction and arises possibly due to the templating action of the HDA molecules in the bilayers.

In a related study, Talham and co-workers have studied systematically the reduction of $AuCl_4^-$ ions by UV irradiation in LB films of different organic molecules such as octadecylamine (ODA), 4-hexadecylaniline (HDA), benzyldimethylstearylammonium chloride (BDSAC) and the phospholipids dipalmitoyl-DL-á-phosphatidyl-L-serine (DPPS) and dipalmitoyl-L-á-phosphatidylcholine (DPPC) [37]. While gold nanoparticles were observed in ODA, HDA and BDSAC films (but not in the phospholipids), the nanoparticles were highly irregular in shape with no evidence for fractal structures [37]. Recently Sastry and co-workers have synthesized fractal gold nanostructures by the reduction of chloroaurate ions constrained to a monolayer at the air-water interface using anthranilic acid as reducing agent [38]. Silver and gold fractal structures have been observed to form in solution often under sonochemical

[39] or ultrasonic agitation [40, 41], and in the presence of specific surface modifiers [42, 43, 44] but not in thin film form on solid supports. The gold fractal nanostructures obtained in this study are characteristic of diffusion-limited aggregated (DLA) structures [45]. Indeed, the fractal dimensions of the gold nanostructures in our HDA films (1.6 and 1.8; Figs. 3.18. (A) and (B) respectively) are in the range expected for DLA structures (<2) [45,46]. While the exact mechanism leading to formation of the fractal gold nanoparticles is not clear, however we believe that the strong binding of the HDA molecules with the gold nanoparticle surface inferred in our earlier report on HDA-induced gold nanoparticle formation in organic media [47] may be partly responsible for this. Unlike in the case where reduction of the $AuCl^-_4$ ions is carried out by an external reducing agent [37, 38] and therefore would be quite rapid, the reduction of the gold ions in this study is carried out by the host HDA molecules, which also bind strongly to the nucleating gold nanoparticles. Consequently, the diffusivity of the freshly nucleated gold nanoparticles in the HDA matrix is expected to be much smaller than for gold nanoparticles either reduced by external means or formed in weakly interacting hosts. We believe that this difference in diffusivity of the gold nanoparticles in the organic host is responsible for the spherical/irregular gold nanoparticles (fast diffusion) and fractal nanostructures (slow nanoparticle diffusion) observed in the different organic hosts.

3.6 Summary

In this chapter, it has been shown that gold, silver and CdS nanoparticle films may be synthesized in patterned fatty lipid films by an ion complexation and reduction process thus addressing an important gap in available protocols for realizing spatially programmed nanoparticle assemblies. While there is little control over the growth/chemical composition of nanoparticles in the prevalent methods such as the Langmuir – Blodgett technique, this approach is promising in realising a plethora of intricate structures by applying interesting chemistry to the patterned films of the fatty lipid-metal ion complexes. For example, carrying out the ion exchange process either simultaneously or sequentially and subjecting the metal ion-lipid composite films to a variety of reactions may generate a number of technologically important semiconductor and binary/ternary oxide nanoparticles. In this protocol the reduction process occurred using an external reducing agent however when the lipid matrix itself acts as a reducing agent that time we have obtained dendritic fractal nanostructures within the film.

Therefore, the nanostructures in the lipid matrix depend on the host matrix and reduction process.

3.7 References

[1] (a) Sastry, M.; Rao, M.; Ganesh, K.N. *Acc.Chem.Res*. **2002**, *35*, 847. (b) Sastry, M.; Patil, V.; Mayya, K.S.; *Langmuir* **1998**, *14*, 2707. (c) Sastry, M.; Patil, V.; Sainkar, S.R. J.*Phys.Chem.B* **1998**, *102*, 1404. (d) Mayya, K.S.; Patil, V.; Kumar, P.M.; Sastry, M. *Thin Solid Films* **1998**, *312*, 300.

[2] Philip, D.; Stoddart, J. *Angew.Chem.Int.Ed*., **1996**, *35*, 1154.

[3] Hybrid Organic Inorganic Composites; Mark, J.E.; Lee, C. Y-C.; Binaconi, P.A., *Ed*. *American Chemical Society*, *Washington*, **1995**, Vol.*585*.

[4] Schmidt, H.; Wolter, H. *J. Non-Cryst.Solids* **1990**, *121*, 428.

[5] Novak, B.M. *Adv.Mater*. **1993**, *5*, 422.

[6] Frisch, H.L.; Mark, J.E. *Chem.Mater*, **1996**, *8*, 1735.

[7] Colvin, V.L.; Goldstein, A.N.; Alivisatos, A.P. *J.Am.Chem.Soc*. **1992,** *114*, 5221.

[8] Bandyopadhyay, K.; Patil, V.; Vijayamohanan,K.; Sastry, M. *Langmuir*, **1997,** *13*, 5244.

[9] Yonezawa, T.; Onoue, S.; Kunitake, T. *Adv.Mater*. **1998**, *10*, 414.

[10] Gole, A.; Sainkar, S.R.; Sastry, M. *Chem.Mater,*. **2000**, *12*, 1234.

[11] Freeman, R.G.; Grabar, K.C.; Allison, K.J.; Bright, R.M.; Davis, J.A.; Guthrie, A.P.; Hommer, M.B.; Jackson, M.A.; Smith, P.C.; Walter, D.G.; Natan, M.J. *Science*, **1995**, *267*, 1629.

[12] Peschel, S.; Schmid, G. *Angew.Chem.Int.Ed.Engl*. **1995**, *34*, 1442.

[13] Whetten, R.L.; Khoury, J.T.; Alvarez, M.M.; Murthy,S.; Vezmar, I.; Wang, Z.L.; Stephens, P.W.; Cleveland, C.L.; Luedtke, W.D.; Landman, U. *Adv.Mater***. 1996**, *8*, 428.

[14] (a) Wang, Z.L. *Adv.Mater*. **1998**, *10*, 13; (b) Petit, C.; Taleb, A.; Pileni, M.-P. *Adv.Mater*. **1998**, *10***,** 259.

[15] Fendler, J.H.; Meldrum, F.C. *Adv.Mater*. **1995**, *7*, 607 and references therein.

[16] Sastry, M.; Mayya, K.S.; Patil, V.; Paranjape, D.V.; Hegde, S.G. *J.Phys.Chem.B*. **1997**, *101*, 4954.

[17] Sastry, M.; Mayya, K.S. *J.Nano.Res.* **2000**, *2*, 183.

[18] Hu, K.; Brust, M.; Bard, A.J. *Chem.Mater*. **1998**, *10*, 1160.

[19] Fink, J.; Kiely, C.J.; Bethell, D.; Schiffrin, D. *Chem.Mater*. **1998**, *10*, 922.

[20] Sarathy,K.V.; Thomas, P.J.; Kulkarni, G.U.; Rao, C.N.R. *J.Phys.Chem.B*. **1999**, *103*, 399.

[21] Musick,M.D.; Keating, C.D.; Lyon, L.A.; Botsko, S.L.; Pena, D.J.; Holliway, W.D.; McEvoy, T.M.; Richardson, J.N.; Natan, M.J. *Chem.Mater*. **2000**, *12*, 2869.

[22] Decher, G. *Science*, **1997**, *277*, 1232 and references therein.

[23] Lvov, Y.; Ariga, K.; Onda, M.; Ichinose, I.; Kunitake, T. *Langmuir*. **1997**, *13*, 6195.

[24] Cassagneau, T.; Mallouk, T.E.; Fendler, J.H. *J.Am.Chem.Soc*. **1998**, *120*, 7848.

[25] He, H.X.; Zhang H.;, li, Q.G.; Zhu, T.; Li, S.F.Y.; Liu, Z.F. *Langmuir*, **2000**, *16*, 3846.

[26] Aizenberg, J.; Braun, P.V.; Wiltzius, P. *Phys.Rev.Lett.* **2000**, *84*, 2997.

[27] Ganguly, P.; Sastry, M.; Pal, S.; Shashikala, M.N. *Langmuir*, **1995,** *11***,** 1078.

[28] Sauerbrey, G. *Z.Phys*. (Munich) **1959**, *155*, 206.

[29] Henglein, A. *J.Phys.Chem*. **1993,** *97*, 5457.

[30] Sastry, M.; Bandyopadhyay, K.; Mayya, K.S. *Coll.Surf.A.* **1997**, *127*, 221.

[31] Pal, S. *Ph.D. Thesis, University of Poona*, **1996**.

[32] Jeffrey, J.W. *Methods in Crystallography; Academic Press: New York*, **1971**.

[33] Cuvillier N.; Rondelez F. *Thin Solid Films*, **1998**, *19*, 327.

[34] Hostetler, M. J.; Stokes J.J. Murray, R.W. *Langmuir*, **1996**, *12*,, 3604.

[35] Patil, V.; Malvankar R.B.; Sastry, M. *Langmuir*, **1999**, *15*, 8197.

[36] (a) Underwood, S.; Mulvaney, P. *Langmuir*, **1994**, *10*, 3427; (b) Mayya, K. S.; Patil, V.; Sastry, M. *Langmuir*, **1997,** *13*, 3944.

[37] Revaine, S.; Fanucci, G. E.; Seip, C. T.; Adair, J. H.; Talham, D.R. *Langmuir*, **1998**, *14***,** 708.

[38] Swami, A.; Kasture, M.; Pasricha, R.; Sastry, M. *J.Mater.Chem*., **2004**, *14*, 709.

[39] Nikitenko, S. I.; Koltypin, Y.; Mastai, Y.; Koltypin, M.; Gedanken, A. *J. Mater. Chem*., **2002**, *12*, 1450.

[40] Xiao, J.; Xie, Y.; Tang, R.; Chen, M.; Tian, X. *Adv. Mater*., **2001**, *13***,**1887

[41] Zhu, J.; Liao, X.; Chen, H-Y. *Mater. Res. Bull.*, **2001**, *36***,** 1687.

[42] Zhou,Y.; Yu, S. H.; Wang, C. Y.; Li, X. G.; Zhu, Y. R.; Chen, Z. Y. *Adv. Mater*.,**1999**,*11***,** 850.

[43] Wang,, X.; Naka, K.; Itoh, H.; Park, S.; Chujo, Y. *Chem.Commun*., **2002,** 1300.

[44] Selvan, S. T. *Chem. Commun.*, **1998,** 351.

[45] Lin, M. Y.; Lindsay, H. M.; Weitz, D. A.; Ball, R. C.; Klein, R.; Meakin, P. *Nature*, **1989**, 339**,** 360.

[46] Solecka-Cermakova, K.; Vlckova, B.; Lednicky, F. *J. Phys. Chem*., **1996,** *100***,** 4954.

[47] Selvakannan, P. R.; Mandal, S.; Pasricha, R.; Adyanthaya, S. D.; Sastry, M. *Chem. Commun*., **2002**, 185.

Chapter 4

Synthesis of phase-pure metal core-shell nanoparticles using Keggin ions as UV-switchable reducing agents

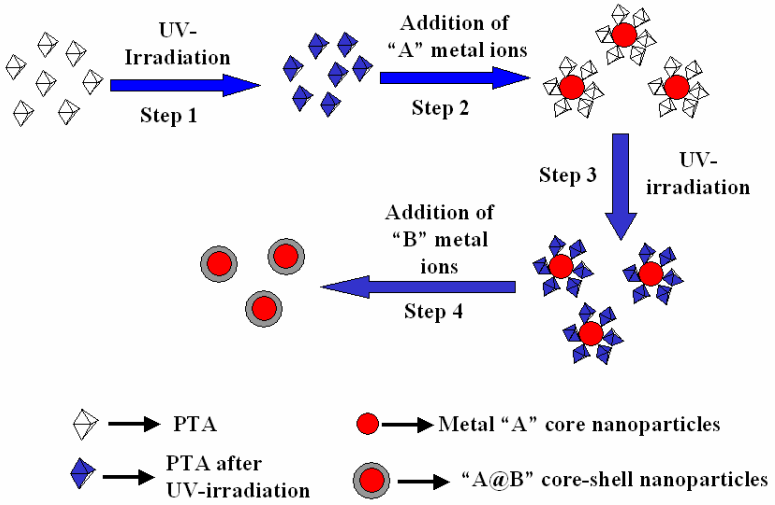

In this chapter the synthesis of Au @ Ag/Pd/Pt core-shell nanoparticles has been described. This is accomplished by utilizing Keggin ions bound to the surface of gold nanoparticles as UV-switchable reducing agents. Exposure of Keggin ion-capped gold nanoparticles to aqueous solutions of Ag^{+}, Pd^{2+} and Pt^{4+} ions after UV activation of the Keggin ions results in selective reduction of the metal ions only on the surface of the nanoparticles and thus, to phase-pure core-shell nanostructures. The reducing capability of the Keggin ions can be switched on using UV irradiation and photoactivated Keggin ions on the surface of the gold core act as highly localized reducing agents for the 2^{nd} metal ions thus excluding the possibility of nucleation of fresh Ag, Pd and Pt nanoparticles in solution. Core-shell nanoparticles are very important as catalysts. In this chapter it has been also shown that Keggin ion-capped Pd nanoparticles may be phase-transferred into non-polar organic solvetnts using octadecylamine as phase-transfer reagent. This results in a new class of catalyst wherein both the Pd core and Keggin ion shell may be used in a range of catalytic reactions leading to a truly multifunctional catalyst dispersible in various organic solvents.

Part of the work presented in this chapter has been published in: (1) Mandal, S.; PR. Selvakannan; Pasricha, R.; Sastry. M. *J.Am.Chem.*Soc. **2003**, 125, 8440.; (2) Mandal, S.; Mandale, A. B.; Sastry, M. *J.Mater.Chem.* **2004**, *14*, xxx.; (3) Mandal, S.; Das, A.; Srivastava, R.; Sastry, M. *Langmuir*, (Accepted).

4.1 Introduction.

The design, synthesis, and characterization of nanophase materials are subjects of intense research due to the exciting optoelectronic and physicochemical properties of nanoscale matter [1]. Nanomaterials are expected to have potential applications in optoelectronics, semiconductors, catalysis, magnetic devices, drug delivery, and so on [2-4]. The interest in core-shell nanoparticles is not just due to the enhancement of colloidal stability, but has also been driven by the interest in creating nanomaterials with unique and complex properties. Bimetallic nanoparticles, either in the form of an alloy or in the core-shell structure, are being investigated at some depth because of their improved catalytic properties [5] or change in the electronic/optical properties [6] relative to the individual, separate metals. It is postulated that their interesting physicochemical properties result from a combination of two kinds of metals and their fine structures. Bimetallic nanoparticles as alloys are conveniently synthesized by simultaneous reduction of two or more metal ions [6b, 7-10]. Many methods have been reported on their preparation by alcohol reduction [11], citrate reduction [6b], borohydride reduction [12], polyol process [13], solvent extraction/reduction [14], thermal decomposition [15], photolytic reduction [16], decomposition of organometallic precursors [17], and electrolysis of bulk metals etc [18]. On the other hand, experimental procedures for the formation of core-shell nanostructures are rather cumbersome and involve several steps. Generally, growth of core-shell structures can be accomplished by the successive reduction of one metal ion over the core of another [19-22]. Often this leads to the formation of fresh nuclei of the second metal in solution, in addition to a shell around the first metal core [22], and is clearly undesirable from the application point of view. A challenge would be to immobilize a reducing agent on the surface of the core metal which, when exposed to the second metal ions, would selectively reduce them on the surface thereby leading to phase-pure core-shell structures. A desirable feature of this approach for obtaining phase-pure core-shell nanoparticle structures would be a reducing agent bound to the surface of the core nanoparticle that could be selectively activated (i.e., whose reducing capability can be switched off and on at will). Keggin ions (polyoxometalates) [23] and the amino acid tyrosine [24] have been identified as switchable reducing agents that can be bound to gold nanoparticles and thereafter, activated by a stimulus to reduce a second metal ion. Polyoxometalates such as Keggin ions undergo stepwise multielectron redox processes without structural change [25] and may be reduced

electrolytically, photochemically, and with suitable reducing agents. Troupis, Hiskia, and Papaconstantinou have shown that exposure of photochemically reduced [$(SiW_{12}O_{40})^{4-}$] Keggin ions to aqueous Ag^{+}, Pd^{2+}, $AuCl_4^{-}$, and $PtCl_6^{2-}$ ions resulted in the formation of stable metal nanoparticles capped by the Keggin ions [26]. It is possible to activate again the surface bound Keggin ions by UV-irradiation and using them as a UV-switchable reducing agent for the second metal ions to synthesize the phase pure core-shell nanoparticles. In particular core-shell nanoparticles are highly attractive for their improved catalytic properties compared to individual metals. Application of metal nanoparticles in catalysis has predictably centred on Pt and Pd nanoparticles. The most important palladium-catalyzed reaction in organic chemistry, apart from catalytic hydrogenation, is the Heck reaction [27]. This reaction allows the preparation of substituted alkenes by alkylation or arylation of alkenes with vinyl or aryl halides. Besides Pd nanoparticles, polyoxometalates (heteropolyacids, HPAs) have several advantages as catalysts, which make them economically and environmentally attractive. Being stronger acids, HPAs will have significantly higher catalytic activity than mineral acids. In particular in organic media, the molar catalytic activity of HPA is often 100-1000 times higher than that of H_2SO_4 [28]. This makes it possible to carry out the catalytic process at a lower catalyst concentration and/or at a lower temperature. In UV-irradiated Keggin ion reduced Pd nanoparticles, Keggin ions stabilise the Pd nanoparticles by capping the Pd nanoparticle surface. Therefore it is possible to use the Keggin ion-capped Pd nanoparticles as multifunctional catalyst where Pd and Keggin ions will individually show their catalytic activity. For applications as catalyst in organic reactions the synthesis of nanoparticles in organic media is important. We also show that it is possible to phase transfer the Keggin ion-capped Pd nanoparticles into organic solvents and use them as multifunctional catalyst for different organic reactions. In this chapter a simple and reliable protocol for the synthesis of phase-pure core-shell metal nanoparticles using Keggin ions as UV-switchable reducing agent has been described. In this chapter synthesis of Keggin ion-mediated aqueous Pd nanoparticles and their phase transfer into toluene phase has also been described. The resulting organically dispersible Pd core-Keggin shell nanostructures are excellent candidates for multifunctional catalysis.

4.2 Synthesis of Au core-Ag shell nanoparticles using Keggin ions as UV-switchable reducing agents

In this section, the synthesis of phase pure Au core-Ag shell nanoparticles using Keggin ions as UV-swithable reducing agent has been described. It is well known that polyoxometalates such as Keggin ions undergo stepwise multielectron redox processes without undergoing a structural change [25]. They may be reduced electrolytically, photochemically and with suitable reducing agents and photochemically reduced polyoxometalates of the Keggin structure [$(PW_{12}O_{40})^{3-}$ and $(SiW_{12}O_{40})^{4-}$] when exposed to aqueous metal ions such as Ag^{+}, $AuCl_4^{-}$, Pd^{2+} and $PtCl_6^{2-}$ resulted in the formation of stable metal nanoparticles capped by the Keggin ions [24]. The surface-bound Keggin ions have been further UV irradiated and used as highly localized reducing agents in the synthesis of metal core-shell nanoparticles. The entire process has been illustrated in the schematic shown in Fig.4.1.

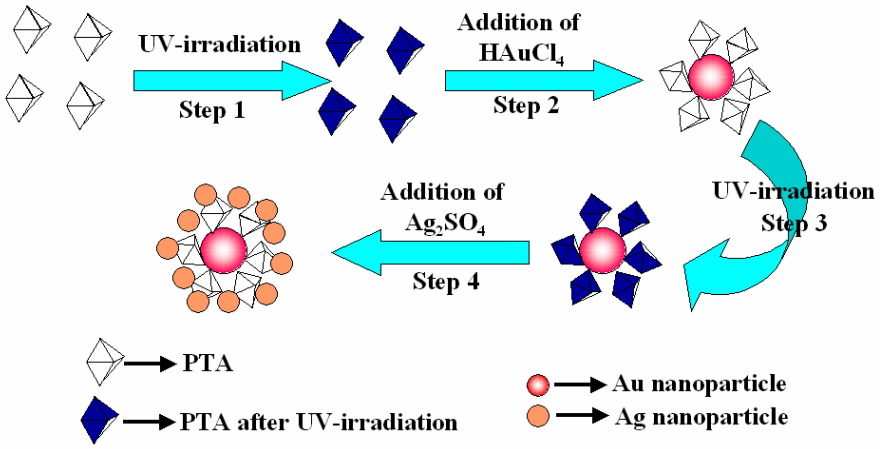

Figure 4.1: Schematic shows the Keggin ion-mediated synthesis of Au core-Ag shell nanoparticles. For simplicity, Keggin ions are shown as octahedral particles.

In Fig. 4.1, step 1 shows the photochemical reduction of phosphotungstic acid (PTA) by UV-irradiation resulting in the reduction of Keggin ions, which on exposure to $AuCl_4^{-}$ ions resulted in the formation of stable gold nanoparticles capped with Keggin ions as shown in step 2. In step 3, the reducing capability of the surface bound Keggin ions was restored by further exposure to UV light, after the uncoordinated Keggin ions were removed from the solution by thorough dialysis. Step 4 shows that when the activated Keggin ions capped gold nanoparticles

were exposed to Ag^{+} ions, the surface bound Keggin ions act as highly localized reducing agents and thereby result into the formation of phase pure Au core-Ag shell nanoparticles.

4.2.1 UV-vis. Spectroscopy measurements:

In a typical experiment 30 mL of 10^{-2} M aqueous deaerated solution of phosphotungstic acid [PTA, $H_3(PW_{12}O_{40})$, obtained from Aldrich and used as-received, solution pH 2.5] was added to 2 mL of propan-2-ol, and the mixture was irradiated by UV light for 4 h (Pyrex filter, >280 nm, 450-W Hanovia medium-pressure lamp; step 1, Fig.4.1). This leads to reduction of $(PW_{12}O_{40})^{3-}$ ions and is seen as a blue color appearing in the solution (test tube 1, inset of Fig.4.2).

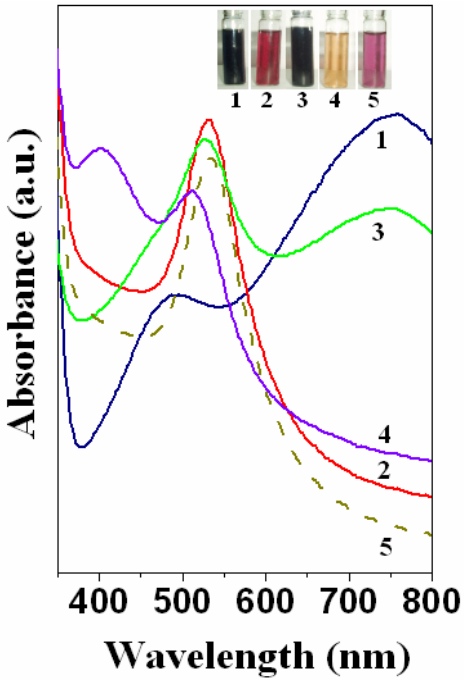

Figure 4.2: UV-vis spectra recorded from 10^{-2} M aqueous solution of PTA after UV irradiation (curve 1); UV-irradiated PTA solution after addition of 10^{-3} M $HAuCl_4$ (curve 2); solution 2 after further UV irradiation (curve3); solution 3 after addition of 10^{-3} M Ag_2SO_4 solution (curve 4); and solution 2 after addition of 10^{-3} M Ag_2SO_4 (curve 5). All UV-vis spectra have been adjusted for solution dilution effects. Pictures of sample bottles containing solutions 1-5 are shown in the inset (see text for details).

The UV-vis spectrum of this solution (curve 1, Fig.4.2) shows the presence of an absorption band at 760 nm that is characteristic of one-electron-reduced PTA [25], $[PW_{12}O_{40}]^{4-}$. To 5 mL of this irradiated PTA solution was added 15 mL of 10^{-3} M $HAuCl_4$ solution under continuous stirring for 10 min, and then the solution was allowed to age for 2 h (step 2, Fig.4.1). The

solution changed color from blue to pink (test tube 2, inset of Fig.4.2), indicating formation of gold nanoparticles. The UV-vis spectrum recorded from the PTA-gold solution (curve 2, Fig.4.2) shows a fairly sharp absorption band centered at 540 nm due to excitation of surface plasmon vibrations in gold nanoparticles [6b]. This solution was extremely stable over time, indicating that the Keggin ions are bound to the nanoparticle surface and stabilize them electrostatically and stereochemically (Fig.4.1, step 2) [26,29]. Uncoordinated PTA ions in solution were removed by thoroughly dialyzing the PTA-gold nanoparticle solution against distilled water for 2 days, using a 12K cutoff dialysis bag. The dialyzed solution was also extremely stable over time. Following dialysis of the PTA-gold nanoparticle solution, it was UV-irradiated again for 4 h (step 3, Fig.4.1). The UV-vis spectrum of the PTA-gold nanoparticle solution after irradiation is shown as curve 3 in Fig.4.2. The solution color changed from pink to a bluish-red (test tube 3, inset of Fig.4.2) and was accompanied by an increase in absorption at 760 nm. The increase in absorption at long wavelengths clearly indicates that the PTA ions on the surface of the gold nanoparticles have been reduced. To 15 mL of this solution was added 15 mL of 10^{-3} M aqueous solution of Ag_2SO_4 under stirring (step 4, Fig.4.1). Within 15 min, the solution changed color to a light brown (test tube 4, inset of Fig.4.2). The UV-vis spectrum from this solution (curve 4, Fig.4.2) shows a damping and blue shift of the gold surface plasmon vibration band, accompanied by the appearance of a distinct absorption band centered at 415 nm [30]. These observations are symptomatic of formation of silver shells around the PTA capped gold nuclei, as depicted in the scheme in Fig.4.1. A control experiment was performed wherein Ag^+ ions were added to the PTA-capped gold nanoparticle *without* additional UV irradiation (test tube 5, inset of Fig.4.2). Little change in the solution color occurred (compare test tubes 2 and 5, inset of Fig.4.2) and was supported by negligible changes in the solution Uv-vis spectra before (curve 2, Fig.4.2) and after ion exposure (curve 5, Fig.4.2. Curve 5 alone has been marginally shifted down since it was identical to curve 2). Thus, photochemical charging of PTA molecules bound to the gold nanoparticle surface is the crucial step in this work that sets it apart from other bimetallic nanoparticle core-shell synthesis protocols that employ reducing agents present uniformly in the reaction medium. That the reducing capability of the Keggin ions can be switched on using UV irradiation is an additional feature that enhances the versatility of the technique.

4.2.2 X-ray diffraction (XRD) measurements:

The presence of Keggin ions in the dialyzed PTA-nanogold solution was established by X-ray diffraction analysis of a drop-cast film on a glass substrate (curve 2 in Fig.4.3).

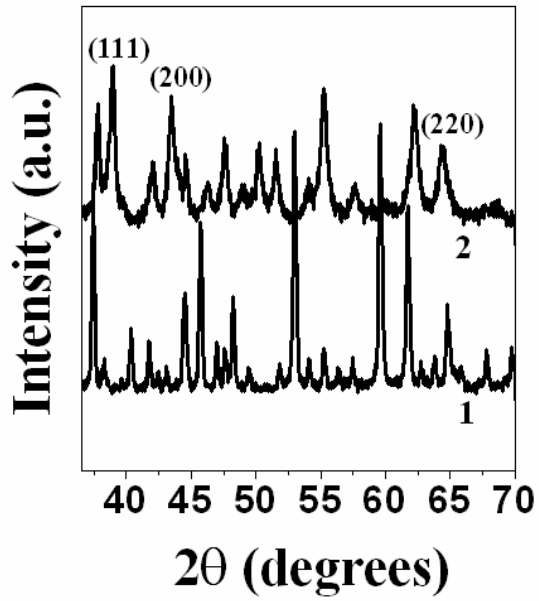

Figure 4.3: XRD patterns recorded from drop-coated films of PTA (curve 1) and PTA-gold nanoparticle solution after dialysis (curve 2). The principal Bragg reflections of fcc gold are indexed (curve 2).

The Bragg reflections characteristic of fcc gold are identified in this XRD pattern, clearly indicating that the particles are nanocrystalline. Characteristic Bragg reflections from the Keggin ions are observed (curve 1 in Fig.4.3) [31], indicating that UV activation and reduction of $AuCl_4^-$ ions has not disturbed their basic structure.

4.2.3 Transmission Electron Microscopy (TEM) measurements:

Samples for TEM measurements were prepared by drop coating film on carbon-coated copper grids from the Keggin-capped Au core and Au core-Ag shell nanoparticle solutions.

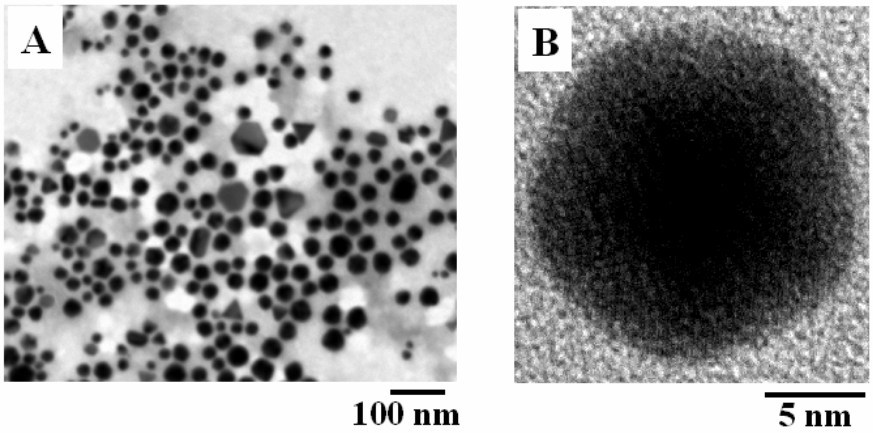

Figure 4.4: (A) TEM picture of gold nanoparticles reduced by UV-irradiated PTA solution. (B) High-resolution TEM image of one of the gold nanoparticles.

.

Fig.4.4A shows a representative low-magnification transmission electron microscopy (TEM) image of PTA-capped gold nanoparticles. The nanoparticles are polydisperse (size ranging from 15 to 70 nm) and have irregular morphology. Fig.4.4B shows a high-resolution TEM image of one of the gold nanoparticles. The contrast is uniform throughout the particle, thus indicating that it is a single nanocrystal. A number of multiply twinned gold nanoparticles could also be observed, which at higher magnification clearly showed the lattice planes of fcc gold.

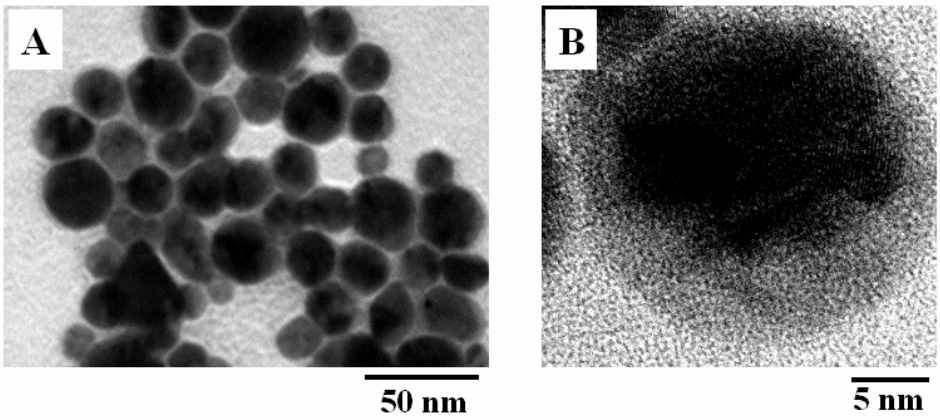

Figure 4.5: (A) TEM picture of gold core-silver shell nanoparticles by sequential reduction of gold and silver ions by UV-irradiated PTA solution. (B) High-resolution TEM image of one of the Au core-Ag shell nanoparticles.

Fig.4.5A shows a representative TEM picture of a drop-cast film of Au core-Ag shell nanoparticles grown as described above. As in the case of gold nanoparticles alone, the

particles are quite polydisperse, show a small increase in size (ranging from 20 to 100 nm), and are of varying morphology. A high-resolution TEM image of one Au core-Ag shell nanoparticle is shown in Fig.4.5B. A distinct variation in contrast between the dark gold core and the lighter silver shell is clearly seen. The thickness of the shells varied across particles and often exhibited morphology different from that of the core.

Thus photochemically reduced phosphotungstate Keggin ions have been used in the formation of Au core-Ag shell nanoparticles. The use of Au nanoscale surface-bound UV-switchable reducing agents such as that provided by Keggin ions enables the reduction of Ag^{+} ions only on the surface of the gold particles, thus obviating the possibility of nucleation of fresh Ag nanoparticles in solution.

4.3 Synthesis of aqueous phase-pure Au@Pd and Au@Pt core-shell nanoparticles using surface bound Keggin ions as highly localized reducing agent

In the earlier section it has been shown that phase-pure Au core-Ag shell nanoparticles synthesized using Keggin ions as UV-switchable reducing agent. The surface bound Keggin ions on gold nanoparticles act as highly localized reducing agent for second metal ions and reduced them only on the surface of the gold core nanoparticles and form phase-pure core-shell nanoparticles. In this section we show that this protocol is very general and reliable for other core-shell nanoparticle combinations. Exposure of Keggin ion-capped gold nanoparticles to aqueous solutions of Pd^{2+} and Pt^{4+} ions after UV activation of the Keggin ions results in selective reduction of the metal ions only on the surface of the nanoparticles and thus, to phase-pure core-shell nanostructures. The entire process has been illustrated in the schematic shown in Fig.4.6.

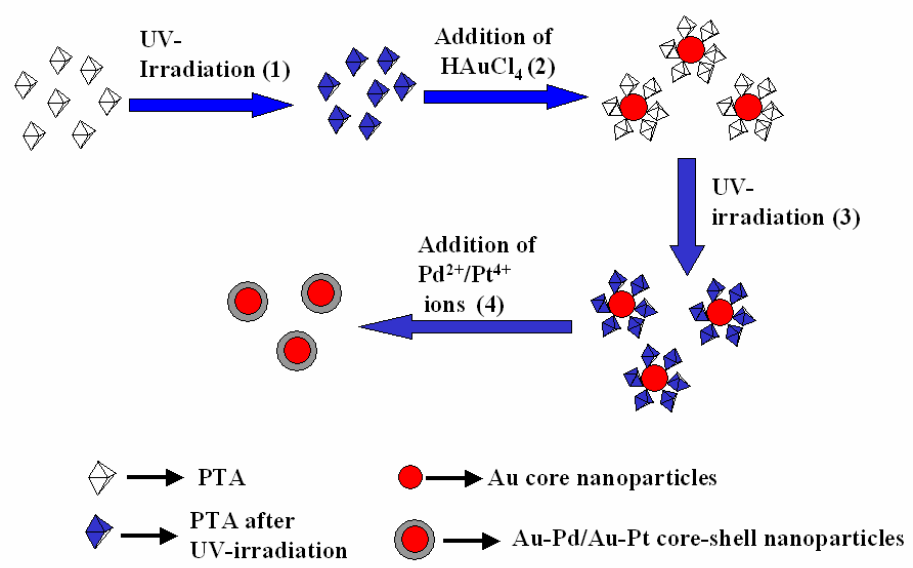

Figure 4.6: Schematic illustrating the Keggin ion-mediated synthesis of Au core-Pd/Pt shell nanoparticles.

In a typical experiment 30 mL of 10^{-2} M aqueous deaerated solution of phosphotungstic acid (PTA) was added to 2 mL of propan-2-ol, and the mixture was irradiated by UV light for 4 h (Pyrex filter, >280 nm, 450-W Hanovia medium-pressure lamp (step 1 in Fig. 4.6). This leads to reduction of $(PW_{12}O_{40})^{3-}$ ions and is seen as a blue color appearing in the solution. To 5 mL of this irradiated PTA solution, 15 mL of 10^{-3} M $HAuCl_4$ solution was added under continuous stirring for 10 min, and then the solution was allowed to age for 2 h (step 2 in Fig.4.6). The solution changed color from blue to pink indicating formation of gold nanoparticles. Uncoordinated PTA ions in solution were removed by thoroughly dialyzing the PTA-gold nanoparticle solution against distilled water for 2 days, using a 12 K cutoff dialysis bag. The dialyzed solution was also extremely stable over time and indicating that the Keggin ions are bound to the nanoparticle surface and stabilize them electrostatically and stereochemically. Following dialysis of the PTA-gold nanoparticle solution, it was UV-irradiated again for 3 h (step 3, Fig.4.6) and the solution color changed from pink to a bluish-red. To 15 mL each of this solution, 15 mL of 10^{-4} M aqueous solutions of $Pd(NO_3)_2$ and chloroplatinic acid (H_2PtCl_6) were added separately under stirring condition (step 4, Fig.4.6).

4.3.1 UV-vis. Spectroscopy measurements:

The optical properties of the core-shell nanoparticle solutions at different stages of preparation (steps 1-4, Fig.4.6) were shown in Fig. 4.7.

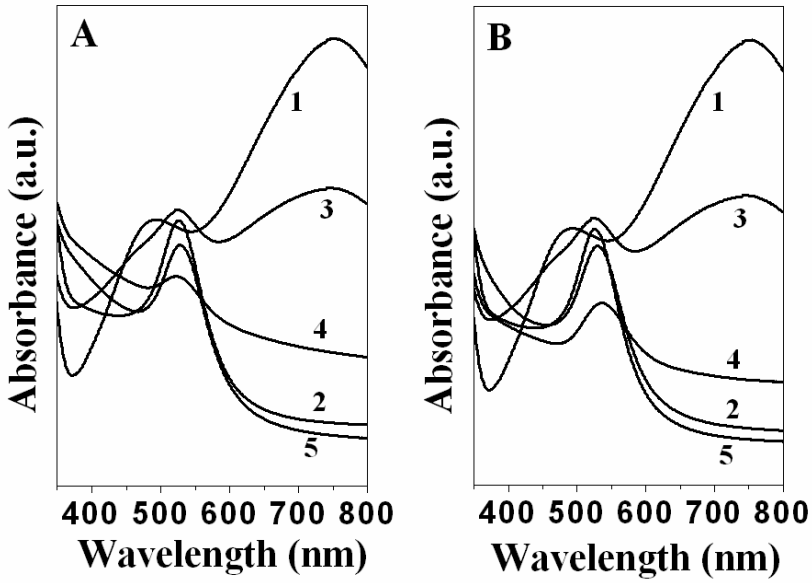

Figure 4.7: (A) and (B) show the UV-vis spectra of the Au core-Pt/Pd shell nanoparticle solutions at different stages of reaction. Curve 1 in (A) and (B)- 10^{-2} M aqueous solution of PTA after UV irradiation; curve 2 in (A) and (B)- UV-irradiated PTA solution after addition of 10^{-3} M $HAuCl_4$; curve 3 in (A) and (B)- PTA-capped Au nanoparticle solution after further UV irradiation; Curve 4 in (A) and (B)- UV-irradiated PTA-capped Au nanoparticle solution after addition of 10^{-4} M aqueous solutions of $Pd(NO_3)_2$ and H_2PtCl_6 respectively and curve 5 in (A) and (B)- PTA-capped Au nanoparticle solution after addition of10^{-4} M $Pd(NO_3)_2$ and H_2PtCl_6 solutions respectively (without prior UV-irradiation, see text for details).

Fig.4.7 (A) and (B) show the UV-vis spectra of the Au core-Pd shell and Au core-Pt shell nanoparticle solutions at different stages of preparation (steps 1-4, Fig.4.6). Curve 1 in Fig.4.7 (A) and (B) correspond to the spectrum recorded from UV-irradiated PTA solution (step 1, Fig.4.6); the presence of an absorption band at 760 nm is seen and is characteristic of one-electron-reduced PTA, $[PW_{12}O_{40}]^{4-}$ [25]. Curve 2 in Fig.4.7 (A) and (B) correspond to UV-vis absorption of the UV-irradiated PTA solution to which $HAuCl_4$ solution was added (step 2, Fig.4.6). A strong absorption band at ca. 526 nm is observed. This absorption band arises due to excitation of surface plasmon vibrations in the gold nanoparticles [6b]. Following dialysis of the PTA-gold nanoparticle solution, it was UV-irradiated again for 4 h (step 3, Fig.4.6). The UV-vis spectrum of the PTA-gold nanoparticle solution after irradiation is shown as curve 3 in Fig.4.7 (A) and (B). At this stage, the solution color changed from pink to a bluish-red, these changes are reflected in the UV-vis absorption spectrum as an increase in absorption at 760 nm.

This increase in absorption at long wavelengths clearly indicates that the PTA ions bound to the surface of the gold nanoparticles have been reduced. Curves 4 in Fig.4.7 (A) and (B) correspond to the UV-vis spectra recorded from the UV-irradiated PTA-capped gold nanoparticle solution after addition of palladium nitrate and H_2PtCl_6 solutions respectively (step 4, Fig.4.6). The UV-vis spectra from these solutions show a damping and broadening of the gold surface plasmon vibration band relative to the as-prepared PTA-capped gold nanoparticle solution (compare curves 2 and 4 in Fig.4.7 A and B). The damping of the gold core nanoparticle plasmon band consequent to reaction with Pt and Pd ions is a clear indication of reduction of the ions and formation of a metallic shell of Pt and Pd around the gold core.

4.3.2 X-ray Photoemission Spectroscopy (XPS) measurements:

A chemical analysis of these samples was performed using X-ray Photoemission Spectroscopy (XPS), to confirm the presence of Pd and Pt in Au-Pd and Au-Pt core-shell nanoparticles. The samples of PTA-capped Au, Au core-Pt shell and Au core-Pd shell nanoparticles were solution casted in the form of films onto Si (111) substrates and the XPS measurements were done as described in section *2.7.2* of chapter 2. The core level spectra were background corrected using the Shirley algorithm [32] and the chemically distinct species were resolved using a non-linear least squares fitting procedure. The Au 4f core level spectra recorded from the Au core-Pt/Pd shell nanoparticles at various stages of preparation are shown in Fig.4.8A while the Pd 3d from the Au core-Pd shell sample and Pt 4f core levels from the Au core-Pt shell nanoparticles are shown in Fig.4.8 B and C respectively. The general scan spectra of the above samples showed the presence of C 1s, P 2p, W 4f, Pt 4f and Pd 3d core levels with no evidence of impurities. As mentioned earlier, charging corrections in all the core level spectra were effected taking the adventitious C 1s binding energy (BE) to be 285 eV. The Au 4f spectrum from the PTA-capped gold nanoparticles (curve 1), Au core-Pd shell (curve 2) and Au core-Pt shell nanoparticles (curve 3) could in all cases be decomposed into a single spin-orbit pair (spin-orbit splitting ~ 3.6 eV). The Au $4f_{7/2}$ peak had a BE 84.3 eV, characteristic of Au(0) [33]. The absence of a higher BE Au 4f component clearly shows that all the $AuCl_4^-$ ions are fully reduced by the PTA anions after UV irradiation.

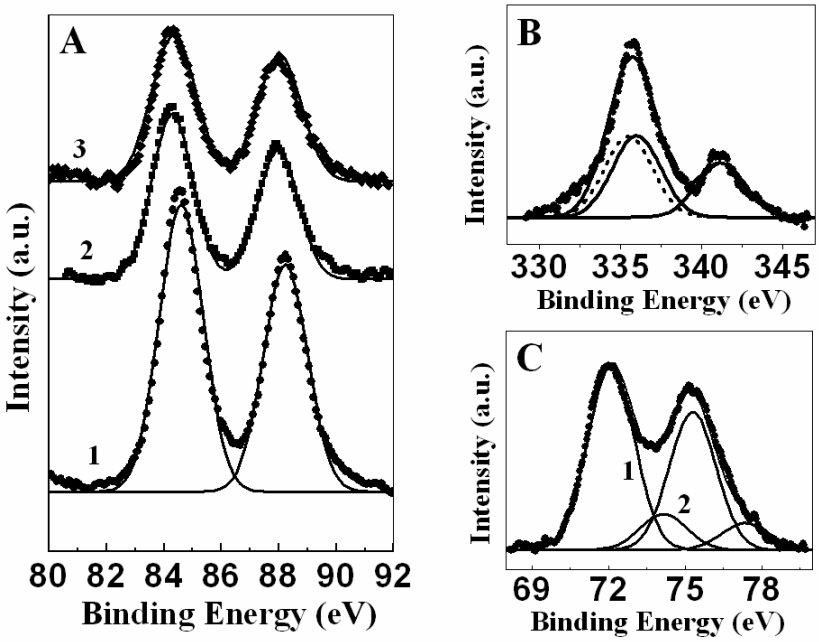

Figure 4.8: (A) Au 4f core level spectra recorded from PTA-capped Au nanoparticles (curve 1), Au-Pd (curve 2) and Au-Pt (curve 3) core-shell nanoparticles. The spectra have been shifted vertically for clarity. The spectrum in curve 1 has been decomposed into a spin-orbit pair. (B) Pd 3d and Au 4d core level spectra recorded from Au-Pd core-shell nanoparticles. The solid lines correspond to the Pd 3d spin-orbit pair while the dashed line is due to the Au $4d_{5/2}$ spin-orbit component. (C) Pt 4f core level spectrum recorded from the Au-Pt core-shell nanoparticles. The spectrum has been resolved into two spin-orbit pairs.

The reduction in intensity of the Au 4f spectrum after further reduction of Pd and Pt ions (curves 2 and 3) indicate the formation of a concentric shell in both cases. The presence of the Pd/Pt shell would lead to be enhanced inelastic scattering of the Au 4f electrons and a consequent reduction in intensity. The Pd 3d core level spectrum recorded from the Au-Pd core-shell nanoparticle sample could be resolved into a single spin-orbit pair (spin-orbit splitting ~ 5.4 eV) with a $3d_{5/2}$ binding energy (BE) of 335.8 eV (Fig.4.8B, solid lines). This BE is characteristic of Pd in the fully reduced state [34]. In this BE window, we also observe the presence of the Au $4d_{5/2}$ component (Fig.4.8B, dashed line) at a BE of 335.5 eV. The fact that the spectrum could be decomposed into a single spin-orbit pair indicates the complete reduction of Pd^{2+} ions by the UV irradiated PTA ions bound to the surface of the gold nanoparticle core. Fig.4.8C shows the Pt 4f core level spectrum recorded from the Au-Pt core-shell nanoparticle sample. Unlike in the case of the Pd ion reduction on the surface of PTA-capped gold nanoparticles, the Pt 4f spectrum had to be decomposed into two spin-orbit pairs

(spin-orbit splitting ~ 3.2 eV) with $4f_{7/2}$ BEs of 71.2 eV (curve 1, Fig.4.8C) and 74.2 eV (curve 2, Fig.4.8C) respectively. The low BE component corresponds to metallic Pt [35] while the high BE component is assigned to unreduced $PtCl_6^{2-}$ ions that are bound to the surface of the Pt metal shell.

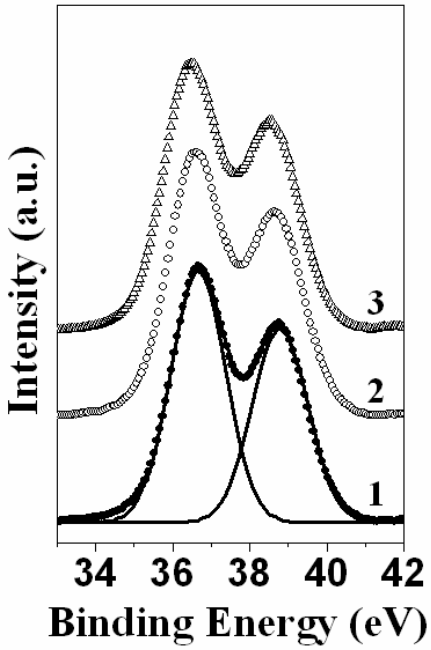

Figure 4.9: W 4f core level spectra recorded from the PTA-capped nanoparticles (curve 1), Au-Pd (curve 2) and Au-Pt (curve 3) core-shell nanoparticles. The spectra have been shifted vertically for clarity. The spectrum in curve 1 has been decomposed into a spin-orbit pair; the other two spectra could also be stripped into single spin-orbit pair but have not been shown for clarity.

The presence of phosphotungstic acid in PTA-capped Au nanoparticles, Au-Pd and Au-Pt core-shell nanoparticles is clearly indicated by the presence of the W 4f core level signal in all the samples (in Fig.4.9). Fig.4.9 shows W 4f core level spectra recorded from the PTA-capped Au nanoparticles (curve 1), Au-Pd (curve 2) and Au-Pt (curve 3) core-shell nanoparticles. The W 4f spectrum in all cases could be resolved into a single spin-orbit pair (splitting ~ 2.12 eV) with a $4f_{7/2}$ binding energy (BE) of 36.36 eV [36].

4.3.3 Transmission Electron Microscopy (TEM) measurements:

TEM samples of PTA-capped Au core, Au core-Pt shell and Au core-Pd shell nanoparticles were prepared by drop coating of the nanoparticle solutions on carbon-coated copper grids.

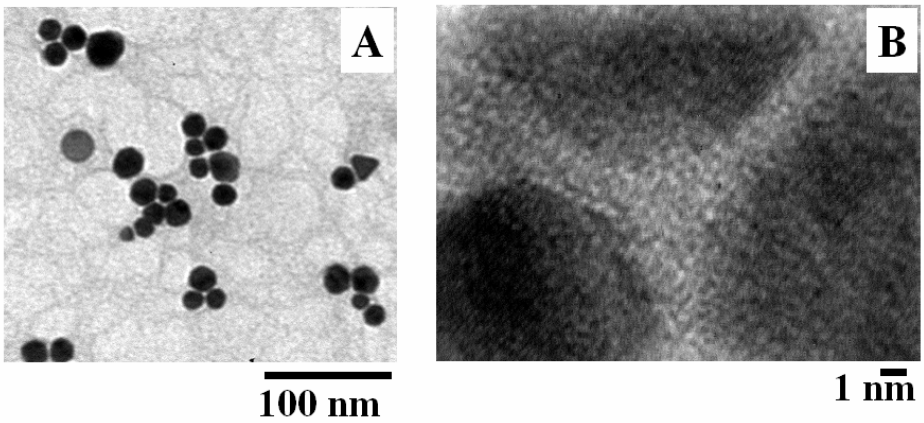

Figure 4.10: (A) TEM picture of PTA-capped gold nanoparticles. (B) High-resolution TEM image of the gold particles.

Fig.4.10A shows a representative low-magnification TEM image of PTA-capped Au nanoparticles. The nanoparticles are polydisperse with sizes ranging from 15 to 50 nm and have an irregular morphology. Fig.4.10B shows a HRTEM image of one of the gold nanoparticles. The contrast is uniform throughout the particle, thus indicating that it is a single nanocrystal. A number of multiply twinned gold nanoparticles could also be observed, which at higher magnification clearly showed lattice planes (2.35 Å spacing) corresponding to the (111) planes of fcc gold (Fig.4.10B).

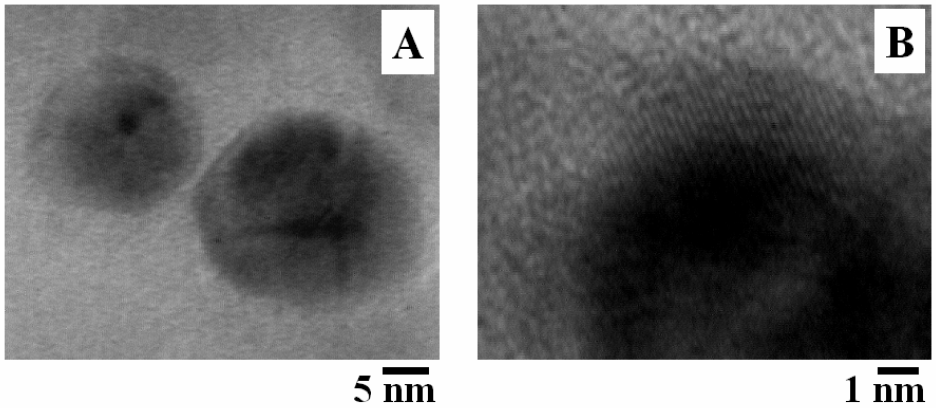

Figure 4.11: A and B – low and high-resolution TEM images recorded from gold core-palladium shell nanoparticles.

Fig.4.11A and B show representative low and high-resolution TEM images recorded from drop-cast films of Au core-Pd shell nanoparticles. As in the case of the PTA-capped gold

nanoparticles core, the particles are quite polydisperse and show a small increase in the particle size (Fig.4A, now ranging from 20 to 70 nm). At higher resolution (Fig.4B), a distinct variation in contrast between the dark gold core and the lighter palladium shell is clearly seen. The lattice planes of the Pd shell are clearly imaged (1.95 Å spacing) which corresponds to the (200) planes (Fig.4.11B).

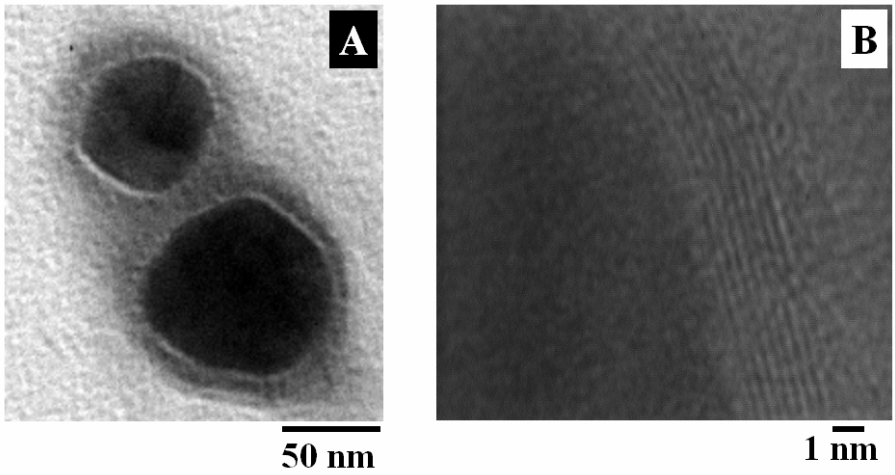

Figure 4.12: (A) TEM picture of gold core-platinum shell nanoparticles by sequential reduction of gold and platinum ions by UV-irradiated PTA solution. (B) High-resolution TEM image of one of the Au core-Pt shell nanoparticles.

Fig.4.12 A and B show representative low and high-resolution TEM pictures recorded from the Au core-Pt shell nanoparticles. As in the case of Au core-Pd shell nanoparticles, reaction of the PTA-capped gold nanoparticles with $PtCl_6^{2-}$ ions after UV activation results in an increase in the average size of the nanoparticles (sizes ranging from 40 to 85 nm) clearly indicating formation of a Pt concentric shell around the gold core. The presence of a Pt shell is more directly indicated in the high resolution TEM image recorded from one of the particles (Fig.4.12B) where the difference in contrast between the gold core and Pt shell is clearly seen. That the Pt layer is crystalline is inferred from the (222) lattice planes imaged in Fig.4.12B.

From the above discussion it is clear that after UV-irradiation, surface bound PTA molecules on the Au nanoparticle core act as highly localized reducing agents for Pd and Pt metal ions. That the PTA anions are indeed UV-switchable reducing agents is demonstrated by the following control experiment. In this experiment, Pd^{2+} and Pt^{4+} ions were added separately to PTA-capped gold nanoparticle solutions *without* subjecting the PTA-capped gold

nanoparticle solution to UV irradiation. Negligible changes are observed in the UV-vis absorption spectra of the PTA-capped gold nanoparticle solutions before and after addition of the Pd^{2+} and Pt^{4+} ions (compare curves 5 and 2 in Fig.1A and B respectively). Thus, photochemical charging of PTA molecules bound to the gold nanoparticle surface is the crucial step in protocol that sets it apart from other bimetallic nanoparticle core-shell synthesis protocols that employ reducing agents present uniformly in the reaction medium. That the reducing capability of the Keggin ions can be switched on using UV irradiation is an additional feature that enhances the versatility of the technique.

4.4 Synthesis of Keggin ion-capped hydrophobized Pd nanoparticles for multifunctional catalysis

In this section the synthesis of Keggin ion-capped aqueous Pd nanoparticles and their phase transfer into toluene phase by octadecylamine (ODA) is described. It is also shown that the resulting organically dispersible Pd core-Keggin shell nanostructures are excellent candidates for multifunctional catalysis. In particular, the high surface area to volume ratio of the metal nanoparticles makes them highly attractive for catalysis. Application of metal nanoparticles in catalysis has predictably centered onto Pt and Pd nanoparticles. As far as Pd nanoparticles are concerned, various procedures have been developed for preparing nanoparticles with controlled sizes and shapes in an aqueous environment [37]. Synthesis of metal nanoparticles in aqueous medium is convenient because of water's ability to solubilize a variety of ions and stabilizing molecules. We have used the reduction property of photoreduced Keggin ions (which has been already discussed in the introduction part of this chapter) to synthesize in-situ the stable Keggin ion-capped palladium nanoparticles in aqueous medium. On the other hand, synthesis of nanoparticles in organic media is important for applications in catalysis. Hydrophobized metal nanoparticles can be obtained in organic media either by preparing them directly [38] or by transferring nanoparticles from aqueous to organic phases [39]. The phase transfer approach has the advantage that there are many well-developed procedures available for the preparation of well-defined metal nanoparticles in aqueous media. One of the more popular methods for the synthesis of hydrophobized Pd nanoparticles in an organic medium involves the phase transfer of aqueous $PdCl_4^{2-}$ ions into non-polar organic solvents by using molecules such as tetraalkyl ammonium salts, followed by their reduction by

borohydride treatment and capping with alkanethiols [40] or phosphene derivatives [39]. Sastry and co-workers have developed a phase transfer technique for metal nanoparticles from aqueous phase to organic phase using octadecylamine as a phase transferring reagent [41]. Motivations from these earlier works, Keggin ion-capped Pd nanoparticles were phase transferred from aqueous to organic medium using octadecylamine as phase transferring reagent and were used as a multifunctional catalyst where Pd and Keggin ions show their catalytic activity individually.

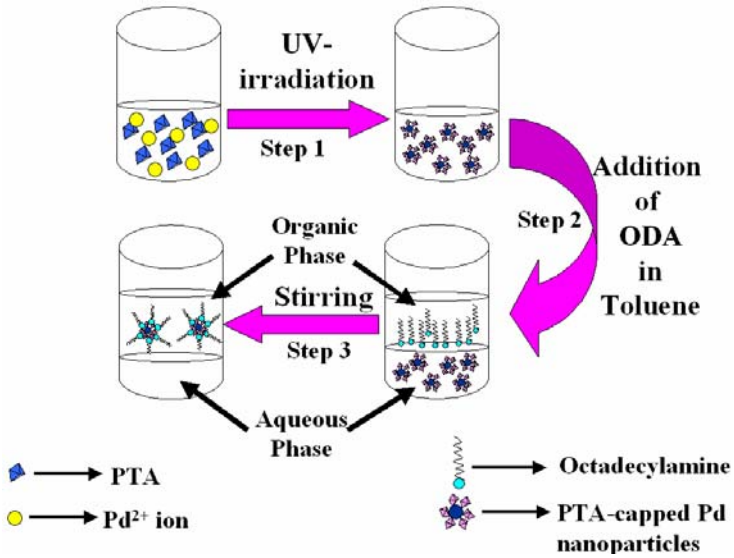

Figure 4.13: Schematic illustrating the synthesis of Keggin ion-capped Pd nanoparticles in aqueous medium and phase-transfer of Keggin-capped Pd nanoparticles by ODA through electrostatic complexation into organic phase.

The entire process of synthesis and phase transfer of Keggin capped Pd nanoparticles has been illustrated in the schematic shown in Fig.4.13. In Fig 4.13, step 1 shows the in-situ formation of Keggin ion capped stable palladium nanoparticles by UV-irradiation of mixture of Pd^{2+} and Keggin ions $[(PW_{12}O_{40})^{3-}]$ solution in aqueous medium. Step 2 shows the addition of octadecylamine (ODA) in toluene with aqueous solution of Keggin-capped Pd nanoparticle. Step 3 shows that after stirring the biphasic mixture, Keggin ion-capped Pd nanoparticles were phase transferred from aqueous to toluene phase using octadecylamine molecules as phase transferring reagent, resulting into hydrophobized Keggin ion-capped Pd nanoparticles. The phase transfer of Keggin ion-capped Pd nanoparticles to the organic phase has occurred by complexation with the octadecyllamine molecules through electrostatic interaction. Since the pH of the Keggin ion-capped Pd nanoparticle solution is 2.3, the octadecylamine (ODA)

molecules are expected to be completely protonated (pK_b of ODA = 10.5), thus leading to maximum electrostatic interaction between negatively charged Keggin-capped Pd nanoparticles and protonated amine groups of the ODA molecules and thus facilitate the phase transfer of Keggin-capped Pd nanoparticles into organic phase.

4.4.1 UV-vis. Spectroscopy measurements:

In a typical experiment 75 ml of a $2x10^{-3}$ M aqueous deaerated solution of PTA [$H_3(PW_{12}O_{40}$, pH = 2.8), obtained from Aldrich and used as-received] was taken in a test tube along with 75 ml of a 10^{-3} M aqueous deaerated solution of $Pd(NO_3)_2$ and 5 ml of propan-2-ol. This mixture was irradiated by UV light (Pyrex filter, >280 nm, 450 W Hanovia medium pressure lamp) for ½ an hour. UV irradiation leads to the in-situ reduction of Pd^{2+} ions by the electron-rich $(PW_{12}O_{40})^{4-}$ ions (which are formed by the photochemical reduction of $(PW_{12}O_{40})^{3-}$ ions) and is clearly seen by the appearance of a brownish color in solution. 20 ml aqueous solution of PTA-Pd was then taken in a beaker along with 20 ml of 10^{-3} M ODA in toluene. During stirring of the biphasic mixture, $2x10^{-1}$ M aqueous NaCl solution was added and stirring continued for 25 min. At the end of this reaction, the appearance of a brownish colour in the organic phase could clearly be seen indicating phase transfer of PTA-Pd nanoparticles into toluene. The toluene solution was rotovapped yielding a blackish powder of the PTA-Pd nanoparticles hydrophobized by ODA. This powder could be readily redispersed in other organic solvents such as chloroform indicating that ODA-hydrophobization protects the particles against aggregation during drying. Fig.4.14A shows the UV-vis spectra recorded from the PTA-capped Pd nanoparticles in water (curve 1) and PTA-Pd nanoparticles after phase-transfer by ODA into toluene (curve 2). In both spectra, the broad absorption observed is typical of platinum-group metal nanoparticles [37(a), 42] and clearly indicate reduction of palladium ions by photochemically reduced PTA. Curve 3 in Fig.4.14A shows the UV-vis spectrum recoded from the aqueous part after phase transfer. The absence of an absorption band clearly indicates the almost complete transfer of PTA-Pd nanoparticles by ODA molecules into toluene. The phase transfer of the PTA-capped Pd nanoparticles occurs through electrostatic complexation of the protonated ODA molecules with PTA anions bound the nanoparticles.

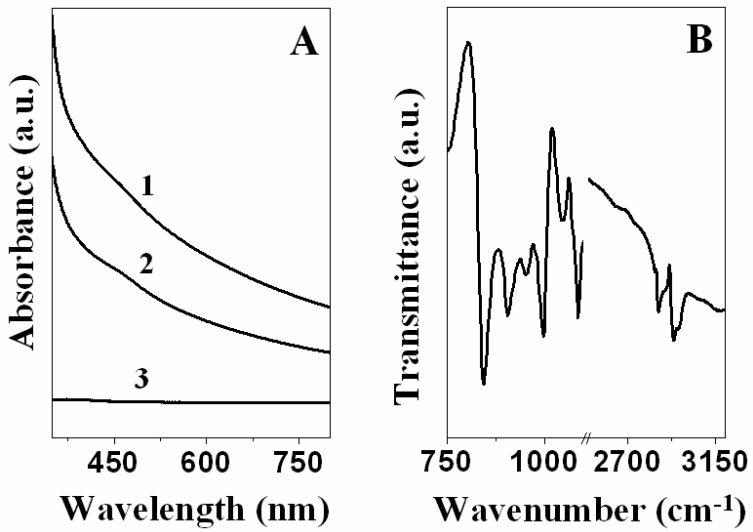

Figure 4.14: (A) UV-vis spectra recorded from PTA-Pd nanoparticles in water before (curve 1) and after phase transfer into toluene (curve 3); curve 2 corresponds to the spectrum from toluene after phase transfer of the PTA-Pd nanoparticles. The spectra have been shifted vertically for clarity. (B) FTIR spectrum recorded from ODA-hydrophobized PTA-Pd nanoparticles after phase transfer into toluene.

4.4.2 Fourier transform infrared (FTIR) spectroscopy measurements:

Fourier transform infrared FTIR spectroscopy measurements of drop casted films of phase transferred PTA-Pd nanoparticles on Si(111) substrate were measured as described in earlier chapter, section *2.3.2*. Fig.4.14B shows the Fourier transform infrared (FTIR) spectrum recorded from ODA-hydrophobized PTA-Pd nanoparticles. The W-O symmetric and asymmetric stretching vibrations at 996 and 953 cm^{-1} respectively and the P-O asymmetric stretching vibration at 1082 cm^{-1} are seen [43], indicating PTA stabilization of the Pd nanoparticles in toluene. In the 2500-3200 cm^{-1} window, the methylene antisymmetric and symmetric vibrations at 2920 and 2850 cm^{-1} respectively from the hydrophobizing ODA molecules are observed.

4.4.3 X-ray Photoemission Spectroscopy (XPS) measurements:

To confirm the presence of Pd and W in hydrophobized Keggin ion-capped Pd nanoparticles, a chemical analysis of the phase transferred PTA-Pd nanoparticles cast in the form of a film on Si(111) substrate was performed using XPS.

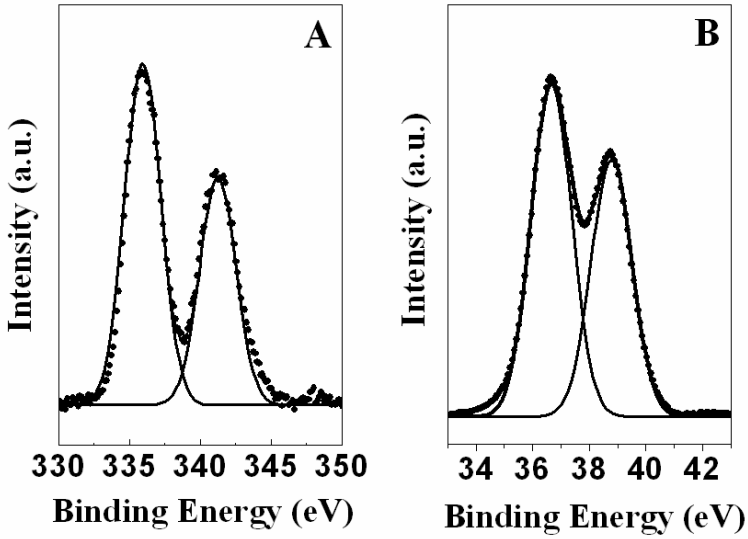

Figure 4.15: (A) and (B) Pd 3d and W 4f core level spectra respectively recorded from hydrophobized PTA-Pd nanoparticles after phase transfer into toluene.

Fig.4.15A and B show the Pd 3d and W 4f X-ray photoemission spectroscopy (XPS) core level spectra recorded from the ODA-hydrophobized PTA-Pd nanoparticles respectively. The Pd 3d spectrum could be resolved into a single spin-orbit pair (spin-orbit splitting ~ 5.2 eV) with a $3d_{5/2}$ binding energy (BE) of 335.9 eV. There was no evidence for additional component indicating complete reduction of Pd(II) to Pd(0) [34]. In Fig.4.15B the W 4f spectrum could be resolved into a single spin-orbit pair (splitting ~ 2.05 eV) with a $4f_{7/2}$ binding energy (BE) of 36.6 eV [36]. This confirms the presence of PTA ions bound to the underlying Pd nanoparticle core.

4.4.4 Transmission Electron Microscopy (TEM) measurements:

Samples for TEM analysis of the PTA-capped Pd nanoparticles before and after phase transfer into organic phase are shown in Figs. 4.16 and 4.17 respectively.

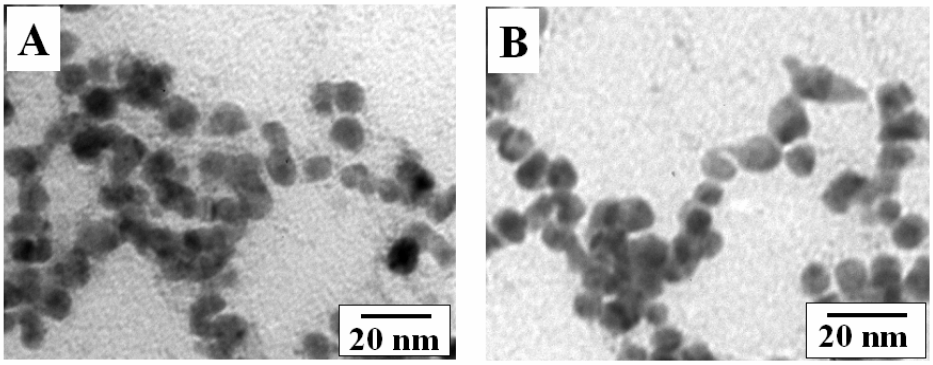

Figure 4.16: (A) and (B) show the TEM pictures at different magnification of PTA-Pd nanoparticles in the aqueous phase before phase transfer.

Fig.4.16 A and B show representative transmission electron microscopy (TEM) images at different magnification recorded from PTA-capped Pd nanoparticles in water before phase-transfer. The Pd nanoparticles are irregularly shaped and rather polydisperse in size (average diameter = 9 ± 2 nm). The particles are well dispersed with little evidence of aggregation indicating stabilization of Pd particles by PTA.

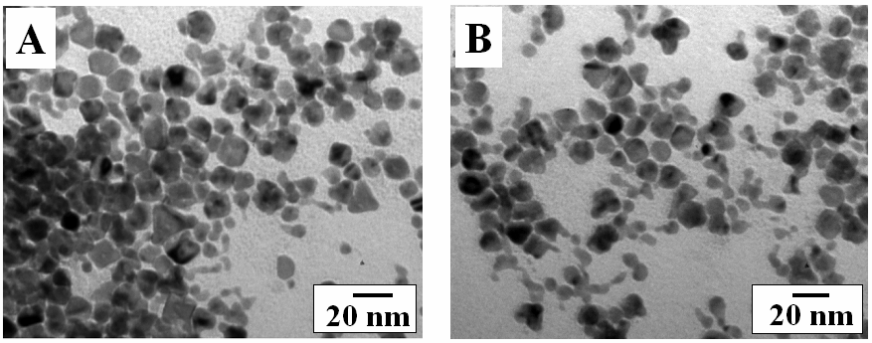

Figure 4.17: (A) and (B) represent the TEM pictures at different magnification of PTA-Pd nanoparticles in toluene after complexation with ODA.

Fig.4.17 A and B show representative TEM images recorded from the ODA-hydrophobized PTA-Pd nanoparticles in toluene after phase-transfer. A large number of irregularly shaped Pd nanoparticles are observed in the TEM image. From an analysis of the Pd nanoparticles in this and other images, an average particle size of 9.5 ± 2 nm was determined. Another interesting feature of the TEM image is the very regular separation between the Pd nanoparticles. This is clearly due to the ODA molecules capping the nanoparticles and preventing their aggregation after solvent evaporation.

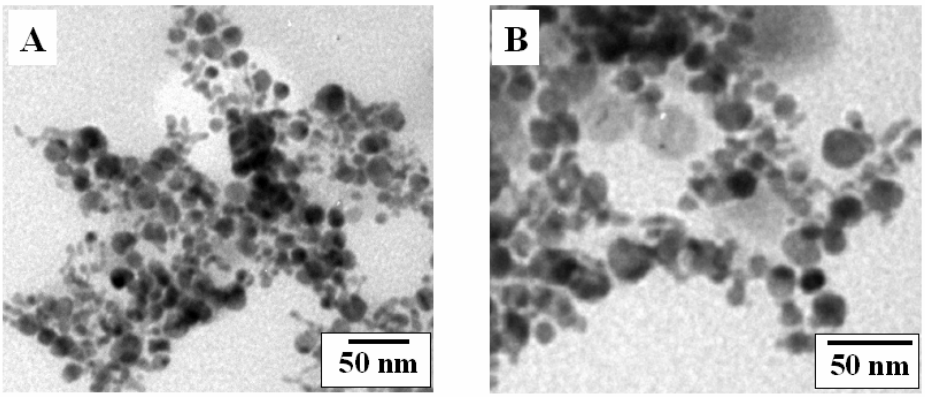

Figure 4.18: (A) and (B) represent the TEM image of the [ODA-PTA-Pd] catalyst after third recycles of the Heck reaction.

Fig.4.18 A and B show representative TEM images recorded from the reaction mixture of Heck reaction after the third recycle. Comparing the TEM images of the [ODA-PTA-Pd] catalyst before and after the third recyle reaction (Fig. 4.17 and 4.17 respectively), it is observed that there is a small increase in the average size of the nanoparticles. However, we observe that there is no aggregation or appreciable sintering of palladium nanoparticles as a consequence of the Heck reaction clearly indicating that the structural intergrity of the catalyst is not altered during such reactions.

4.4.5 Catalytic activity measurements:

To evaluate the catalytic performance of the ODA-hydrophobized PTA-Pd nanoparticles, different reactions such as Heck olefination of halobenzenes, ring opening of epoxides and acylation reactions have been carried out. The Heck reaction is one of the most versatile tools in modern synthetic chemistry and has great potential for future industrial applications. Therefore we were interested in evaluating the performance of our ODA-hydrophobized PTA-Pd catalyst for arylation of methylacrylate with halobenzene (scheme 1).

Scheme 1.

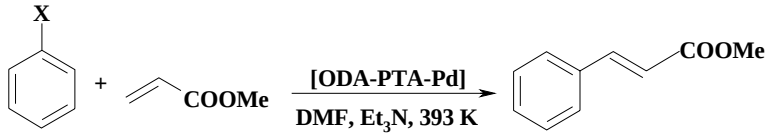

X = I / Br; [ODA-PTA-Pd] = ODA-hydrophobized PTA-Pd catalyst

In a typical Heck reaction 5 mM halobenzene, 10 mM methylacrylate, 7.5 mM triethylamine, 5mL of [ODA-PTA-Pd] catalyst in chloroform and 2.5 mL DMF solvent were taken in a 50-mL glass batch reactor. The reactor was flushed with N_2, the temperature was raised to a desired value (393 K) and the reactions were conducted for 3-24 h. The reactor was cooled to 298 K, the product isolated and analysed quantitatively by gas chromatography (Varian 3400; CP-SIL8CB column; 30 m long and 0.53 mm i.d.). The products were identified by GC-MS (Shimadzu QP-5000; with a 30 m long and 0.53 mm i.d. and 0.25 μm-thick capillary column DB-1), GC-IR (Perkin Elmer 2000; BP-1 column; 25 m long and 0.32 mm i.d.). During synthesis of PTA-capped Pd nanoparticles in aqueous medium we had taken 10^{-3} M $Pd(NO_3)_2$ and $2x10^{-3}$ M PTA solution. We have carried out atomic absorption spectroscopy (AAS) measurements on the aqueous solution of PTA-capped Pd nanoparticles before and after phase transfer using ODA molecules to quantify the extent of phase transfer of the PTA capped-Pd nanoparticles. AAS results showed the concentrations of palladium in the aqueous medium before and after phase transfer to be 106.5 and 5.4 ppm respectively. Therefore, from the AAS studies it is confirmed that 95 % of palladium nanoparticles have been transferred into the organic medium by electrostatic complexation with ODA. This result is further ascertained by the UV-vis data of aqueous phase after phase transfer (curve 3 in Fig.4.14 A). Since the concentration of $Pd(NO_3)_2$ solution used for nanoparticle synthesis was 10^{-3} M and complete reduction of the Pd ions was ensured in the experimental conditions, the concentration of Pd phase transferred into the organic solvent is estimated from the AAS studies to be 0.95×10^{-3} M. Hence, in the Heck reactions the concentration of the ODA-hydrophobized PTA-Pd [ODA-PTA-Pd] catalyst is 0.95×10^{-3} M. A similar transfer ratio (95 %) was also determined from AAS measurements for the PTA ions leading to a $0.95 \times 2 \times 10^{-3}$ M concentration of the Keggin ions in the organic phase.

Table 1: Heck olefination of halobenzene with methylacrylate using [ODA-PTA-Pd] and [ODA-Pd] catalysts

Catalysts	Substrates		Entry	Conversion	Selectivity		Time	TOF (h^{-1})
					Trans	Cis		
[ODA-PTA-Pd]	Iodo-benzene (5 mM)	Methyl-acrylate (10 mM)	Recycle-0 Recycle-1 Recycle-2 Recycle-3	97.5% 96.9% 96.7% 95.2%	99.1% 99% 99.2% 99%	0.9% 1% 0.8% 1%	3 h	1710 1700 1696 1669
[ODA-PTA-Pd]	Bromo-benzene (5 mM)	Methyl-acrylate (10 mM)		96%	97.5%	2.5%	24 h	44
[ODA-Pd]	Iodo-benzene (5 mM)	Methyl-acrylate (10 mM)	Recycle-0 Recycle-1 Recycle-2 Recycle-3	88% 87.5% 87.2% 86.7%	99.1% 98.9% 97.9% 98.2%	0.9% 1.1% 2.1% 1.8%	3 h	3106 3088 3078 3060

Table 1 shows the activity of the ODA-hydrophobized PTA-Pd nanoparticles catalyst for Heck reaction of different substrates. In this Heck reaction, the conversion of iodobenzene and bromobenzene with methylacrylate into methylcinnamate occurred at 97.5% (selectivity = 99.1 %, TOF 1710 h^{-1}) and 96% efficiency (selectivity = 97.5 %, TOF 44 h^{-1}) respectively (Table 1). Recently Christensen [44] and Fox [45] have reported on the Heck reactions of bromobenzene with acrylic acid and iodobenzene with methylacrylate respectively. Comparing with the above literatures the performance of our catalyst is superior in terms of yield of the product. An important point concerning the use of catalysts is their lifetime/reusability; therefore, we have checked the recycleability of our catalyst [ODA-PTA-Pd] in Heck reactions. The catalyst [ODA-PTA-Pd] was efficiently recycled three times for the Heck olefination of iodobenzenes with methylacrylate, which is shown in Table1 and it clearly shows that there is no change in the activity of the catalyst even after three recycles. The fresh reaction (cycle 0) showed 97.5%

conversion of iodobenzene after 3 h with TOF of 1710 h^{-1}. After the first, second and third recycles of the Heck reaction, the conversion of iodobenzene obtained were 96.9%, 96.7% and 95.2% with TOFs of 1700, 1696 and 1669 h^{-1}, respectively (Table 1). Thus, the recycled catalyst shows activities comparable to the fresh catalyst. These studies show that the catalyst is still active for Heck olefination of iodobenzene even after three recycles, which indicates that the nanostructure and dispersivity of the palladium nanoparticles have not changed after the recycle reactions. To check the possibility of reduction of catalytic activity after PTA molecules capping the Pd nanoparticles, a control experiment was performed with ODA-capped bare Pd nanoparticles (without capping with Keggin ions). For synthesizing such ODA capped-Pd nanoparticles, borohydride reduced Pd nanoparticles (without Keggin ion capping) were phase transferred into chloroform phase using ODA molecules as phase transfer agents. In this experiment, 100 ml of 10^{-4} M aqueous solution of palladium nitrate ($Pd(NO3)_2$) was reduced by 0.01 g of sodium borohydride ($NaBH_4$) at room temperature to yield palladium nanoparticles. 100 ml aqueous solution of Pd nanoparicles was then taken in a beaker along with 20 ml of 10^{-3} M ODA in chloroform and stirred for 2 hours, which resulted in the transfer of the palladium nanoparticles into the organic phase as evidenced by the brownish coloration of the organic phase (and a corresponding loss of color from the aqueous phase). We have carried out atomic absorption spectroscopy (AAS) measurements of aqueous solution of Pd nanoparticles before and after phase transfer using ODA molecules to quantify the extent of phase transfer of ODA-Pd nanoparticles. AAS results showed the concentration of palladium in aqueous medium before and after phase transfer to be 10.6 and 0.056 ppm respectively. From the AAS studies, we estimate that 94.4 % of palladium nanoparticles have been transferred into organic medium. Since 100 ml of 10^{-4} M palladium nanoparticles were transferred into 20 ml chloroform using ODA with a phase-transfer efficiency 94.4 %, the concentration of Pd in organic medium would be $0.944 \times 5 \times 10^{-4}$ M. We have checked the catalytic activity of the ODA-capped Pd nanoparticle catalyst [ODA-Pd] for the Heck reaction with iodobenzene and methylacrylate. The [ODA-Pd] catalyst showed good catalytic activity of the Heck olefination of iodobenzene with methylacrylate. We have also checked the recycleability of the [ODA-Pd] catalyst in the Heck reaction of iodobenzene and methylacrylate. The catalyst [ODA-Pd] was efficiently recycled three times for the Heck reaction, details of which are shown in Table 1. The fresh reaction (recycle 0) showed 88 % conversion of iodobenzene after 3 h with TOF of

3106 h^{-1} (Table 1). After the first, second and third recycles of the Heck reaction, the conversions of iodobenzene obtained were 87.5, 87.2 and 86.7% with TOF 3088, 3078 and 3060 h^{-1}, respectively (see Table 1). The recycle results show that the catalyst is still active for Heck olefination of iodobenzene even after three recycles, which indicates that the nanostructure and dispersivity of the palladium nanoparticles have not changed after the recycle reactions. This is supported by the TEM images of the catalyst from the reaction mixture of Heck reaction before and after the third recycle (Figs.4.19A and B). In both cases, it is observed that the Pd nanoparticles are irregularly shaped. Comparing the TEM images of [ODA-Pd] catalyst before and after reaction (Figs.4.19 A and B) one sees that they're a small change in the average size of the nanoparticles. However, there is little aggregation or appreciable sintering of the palladium nanoparticles due to recycling (Figs.4.19 A and B). The inset of the Figs. 4.19 A and B show the selected area diffraction (SAED) patterns recorded from the palladium nanoparticles in the main part of the figure. In both the cases, the diffraction rings could be indexed on the basis of a face centered cubic (fcc) palladium unit cell structure.

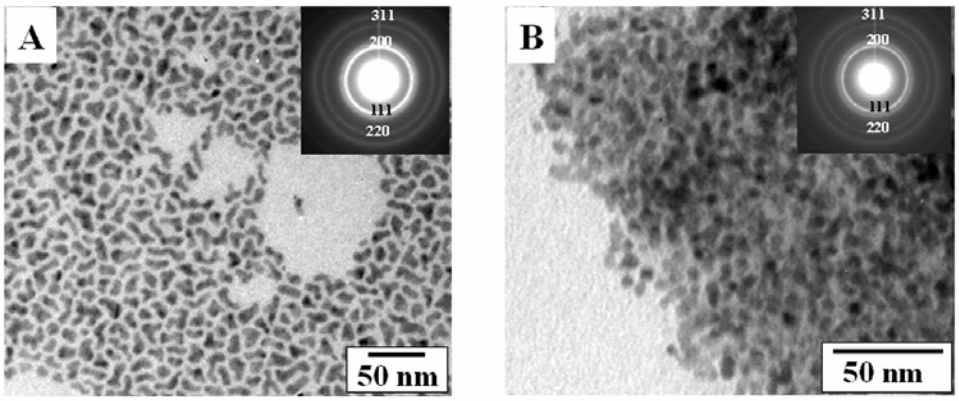

Figure 4.19: (A) and (B) representative TEM images of the [ODA -Pd] catalyst before and after the third recycle of the Heck reaction. The inset of these figures show the selected area diffraction (SAED) patterns recorded from the palladium nanoparticles in the main part of the figure. In both the cases the diffraction rings have been indexed based on the fcc structure of Pd.

The Heck reaction of iodobenzene and methylacrylate with [ODA-Pd] catalyst showed a remarkable jump in activity in comparison to the results obtained under the same reaction conditions with [ODA-PTA-Pd] catalyst (see the table 1). In ODA hydrophobized PTA-capped Pd nanoparticles PTA molecules are bound with the surface of the palladium nanoparticles and thereby limiting accessibility for the reactant molecules to the Pd catalytic surface in [ODA-PTA-Pd] catalyst whereas a large fraction of highly reactive Pd sites in [ODA-Pd] catalyst that

would be easily accessible to reactant molecules and thus to an enhanced catalytic activity of this catalyst relative to the [ODA-PTA-Pd] catalyst.

To test the activity of PTA ions present in the ODA-hydrophobized PTA-Pd nanoparticle catalyst, we performed the ring opening reactions of epoxy compounds and acylation reaction (Schemes 2 and 3 respectively).

Scheme 2.

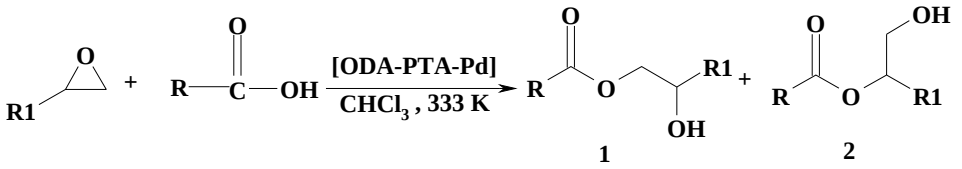

R1 = CH_2Cl / Ph; R = CH_3 / Ph; [ODA-PTA-Pd] = ODA-hydrophobized PTA-Pd catalyst

Scheme 3.

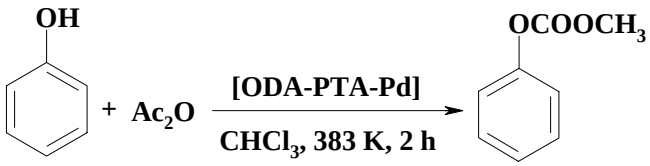

[ODA-PTA-Pd] = ODA-hydrophobized PTA-Pd catalyst

In a ring opening of epoxides reaction, 2 mM of epoxide, 2 mM of organic acid and 5ml of [ODA-PTA-Pd] catalyst in chloroform were taken in a 50-ml glass batch reactor. The reactor was flushed with N_2, temperature was raised to a desired value (333 K) and the reactions were conducted for 3-10 h. The reactor was cooled to 298 K, the product isolated and analysed quantitatively by gas chromatography (Varian 3400; CP-SIL8CB column; 30 m long and 0.53 mm i.d.). The products were identified by GC-MS (Shimadzu QP-5000; with a 30 m long and 0.53 mm i.d. and 0.25 μm-thick capillary column DB-1), GC-IR (Perkin Elmer 2000; BP-1 column; 25 m long and 0.32 mm i.d.). During synthesis of PTA-capped Pd nanoparticles in the aqueous medium, we had taken 10^{-3} M $Pd(NO_3)_2$ and $2x10^{-3}$ M PTA solution. AAS results from the aqueous solution of PTA-capped Pd nanoparticles before and after phase transfer into toluene showed that 95 % of PTA-capped Pd nanoparticles were phase transferred into the organic medium. Therefore, the concentration of PTA in toluene would be 0.95 x 2 x 10^{-3} M

and this would also be the concentration of the catalyst in chloroform in ring opening of epoxide as briefly discussed in the experimental section.

In an acylation reaction, 10 mM of phenol, 11 mM of acetic anhydride and 5ml of [ODA-PTA-Pd] catalyst in chloroform were taken in a 50-ml glass batch reactor. The reactor was flushed with N_2, temperature was raised to a desired value (383 K) and the reaction was conducted for 2 h. The reactor was cooled to 298 K, the product isolated and analysed quantitatively by gas chromatography (Varian 3400; CP-SIL8CB column; 30 m long and 0.53 mm i.d.). The products were identified by GC-MS (Shimadzu QP-5000; with a 30 m long and 0.53 mm i.d. and 0.25 μm-thick capillary column DB-1), GC-IR (Perkin Elmer 2000; BP-1 column; 25 m long and 0.32 mm i.d.). Note that in the acylation reaction, the concentration of the ODA-PTA-Pd catalyst is $0.95 \times 2 \times 10^{-3}$ M.

Table 2: Ring-opening reaction of epoxy compounds using ODA-hydrophobized PTA-Pd catalyst [ODA-PTA-Pd]

Substrates		Entry	Conversion	Selectivity		Time	TOF (h^{-1})
				Product 1	Product 2		
Epichlohydrin (2 mM)	Acetic acid (2 mM)	Recycle-0	82.5%	90.2%	9.8%	6 h	144
		Recycle-1	81.7%	91.5%	8.5%		143
		Recycle-2	80.5%	90.7%	9.3%		142
		Recycle-3	80.2%	90.3%	9.7%		141
Epichlohydrin (2 mM)	Benzoic acid (2 mM)		92.9%	92.8%	6.5%	10 h	20
Styrene oxide (2 mM)	Acetic acid (2 mM)		88.8%	97.6%	0.9%	6 h	31

Table 3: Acylation reaction of phenol using ODA-hydrophobized PTA-Pd catalyst [ODA-PTA-Pd]

Substrates		Conversion	Selectivity	Time	TOF
Phenol (10mM)	Acetic anhydride (11mM)	55.8%	100%	2 h	293 h^{-1}

In the ring opening reaction of epichlorohydrine with acetic acid and benzoic acid, the conversions were 82.5% with TOF 144 h^{-1} and 92.9% with TOF 20 h^{-1} respectively and the conversion of ring opening reaction of styrene oxide with acetic acid was 88.8% with TOF 31 h^{-1} (Table 2). The catalyst [ODA-PTA-Pd] was efficiently recycled three times for the ring opening reaction of epichlorohydrine with acetic acid, the results of which are shown in Table 2. From this table, it is clearly seen that there is no detectable change in the activity of this catalyst even after three recycles. In the cylation reaction of phenol with Ac_2O, the conversion was 55.8 % with a TOF 293 h^{-1} (see Table 3). From the above results, it is confirmed that the [ODA-PTA-Pd] catalyst is also effective as an acid catalyst due to presence of Keggin ions on the surface of Pd nanoparticles with excellent recycle characteristics.

4.5 Summary

In this chapter, it has been shown that phase pure metal core-shell nanoparticles can be synthesized using Keggin ions as UV-switchable reducing agent. The immobilization of a reducing agent on the surface of the core metal when exposed to the second metal ions would selectively reduce them on the surface thereby leading to phase-pure core-shell structures. In this chapter it has been described that surface bound Keggin ions on the Au core nanoparticles could be activated for reduction of 2^{nd} metal ions such as Ag^{+}, Pt^{4+}, Pd^{2+} ions selectively on the surface of the core-gold particles as a highly localized reducing agent excluding the possibility of nucleation of fresh Pd and Pt nanoparticles in solution and results the formation of desired phase pure core-shell nanoparticles. The reducing capability of the Keggin ions can be switched on using UV irradiation is an additional feature that enhances the versatility of the technique. Core-shell nanoparticles are very important as catalysts. Keggin ions capped stable Pd nanoparticles have been synthesized by reduction of aqueous $Pd(NO_3)_2$ by photoexcited Keggin ions (phosphotungstate anions). The Keggin ion-capped Pd nanoparticles have been phase-transferred into non-polar organic solvetnts such as toluene by electrostatic complexation with cationic surfactants such as octadecylamine at the liquid-liquid interface. This results in a new class of catalyst wherein both the Pd core and Keggin ion shell may be used in a range of catalytic reactions leading to a truly multifunctional catalyst dispersible in organic solvents. Therefore by this protocol it is possible to realize a large combination of core-shell

nanostructures using Keggin ions with potential application in engineered nanomaterials and catalysis.

4.6 References

[1] Alivisatos, A. P. *Science*, **1996**, *271*, 933.

[2] Toshima, N.; Yonezawa, T. *New J. Chem*., **1998**, 1179.

[3] (a) Kamat, P. V. *Chem. Rev*., **1993**, *93*, 267. (b) Lewis, L. N. *Chem. Rev*., **1993**, *93*, 693. (c) Gates, B. C. *Chem. Rev*., **1995**, *95*, 511.

[4] (a) Hoffman, A. J.; Mils, G.; Yee H.; Hoffman, M. R. *J. Phys. Chem*., **1995**, *99*, 4414. (b) Lee, A. F.; Baddeley, C. J.; Hardacre, C.; Ormerod, R. M.; Lambert, R. M.; Schmid G.; West, H. *J Phys. Chem.*, **1995**, *99*, 6096.

[5] (a) Toshima, N.; Yonezawa T.; Kushihashi, K. *J. Chem. Soc.,Faraday Trans*., **1993**, *89*, 2537. (b) Toshima, N.; Harada, M.; Yamazaki Y.; Asakura,. K. *J. Phys. Chem*., **1992**, *96*, 9927. (c) Wang Y.; Toshima, N. *J. Phys. Chem. B*, **1997**, *101*, 5301.

[6] (a) Han, S. W.; Kim Y.; Kim, K. *J. Colloid Interface Sci*. **1998**, *208*, 272. (b) Link, S.; Wang Z. L.; El-Sayed, M. A. *J. Phys. Chem. B*, **1999**, *103*, 3529.

[7] Damle, C.; Kumar A.; Sastry, M. *J. Phys. Chem. B*, **2002,** *106*, 297.

[8] Torigoe, K.; Nakajima, Y.; Esumi, K. *J. Phys. Chem.*, **1993**, *97*, 8304.

[9] (a) Liz-marzan L. M.; Philipse, A. P. *J. Phys. Chem.*, **1995**, *99*, 15120. (b) Damle, C.; Biswas K.; Sastry, M. *Langmuir*, **2001**, *17*, 7156.

[10] (a) Toshima, N.; Harada, M.; Yamazaki Y.; Asakura, K. *J. Phys.Chem*., **1992**, *96*, 9927. (b) Mizukoshi, Y.; Yamamoto, T.; Nagata, Y.; Okitsu K.; Maeda, Y. *J. Phys. Chem. B*., **1997,***101*,7033.

[11] (a) Toshima N.; Wang, Y. *Langmuir*, **1994**, *10*, 4574. (b) Yonezawa T.; Toshima, N. *J. Mol. Catal.*, **1993**, *83*, 167. (c) Harada, M.; Asakura, K.; Ueki, Y.; Toshima, N. *J. Phys. Chem.*, **1993**, *97*, 10742. (d) Liu, H.; Mao G.; Meng, M. *J. Mol. Catal.*, **1992**, *74*, 275.

[12] Mallin M. P.; Murphy, C. J. *Nano Lett.*, **2002**, *2*, 1235.

[13] Silvert, P. -Y.; Vijayakrishnan,V.; Vibert, P.; Herrera-Urbina R.; Elhsissen, K. T. *Nanostruct. Mater*., **1996**, *7*, 611.

[14] Esumi, K.; Shiratori, M.; Ishizuka, H.; Tano, T.; Torigoe K.; Meguro, K. *Langmuir*, **1991**, *7*, 457.

[15] Esumi. K.; Tano, T.; Torigoe K.; Meguro, K. *Chem. Mater*., **1990**, *2*, 564.

[16] Remita, S.; Mostafavi M.; Delcourt, M. O. *Radiat. Phys. Chem.*, **1996**, *47*, 275.

[17] (a) Bradley, J. S.; Hill, E. W.; Klein, C.; Chaudret B.; Duteil, A. *Chem. Mater.*, **1993**, *5*, 254. (b) Pan, C.; Dassenoy, F.; Casanove, M. J.; Philippot, K.; Amiens, C.; Lecante, P.; Mosset A.; Chaudret, B. *J. Phys. Chem. B*, **1999**, *103*, 10098.

[18] (a) Reetz, M. T.; Helbig W.; Quaiser, S. A. *Chem. Mater.*,**1995**, *7*, 2227; (b) Reetz M. T.; Quaiser,. S. A *Angew. Chem., Int. Ed.Engl.*, **1995**, *34*, 2240.

[19] Schmid, G.; Lehnert, A.; Malm J.-O.; Bovin, J.-O. *Angw. Chem.,Int. Ed. Engl.*, **1991**,*30*, 874.

[20] Teng, X.; Black, D.; Watkins, N.J.; Gao Y.; Yang, H. *Nano Letters*, **2003**, *3*, 261.

[21] Ah, C. S.; Hong S. D.; Jang, D.-J. *J. Phys. Chem. B*, **2001**, *105*, 7871.

[22] Srnova-Sloufova, I.; Lednicky, F.; Gemperle A. J. Gemperlova, *Langmuir*, **2000**, *16*, 9928.

[23] Mandal, S.; PR. Selvakannan.; Pasricha, R.; Sastry, M. *J. Am. Chem. Soc*.**2003**, *125*, 8440.

[24] PR. Selvakannan.; Swami, A.; Srisathiyanarayanan, D.; Shirude, P.S.; Pasricha, R.; Mandale, A.B.; Sastry, M. *Langmuir*, **2004**, *20*, 7825.

[25] Papaconstantinou, E. *Chem. Soc. Rev.*, **1989**, *18*, 1.

[26] Troupis,A.; Hiskia A.; Papaconstantinou, E. *Angew. Chem., Int. Ed.*, **2002**, *41*, 1911.

[27] Rahim, E. H.; Kamounah, F. S.; Frederiksen, J.; Christensen, J. B. *Nano Letters*, **2001**, *1*,499.

[28] Kozhevnikov, I. V. *Russ. Chem. Rev.*, **1987**, *56*, 811.

[29] Watzky, M. A.; Finke, R. G. *Chem. Mater.* **1997**, *9*, 3083.

[30] (a) Henglein, A. *J.Phys.Chem.* **1993**, *97*,5457. (b) Sastry, M.; Bandyopadhyay, K.; Mayya, K.S. *Coll.Surf.A.* **1997,***127*, 221.

[31] Perez-Maqueda, L. A.; Matijevic, E. *Chem. Mater.* **1998**, *10*, 1430.

[32] Shirley, D. A. *Phys. Rev. B*, **1972**, *5*, 4709.

[33] Kumar, A;. Mandal, S.; Selvakannan, PR.; Pasricha, R.; Mandale A. B.; Sastry, M. *Langmuir*, **2003,** *19*, 6277.

[34] Lu, W.; Wang, B.; Wang, K.; Wang X.; Hou, J. G. Langmuir, 2003, 19, 5887.

[35] *Practical Handbook of Spectroscopy* edited by J. W. Robinson, *CRC Press*, **1991**, p.364.

[36] Medina, A.; Solis, J.L.; Rodriguez J.; Estrada, W. *Solar Energy Materials & Solar Cells*, **2003**, *80*, 473.

[37] (a) Yonezawa, T.; Imamura, K.; Kimizuka, N. *Langmuir*, **2001,** *17*, 4701 (b) Liu, J.; Alvarez, J.; Ong, W.; Roma´n, E.; Kaifer, A. E. *Langmuir* **2001,** *17,* 6762.

[38] Kim, S-W.; Park, J.; Jang, Y.; Chung, Y.; Hwang, S.; Hyeon T.; Kim, Y. W. Nano Letters 2003, 3,1289.

[39] Tamura M.; Fujihara, H. J. Am. Chem. Soc. 2003 ,125, 15743.

[40] Quiros, I.; Yamada, M.; Kubo, K.; Mizutani, J.; Kurihara, M.; Nishihara, H. *Langmuir* **2002,** *18*, 1413.

[41] Sastry, M.; Kumar, A.; Mukherjee, P. *Colloids Surf., A* **2001**, *181*, 255. (b) Kumar, A.; Mandal, S.; PR. Selvakannan, Pasricha, R.; Mandale, A. B.; Sastry, M. *Langmuir* **2003,** *19*, 6277. (c) Kumar, A.; Joshi, H.; Pasricha, R.; Sastry, M. *J. Colloid Interface Sci.* **2003,** *264*, 396. (d) Kumar, A.; Joshi, H.; Mandale, A. B.; Srivastava, R.; Adyanthaya, S.D.; Pasricha, R.; Sastry, M. *J. Chem. Sci.* **2004,** *116*, 293.

[42] Li, Y.; Hong, X. M.; Collard D. M.; El-Sayed, M. A. *Organic Letters*, **2000**, *2*, 2385.

[43] Koliadima, A.; Pe´rez-Maqueda, L. A.; Matijevic, E. *Langmuir*, **1997,** *13,* 3733.

[44] Rahim, E. H.; Kamounah, F. S.; Frederiksen, J.; Christensen, J. B. *Nano Letters*, **2001**, *1*,499.

[45] Gopidas, K. R.; Whitesell, J. K.; Fox, M. A. *Nano Letters*, **2003**, *3*,1757.

Chapter 5

Synthesis and assembly of metal and semiconductor nanoparticles using Keggin ions as a new class of inorganic scaffolds

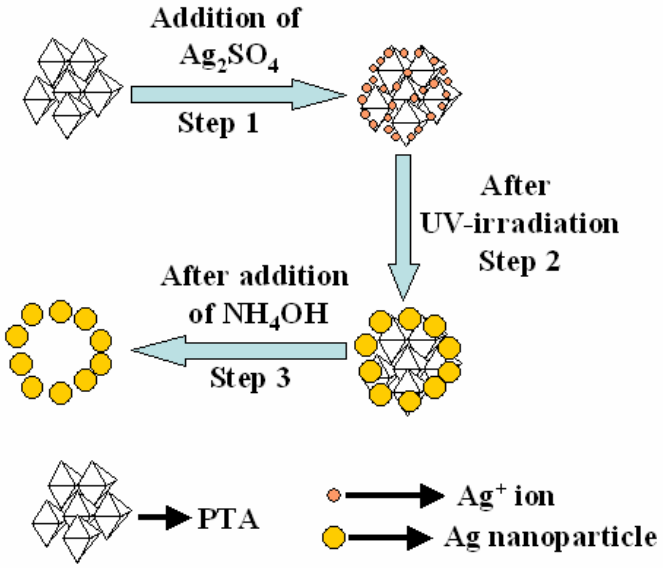

In this chapter it demonstrated that metal-Keggin ion colloidal particles are excellent templates for the synthesis of organized assemblies of metal/semiconductor nanoparticles, wherein the Keggin ion host plays the role of a UV-switchable reducing agent for synthesis of metal nanoparticles. Keggin ions may be used as a new class of inorganic scaffolds in the synthesis of metal and semiconductor nanoparticles assemblies. Treatment with alkali results in dissolution of the Keggin template leaving behind the metal/semiconductor nanoparticles network reasonably intact.

Part of the work presented in this chapter has been published in: (1) Mandal, S.; Rautaray, D.; Sastry. M. *J.Mater.Chem*. **2003**, *13*, 3002.; (2) Mandal, S.; Rautaray, D.; Sanyal, A.; Sastry, M. *J.Phys.Chem.B*. **2004**, *108*, 7126.

5.1. Introduction.

The organization of nanoparticles into two- and three-dimensional (2D/3D) architectures is a potential route to construct electronic and optical devices [1]. Much effort has been exerted in exploring the strategies to organize nanoparticles into ordered assembly. While the unusual properties of individual (non-interacting) nanoparticles are well understood, however in many situations it will be desirable to assemble the nanoparticles either in solution or on suitable substrates to facilitate communication to each other. In more scientific terms, tuning the *collective properties* of nanoparticle ensembles is also an important aspect of nanotechnology [2]. The ultimate goal, insofar as the growth of nanoparticle superstructures is concerned, is the realization of crystalization of nanoparticles wherein both the size of the nanoparticles and the inter-particle separation may be tailored at will and thus, enable one to tune the collective properties of the ensemble. For example, stringing together metal nanoparticles into linear superstructures with a view to use them as wave-guides for electromagnetic energy transport is a recent exciting concept with obvious application potential [3]. The growth of ordered two-dimensional (2D) and three-dimensional (3D) structures assembled from nanoparticles have stimulated intense interest due to their potential use in advanced technologies [4-6] such as photonics and plasmonics. The different techniques for the assembly of inorganic nanoparticles into materials with higher order architecture are collectively termed nanotectonics. These include shape-directed assembly [7] and programmed assembly [8] of nanoparticles comprising surface attached molecules, ligands, and recognition sites, as well as the formation of complex hybrid nanostructures by in-situ transformation of unstable nanoparticle-based precursors [6]. Several approaches have been developed to position nanoparticles precisely in both two- [9,10] and three-dimensional arrays [11-13]. To date, these 2D and 3D architectures have been constructed through covalent or non-covalent interconnect strategies and people have used different templates to assemble the nanoparticles through covalent or non-covalent interaction [14,15]. The template directed assembly includes the use of nanoparticles, which are spatially confined within organized interiors such as tobacco mosaic virus (TMV) [16], DNA oligonucleotides [8,17], carbon nanotubes [18,19], colloidal crystals [20] coated polymer beads [21] and bacterial membranes [22]. Synthesis of hierarchical ordered inorganic framework materials using different templates is of great importance because of their applications in catalysis [23] separation techniques [24] and

materials chemistry. Over the last decade researchers have also used organic compounds as templates for the generation of inorganic structures and materials [25,26]. There is considerable current interest in the production of inorganic framework materials containing well-defined pore networks such as microporous [27] and mesoporous materials [28]. In addition to organic templates, inorganic templates can also be used in the formation of inorganic materials [29-31]. The process of transcription can be divided into several steps: first, an organic and inorganic template which consists of either preformed or self-assembled entities is brought into contact with an inorganic precursor or small particles of the actual inorganic material that will be formed. Deposition of the inorganic material on the inner or outer surface of the template will then result in the formation of an organic–inorganic or different inorganic hybrid material. The organic or inorganic template material can be removed by heat treatment [32], microwave irradiation [33], washing with organic solvents [34], calcinations [35] or by simple dissolution of the core particles [36], which finally results in the formation of an inorganic material possessing a morphology directly related to the organic or inorganic template. Matijevic and co-workers have shown that salts of Keggin ions with caesium [37] and thorium and zirconium [38] cations can form uniform micron-sized colloidal particles in aqueous medium. Polyoxometalates (POM) are one of the most widely used inorganic components in the design of hybrid materials due to their potential application in catalysis, sorption, magnetism, and photochemistry. Keggin ions form a subset of polyoxometalates and have the general formula $(XM_{12}O_{40})^{(8-n)-}$, where 'M' stands for W or Mo and 'X' stands for heteroatoms such as P, Si, Ge with n being the valency of X [39]. The Keggin ions, accompanying cations and other components such as water are arranged in a well-defined secondary three-dimensional structure, the stability of which depends on the nature of counterions, amount of water, etc [40]. In this chapter it is shown that metal-Keggin ion colloidal particles are excellent templates for the synthesis of organized assemblies of metal/semiconductor nanoparticles, wherein the Keggin ion host plays the role of a UV-switchable reducing agent for synthesis of metal nanoparticles. Keggin ions may be used as a new class of inorganic scaffolds in the synthesis of metal and semiconductor nanoparticle assemblies. Treatment with alkali results in dissolution of the Keggin template leaving behind the metal/semiconductor nanoparticle network reasonably intact.

5.2 Synthesis and assembly of silver nanoparticle using Ag^+-Keggin ion colloidal particles as novel templates.

This section describes the use of Ag^+-Keggin ion colloidal particles as excellent templates for the synthesis of organized assemblies of silver nanoparticles wherein the Keggin ion host plays the role of a UV-switchable reducing agent. As mentioned in the section *4.1* of the earlier chapter, photo-reduced Keggin ions can act as reducing agents for metal ions and thus we have used this property of Keggin ions to synthesize in-situ silver nanoparticles assembled on the Ag^+-Keggin colloidal templates. The entire process is illustrated in the schematic shown in Fig.5.1.

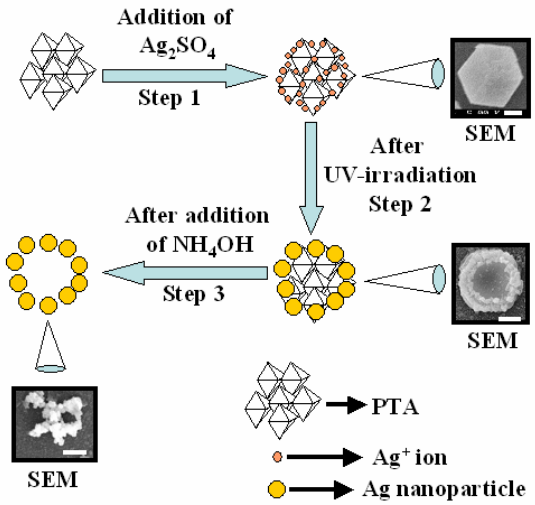

Figure 5.1: Scheme illustrating the various steps involved in the phosphotungstate ion-templated synthesis of silver nanoparticles (see text for details).

In Fig 5.1 it is shown that crystalline, micron size colloidal particles of Ag^+ ions complexed with phosphotungstate Keggin ions [$(PW_{12}O_{40})^{3-}$, PTA; step 1] may be used as templates for the in-situ synthesis of silver nanoparticles. UV-irradiation of the colloidal particles results in photochemical reduction of the PTA anions and thereafter, electron transfer to the Ag^+ ions from the electron rich PTA ions and the consequent formation of silver nanoparticles (step 2, Fig.5.1). The crystalline PTA matrix thus acts as a UV-switchable reducing agent in the generation of metal nanoparticles within an open, inorganic framework. We have observed the assembly of the silver nanoparticles into interesting superstructures on the surface of the colloidal particles, possibly due to facile diffusion of the metal atoms within the channels of the

open-framework Keggin particle. The Keggin ion template may be removed by simple dissolution in an alkaline medium leaving behind reasonably intact silver nanoparticle superstructures (step 3, Fig.5.1).

5.2.1 UV-vis. Spectroscopy measurements:

10 ml of 10^{-3} M aqueous deaerated solution of phosphotungstic acid [PTA, $H_3(PW_{12}O_{40})$, obtained from Aldrich and used as-received] was taken in a test tube along with 30 ml of 10^{-3} M aqueous deaerated solution of Ag_2SO_4 and 2 ml of propan-2-ol. This mixture was irradiated by UV light (pyrex filter, > 280 nm, 450 W Hanovia medium pressure lamp) for 4 h (Steps 1 & 2, Scheme in Fig.5.1). UV-irradiation leads to the *in-situ* reduction of Ag^+ ions by the electron rich $(PW_{12}O_{40})^{4-}$ ions (which are formed by the photochemical reduction of $(PW_{12}O_{40})^{3-}$ ions) and is clearly seen by the appearance of a brownish yellow color in the solution. 2 ml of 10 % NH_4OH was added to the UV-irradiated solution of Ag nano-PTA for dissolving the crystalline Keggin core template. UV-vis spectroscopy measurements of the Ag-PTA solution at different stages of treatment were carried out.

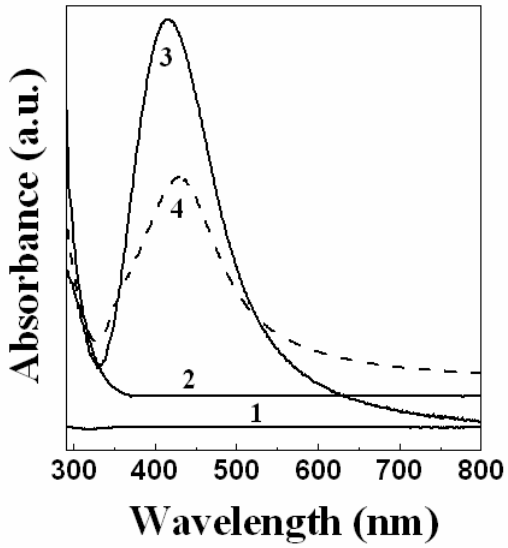

Figure 5.2: UV-vis spectra recorded from: curve 1 – aqueous mixture of 10^{-3} M phosphotungstic acid and $3x10^{-3}$ M Ag_2SO_4 before UV irradiation; curve 2 – UV-irradiated $3x10^{-3}$ M aqueous solution of Ag_2SO_4 in the absence of PTA; curve 3 – the solution shown as curve 1 after UV irradiation for 4 h; curve 4 – solution shown as curve 3 after addition of 10% NH_3 (aq) solution.

Fig.5.2 shows the UV-vis spectra of aqueous mixtures of 1 x 10^{-3} M phosphotungstic acid (PTA) and 3 x 10^{-3} M Ag_2SO_4 solution at different stages of treatment. Prior to UV-irradiation,

it is observed that there is little absorption in the visible region of the electromagnetic spectrum. The UV-vis absorption spectrum recorded after UV-irradiation of the 10^{-3} M PTA/3 x 10^{-3} M Ag_2SO_4 aqueous solution for 4 h is shown as curve 3 in Fig.5.2 (step 2, Fig.5.1).A prominent and sharp absorption band is observed to form at 430 nm. This absorption band is characteristic of silver nanoparticles and arises due to excitation of surface plasmon vibrations in the nanoparticles [41]. It is possible that the Ag^+ ions within the colloidal crystals are reduced by direct exposure to UV-irradiation and not due to electron transfer from photochemically excited PTA ions. In order to exclude this possibility, a control experiment was also performed wherein a 3 x 10^{-3} M aqueous solution of Ag_2SO_4 was irradiated by UV light for 4 h without PTA ions. The UV-vis absorption spectrum recorded from this solution is shown as curve 2 in Fig.5.2. There is no evidence of absorption in the 400-450 nm window clearly showing the silver nanoparticles are formed due to the reduced Keggin ions and not due to direct UV-reduction of the Ag^+ ions in the colloidal particles. The UV-vis spectrum of the Ag nano-PTA particles in solution after alkali treatment is shown as curve 4, Fig. 5.2 (step 3, Fig. 5.1). A slight broadening of the absorption band is observed with the absorption maximum remaining unchanged at 430 nm. Though the slight broadening of the surface plasmon absorption band indicates some degree of aggregation of the silver nanoparticles consequent to removal of the PTA scaffold, we did not observe any long-term instability in the solution over weeks of storage. In an alkaline medium, it is known that phosphotungstate ions dissociate into phosphate (PO_4^{3-}) and tungstate (WO_4^{2-}) ions [42]. It is therefore probable that such phosphate and tungstate ions bind to the silver nanoparticles and stabilize them against aggregation.

5.2.2 Scanning electron microscopy (SEM) and energy dispersive analysis of X-rays (EDX) measurements:

Samples for scanning electron microscopy (SEM) and energy dispersive analysis of X-rays (EDX) measurements were prepared by drop-coating films on Si (111) wafers from the Ag-PTA solutions at different stages of treatment. EDX spectra were recorded in the spot-profile mode by focusing the electron beam onto specific regions of the film.

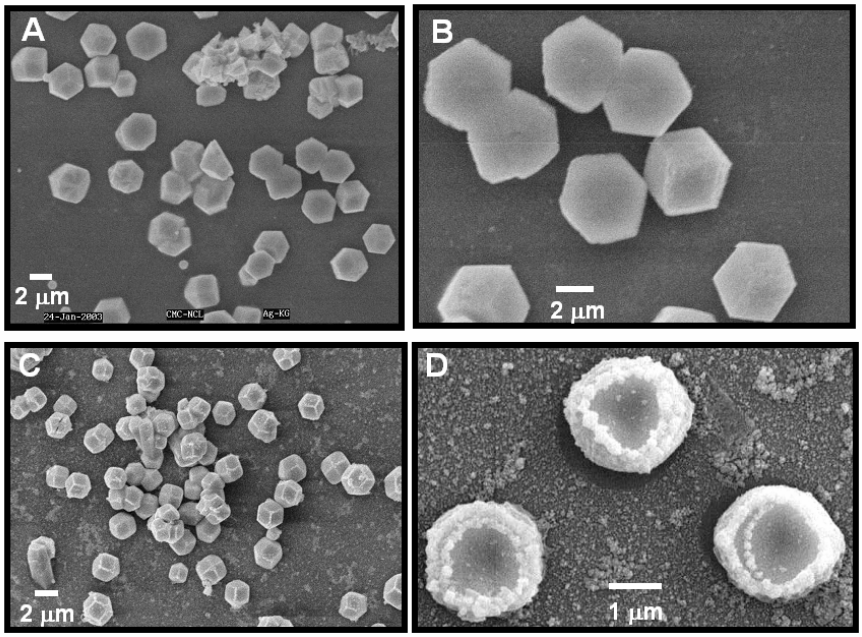

Figure 5.3: (A) and (B) - Low and high magnification SEM images of PTA–Ag^+ ion solution before UV-irradiation, respectively. (C) and (D) - Low and high magnification SEM images of PTA–Ag^+ solution after UV-irradiation, respectively.

Figs.5.3 A and B show representative scanning electron microscopy (SEM) images recorded at different magnifications from a drop-coated film of the aqueous mixture of PTA and silver sulfate on a Si (111) substrate. Densely populated colloidal particles of the Ag^+-PTA complex are seen on the surface of the substrate. The particles are extremely uniform in size (average size ~ 2.3 μm) and exhibit well-defined morphology that appears to be predominantly rhombohedral (Fig.5.3B). Representative SEM pictures recorded from drop-coated films of this UV-irradiated solution on a Si (111) wafer are shown in Figs.5.3 C and D at different magnifications. Comparison of the low magnification images recorded before (Fig.5.3A) and after UV-irradiation indicates an interesting increase in contrast of the edges of the nanoparticles relative to the rest of the particle surface after UV-irradiation. This is much more clearly seen in the higher magnification SEM image of some of the particles (Fig.5.3D) where the presence of spherical silver nanoparticles arranged along the edges in a quasi-circular fashion is observed. The silver particles range in size from 80 nm to 150 nm and are thus, not monodisperse. The silver nanoparticles formed by electron transfer from the UV-irradiated Keggin ions to the Ag^+ ions are preferentially assembled at the edges of the colloidal crystals.

Thus, the high-energy edge regions of the colloidal particles play a crucial role in assembling the in-situ formed silver nanoparticles. A detailed chemical analysis of the surface of the colloidal particles after formation of silver nanoparticles as described above was done using spot-profile energy dispersive analysis of X-rays (EDAX). Fig.5.4A shows an enlarged SEM image of one of the colloidal particles decorated with silver nanoparticles and spot-profile EDAX spectra from specific regions of the particle surface (Figs.5.4 B and C). The bright regions populated by the particles is clearly rich in silver (Fig.5.4A) while away from the particle edge, the silver signal is relatively weak and is accompanied by a strong W signal. This result clearly shows that the silver particles are formed at the edges of the colloidal particle and is accompanied by depletion from other regions of the particle. We believe that this occurs by diffusion of the silver atoms to the surface via channels in the open Keggin structure framework and aggregation at the edges leading to the characteristic assembly of the silver nanoparticles observed.

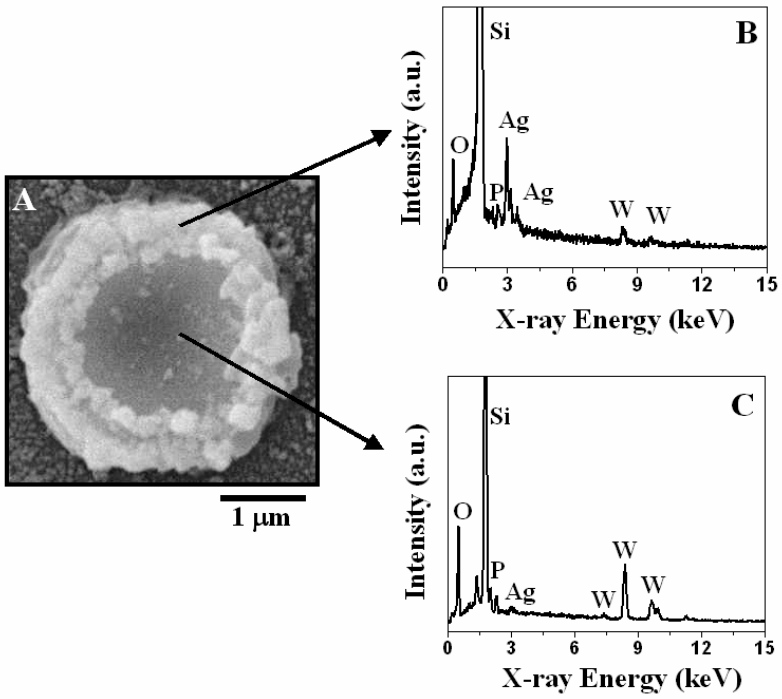

Figure 5.4: (A) SEM image of a colloidal particle in a drop-coated film on a Si(111) substrate from PTA–Ag^{+} solution after UV-irradiation. The accompanying EDX profiles (B and C) have been recorded from the regions indicated by arrows in the SEM picture.

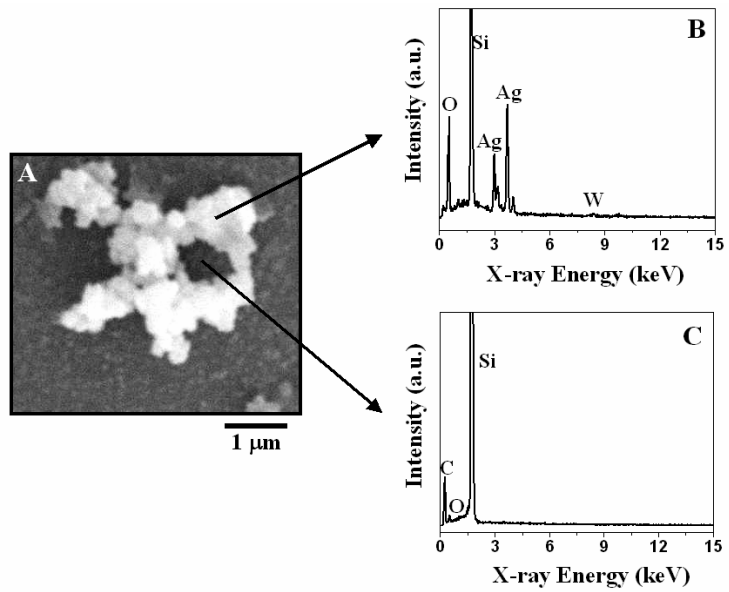

Figure 5.5: (A) SEM image of a drop-coated film on a Si(111) substrate from a UV-irradiated PTA–Ag^{+} solution after alkali treatment. The accompanying EDX profiles (B and C) have been recorded from the regions indicated by arrows in the SEM picture.

Fig. 5.5A shows a high magnification scanning electron microscopy image recorded from a drop-coated film of the silver nanoparticle structures after alkali treatment of UV-irradiated Ag nano-PTA solution. The image clearly shows that the Keggin colloidal particle scaffold has dissolved leaving behind the silver nanoparticle assembly reasonably intact. The removal of the Keggin scaffold is clearly shown in the spot profile EDX analysis of the gap region (Fig. 5.5C) – there is no evidence of either Ag or tungsten and only peaks characteristic of the Si substrate are observed. It is interesting to note that there is very little spillover of the silver nanoparticles into the core of the template indicating a high degree of fidelity to the PTA template for assembling the inorganic materials. The EDX spectrum from the bright regions populated by the particles (Fig. 5.5B) shows that it is composed primarily of silver and a small percentage of tungsten and phosphorus. Removal of the PTA scaffold does lead to some aggregation of the smaller silver nanoparticles and would thus explain the broadening of UV-vis spectrum observed after alkali dissolution of the Keggin scaffold (Fig. 5.2, curve 4). The presence of W and P signals, thus clearly indicates the presence of the tungstate (WO_4^{2-}) and phosphate (PO_4^{3-}) decomposition products on the surface of the silver nanoparticles, which stabilize the smaller silver nanoparticles in the aggregated structures. The surface capping also

prevents uncontrolled aggregation of the silver nanoparticle super-assemblies in solution and would explain the long-term stability of the alkali-treated Ag nano- PTA solutions.

5.2.3 X-ray diffraction (XRD) measurements:

X-Ray diffraction (XRD) analysis of drop-coated films of the Ag– PTA solution at different stages of chemical treatment on glass substrates were carried out as described in earlier section *2.4.2*. The XRD pattern recorded from a drop-coated film of the UV-irradiated sample on a glass substrate is shown as curve 2 in Fig. 5.6A. The Bragg reflections corresponding to the Keggin structure are intact indicating that the formation of silver nanoparticles on the Keggin colloidal particle template does not disrupt the Keggin structure. The Fig. 5.6B shows the XRD pattern obtained from the Ag^{+}–PTA colloidal particles after UV-irradiation (curve 1) in the region of the principal Bragg reflections of silver. The (111) and (200) Bragg reflections of fcc silver are clearly observed along with some of the peaks of the Keggin structure. Relative to the Keggin ion Bragg reflections, the silver peaks are broad indicating that the silver particles are quite small.

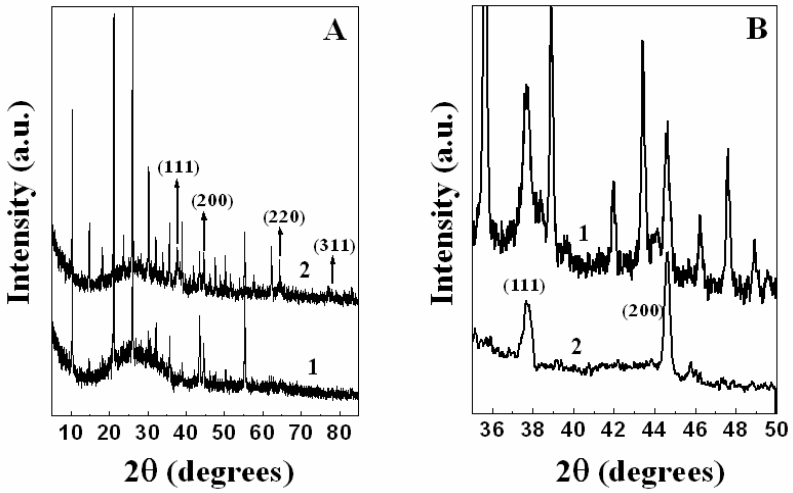

Figure 5.6: (A) XRD patterns recorded from drop-coated films on glass substrates of the PTA–Ag^{+} ion solution before (curve 1) and after UV irradiation (curve 2). (B) shows a magnified view of the XRD spectra of the UV-irradiated Ag nano-PTA solution before (curve 1) and after alkali treatment (curve 2).

It is possible that the 80–150 nm size silver nanoparticles observed in the SEM images are composed of smaller silver nanoparticles separated by Keggin ions. This is purely speculative

since we have not been able to image the individual silver nanoparticles in the assembly. The XRD pattern recorded from a drop-coated film of the Ag nano-PTA solution after alkali dissolution of the Keggin scaffold is shown in the Fig. 5.6B (curve 2). It is clear that the Bragg reflections of the Keggin scaffold have disappeared leaving behind just the Bragg reflections of the Ag nanoparticle assembly. The fact that the (200) Bragg reflection is more intense than the (111) reflection indicates oriented growth of the silver nanoparticles on the Keggin scaffold.

5.2.4 Transmission Electron Microscopy (TEM) measurements:

Samples for TEM analysis were prepared by drop-coating films of the Ag–PTA solution after treatment with alkali (NH_4OH) solution (step 3, Fig. 5.1) on carbon-coated copper TEM grids as described in section *2.6.2*.

Figure 5.7: TEM picture of the UV-irradiated PTA–Ag nanoparticle solution after alkali treatment.

An attempt was made to resolve the silver particles into smaller silver nanoparticles by TEM and a representative image of the silver nanoparticle assembly after alkali dissolution of the Keggin scaffold is shown in Fig. 5.7. As in the case of the SEM images, regular and well-defined pores are observed where the Keggin scaffold originally existed. The silver particles themselves are quite large and are possibly arranged in a three-dimensional fashion making it difficult to image possible smaller subunits in the transmission mode.

Thus silver nanoparticles can be synthesized and assembled also using crystalline Ag^{+}–Keggin ion colloidal particles as precursors and the Keggin ions play a multifunctional role, provide the crystalline framework to support the metal cations and also participate in the reduction of the metal ions without disruption to the well defined Keggin structure.

5. 3 Synthesis and assembly of CdS nanoparticles in Keggin ion colloidal particles as templates

In this section, the formation of rod like CdS nano-structures using Cd^{2+}-Keggin colloidal particles as a template has been described. In the first step, reaction of cadmium ions with phosphotungstate Keggin anions leads to the growth of highly dense and crystalline cadmium phosphotungstate colloidal particles with needlelike morphology of submicron dimensions. Further treatment of the crystalline cadmium phosphotungstate colloidal particles with H_2S gas leads to the in-situ growth of CdS nanoparticles without disruption to the host Keggin ion colloidal particle morphology. In the last step, alkali treatment results in dissolution of the PTA template, leaving behind fused CdS nanoparticles in the form of nanorods.

5.3.1 UV-vis. Spectroscopy measurements:

10 mL of 10^{-3} M aqueous solution of phosphotungstic acid [PTA, $H_3(PW_{12}O_{40})$, obtained from Aldrich and used as received] was taken in a test tube along with 10 mL of 10^{-3} M aqueous solution of $CdCl_2$. After 4 h of the mixing, H_2S gas was bubbled in the reaction mixture of $CdCl_2$ and phosphotungstic acid solutions for 15 min. During the bubbling of H_2S gas the solution turns yellow, which indicates the formation of CdS nanoparticles in the solution. 2 mL aliquot of 10% NH_4OH was added to the 10 mL of H_2S bubbled solution of CdS nano-PTA for dissolving the crystalline Keggin core template. UV-vis spectroscopy measurements of the CdS-PTA solution at different stages of treatment (after mixing of $CdCl_2$ with phosphotungstic acid solutions, after passing the H_2S gas into the reaction mixture and after dissolving the Keggin template by alkali treatment) were carried out.

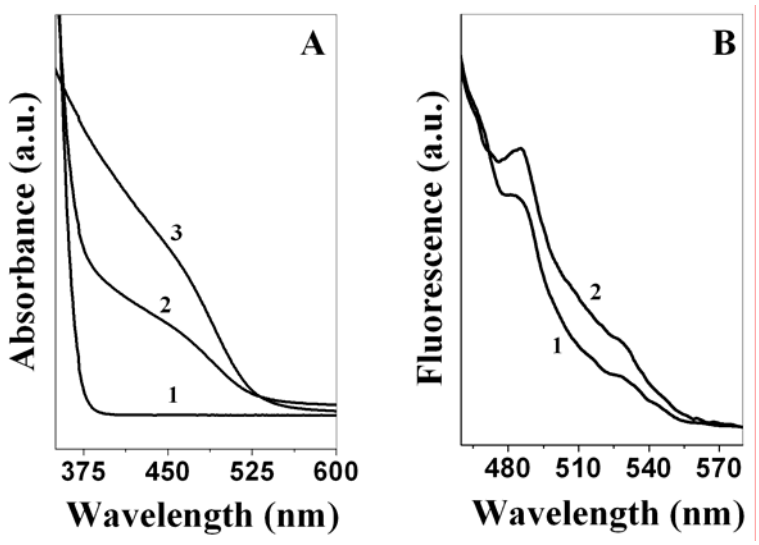

Figure 5.8: (A) UV-vis spectra recorded from Cd^{2+}-Keggin ion solution (curve 1); after treatment with H_2S gas of the Cd^{2+}-Keggin ion solution (curve 2); after treatment of CdS-PTA solution with alkali (curve 3). (B) shows the fluorescence emission spectra recorded from the CdS-PTA solution before (curve 1) and after (curve 2) alkali treatment.

Fig. 5.8A shows the UV-vis absorption spectra recorded from the solution of the CdS-PTA solution at different stages of treatment such as after mixing of $CdCl_2$ with phosphotungstic acid solutions (curve 1), after passing H_2S gas into the reaction mixture (curve 2), and after dissolving the Keggin template by alkali treatment (curve 3). Prior to H_2S treatment, it is observed that there is no absorption in the visible region of the electromagnetic spectrum (curve 1) from the Cd^{2+}-PTA solution. The UV-vis absorption spectra recorded from the CdS-PTA solution before and after alkali treatment are shown as curves 2 and 3, respectively, in Fig. 5.8 A. As mentioned before, reaction of the Cd^{2+}-PTA solution with H_2S resulted in the solution turning yellow, a feature characteristic of formation of CdS nanoparticles. In Fig. 5.8A the absorption is observed at 460 nm for the Cd^{2+}-PTA solution after hydrogen sulfide reaction and that was clearly missing in the solution before H_2S treatment (curve 1). This absorption band is characteristic of CdS nanoparticles and arises due to excitonic transitions in the nanoparticles [43]. From the absorption wavelength, the size of CdS nanoparticles synthesized within the Keggin colloidal particle scaffold was estimated to be roughly 5 nm using the equation obtained by Brus [44]. After alkali treatment to destroy the Keggin ion structure in the CdS nano-Keggin ion colloidal particles, it is observed that the CdS nanoparticles formed in the Keggin ion hosts are quite stable having an absorption at ca. 465 nm (curve 3 in Fig.5.8A).

Fig. 5.8B shows the fluorescence spectra recorded from the CdS-PTA solution before (curve 1) and after (curve 2) alkali treatment. In both samples, two emission bands centered at

485 and 530 nm are observed. The peak at 485 nm corresponds to the band gap or near band gap emission resulting from recombination of the electron-hole pairs in the CdS nanoparticles whereas the broader band at 530 nm is believed to originate from trapped charge carrier recombination due to surface defects. The UV-vis absorption and fluorescence spectroscopy measurements clearly indicate that removal of the Keggin ion host by alkali treatment does not alter the optical properties of the CdS nanoparticle hosts significantly.

5.3.3 Fourier Transform Infra-Red (FTIR) Spectroscopy measurements:

Samples for Fourier transform infrared (FTIR) spectroscopy measurements from the CdS-PTA solutions at different stages of treatment (as indicated above) were prepared by solution-casting films onto Si(111) wafers.

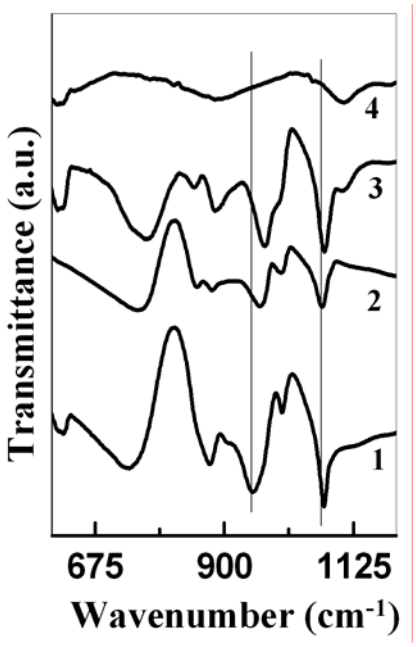

Figure 5.9: FTIR spectra recorded from the drop-coated film on Si (111) wafer of pure phosphotungstic acid (PTA) solution (curve1), Cd^{2+}-PTA complex (curve 2), Cd^{2+}- PTA solution after treatment with H_2S gas (curve 3) and CdS-PTA solution after alkali treatment (curve 4).

Fig.5.9 represents the FTIR spectra in the region 600-1200 cm^{-1} for the pure phosphotungstic acid (curve 1) and CdS-PTA solution at different stages of treatment such as after mixing of $CdCl_2$ with phosphotungstic acid solutions (curve 2), after passing H_2S gas into the reaction mixture (curve 3), and after dissolving the Keggin template by alkali treatment (curve 4). Curve 1 shows the W-O asymmetric stretching vibration frequency at 946 cm^{-1} and the P-O

asymmetric stretching vibration at 1076 cm^{-1} for pure phosphotungstic acid, and curves 2 and 3 show a shifted W-O bond stretching vibration at 960 and 970 cm^{-1}, respectively, indicating salt formation of phosphotungstic acid [45-47] with Cd^{2+} ions. Curve 4 in Fig.5.9 shows the FTIR spectrum recorded from the CdS-PTA solution after alkali treatment. In this spectrum, it is observed that the W-O and P-O stretching vibration bands are absent, suggesting that the PTA template has completely decomposed upon alkali treatment.

5.3.4 Isothermal Titration Calorimetric (ITC) & Conductance measurements:

It is important to study the strength and nature of the interaction between the Cd^{2+} ions and phosphotungstate anions and therefore isothermal titration calorimetric (ITC) and conductance measurements of mixing of cadmium chloride and phosphotungstic acid solutions have been carried out. Isothermal titration calorimetric (ITC) measurements were carried out to characterize the interaction between Cd^{2+} ions and phosphotungstic acid (PTA) in a MicroCal VP-ITC instrument at 300 K. The calorimeter consists of two cells: a reference cell filled with pure solvent (water) and a sample titration cell filled with 1.47 mL of 10^{-3} M aqueous phosphotungstic acid (PTA) solution. A $5x10^{-3}$ M aqueous $CdCl_2$ solution was added from the syringe into the titration cell containing the PTA solution in small steps of 10μL. The heat evolved/absorbed during reaction of Cd^{2+} ions with PTA anions was measured, the time between successive injections of Cd^{2+} ions being 2 min. Fig. 5.10A shows the raw data obtained during injection of 10μL of $5x10^{-3}$ M $CdCl_2$ solution into the titration cell containing 1.47 mL $1x10^{-3}$ M PTA. It is observed that during each injection cycle, exothermic reaction occurs, indicating strong binding of Cd^{2+} ions with the phosphotungstate anions present in the titration cell. During the initial injection cycles, the exothermic peak heights are roughly similar, indicating complete complexation between Cd^{2+} cations and phosphotungstate anions during these cycles. As the injections progress, the exothermicity of the peaks decreases because the available binding sites become depleted. Toward the end of the injection cycles, it is observed that little binding takes place and that Cd-phosphotungstate colloidal particles have already formed.

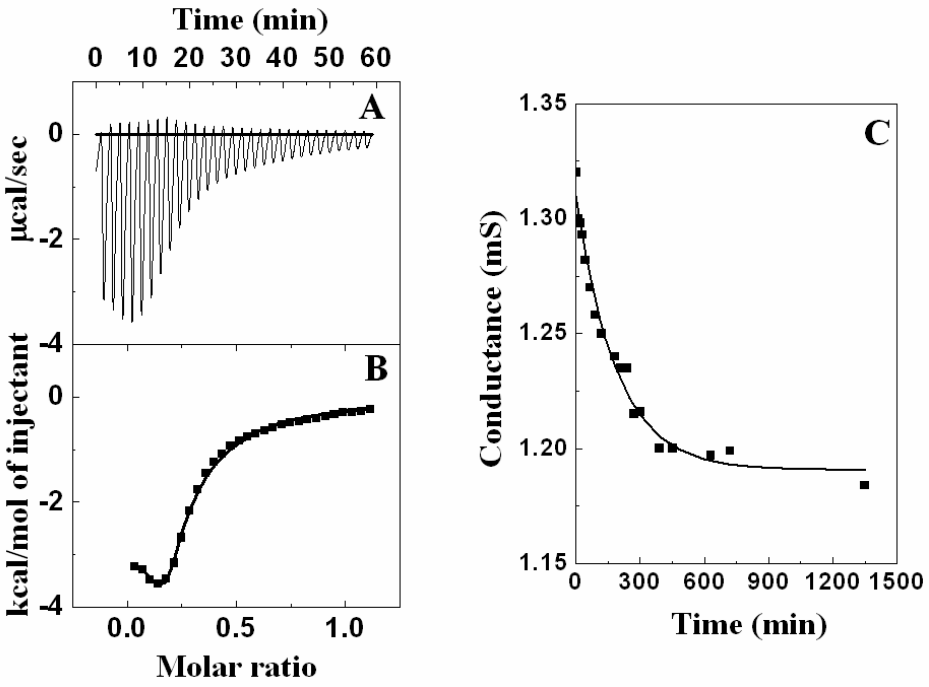

Figure 5.10: (A) ITC titration data obtained during injection of 10µL of $5x10^{-3}$ M $CdCl_2$ solution into the titration cell containing 1.47 mL of $1x10^{-3}$ M PTA. (B) Plot of binding isotherm obtained from the data shown in A during injection of 10µL of $5x10^{-3}$ M $CdCl_2$ solution into the titration cell containing 1.47 mL of $1x10^{-3}$ M PTA (see text for details). (C) Conductivity data recorded as a function of time of mixing of equal volumes of 10^{-3} M $CdCl_2$ and 10^{-3} M PTA aqueous solutions (see text for details).

Fig. 5.10B shows the binding isotherm where the total heat per injection (kilocalories per mole of Cd^{2+} ions injected) is plotted against the molar ratio of Cd^{2+} ions and PTA in the titration cell, this data having been analyzed using Origin (*Microcal*) software. The precise shape of the binding isotherm contains all of the information necessary to completely characterize the thermodynamics of the binding reaction. From the curve-fitting process of the binding isotherm, the stoichiometry (n), binding constant (K), heat of binding (ΔH), and entropy of binding (ΔS) can be estimated. By fitting the binding isotherm, the enthalpy change (ΔH= -3148 kcal/mol) and the binding constant (K= $1.604x10^5$ M^{-1}) were estimated with the assumption of a two-site binding model for the formation of Cd^{2+}-PTA complex. Thus, the formation of the Cd^{2+}-PTA complex is driven by a large negative enthalpy change and high value of binding constant (K), reflecting the strong interaction between Cd^{2+} and PTA ions.

The conductance of a mixture consisting of equal volumes of 10^{-3} M phosphotungstic acid and 10^{-3} M cadmium chloride solutions during the formation of Cd^{2+}-PTA complex was monitored using a picoconductivity meter (LabIndia). Fig.5.10C shows the conductivity

measured from a mixture consisting of equal volumes of 10^{-3} M $CdCl_2$ and 10^{-3} M PTA aqueous solutions as a function of time of reaction. From the conductivity measurements, it is clearly seen that the conductance decreases with time, which indicates the formation of Cd^{2+}-PTA colloidal particles in agreement with the ITC measurements presented above.

5.3.5 Scanning electron microscopy (SEM) and energy dispersive analysis of X-rays (EDX) measurements:

Samples for scanning electron microscopy (SEM), and energy dispersive analysis of X-rays (EDX) measurements from the CdS-PTA solutions at different stages of treatment (as indicated above) were prepared by solution-casting films onto Si(111) wafers. EDX spectra were recorded in the spot-profile mode by focusing the electron beam onto specific regions of the film.

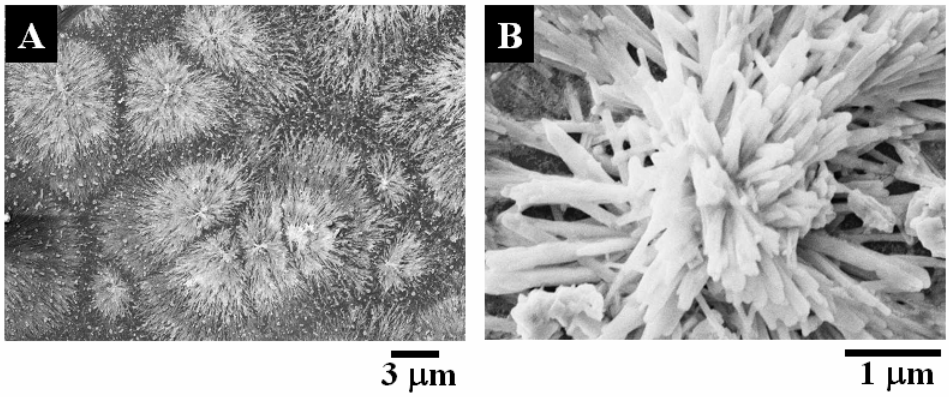

Figure 5.11: (A) and (B) Low and high magnification SEM images of drop-coated films from the Cd^{2+}- PTA colloidal solution on Si (111) wafer before H_2S treatment.

In Fig.5.11 A and B show representative SEM images recorded at different magnifications from a drop-coated film of the aqueous mixture of PTA and $CdCl_2$ on a Si(111) substrate after 4 h of reaction. Densely populated colloidal particles of the Cd^{2+}-PTA complex of predominantly needlelike morphology are observed, which are assembled into aggregates of quasi-circular superstructure. The needle-shaped colloidal particles are extremely uniform in size (lengths ranging from 1.3 to 2.4 μm and widths ranging from 78 to 125 nm) and were observed over the entire substrate surface. In earlier reports on the formation of colloidal particles of Keggin ions with metal cations, Matijevic et al. have shown that salts of Keggin ions with cesium [48] and thorium and zirconium [49] cations form uniform micron-sized

colloidal particles of mainly spherical morphology in an aqueous environment. To better understand the formation of quasi-circular superstructures of needlelike Cd^{2+}-Keggin ion colloidal particles, we have carried out time-dependent SEM analysis of the Cd^{2+}-PTA complex after mixing the solutions of $CdCl_2$ and PTA.

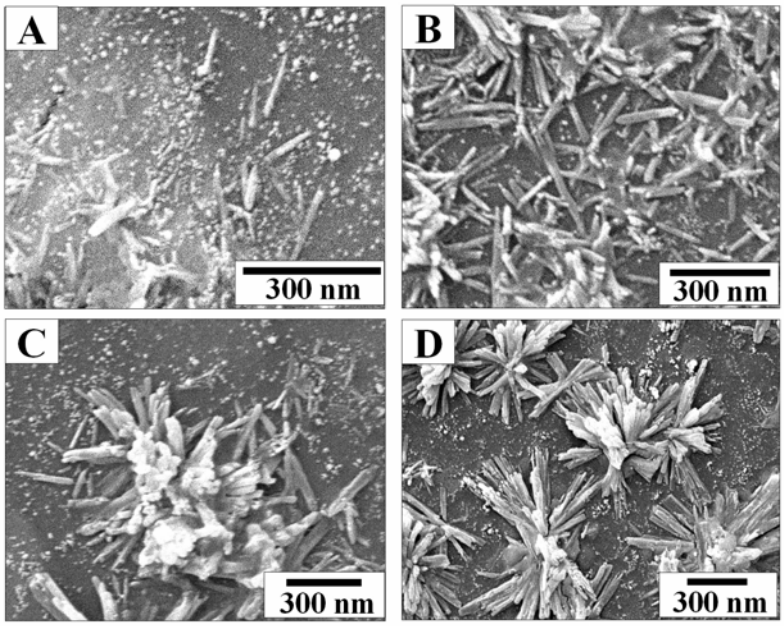

Figure 5.12: SEM images of drop-coated films from the Cd^{2+}-PTA solution at different times of reaction: (A) immediately after mixing of PTA with Cd^{2+} ions, (B) 1 h, (C) 2 h, and (D) 4 h after reaction (see text for details).

A-D of Fig.5.12 show representative SEM images recorded from drop-coated films on a Si(111) substrate of the aqueous mixture of PTA and $CdCl_2$ after 0 h (after immediately mixing), 1, 2, and 4 h of reaction, respectively. As the reaction time increases, it is observed that the density of needlelike Cd^{2+}-Keggin ion colloidal particles increases (Fig.5.12 A, B). After a critical concentration of the colloidal particles is achieved, hierarchical assembly of the needle-shaped structures into quasi-circular super assemblies is observed (Fig. 5.12 C, D; after ca. 2 h of reaction). Our observation that Cd^{2+} ions complexed with phosphotungstate anions leads to the formation of needle-shaped colloidal particles and the metal cation in directing the morphology of the Keggin ion colloidal particles has important implications in crystal engineering and nanocomposite synthesis.

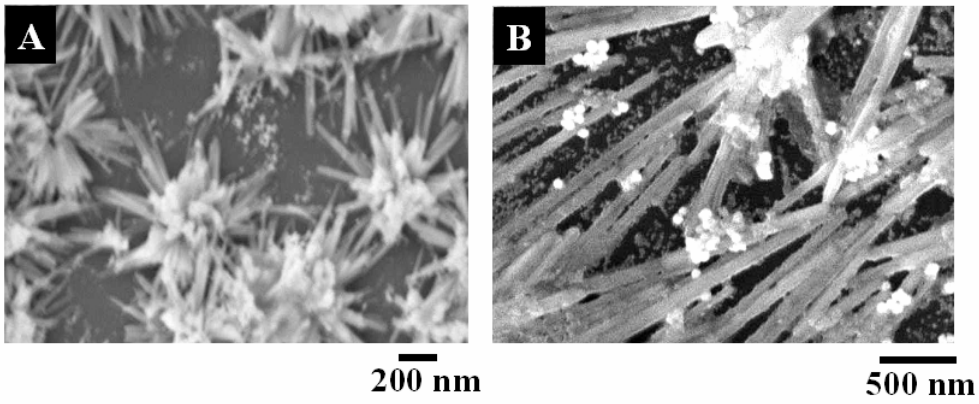

Figure 5.13: (A) and (B) show the low and high magnification SEM images of drop-coated films on Si (111) wafer from the Cd^{2+}-PTA solution after H_2S treatment.

SEM pictures recorded from drop-coated films of the Cd^{2+}-PTA solution after H_2S gas treatment on Si (111) substrates are shown in Fig. 5.13 A and B at different magnifications. Comparison of the images recorded before (Fig.5.11 A, B) and after (Fig. 5.13 A and B) H_2S gas treatment clearly shows that there is negligible change in the overall morphology of the Cd^{2+}- PTA colloidal particle template after reaction with H_2S. Thus, the Keggin ion colloidal scaffold is able to bear up the strain associated with the CdS nanoparticle formation.

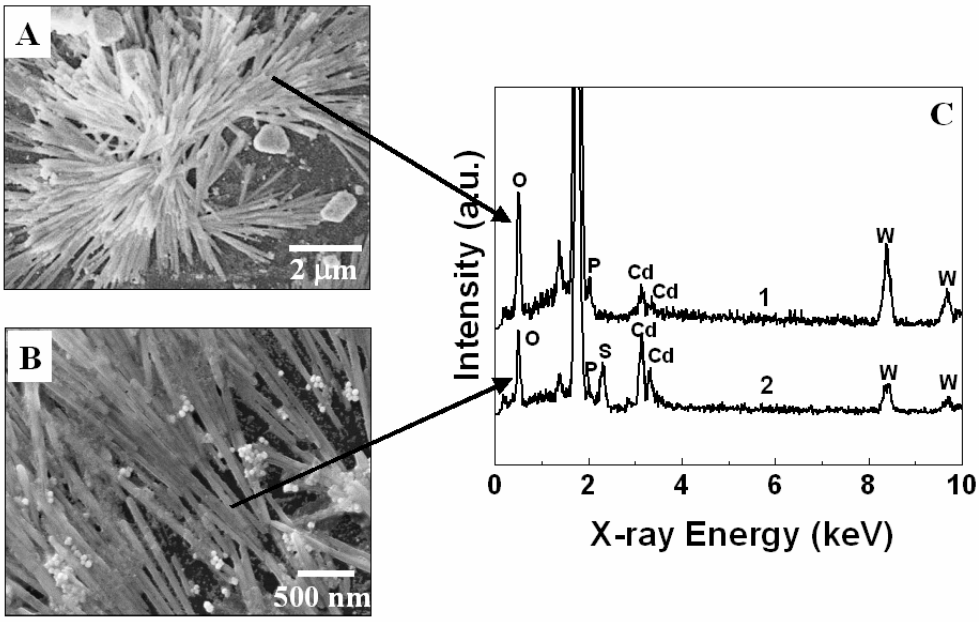

Figure 5.14: (A) SEM pictures of needle-shaped colloidal particles by drop-coating films of Cd^{2+}-PTA solution on a Si(111) substrate before H_2S gas treatment. (B) SEM picture of the drop-coated film on a Si(111) substrate after H_2S gas treatment. (C) The accompanying EDAX profiles (curves 1 and 2) have been recorded from the regions indicated by arrows in the SEM picture (see text for details).

Fig. 5.14A shows an additional SEM image of aggregates of the needle-shaped Cd^{2+}-PTA colloidal particles before H_2S gas treatment along with spot-profile EDX spectra from specific regions of the colloidal particle surface (curve 1, Fig. 5.14C). The presence of strong Cd, W, and P signals is clearly observed in the EDX spectrum, indicating complexation of cadmium ions with the Keggin anions in the colloidal particles. A quantitative analysis of the Cd and W EDX peaks after ZAF correction (inbuilt in the software of the instrument) yielded a 1: 7 atomic ratio for Cd:W in reasonable agreement with the expected stoichiometry of the chemical structure $Cd_3 (PW_{12}O_{40})_2$. Fig.5.14B shows an SEM image Cd^{2+}-PTA film after reaction with H_2S gas whereas curve 2 in Fig. 5.14C shows the spot-profile EDX spectrum from a representative region of the particle surface. In addition to the Cd, W, and P signals present in the as-prepared Cd^{2+}-PTA colloidal particles (curve 1), a strong S signal is seen in the H_2S gas exposed film (curve 2). A quantitative analysis of the Cd and S peaks yielded a 1:1.2 atomic ratio for Cd:S in reasonable agreement with the expected stoichiometry for cadmium sulfide.

5.3.6 X-ray diffraction (XRD) measurements:

Samples for X-ray diffraction (XRD) measurements from the CdS-PTA solutions at different stages of chemical treatment (as indicated above) were prepared by solution-casting films onto glass substrates. The X-ray diffraction pattern recorded from the drop-coated film of Cd^{2+}-Keggin ion solution is shown as curve 1 in Fig.5.15.

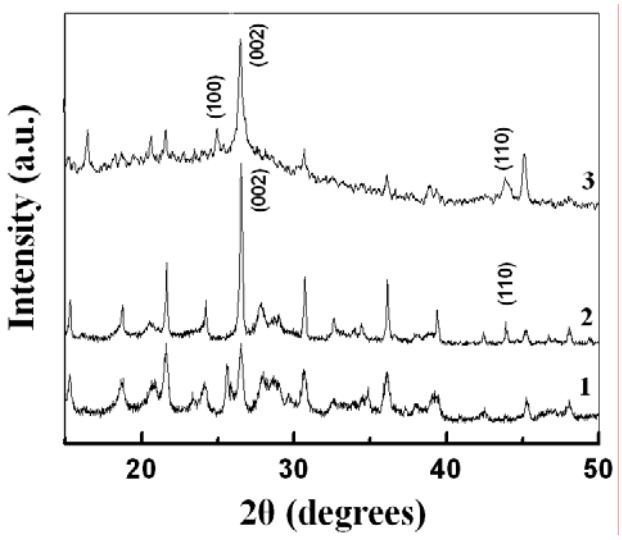

Figure 5.15: XRD patterns recorded from drop-coated films on glass substrates from the Cd^{2+}-PTA solution before (curve 1) and after treatment with H_2S gas (curve 2). Curve 3 shows the XRD pattern of the CdS-PTA solution after alkali treatment. The Bragg reflections from CdS nanoparticles are indexed in curve 2 and 3 (text for details).

A number of sharp Bragg reflections are observed that are characteristic of the Keggin structure [48, 49]. Thus, the Cd^{2+}-PTA colloidal particles observed in the SEM images (Fig. 5.11 A,B) are crystalline with no discernible disturbance to the Keggin structure. The XRD pattern recorded from a drop-coated film of the Cd^{2+}-PTA complex after treatment with H_2S gas on a glass substrate is shown as curve 2 in Fig.5.15. A few additional Bragg reflections appear after H_2S gas treatment (compare with curve 1). These Bragg reflections are indexed in the figure and correspond to hexagonal CdS [48, 49]. The observation that the characteristic Bragg reflections of the Keggin structure are retained after nano CdS formation (curve 2) is in agreement with the microscopic evidence of retention of needlelike morphology. In Fig. 5.15, it is also noted that the peak at 45° in all the XRD curves (1-3) is from the sample holder of the instrument. The XRD pattern recorded from the CdS-PTA solution after alkali treatment is represented by curve 3 in Fig. 5.15. The Bragg reflections arising from the Keggin ions are almost completely diminished in intensity leaving behind the CdS Bragg reflections. An additional peak at $2\theta = 16.4°$ is observed, which may be due to the formation of ammonium phosphate $[(NH_4)_3PO_4]$ during the dissolution of the PTA template by NH_4OH. The broad XRD peaks from the CdS nanoparticles after removal of the Keggin ion template indicate that the CdS particles are quite small.

5.3.7 Transmission Electron Microscopy (TEM) measurements:

Samples for transmission electron microscopy (TEM) analysis of the CdS-PTA solution before and after alkali (NH_4OH) treatment were prepared by drop coating on carbon-coated copper TEM grids.

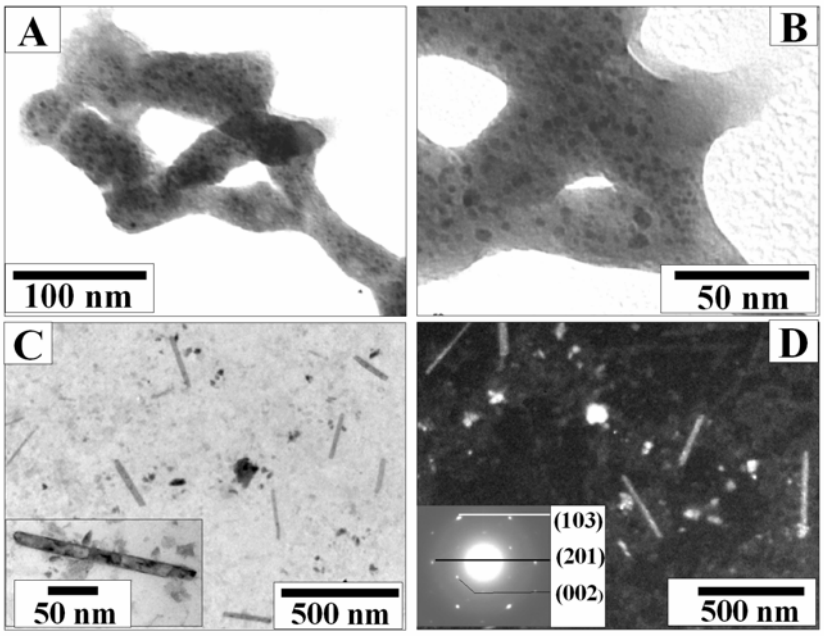

Figure 5.16: (A) and (B) Low and high magnification TEM images from the Cd^{2+}-PTA solution after H_2S treatment. (C) and (D) Bright and dark field TEM images of CdS nanorods formed after the alkali treatment of the CdS-PTA solution. The inset in (C) shows an image of one of the CdS nanorods in greater detail, and the inset in (D) shows the SAED pattern of the CdS nanorods shown in (C).

From the SEM images of the Cd^{2+}-Keggin ion colloidal particles subjected to H_2S treatment (Fig. 5.13 A and B), it is not possible to clearly distinguish the individual CdS nanoparticles formed in the needlelike colloidal particles and therefore we have carried out the TEM measurements. Parts A and B of Fig.5.16 show TEM micrographs recorded at different magnifications from drop-coated films of the Cd^{2+}- PTA solution after H_2S gas treatment on a carbon-coated copper TEM grid. It is clearly seen that the CdS nanoparticles (dark spots on a gray background) are present in reasonably high density on the CdS-PTA needlelike particles. The presence of the particles is most likely on the surface of the Keggin ion template and could arise by diffusion of the Cd^{2+} ions to the colloidal particle surface followed by reaction with sulfide ions. ITC measurements presented earlier have shown that the Cd^{2+} ions bind extremely strongly with the PTA anions (Fig.5.10A,B). It is highly likely that consequent to treatment of the Cd-PTA colloidal particles with H_2S gas, the CdS nanoparticles thus formed are capped by strongly interacting PTA scaffold there by confining the size of the CdS particles to the nanometer range. Capping of CdS nanoparticles by the PTA template also prevents the further growth of CdS nanoparticles to larger sizes. The EDX analysis discussed earlier indicates that

almost all of the Cd^{2+} ions in the colloidal particles are consumed in CdS nanoparticle formation. The size of the CdS nanoparticles was estimated from these images to be in the range 5-6 nm, in good agreement with the size determined from UV-vis absorption measurements. The CdS-PTA solution was then treated with alkaline solution to decompose the Keggin ion templates and the TEM images recorded from this sample are shown in Fig.5.16C (bright field image) and D (dark field image). The inset of Fig.5.16C shows a TEM image of one of the CdS nanostructures obtained after alkali treatment at higher magnification. After alkali treatment, it is observed that the large colloidal templates within which the spherical CdS nanoparticles reside are removed (compare Fig.5.16 A and C). Furthermore, the CdS nanoparticles appear to assemble into rodlike structures of ca. 200-280 nm length (Fig. 5.16C). The widths of the CdS nanorods range from ca. 15 to 17 nm. That these nanorods are indeed due to CdS is indicated by the dark field image shown in Fig. 5.16D. The inset of Fig.5.16D shows the selected area electron diffraction (SAED) pattern of the CdS nanorods shown in Fig.5.16C. The electron diffraction spots could be indexed on the basis of the hexagonal structure of CdS thus showing that the CdS structures are nanocrystalline. It is not surprising that growth of CdS nanoparticles on the needlelike Cd-PTA colloidal particles should retain the symmetry of the underlying scaffold from which they originate (Fig.5.16A, B). Removal of the Keggin ion scaffold consequent to alkali treatment frees the CdS nanoparticles to fuse into superstructures. We believe the removal of the Keggin ion scaffold is a relatively slow process thereby resulting in slow assembly of the CdS nanoparticles followed by their fusion that would naturally reflect the symmetry of the underlying needlelike colloidal particles. The TEM analysis shows that removal of the stabilizing influence of the Keggin ion colloidal scaffold results in assembly of the spherical CdS nanoparticles into nanorods.

Thus Cd^{2+} ions complexed with phosphotungstate anions leads to the formation of needle-shaped colloidal particles and after treating with H_2S gas yield CdS nanoparticles within the Keggin crystal host without affecting the crystallinity of the host. After dissolving the host template Keggin ions by alkali treatment the CdS nanoparticles further assembled and transformed into nanorods.

5.4 Summary

In this chapter, it has been shown that Ag^{+}–Keggin ion and Cd^{2+}-Keggin ion colloidal particles are excellent templates for the synthesis and assembly of silver and CdS nanoparticles. More specifically, we have shown that the formation of aqueous colloidal particles of Ag^{+} and Cd^{2+} ions complexed with phosphotungstate $(PW_{12}O_{40})^{3-}$ Keggin ions can be used as a new class of inorganic scaffolds in the synthesis of metal and semiconductor nanoparticle assemblies. For synthesis of silver nanoparticles, the Keggin ion host plays the role of a UV-switchable reducing agent. The crystalline Keggin ion host has been reduced photochemically resulting in electron transfer to the entrapped silver ions and consequent formation of silver nanoparticle assemblies on the underlying colloidal particle surface. Treatment with alkali results in dissolution of the colloidal particle template leaving behind the silver nanoparticle network reasonably intact. Cd^{2+} ions complexed with phosphotungstate Keggin ions form needle-shaped colloidal particles and after treating with H_2S gas yielded CdS nanoparticles within the Keggin crystal host without affecting the crystallinity of the host. It has been also shown that the Keggin ion host may be decomposed by alkali treatment to release the CdS nanoparticles and facilitate further assembly and shape transformation to nanorods. Thus, the possibility of using the Keggin ion framework as a versatile nanoreactor and UV-switchable reducing matrix is exciting and can be extended to the creation of other highly organized hybrid (nano)inorganic structures with possible applications in catalysis and novel optical materials.

5.5 References

[1] (a) Shipway, A.N.; Katz, E.; Willner, I. *ChemPhysChem* **2000**, *1*, 18. (b) Remacle, F.; Levine, R.D. *ChemPhysChem* **2001**, 2, 20.

[2] Collier, C.P.; Saykally, R.J.; Shiang, J.J.; Henrichs, S.E.; Heath, J.R. *Science* **1997**, *277*, 1978.

[3] Maier, S.A.; Brongersma, M.L.; Kik, P.G.; Meltzer, S.; Requicha, A.A.G.; Atwater, H.A. *Adv.Mater*. **2001**, *13*, 1501.

[4] Hu, J.; Odom, T. W.; Lieber, C. M. *Acc. Chem. Res*. **1999**, *32*, 435.

[5] Patzke, G. R.; Krumeich, F. K.; Nesper, R. *Angew. Chem. Int. Ed*. **2002**, *41*,2446.

[6] Li, M.; Mann, S. *Langmuir* **2000**, *16*, 7088.

[7] Li, M.; Schnablegger, H.; Mann, S. *Nature,* **1999**, *402*, 393.

[8] (a) Mirkin, C. A.; Letsinger, R. L.; Mucic, R. C.; Storhoff, J. J.; *Nature*, **1996**, *382*, 607. (b) Alivisatos, A. P.; Johnsson, K. P.; Peng, X.; Wilson, T. E.; Loweth, C. J.; Bruchez, M.; Schultz, P. G. *Nature*, **1996**, *382*, 609.

[9] Zeng, H.; Li, J.; Liu, J.P.; Wang, Z.L.; Sun, S. *Nature* **2002**, *420*, 395.

[10] Liu, X.; Fu, L.; Hong, S.; Dravid, V.P.; Mirkin, C. A. *Adv. Mater*. **2002**, *14*, 231.

[11] Velv, O. D.; Tessier, P.M.; Lenhoff, A. M.; Kaler, E. W. *Nature*, **1999**, *401*, 548.

[12] Wang, D.; Maceira, V.S.; Liz-Marzan, L. M.; Caruso, F. *Adv. Mater*. **2002**, *14*, 908.

[13] Lin, Y.; Skaff, H.; Emrick, T.; Dinsmore, A. D.; Russel, T. P. *Science* **2003**, *299*, 226.

[14] (a) Brust, M.; Bethell, D.; Schiffrin, D.J.; Kiely, C. J. *Adv. Mater*. **1995**, *7*,795. (b) Brust, M.; Bethell, D.; Kiely, C. J.; Schiffrin, D.J. *Langmuir* **1998**, *14*, 5425.

[15] (a) Mucic, R. C.; Storhoff, J. J.; Mirkin, C. A.; Letsinger, R. L.; J.Am.Chem.Soc. 1998, 120,12674. (b) Teranishi, T.; Haga, M.; Shinozawa, Y.; Miyake, M. *J. Am.Chem.Soc.* **2000**, *122*, 4237.

[16] Shenton, W.; Douglas, T.; Young, M.; Stubbs, G.; Mann, S. *Adv.Mater.* **1999**, *11*, 253.

[17] Kumar, A.; Pattrakine, M.; Bhadbhade, M.; Mandale, A. B.; Ganesh, K. N.; Datar, S. S.; Dharmadhikari, C.V.; Sastry, M. *Adv.Mater.* **2001**, *13*, 341.

[18] Che, G.; Lakshmi, B. B.; Martin, C. R.; Fisher, E. R. *Langmuir* **1999**, *15*, 750.

[19] Xue, B.; Chen, P.; Hong, Q.; Lin, J.; Tan, K. L. *J. Mater. Chem.* **2001**, *11*, 2378.

[20] Davis, S. A.; Patel, H. M.; Mayes, E. L.; Mendelson, N. H.; Franco, G.; Mann, S. *Chem. Mater*.**1998**, *10*, 2516.

[21] Caruso, F.; Lichtenfeld, H.; Giersig, M.; Mo¨hwald, H. *J. Am. Chem. Soc.* **1998**, *120*, 8523.

[22] Hall, S. R.; Shenton, W.; Engelhardt, H.; Mann, S. *Chem. Phys. Chem*. **2001**, *3*, 184.

[23] Tanev, P. T.; Chibwe, M.; Pinnavaia, T. J. *Nature* **1994**, *368*, 321.

[24] Jun, Y. N.; Dabbs, D. M.; Aksay, I. A.; Erramilli, S. *Langmuir* **1994**, *10*, 3377.

[25] Raman, N. K.; Anderson M. T.; Brinker, C. J. *Chem. Mater*.**1996**, *8*, 1682.

[26] Mann, S.; Burkett, S. L.; Davis, S. A.; Fowler, C. E.; Mendelson, N. H.; Sims, S. D.; Walsh, D.; Whilton, N. T. *Chem. Mater*. **1997**, *9*, 2300.

[27] (a) Bein, T. *Chem. Mater*. **1996**, *8*, 1636.; (b) Davis, M. E. *Chem.Eur. J*., **1997**, *3*, 1745.

[28] Goltner C. G.; Antonietti, M. *Adv. Mater.* **1997**, *9*, 431.

[29] Buining, P. A.; Humbel, B. M.; Philipse A. P.; Verkleij, A. J. *Langmuir*, **1997**, *13*, 3921.

[30] Giersig, M.; Ung, T.; Liz-Morzan L. M.; Mulvaney, P. *Adv.Mater*. **1997**, *9*, 570.

[31] Santra, S.; Tapec, R.; Theodoropoulou, N.; Dobson, J.; Hebart A.; Tan, W. *Langmuir*, **2001**, *17*, 2900.

[32] Kawahashi N.; Matijevic, E. *J. Colloid Interface Sci*., **1991**, *143*, 103.

[33] Gallis K. W.; Landry, C. C. *Adv. Mater*., **2001**, *13*, 23.

[34] Lu, Y.; Yin Y.; Xia, Y. *Adv. Mater*. **2001**, *13*, 271.

[35] Caruso, F.; Spasova, M.; Susha, A.; Giersig M.; Caruso, R. A. *Chem. Mater*. **2001**, *13*, 109.

[36] Caruso, F. *Chem. Eur. J*., **2000**, *6*, 413.

[37] Perez-Maqueda L. A.; Matijevic, E. *Chem. Mater*. **1998**, *10*, 1430.

[38] Koliadima, A.; Pe´rez-Maqueda L. A.; Matijevic, E. *Langmuir*, **1997**, *13*, 3733.

[39] Huheey,J. A.; *Inorganic Chemistry*, 3rd edn., Harper and Row, New York, **1983**, p. 698.

[40] Misono, M. *Mater. Chem. Phys*., **1987**, *17*, 103.

[41] (a) Henglein, A. *J.Phys.Chem*. **1993**, *97*,5457. (b) Sastry, M.; Bandyopadhyay, K.; Mayya, K.S. *Coll.Surf.A*. **1997,***127*, 221

[42] Cotton F. A.; Wilkinson, G. *Advanced Inorganic Chemistry*, 5th edn., John Wiley and Sons, New York, **1988**, p. 817.

[43] Henglein, A. *Chem. Re*v. **1989**, *89*, 1861.

[44] Brus, L. E. *J. Chem. Phys.* **1984**, *80*, 4403.

[45] Gole, A.; Sastry, M. *Inorganic Chemistry Communication*, **2001**, *4*, 568.

[46] Pe'rez-Maqueda, L. A.; Matijevic, E. *Chem. Mater*. **1998**, *10*, 1430.

[47] Koliadima, A.; Pe´rez-Maqueda, L. A.; Matijevic, E.*Langmuir* **1997,** *13*, 3733.

[48] Colvin, V. L.; Goldstein, A. N.; Alivisatos, A. P. *J. Am. Chem.Soc*. **1992**, *114*, 5221.

[49] Kundu, M.; Khosravi, A. A.; Kulkarni, S. K. *J. Mater. Sci.* **1997**, *32*, 245.

Chapter 6

Conclusions

The salient features of the work detailed in the thesis and possible avenues for future work are briefly discussed.

6.1 Summary of the work

Nanotechnology in a broad sense deals with the study of materials in the nano dimensions. This includes the studies on colloidal particles, biomolecules, polymers etc., and their interactions with each other. The establishment of efficient synthetic routes for the construction of nanometer-scale architectures/conjugates/materials is of paramount importance if the goals of molecular electronics, sensing, catalysis etc., are to be realized.

The objective of this thesis is to develop a strategy for the synthesis of nanocomposites in thin film form as well as in solution. Metal nanoparticle films may be synthesized in patterned lipid films by a novel ion entrapment and reduction process. The detailed investigations into a new approach for the formation of nanocomposites of metal/semiconductor nanoparticles and lipids by a process driven by electrostatic interactions have been described in this thesis. It is shown that a thermally evaporated lipid film, ionized under appropriate conditions when immersed into different electrolyte solutions, leads to the diffusion of the ions, which can be monitored using a host of techniques. The in-situ reduction of the entrapped ions leads to the formation of metal/semiconductor nanoparticles within the lipid matrix. The process of metal ion incorporation and reduction may be repeated a number of times to increase the nanoparticle density in the lipid matrix. It has been shown that the protein is intercalated within the lipid bilayers and not on the film surface. In this protocol the reduction process occurred using an external reducing agent however, when the lipid matrix itself acts as a reducing agent, then we obtained dendritic fractal nanostructures within the film. Therefore, the nanostructures in the lipid matrix depend on the host matrix and reduction process. This thesis also describes a new approach to the formation of phase pure core-shell nanoparticles using Keggin ions as photo-switchable reducing agents. The core-shell nanoparticles are very important as catalyst and it has been shown that Keggin capped metal nanoparticles act as a new class of catalyst wherein both the metal core and Keggin ion shell may be used in a range of catalytic reactions leading to a truly multifunctional catalyst. In the thesis it has been shown that Keggin ions complexed with different ions (Ag^{+}, Cd^{2+}) form colloidal particles, which are excellent templates for the synthesis and assembly of metal/semiconductor (silver and CdS) nanoparticles. It has also been shown that the Keggin ion host may be decomposed by alkali treatment, leaving behind the metal nanoparticle network reasonably intact.

6.2 Scope for future work

Thermally evaporated lipid films are a versatile method for doing interesting chemistry via entrapment of different ions in the lipid matrix either simultaneously or sequentially and carrying out different reactions to yield, for example, nanoparticles of semiconductors and oxides. More intricate patterns of the defining lipid matrix may also be envisaged and these aspects are being pursued vigorously. It is also possible to generate of patterned films by encapsulation of different proteins/DNA in arrays of the lipids, octadecylamine (ODA) and stearic acid (StA) deposited on one substrate and shows promise for single-chip multianalyte immunoassay, high-throughput biosensor and catalysis applications. Immobilizing various proteins and DNA on a single chip can easily perform multi-step biocatalytic reactions and diagnosis.

The immobilization of a reducing agent on the surface of the core metal would selectively reduce the second metal ions on the surface of core metal and thereby lead to phase-pure core-shell structures. Therefore, by this protocol it is possible to realize a large combination of core-shell nanostructures using Keggin ions with potential applications in engineered nanomaterials and catalysis.

Keggin ions form colloidal particles of different morphology complexed with different ions and organic molecules such as amino acids and they may be used as a new class of organic-inorganic scaffolds in the synthesis of metal nanoparticle assemblies. The possibility of using the Keggin ion framework as a versatile nanoreactor and UV-switchable reducing matrix is exciting and can be extended to the creation of other highly organized hybrid (nano) inorganic structures with possible applications in catalysis and novel optical materials.

List of Publications:

1. *"Electrostatic entrapment of chloroaurate ions in patterned lipid films and the in-situ formation of gold nanoparticles"*
   Saikat Mandal, S.R. Sainkar and Murali Sastry, ***Nanotechnology*** *12* (2001) 358-362.

2. *"Assembly of CdS nanoparticles in patterned structures by a novel ion-entrapment process in thermally evaporated fatty acid films"*
   Saikat Mandal, C. Damle, S.R. Sainkar and Murali Sastry, ***J.Nanosci. Nanotech***. *1* (2001) 281-285.

3. *"Studies on the reversible aggregation of cysteine-capped colloidal silver particles interconnected via hydrogen bonds"*
   Saikat Mandal, A. Gole, N. Lala and Murali Sastry, ***Langmuir*** *17* (2001) 6262-6268.

4. *"One-step synthesis of hydrophobized gold nanoparticles of controllable size by the reduction of aqueous chloroaurate ions by hexadecylaniline at the liquid-liquid interface"*
   PR. Selvakannan, **Saikat Mandal**, R. Pasricha, S.D. Adyantaya and Murali Sastry, ***Chem.Commun***. (2002) 1334-1335.

5. *"Patterned silver nanoparticle assemblies by a novel ion-entrapment process in fatty acid films"*
   Saikat Mandal and Murali Sastry, ***Mater.Res.Bull***. *37* (2002) 1613-1621.

6. *"Benzene and anthracene-mediated assembly of gold nanoparticles at the liquid-liquid interface"*
   A. Kumar, **Saikat Mandal**, S. Mathew, A.B. Mandale, R.V. Chaudhari and Murali Sastry, ***Langmuir*** *18* (2002) 6478-6483.

7. *"Synthesis of a stable gold hydrosol by the reduction of chloroaurate ions by the amino acid, aspartic acid"*
   Saikat Mandal, PR. Selvakannan, S. Phadtare, R. Pasricha and Murali Sastry, ***Proc.Ind.Acad.Sci.,Chem.Sci***. *114* (2002) 513-520.

8. *"A new method for the synthesis of hydrophobized, catalytically active Pt nanoparticles"*
   Saikat Mandal, PR. Selvakannan, D. Roy, R.V. Chaudhari and Murali Sastry, ***Chem.Commun***. (2002) 3002-3003.

9. *"Fractal gold nanostructures by the spontaneous reduction of chloroaurate ions in thermally evaporated hexadecylaniline thin films"*
   Saikat Mandal, S. Phadtare, PR. Selvakannan, R. Pasricha and Murali Sastry, ***Nanotechnology*** *14* (2003) 878-881.

10. *"Keggin ions as UV-switchable reducing agents in the synthesis of Au core-Ag shell nanoparticles"*
    Saikat Mandal, PR. Selvakannan, R. Pasricha and Murali Sastry, ***J.Am.Chem.Soc***. *125* (2003) 8440-8441.

    - **"Highlights in Science Editors' Choice":** ***Science, 301*** **(2003), 279.**

11. "*Gold nanosheets/ribbons by the reduction of aqueous chloroaurate ions near hexadecylaniline monolayers at the air-water interface"*
    A. Swami, A. Kumar, PR. Selvakannan, **Saikat Mandal**, R. Pasricha and Murali Sastry, ***Chem.Mater***. *15* (2003) 17-19.

12. "*Langmuir-Blodgett films of hydrophobized, laurylamine-modified gold nanoparticles organized at the air-water interface"*
    A. Swami, A. Kumar, **Saikat Mandal**, PR.Selvakannan and Murali Sastry, ***J.Coll.Inter.Sci***. *260* (2003) 367-373.

13. "*Capping of gold nanoparticles by the amino acid, lysine, renders them water dispersible"*
    PR. Selvakannan, **Saikat Mandal**, S. Phadtare, R. Pasricha and Murali Sastry, ***Langmuir*** *19* (2003) 3545-3549.

14. "*Understanding the interaction between gold nanoparticles and surface-bound alkyl amine-molecules"*
    A. Kumar, **Saikat Mandal**, PR. Selvakannan, R. Pasricha, A.B. Mandale and Murali Sastry, ***Langmuir*** *19* (2003) 6277-6282.

15. *"A new method for the synthesis of hydrophobic gold nano-tapes"*
    PR. Selvakannan, **Saikat Mandal**, R. Pasricha and Murali Sastry, ***J.Nanosci.Nanotech***. *3* (2003) 372-374.

16. "*Ag^{+}-Keggin ion colloidal particles as novel templates for the growth of silver nanoparticle assemblies"*
    Saikat Mandal, D. Rautaray and Murali Sastry, ***J.Mater.Chem***. *13* (2003) 3002-3005.

17. "*Water-dispersible tryptophan-protected gold nanoparticles prepared by the spontaneous reduction of aqueous chloroaurate ions by the amino acid"*
    PR. Selvakannan, **Saikat Mandal**, S. Phadtare, A. Gole, R. Pasricha, S.D. Adyanthaya and Murali Sastry, ***J.Colloid Interface Sci.*** *269* (2004) 97-102.

18. "*Aqueous foams for the synthesis of gold nanoparticles of variable morphology"*
    Saikat Mandal, S.K. Arumugam, S.D. Adyanthaya, R. Pasricha and Murali Sastry, ***J.Mater.Chem***. *14* (2004) 43-47.

19. *"Synthesis and assembly of CdS nanoparticles in Keggin ion colloidal particles as templates"*
Saikat Mandal, D. Rautaray, A. Sanyal and Murali Sastry, ***J.Phys.Chem.B***. *108* (2004) 7126-7131.

20. *"Hydrophobic, organically dispersible gold nanoparticles of variable shape by the spontaneous reduction of aqueous chloroaurate ions by hexadecylanline molecules"*
PR. Selvakannan, **Saikat Mandal**, A. Kumar, R. Pasricha and Murali Sastry, ***J.Colloid Interface Sci***. *279* (2004) 124-131.

21. *"Pt and Pd nanoparticles immobilized on amine-functionalized zeolite : excellent catalysts for hydrogenation and Heck reactions"*
Saikat Mandal, Debdut Roy, Raghunath V. Chaudhari and Murali Sastry, ***Chem.Mater***. *16* (2004) 3714-3724

22. *"Keggin ion-mediated synthesis of aqueous phase-pure Au@Pd and Au@Pt core-shell nanoparticles "*
Saikat Mandal, Anandrao B. Mandale and Murali Sastry, ***J. Mater. Chem***. *14* (2004) 2868-2871.

23. *"Interfacing biology with nanoparticles"*
Saikat Mandal, S. Phadtare and Murali Sastry, ***Current Applied Physics*** *5* (2005) 118-127.

24. *"Synthesis and assembly of gold nanoparticles in quasi-linear lysine-Keggin ion colloidal particles as a template"*
Ambarish Sanyal, **Saikat Mandal** and Murali Sastry, **Adv. Func. Mater**. (In Press).

25. *"Synthesis of Hydroxyapatite Crystals Using Amino Acid-Capped Gold Nanoparticles as a Scaffold"*
Debabrata Rautaray, **Saikat Mandal** and Murali Sastry, ***Langmuir*** (Accepted).

.

26. *"Keggin ion-mediated Synthesis of Hydrophobized Pd Nanoparticles for Multifunctional Catalysis"*
Saikat Mandal, Avisek Das, Rajendra Srivastava and Murali Sastry, ***Langmuir*** (Accepted).

.